A New Pore-Scale Numerical Simulator

for Investigating Special Core Analysis Data

Thesis submitted for the degree of
Doctor of Philosophy

by

Ahmed Hamdi Boujelben
Institute of Petroleum Engineering
Heriot-Watt University

August 2017

Abstract

The study presented in this thesis addresses various pore-scale phenomena related to the oil industry by implementing new numerical models capable of simulating a wide range of multiphase flow processes such as depressurisation, water flooding, gas injection and various EOR techniques. The aim is not to produce quantitative predictions *per se* but rather to examine the effect of key petrophysical parameters on oil recovery when different production protocols are applied to specific rock analogues. In order to facilitate this, a new pore-scale process simulator is developed – *numSCAL* (numerical Special Core Analysis Laboratory) – with different modules associated with different mechanisms.

A steady-state depletion model is described first and used to investigate the impact of numerous parameters on solution gas drive. We show that parameter combinations that increase bubble density can lead to delayed gas breakthrough and can result in high critical gas saturations. The model is extended to support three-phase flow by incorporating concepts from graph theory. Simulation results highlight the interaction between the underlying phase saturations, spreading conditions and wetting films and emphasise the competition among mechanisms acting in three-phase systems.

Two unsteady-state models are also presented to study water flooding processes in porous media – the first mainly applied to simulate drainage processes and the second used to study the onset of ganglia mobilisation. Results show that parameters affecting the capillary number and viscous ratio play a crucial role in determining the observed invasion regime and final oil recoveries. Conditions required for ganglia mobilisation are derived and used to predict the likelihood of mobilisation at different parts of the reservoir.

The dynamic drainage model is then extended to simulate low salinity (LS) water flooding and polymer injection – secondary and tertiary effects are shown to depend on interactions amongst several key flow parameters (including initial reservoir wettability, flow rate and viscous ratio). In addition, a positive synergistic effect is identified, where the combined injection of LS brine and polymer leads to increased recovery in several scenarios.

The study concludes with an application of the pore-scale modelling technique in a novel research area. A new approach is presented to model drug perfusion surrounding Glioblastoma Multiform (GBM) tumours. Results show that blood flow, transmural transport and tissue diffusion have a direct impact on the average drug concentrations that develop in the vascular network and the surrounding tissue.

To Mhairi Lou

Acknowledgements

This thesis would not have been accomplished without the support and guidance of my supervisor Professor Steven McDougall. His knowledge, kindness, patience, trust, suggestions and ideas have made working on this thesis a rich and insightful experience and for that I am deeply grateful. Thank you Steven.

I would also like to thank Dr Mohamed Regaieg for his assistance and kind help during the first year of my program. Our long discussions about pore network modelling have contributed to many of the ideas presented in this work.

Special thanks go to Dr Michael Watson for his invaluable help that made my introduction to mathematical biology smooth and enjoyable. His contribution and assistance are much appreciated.

None of this research would have been conducted without the financial support provided by Maersk Oil. This support is gratefully acknowledged. Many thanks are also due to TOTAL EOR team for the valuable technical discussions related to the modelling of Low Salinity effect.

Finally, I would like to express my gratitude to my family for their unconditional support and to my fellow PhD students for the moments we shared in the last years.

List of Publications

Boujelben, A., McDougall, S.R., 2016. Dynamic Simulation of Multiphase Flow and Ganglion Mobilisation in Digital Porous Media. Paper presented at the 8th International Conference on Porous Media & Annual Meeting (Interpore), May 9-12, 2016, Cincinnati, Ohio, USA.

Boujelben, A., Watson, M., McDougall, S.R., Yen, Y.F., Gerstner, E.R., Catana, C., Deisboeck, T., Batchelor, T.T., Boas, D., Rosen, B., Kalpathy-Cramer, J. and Chaplain, M. A. J., 2016. Multimodality imaging and mathematical modelling of drug delivery to glioblastomas. Interface Focus, 6(5), issue 20160039.

Boujelben, A., McDougall, S.R., 2017. Dynamic Pore Scale Modelling of Multiphase Flow during Application of EOR Techniques. Paper presented at the 19th European Symposium on Improved Oil Recovery (EAGE), April 24-27, 2017, Stavenger, Norway.

Contents

Chapter 1

Introduction

Global energy consumption has significantly increased in the last few decades and is expected to reach 250 quadrillion Btu by 2040 (compared to 150 quadrillion Btu in 2000) according to the U.S. Energy Information Administration (International Energy Outlook, 2016 [1]). This high consumption has been met to date by maintaining energy production from all available sources at consistent levels with energy demand. Although numerous policies have been adopted in many countries to encourage the harvesting of sustainable and clean energy and restrict CO2 emission, hydrocarbons – crude oil and natural gas in particular – still represent the major source of produced energy in the world. Moreover, these are expected to stay at the top ranking for the next 40 years (Figure 1.1). This puts a great responsibility upon the petroleum industry to keep satisfying world energy demands until alternative energy sources become sufficiently available in the future.

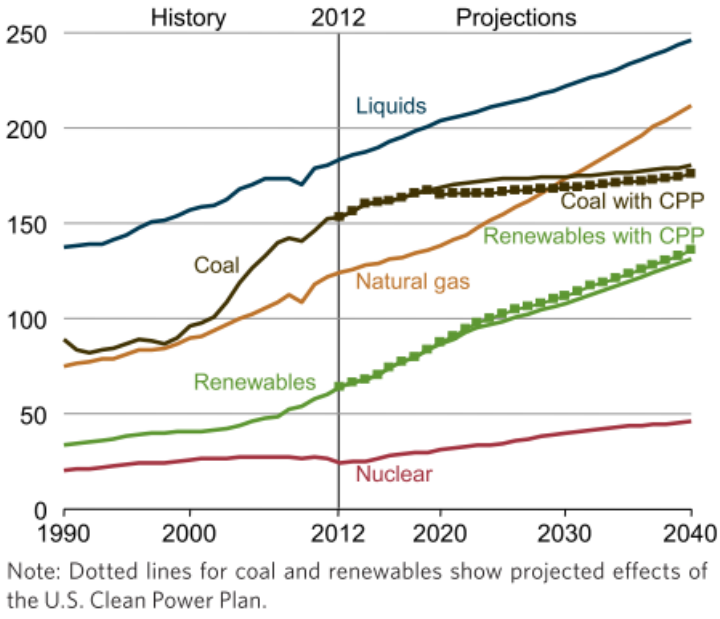

Figure 1.1: World energy consumption (quadrillion Btu) by energy source, 1990 - 2040 (International Energy Outlook, 2016).

One major challenge that faces petroleum engineers lies in the fact that available hydrocarbons found in oil reservoirs can not be fully recovered; in fact, the term "oil reserves" refers to the total estimated amounts of oil that can be practically extracted from the underlying reservoirs. Several techniques have been devised in the last century to maximise hydrocarbon recovery: such methods range from exploiting the natural internal energy of a reservoir (i.e. reservoir depletion), to injecting cheap and readily available fluids into the reservoir to displace the hydrocarbons (i.e. water and gas flooding), to more advanced but costly methods that aim to enhance recovery after traditional approaches have been deployed (i.e. EOR techniques). The efficiency of these methods depends on having a good knowledge of the reservoir properties and the key parameters that affect the flow of various fluids through it. This is usually achieved through experimental analysis of core samples extracted from the reservoir of interest and upscaling the core properties to the field scale using numerical techniques.

Although core analysis data are generally useful to identify petrophysical properties of the underlying reservoir rock, substantial variations and uncertainties can emerge from investigating multiple cores extracted from the same area. Furthermore, fluid flow in the reservoir is a pore-scale phenomenon, and improved understanding of the underlying mechanisms governing any production process requires simulating multi-phase displacements at the appropriate scale in order to gain insights into the possible implications at larger length-scales. Hence, simulating fluid flow at the pore-scale is of key importance to complement core analysis data and build better knowledge of the underlying reservoir.

The main objective of mechanistic pore-scale modelling has been to derive multiphase flow properties – phase saturations, oil recovery, critical gas saturations, relative permeabilities and capillary pressures – from microscopic considerations using 2D and 3D networks of interconnected pore elements and, historically, the purpose of this approach has not necessarily been to calculate the parameters for a specific rock, but rather to predict what effectively controls them at the pore-scale. However, more recent developments have demonstrated that quantitative predictions can be made and recent research on reproducing laboratory production data using network models anchored to real clastic samples has proved moderately successful. Indeed, improved computing protocols now allow models consisting of hundreds of thousands of pores to be considered, representing physical samples of the order of tens of centimetres in scale. Moreover, by varying pore-scale parameters in core-scale network models, uncertainties in petrophysical measurements and laboratory procedures can be analysed more effectively and related experimental data can also be better interpreted.

The Heriot-Watt pore-network modelling group is at the leading edge of research in this area – capable of simulating various phenomena that involve water flooding, nucleation, diffusive gas transport, bubble growth, and fluid production from the micron to the metre scale. However, a generic and unified platform for pore-scale analysis is still lacking and whilst several models have been implemented by numerous researchers using various programming languages in the past (i.e. Fortran, MS Visual C++), serious difficulties persisted – for example, how to maintain the implemented versions, how to ensure communication between different software and how to make these simulators readily available to a general user. In addition, many pore-scale phenomena have not been modelled until recently, and the implementation of these mechanisms into a single application has been necessary to create the desired generic package.

In this context, we present in this thesis a new multifaceted numerical simulator that covers a wide range of pore scale phenomena. The software has been implemented *ab initio* but builds upon acquired knowledge from existing implementations and adds numerous improvements to enhance their initial capabilities. Moreover, novel models and methodologies have been implemented for the first time to simulate advanced pore-scale phenomena. The simulator has been coded using modern computer technologies and is provided with a user-friendly interface. The modules that it supports are intended to help investigate phenomena related to oil recovery ranging from the first primary processes (i.e. depletion) to the secondary recovery mechanisms (i.e. dynamic water or gas injection) to the advanced EOR techniques (i.e. low salinity water injection, polymer injection, surfactant injection).

This thesis comprises 10 main chapters that cover the following topics:

In Chapter 2, we present a literature review, where we discuss the major recent advances in pore network modelling. This includes the methods used to reconstruct digital networks from the underlying rocks and the models implemented to simulate multiphase phenomena at the pore scale including quasi-static flow (i.e. phase distributions are considered time-independent at each iteration of the simulation), quasi-static three-phase flow, unsteady-state flow (i.e. phase variations over time are computed to capture transient behaviours) and steady-state depletion (i.e. phase properties are considered to be time-independent at each pressure drop) in porous media. In this work, "quasi static" and "steady-state" are used interchangeably whenever time-dependency is not modelled and we refer to the models where transient regime is not considered as steady-state models.

An overview of the software we have implemented is given in Chapter 3. We describe the methodology we have adopted to model the pore space and we discuss the different features supported by the simulator. Moreover, we introduce a new approach

to build core-scale networks from digital analogues extracted from micro-CT images and we describe the networks used in the subsequent sensitivity analyses.

We present the basic two-phase steady-state depletion model in Chapter 4 and we discuss the implementation of the various components that characterise this process. The model description is followed by a sensitivity analysis study to examine the key parameters that affect oil recovery during depletion.

A new fully adaptible three-phase model is outlined in Chapter 5. We describe the implemented mechanisms specific to three-phase configurations and we explain the new concepts inherited from graph theory that we used to capture multi-displacement chains. The model is applied later to simulate depletion processes in waterflooded reservoirs under various initial conditions.

Chapter 6 contains the implementation details of an unsteady-state drainage model that has been implemented to simulate processes where the competition between viscous and capillary forces determines the flow pattern. The model is validated against experimental data and is used to study the effect of various petrophysical parameters on oil recovery and flow regime.

A more sophisticated dynamic model (i.e. both capillary and viscous forces are used to compute the evolution of pressure field over time) is presented in Chapter 7 that takes into account the possible mobilisation of trapped ganglia. By introducing new concepts such as natural trapping and fluctuating menisci, we use the model to simulate scenarios involving the displacement of trapped ganglia and to investigate the effect of some petrophysical properties on oil recovevry and mobilisation.

A full study of EOR processes is presented in Chapter 8. The dynamic drainage model is extended to track the evolution of tracer agent concentrations in order to simulate EOR processes, and a new methodology is proposed to quantify the impact of low salinity water and polymer injection. The new approach is used to examine the effect of key flow parameters on these two EOR processes and to capture possible synergies that may emerge when applied simultaneously.

Finally, we introduce new software in Chapter 10 that applies concepts from pore network modelling to simulate biological phenomena. Particularly, we discuss a new approach to simulate drug perfusion in irregular vasculatures around a brain tumour and we use it to investigate the effect of numerous parameters on the efficiency of chemotherapy delivery.

The final chapter presents the main conclusions of this study and suggests areas for future work.

Chapter 2

Pore Network Modelling: Literature Review

2.1 Introduction

A "Porous medium" refers to any material that comprises pores situated within a solid matrix. The terminology is used in numerous areas where materials, such as rocks, soil, cement, vascular networks, soft biological tissue and bones are considered as porous media. In the context of the oil industry, the matrix of any core sample extracted from a reservoir contains an irregular network of interconnected pores referred to as a pore network. Oil, gas and water flow in the pore space of the host rock and the physics that govern flow at the pore scale directly affects the aggregated macroscopic behaviour observed at the core and field scales. Thus, simulating flow within oil reservoirs cannot be accurately undertaken without understanding the key mechanisms governing fluid flow at the microscopic scale.

Pore Network Modelling (PNM) has become an important technique to explore flow properties at the micro scale, its main advantage being its ability to implement pore-scale mechanisms that cannot be captured using conventional reservoir simulators. Such models are able to provide better understanding of how different rock, fluid and flow properties interact at the pore scale and give useful insights into how these associations can affect macroscopic flow properties such as capillary pressure curves, relative permeability curves, oil recovery, and critical phase saturations.

Since the pioneering work of Fatt (1956) [2], who modelled porous media using regular lattices, numerous works have been described in the literature covering a wide range of multi-phase flow processes, including solution gas drive, water and gas flooding, WAG processes and EOR techniques.

In this chapter, we begin by introducing the different approaches described in the literature to model the pore space and extract equivalent digital pore networks. We then go on to present an overview of the main technical concepts associated with modelling flow in porous media. Finally, we discuss the wide range of models described in the literature to simulate pore-scale flow phenomena. These include quasi-static two-phase and three-phase flow models, various unsteady-state approaches, and depletion processes.

2.2 Modelling the Pore Space

The main concept behind pore network modelling is to approximate the void space in a porous medium using capillary elements. Whilst some works in the literature make no distinction between capillary elements, various authors classify them into pore bodies (or nodes), connected by a network of channels, called throats. Pore bodies and throats are usually assigned radii on the order of microns and the fluid flow is assumed to take place inside these capillary elements – this depends greatly on their geometry and intrinsic properties as well as the way in which they are connected to one another. Building a network that accurately captures the main topology and properties of the underlying rock structure is a crucial first step in generating a realistic rock analogue capable of yielding reliable flow simulations in later stages.

2.3 Statistically Generated Networks

One of the most basic methods for creating a network model of a specific rock consists of generating a regular lattice of interconnected capillary elements whose radii are assigned from a statistical distribution. The main two characteristics of such networks are the Pore Size Distribution (PSD) and the Coordination Number (Z).

- **Pore Size Distribution**

Different statistical distributions can be used to assign radii to the capillary elements in a regular lattice (for example, Uniform, Normal, Weibull, Rayleigh) and the choice and parameterisation of the distribution can be determined based on a calibration process (see the "3Rs approach" described later). Here, the aim is to choose a distribution that produces the best match between simulated properties

and the corresponding experimental measures from the studied rock (i.e. absolute permeability, porosity, mercury injection capillary pressure curves and relative permeability curves).

- **Coordination Number**

The coordination number is a measure of the interconnectedness between capillary elements and describes how many throats, on average, meet at each pore body. In a 2D fully-connected square network, Z is equal to four, as each pore body is connected to four neighbouring throats – similarly, Z is equal to six in a 3D fully-connected cubic network. Reducing Z in regular lattices is possible by randomly removing capillary elements until the desired value of Z is achieved.

Fatt (1956) [2] was the first to generate 2D regular networks of cylindrical tubes. Different lattices were considered in his work, including square, triangular, honeycomb and double hexagonal networks. By ranking the tubes according to their entry capillary pressure and then sequentially filling them, he was able to reproduce capillary pressure and relative permeability curves that were in agreement with experimental imbibition data. Fatt also found that PSD was more important than the lattice geometry in terms of predicting experimental results.

Further studies built upon this pioneering work and attempts were made to construct regular networks with better predictive potential. Chatzis and Dullien (1977) [3] studied the properties of both 2D and 3D networks (Figure 2.1) and found that both the dimensionality and the interconnectedness of the network played an important role in predicting the invading phase breakthrough saturation. Consequently, they concluded that 2D networks cannot be used to predict two-phase flow fractions for 3D porous media.

Dixit et al. (1998) [4] investigated a range of hysteresis phenomena by simulating drainage and imbibition in regular 3D networks. They found that the hysteresis effect is strongly affected by the coordination number as well as the initial wettability of capillary elements. Jerauld and Salter (1990) [5] also studied the underlying parameters behind the hysteresis effect by simulating drainage and imbibition in lattices constituted of pore bodies and throats. They reported that the aspect ratio between pore bodies and throats significantly affects the resulting relative permeability curves.

Jerauld et al. (1984) [6] were able to generate distorted lattices using a Voronoi algorithm. Starting with an initial dense and highly connected network, they proceeded to remove the longest throats until a coordination number equal to six was reached. Interestingly, the relative permeability curves obtained using these net-

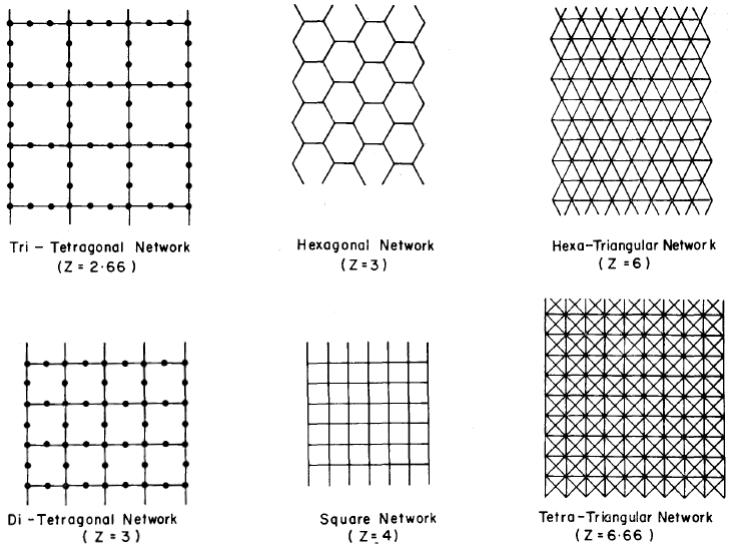

Figure 2.1: Networks used by Chatzis and Dullien (1977) [3]

works were not too different from those generated by randomised regular lattices. Blunt and King (1990) [7] used a similar technique to study the effect of capillary and viscous forces on pore scale displacements.

Lin and Slattery (1982) [8] constructed a randomised 3D network involving seven free parameters. They used this network to calculate permeability, capillary pressure curves and relative permeability curves during steady-state flow. Their results showed a reasonable agreement with the experimental data of Levrett (1939).

Heiba et al. (1992) [9] used a Bethe lattice (Figure 2.2) to generate relative permeability curves using concepts from percolation theory. By adjusting the model input parameters, their simulated results fitted reasonably with the experimental data of Talash (1976) .

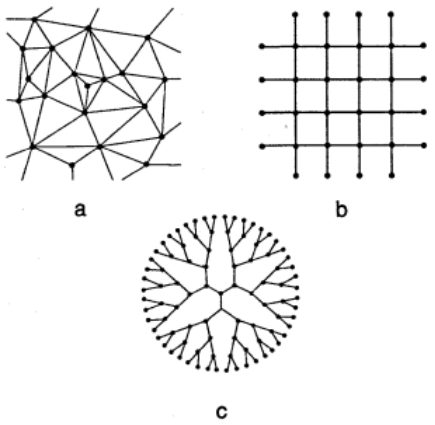

Figure 2.2: Networks used by Heiba et al. (1992) [9] (a) Voronoi tesselation, n=6.2 (b) Square, n=6 (c) Bethe, n=3

2.3.1 Anchoring Regular Networks

To add more predictive potential to regular networks, anchoring methods have been developed that attempt to capture the physical properties of specific rocks (absolute permeability, porosity) as well as the associated experimental flow data (capillary pressure curves, relative permeability curves) in order to build calibrated lattices capable of generating reliable simulations..

Wise (1992) [10] used capillary pressure curves and Young-Laplace equation (2.5) to generate the radii of the capillary elements on a regular lattice. The smallest throats were removed sequentially until the simulated absolute permeability matched the experimental value.

Rajaram et al. (1997) [11] was able to generate anchored regular networks by adequately tuning the PSD in order to fit the simulated capillary pressure curves to experimental data from real soils. The final networks were capable of matching the experimental relative permeability curves.

Fischer and Celia (1999) [12] used the same approach by calibrating regular cubic lattices using experimental capillary curves. The tuned networks generated relative permeability curves in agreement with the experimental data from a repacked porous medium. However, the match with the soil samples data was poor.

The 3Rs approach

McDougall et al. (2002) [13] introduced the "3Rs" technique to build 3D networks with similar properties to that of the studied rock. In their modelling approach, no distinction was made between nodes and throats – the network was considered instead as a lattice of interconnected cylindrical bond elements. Pore size distribution and the coordination number were tuned based on experimental mercury injection data. Four free parameters were also introduced by assigning to each bond a volume and a conductance according to power law relationships described by equations:

$$\begin{cases} V = & \bar{C}\pi r^{\nu} L 10^{6\upsilon-12} \\ G = & \bar{A}\pi r^{\lambda} \frac{10^{6\lambda-24}}{8\mu L} \\ \nu \in [0,3] & \lambda \in [1,4] \end{cases} \tag{2.1}$$

where $\bar{C}$ and$\bar{A}$ are respectively the volume and conductance constants, ν and λ are respectively the volume and conductance exponents, r is the bond inscribed radius, L is the bond length and μ is the viscosity of the fluid inside the bond.

Both exponents could be tuned to best fit so-called R-plots, which were generated by inverting the mercury injection capillary pressure data using the Young-Laplace equation (2.5). Constants were chosen to best match the absolute permeability and the porosity of the sample. By applying this approach, oil-gas relative permeability curves were successfully reproduced. This approach was also deployed successfully in the work of Bondino et al. (2009) [14] to interpret heavy oil pressure depletion experiments.

2.3.2 Limitations

Statistically generated networks have proved to be a useful tool to give an approximate description of various porous media and to provide insights into the impact of simple pore-scale features on flow mechanisms (e.g. the effect of connectivity and PSD on relative permeabilities). Studying the effects of fluid flow and rock parameters on oil trapping, displacement mechanisms, and other pore-scale related phenomena, makes these networks convenient for carrying out valuable sensitivity analyses. However, their inability to capture the complexity and irregular topology of real rocks makes their quantitative predictive potential questionable. More recent research has been carried out to try to reconstruct real networks from scans of the pore space, honouring the geological properties of the target rock. In the next section, we will describe the different methods discussed in the literature to generate pore space models based on imaging techniques.

2.4 Pore Space Models based on Imaging

2.4.1 Digital Pore Space Reconstruction

Although statistically generated pore network models are capable of capturing the broad features of the studied rock (i.e. absolute permeability, porosity), the structure of real rocks is often very different from the idealised networks produced from statistical methods. Thus, new methods have been developed to reconstruct porous media using 3D imaging. These methods can be classified into two main categories.

1. **Direct Methods**

These methods use X-ray microtomography (also referred to as Micro-CT) to recreate a virtual model of a sample without destroying it. This is achieved by creating

multiple digital images of the sample cross-sections with pixel sizes in the micrometer range. Although this technique is widely applied for medical imaging, it has been used in the last two decades to reconstruct the 3D pore space for different rock samples (Arns et al., 2005 [15], Arn et al. 2004 [16], Coker et al. 1996 [17], Rintoul et al 1996 [18], Spanne et al. 1994 [19], Dunsmuir et al. 1991 [20]).

Recent advances in Micro-CT technology has unlocked further imaging capabilities. For instance, Berg et al. (2013) [21] succeeded in reconstructing a 3D cylindrical sample of Berea sanstone and to directly image displacement events (such as drainage and snap-off) in real time. Recent work from the same group (Berg et al., 2015 [22]) has shown the onset of oil mobilisation during imbibition under unsteady-state conditions. Micro-CT images show how oil clusters prefer to break up instead of moving as a large cluster due to frequent snap-off events (Figure 2.3).

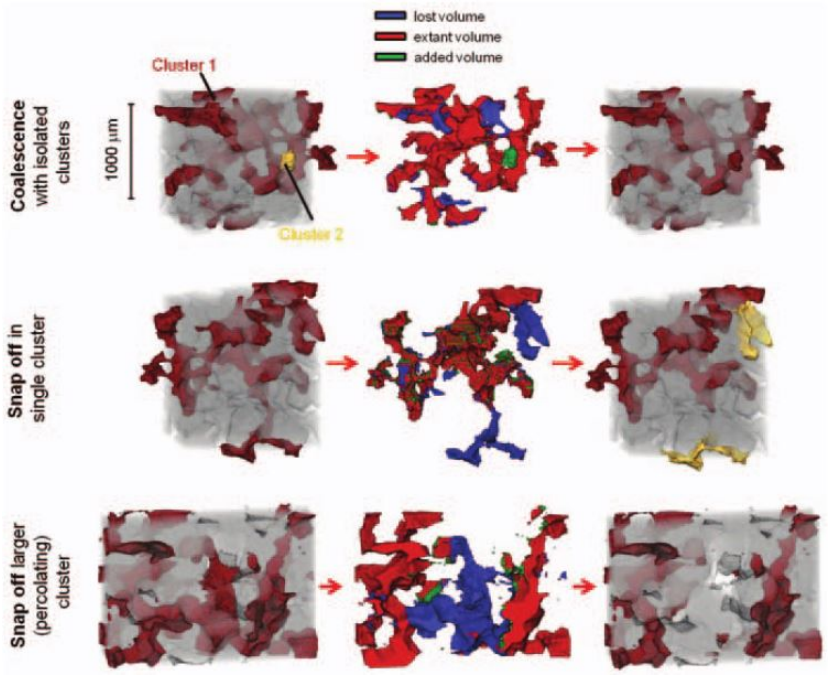

Figure 2.3: Snap-off and coalescence events observed directly in 3D (Berg et al., 2015 [22])

Despite the high-resolution images that can be obtained by applying Micro-CT imaging techniques and the valuable insights that can be obtained about the fundamentals of pore-scale mechanisms, this method is expensive to use and large rock samples are difficult to scan. Carbonates are particularly difficult to analyse using microtomography due to their high heterogeneity.

1. **Indirect Methods**

As an alternative and more accessible approach to microtomography, mathematical approaches have been developed to reconstruct the 3D pore space numerically. Some of these algorithms are now discussed.

- Process-Based methods

Process-based reconstruction aims to rebuild the 3D pore space by taking into account the physical processes that led to its formation. Thus, these methods try to model rock formation through sedimentation, compaction and diagenesis (Figure 2.4).

This approach was first proposed by Bryant et al. (1992a) [23] who generated a model of a porous medium by analysing geometrical data from a random packing of identical spheres, and succeeded (using the extracted network from the 3D pore space) to reproduce experimental relative permeability curves. Sedimentation was omitted in their work but was included in later works (Oren and Bakke, 2002 [24]; Øren et al. 1998 [25]; Bakke et al. 1997 [26]).

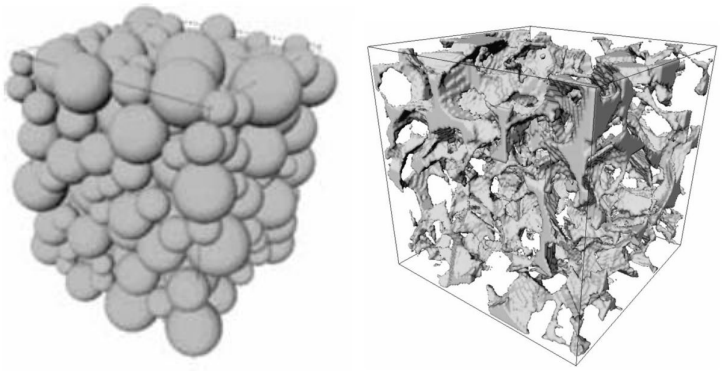

Figure 2.4: Generated pore space using Process Based Method (Oren and Bakke, 2002 [24])

Whilst these networks were capable of reproducing some multiphase transport properties (Valvatne and Blunt, 2005 [27]; Piri and Blunt 2005 [28, 29]; Oren and Bakke, 2002 [24]), several tuning parameters were required. Moreover, only a few diagenetic processes were usually modelled (precipitation of authigenic clays on the free surface and quartz cement overgrowth) [24], which makes the algorithm unsuitable when diagenesis is the dominant process in the rock formation.

- Statistical methods

An alternative to the Process-Based method is the utilisation of statistical methods to build the 3D porous space from 2D thin sections. In the first trials of this approach, the 3D voxel was generated by applying porosity and two point statistics on binary data obtained from the 2D sections (Roberts et al., 1999 [30] ; Adler and Thovert, 1998 [31], Yeong et al., 1998 [32, 33]; Roberts, 1997 [34]; Adler et al., 1992 [35]; Quiblier, 1984 [36]). As the two point statistics resulted in underestimating the real rock connectivity, Okabe and Blunt (2005) [37] improved this approach by

generating a pseudo-3D training image from data extracted from its 2D counterpart and applying a standard 3D multi-point geostatistical simulation to reconstruct the 3D space. The connectivity and porosity of the constructed porous space was preserved, although the permeability could not be matched. The algorithm was also reported to be CPU-intensive.

A more efficient algorithm was developed by Hajizadeh et al. (2011) [38], where a 3D porous medium could be reconstructed from a single 2D section. Using a multi point stochastic algorithm (MSP), the pore space was reconstructed layer by layer using a sequence of 2D MSP simulations and several geometric and flow properties of the porous medium were preserved.

Despite being useful for sandstones, the statistical reconstruction approach could be difficult to apply for rocks with unstationary properties such as carbonates.

2.4.2 Networks Extracted from Pore Space Images

The implementation of flow algorithms that run directly on the digital 3D Micro-CT models of the porous medium might be possible when applying computational fluid dynamics (CFD). For instance, Clemens et al. (2013) [39] simulated micromodel experiments by solving Navier-Stokes, mass conservation and momentum conservation equations, and was able to reproduce viscous fingering regimes during water and polymer flooding.

The lattice Boltzmann method (LBM) is another CFD technique that uses collision and recoloring rules to reproduce the flow of a Newtonian fluid. Several studies based on this approach have been carried out to simulate flow on complex and realistic topologies (Huang, 2014 [40]; Dong, 2011 [41]; Yiotis et al, 2007 [42]; Langaas and Yeomans, 2000 [43]; Chen and Doolen, 1998 [44]).

Although application of CFD techniques can provide a realistic simulation of fluid flow, they are known to be CPU-expensive, and their use is still limited to a small scale. Moreover, application of CFD techniques can be challenging for low capillary number ranges, where the resulting spurious velocities can have the same order of magnitude of the flow velocities under investigation.

A good way to take advantage of the MicroCT imaging is to extract pore networks from the 3D reconstructions. These networks have similar properties to those of the scanned porous medium and PNM techniques can be applied on them in a straightforward fashion.

Several algorithms have been developed in the past to extract networks from digital

rocks.

- **Delaunay Tesselation Algorithm**

This approach divides the space into several polyhedra that constitute the pore bodies. If we consider a sphere-packed porous medium, the void could be modelled as a group of tetrahedra, where each tetrahedron would be created by combining four nearest neighbour spheres (Figure 2.5). The Delaunay tessellation algorithm is usually applied to extract networks from 3D reconstructions obtained by process-based methods (Gladkikh and Bryant 2003 [45]; Mason and Mellor, 1995 [46]; Bryant et al., 1992 [23]).

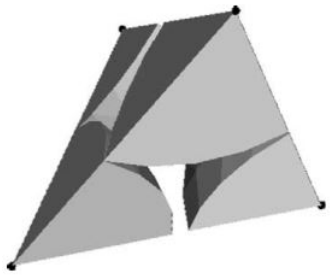

Figure 2.5: Tetrahedral cell resulting from Delaunay tessellation. The vertices of the tetrahedron are the centers of four nearest neighbor spheres. (Gladkikh and Bryant, 2003 [45])

However, this approach is difficult to apply for complex geometries and it is also unsuitable for highly connected porous media, as the maximum coordination number that could be reached is four.

- **Medial Axis Algorithm**

This method was introduced first by Lindquist and Lee (1996) [47] as a tool to analyse the void space in porous media. The algorithm begins by converting the pore space into a binary image, where every voxel represents a grain or a void. A "burning" process is then applied whereby all the void voxels adjacent to grains are removed (or burnt). This process is iterated until only one void voxel remains. If the eroding process affects a voxel from more than two directions, the voxel is labeled as a medial axis voxel. If a particular voxel is crossed by three or more medial axes (axes intersecting axis voxels), it would be considered as a "burn centre". By adopting this definition, a pore could be considered as a "burn centre" and its radius would be calculated as the maximum distance from its centre to its surrounding grain surface.

This method was applied by Lindquist and Venkatarangan (1999) [48] to derive spatial distributions of pore path lengths, pore sizes and throat sizes from a sandstone

imaged using X-Ray microtomography. Jiang (2008) [49] also extracted networks from several digital rocks by using an improved version of the same approach and introducing a new thinning technique.

The algorithm proved to be good at capturing the connectivity of the underlying rock. However other properties, such as pore size distribution, were found to be greatly affected by the partitioning of pores and throats.

- **Maximum Ball Algorithm**

This algorithm was first introduced by Silin and al. (2003) [50] and has been improved in later works (Silin and Patzek, 2006 [51]; Al-Kharusi and Blunt 2007 [52]; Dong and Blunt 2009 [53]). The idea behind the algorithm is to scan iteratively the void space in the 3D reconstruction of the porous medium and to insert the largest balls that can fit between the grain voxels. By the end of the process, the largest balls would constitute the "master voxels" and they would define the pore bodies. The smaller balls connecting the "master voxels" are called "slave voxels" and they are grouped together to constitute the pore throats (Figure 2.6).

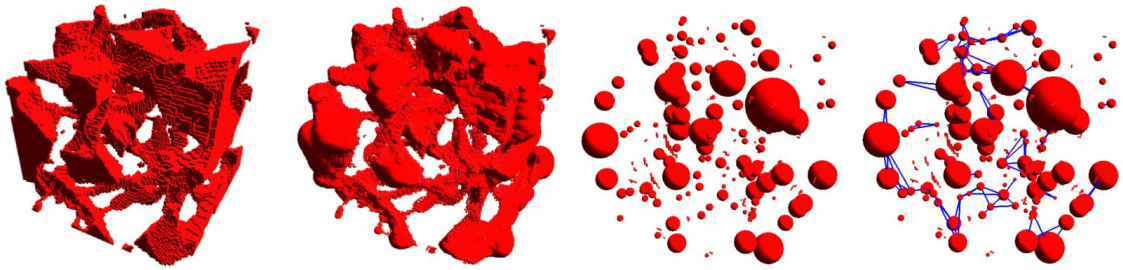

Figure 2.6: Network extraction using Maximum Ball algorithm. From left to right: (i) The pore space of a 200 × 200 × 200 image of Fontainebleau sandstone (ii) Maximal balls (iii) Master voxels (iv) The reconstruction of the pore structure and the connectivity of the pore space. (Silin, 2003 [50])

2.5 Modelling Multi-phase Flow in the Pore Space

Pore network modelling has proved to be an efficient tool to study multi-phase flow in porous media and to understand how the forces and the interaction between fluids at the pore scale can affect flow properties on the macro scale (i.e. relative permeabilities, residual oil, etc.). Several models were built in the past to simulate numerous oil recovery processes (waterflooding, gas injection, depletion, WAG) most of which usually involve displacing one fluid (usually oil) by some other fluid (usually water or gas). Most PNM models work under the assumption of immiscible displacement,

and the flow is mostly assumed to be governed by capillary, viscous and/or gravity forces.

In a two-phase system, when capillary forces are dominating (i.e. during low rate waterflooding or low rate depletion), quasi-static pore network models are usually suitable to simulate fluid displacements – these are simplistic rule-based models which are relatively fast to run. When non-negligible viscous forces are present however, more sophisticated dynamic models need to be considered to track the evolution of each fluid in the underlying networks. The addition of a third phase also requires the introduction of additional mechanisms to take into account three-phase related phenomena such as oil spreading, and chain displacements.

Few reviews exist in the literature summarising the more recent advances in the PNM area. Blunt (2001) [54] wrote a review summarising the early pore network models with emphasis on the description of the pore space description, wettability modelling, three-phase flow, and rate effects. A more recent review by Joekar-Niasar and Hassanizadeh (2012) [55] discussed the major advances in PNM models applied to various processes with more focus on dynamic models, their computational aspect, and the major challenges to improve their efficiency and predictive power.

In this section, we start by presenting a short theoretical background of the fundamental physics that play a major role in the interaction between various fluids at the pore-scale. Then, we go through some of the major models developed in the literature. This includes quasi-static models, three phase models and dynamic unsteady-state models.

2.6 Theoretical Background

2.6.1 Surface and Interfacial Tension

Molecules of a liquid are bound together via forces of molecular attraction known as cohesive forces and these forces cancel each other inside the liquid. However, at a gas/liquid interface, the liquid cohesive forces exceed the attraction forces toward gas molecules (adhesion) which results in an inward pull and the formation of a stretched surface between the two phases characterised by a surface free energy, also termed surface tension (Figure 2.7).

Surface tension is usually represented by the symbol σ or γ and has dimensions of force per unit length. Within the context of a liquid/liquid interface, this force is referred to as interfacial tension.

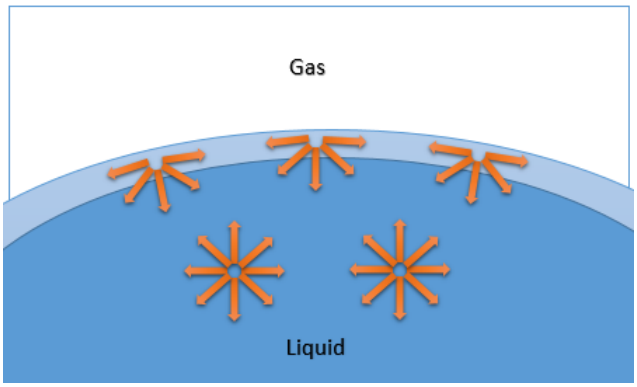

Figure 2.7: Cohesive forces between liquid molecules. On the surface, these forces do not cancel each other, resulting in a net pull inward.

Surface/Interfacial tension plays a significant role in multi-phase flow in porous media and it is also relevant to some enhanced recovery processes, where surfactants are used to decrease it.

2.6.2 Wettability and Contact Angle

The concept of wettability is usually used within the context of a solid surface in direct contact with two fluids. When one fluid has more affinity to that surface than the other, that fluid is called the wetting phase. The other fluid is referred to as the non-wetting phase.

The wettability of a surface (its affinity to one specific phase) can be determined by placing the two phases on the surface and measuring the contact angle on the liquid/solid interface (Figure 2.8). The contact angle, referred to as θ, is related to the surface tensions between the solid and the two fluids, σ_{s1} and σ_{s2}, and the interfacial tension between the two fluids, σ_{12}, via Young's equation:

$$\sigma_{s1} = \sigma_{s2} + \sigma_{12} cos\theta_{12} \tag{2.2}$$

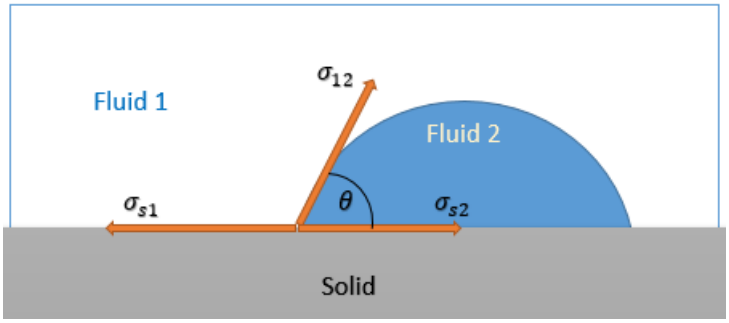

Figure 2.8: Contact angle between fluid 1 and fluid 2 and the associated force balance.

The contact angle can take any value between 0 and 180° and fluid 2 is considered to be the wetting phase if θ_{12} is less than 90°. If we consider an oil-water configuration, the system is referred to as being water-wet when the contact angle is between 0 and 90°, and oil-wet otherwise. If the contact angle is close to 90°, the porous medium is described as being neutral-wet.

The wettability of a rock greatly affects multi-phase flow (the flow regime, trapped fluids, film flow, etc.) and wettability alteration is often associated with enhanced recovery (achieved by low salinity water injection for example).

2.6.3 Spreading Phenomenon

One of the mechanisms that should be considered in any three phase model is the phenomenon of spreading. When gas is present in a porous medium where both oil and water exist, it is possible that oil forms a layer between gas and water. This phenomenon emerges naturally as a result of the force balance between the three phases described by Young's equation (Eq. 2.2). The fact that $cos\theta_{12}$ must be always less than one implies that $\sigma_{s1} - \sigma_{s2} - \sigma_{12}$ must be always negative to ensure the stability of the three phases.

If we consider oil spreading in a water wet medium, the ability of oil to spread between water and gas is described by the oil spreading coefficient defined as:

$$C_s = \sigma_{gw} - \sigma_{go} - \sigma_{ow} \tag{2.3}$$

When C_s is negative, Young's equation is satisfied, no oil spreading is expected and a lens of oil would remain stable in the presence of water. In contrast, when C_s is positive (or null), oil spreads and forms a thin layer between water (Figure 2.9).

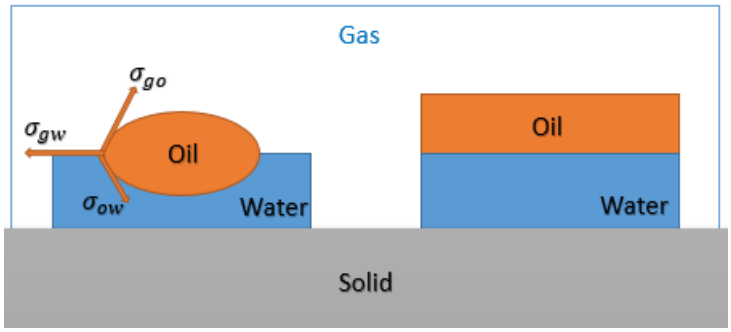

Figure 2.9: Different three-phase systems: (left) non spreading oil ($C_s < 0$) (right) spreading oil ($C_s >= 0$)

2.6.4 Capillary Pressure

The concept of capillary pressure arises when one fluid displaces another in a porous medium. To understand this concept, consider a cylindrical tube where oil (the wetting phase) and gas (the non-wetting phase) are separated by a surface characterised by a tensile force σ and a contact angle θ ($\theta < 90°$) (Figure 2.10).

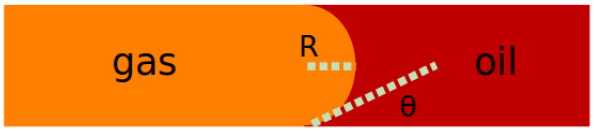

Figure 2.10: The capillary pressure created between gas and oil is a function of the radius of the cylindrical tube, the contact angle and the surface tension.

If we consider this system in equilibrium, the force balance between the elastic force on the surface circular perimeter and the pressure difference applied on the surface area is given by Laplace's equation:

$$P_g - P_o = \sigma(\frac{1}{R_1} + \frac{1}{R_2}) \tag{2.4}$$

where P_o and P_g refer respectively to the oil and gas pressure, and R_1 and R_2 to the principal radii of curvature of the surface. This yields the following relationship - known as the Young-Laplace equation - between the pressure difference across the surface and the radius r of a circular cylinder:

$$P_g - P_o = \frac{2\sigma cos\theta}{r} \tag{2.5}$$

Equation 2.5 shows that a small positive pressure difference between gas and oil is not necessarily enough to trigger a displacement of oil by the gas. Indeed, the pressure difference must overcome the "capillary pressure" given in this case by $\frac{2\sigma cos\theta}{r}$. The same interpretation remains valid for any wetting phase displacement by a non-wetting phase.

Equation 2.5 demonstrates that, during a steady-state displacement by a non-wetting fluid, large pores are expected to be filled first, whilst higher pressure differences are required to invade smaller pores.

Within the context of displacing one phase by another, the capillary pressure that must be overcome increases as the invading phase fills the porous medium. The curve that shows the capillary pressure as a function of the invading phase saturation is described as the capillary pressure curve.

We note that the expression of the capillary pressure given by equation 2.5 is only valid for cylindrical capillaries. For more complex capillary shapes, appropriate geometrical considerations must be taken into account (to be discussed later).

2.6.5 Absolute and Relative Permeability Calculation in PNM

Permeability, usually depicted as κ, is a measure of the capacity of a porous medium to let a fluid flow through it. It is a crucial parameter characterising the flow properties of a rock at the continuum scale.

If we consider single phase flow of a fluid in a porous medium then the permeability (called also absolute permeability in this context) is defined through Darcy's law, which is given by:

$$\upsilon = \frac{\kappa}{\mu}\frac{\Delta P}{L} \tag{2.6}$$

where υ is the Darcy (frontal) velocity, μ is the dynamic fluid viscosity, ΔP is the pressure difference across the porous medium, and L is the porous medium length.

When two phases are present in the rock, for example oil and gas, the concept of "effective permeability" is introduced to describe the permeability to oil in the presence of gas (and vice versa) – calculated by applying 2.6 for the oleic or gaseous phase as appropriate. *Relative* permeability is a dimensionless measure and is calculated as the ratio of the effective phase permeability to the absolute permeability of the sample.

In the context of pore network modelling, the absolute and relative permeability can be calculated by following a straightforward methodology. For the sake of clarity, consider a regular lattice which has dimensions $N_x \times N_y \times N_z$ where N_x, N_y and N_z are the number of nodes (interconnections) in the x, y and z directions respectively. Although most models distinguish between pore bodies and throats, we will describe here only a simple interconnected network of cylindrical capillaries.

For a single circular element of radius r and length L, the flow q through the element is given by Poiseuille's law:

$$q = \frac{\pi r^4}{8\mu}\frac{\Delta P}{L} \tag{2.7}$$

where μ is the viscosity of the fluid inside the capillary element, and ΔP the pressure

difference acting across it.

At each junction, conservation of mass requires that the sum of the flows q_i must add up to zero, therefore:

$$\sum_{i=1}^{6} q_i = 0 \tag{2.8}$$

(Note that Equation 2.8 is equivalent to Kirkchoff's law for a resistor network). Consideration of the entire network yields a set of linear pressure equations which can be solved using linear algebra methods. The obtained solution can then be used to calculate the elemental flows in each capillary element. The total network flow Q is then computed by summing the flows of the outlet capillaries and substituted into Darcy's equation to deduce the total network permeability κ.

If more than one fluid are flowing in the system, the process is applied for each fluid in turn, whilst freezing the other fluid. This yields the effective permeability (and consequently the relative permeability) of each fluid.

2.7 Two Phase Quasi Static Flow in Porous Media

Many pore network models have been developed in the literature to simulate two-phase quasi-static flow in porous media. This type of flow is characterised by the dominance of capillary forces and the absence of viscous gradients. Most of these models aim to track the evolution of the underlying system as one phase saturation increases.

These models aim to simulate both drainage (displacement of a wetting phase by a non-wetting phase) and imbibition (a process where the wetting phase saturation increases). By implementing the governing pore-scale mechanisms (i.e. piston-like displacement, snap-off, pore-body filling, etc.), quasi-static models can be used to reproduce experimental data (capillary pressure curves, relative permeability curves, residual saturations) or simply to study the sensitivity of the system under investigation to a range of parameters related to the rock or the fluids.

One of the earliest quasi-static models was developed by Wilkinson (1983) [56] who introduced the idea of invasion percolation. Concepts from percolation theory (Frisch and Hammersley, 1963 [57]; Broadbent and Hammersley, 1957 [58]) were used to model the problem of displacement of one fluid by another in porous media as an invasion process where each interface advance corresponded to the least

resistant capillary barrier. The model assumed a constant flow rate instead of a constant pressure gradient, which implied a sequential filling of the pores. Using several Monte Carlo simulations, it was shown that, within the context of one fluid displacing another in a regular random lattice, the saturation of the invading phase at breakthrough could be predicted as the percolation threshold of the underlying network. The model, however, ignored the effect of trapping of the defending phase, which might not be the case in real drainage scenarios.

The experimental work of Lenormand et al. (1983) [59] gave several new insights into the pore-scale mechanisms during drainage, imbibition and the displacement of residual blobs. Using a small network made of rectangular ducts, three main mechanisms were observed:

- **piston-like displacement**: a reversible displacement, where a non-wetting phase invades a specific duct if the the pressure difference between the two phases overcomes a certain threshold pressure ($\frac{2\sigma}{r}cos\theta$ for a cylindrical duct of radius r; σ and θ are, respectively, the surface tension and the contact angle between the fluids) .

- **Snap-off**: a mechanism that occurs during imbibition, where the *wetting* phase flows along the edges of the ducts and fills them (Figure 2.11) once a certain capillary pressure condition is satisfied ($\frac{\sigma}{r}cos\theta$ for a cylindrical duct of radius r). This pressure threshold required for snap-off is always less than that required for piston like displacement.

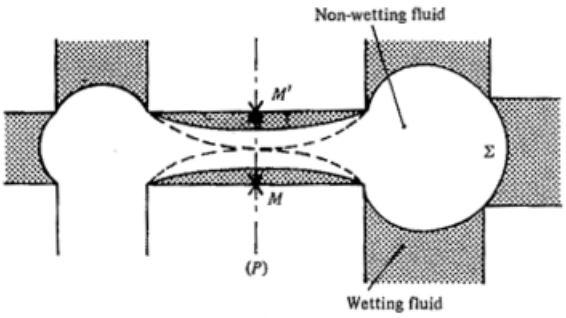

Figure 2.11: Snap-off in a rectangular duct. The dashed curve shows the critical position before the snap-off event. (Lenormand et al, 1983) [59]

- **Cooperative node filling**: This mechanism occurs when two menisci meet at a node linking two throats. Depending on the configuration of fluids, a decrease of capillary pressure could lead to an instability of the menisci and, therefore, to a spontaneous filling of the node. Figure 2.12 shows two scenarios where cooperative pore filling is taking place. The capillary entry pressure for

filling a node is affected by the largest radius of curvature that can be obtained, which is directly linked to the number of adjacent oil-filled throats.

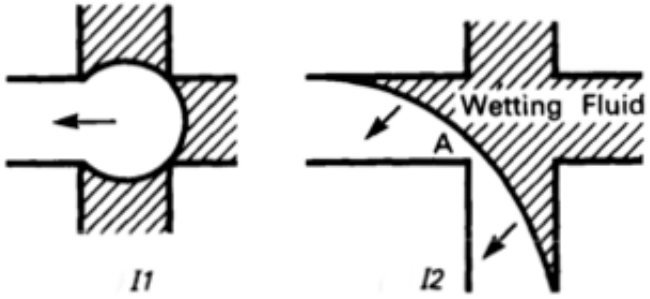

Figure 2.12: Cooperative pore filling mechanisms: (I1) the nonwetting fluid is only in one duct. An instability appears when the meniscus no longer touches the walls. (I2) The nonwetting fluid is in two adjacent ducts and the collapse occurs when the meniscus reaches point A. (Lenormand, 1984 [60])

The threshold pressure difference necessary to mobilise blobs of trapped non-wetting phase was also derived in this work based on experimental observations. The authors admitted, however, that the formulations presented were probably too simplistic (for example, no contact angle hysteresis was included) and did not take into consideration the real topology of the rock or the blob shapes.

McDougall and Sorbie (1995) [61] studied the effect of wettability during waterflooding by simulating waterflooding in a 20x20x20 3D regular cubic network for both mixed-wet (the largest pores are oil-wet) and fractional-wet (oil-wettability is attributed randomly) configurations. The generated capillary pressure and relative permeability curves emphasised the importance of the fraction of oil-wet pores and showed that common experimental wettability tests might lead to misleading results if the porous medium is fractional-wet. They also showed that a fraction of oil-wet pores close to 0.5 yields the best recovery in both mixed-wet and fractional-wet systems (Figure 2.13). Finally, a novel test was suggested to differentiate between the different wettability cases.

The effects of wettability were also studied by Blunt (1997) [62], who simulated primary drainage, water injection and oil re-injection using numerous fractions of oil-wet pores, contact angles and initial water saturations. The novelty of the model lies in the introduction of new concepts, such as water remaining in the pore corners after primary drainage (Figure 2.14), wettability alteration and the emergence of oil layers that can be "sandwiched" during forced waterflooding and contribute to an increased connectivity of oil clusters. Capillary pressure thresholds were derived for the different mechanisms of invasion in rectangular capillaries. Results showed that waterflooding is more efficient in weakly water-wet and moderately oil-wet systems

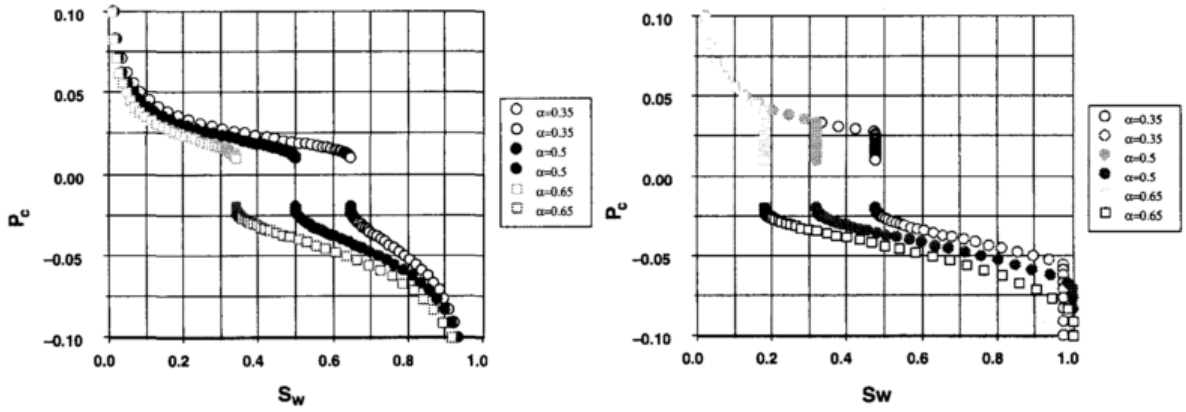

Figure 2.13: Waterflood capillary pressure curves for: three fractional-wet systems (left) and three mixed-wet systems (right). (McDougall and Sorbie, 1995 [61])

which is consistent with the study of McDougall and Sorbie (1996) [61].

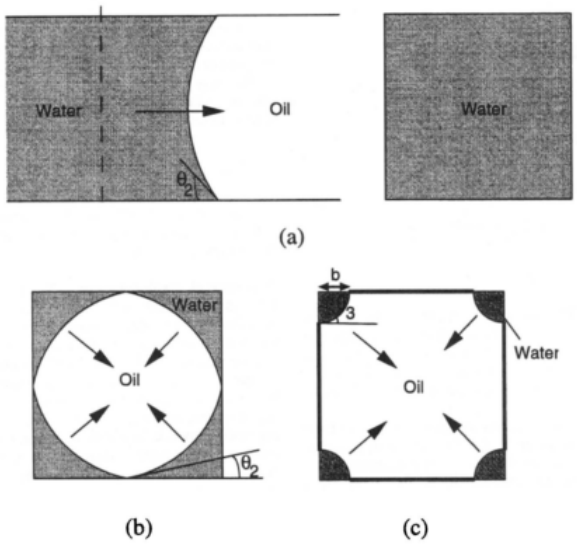

Figure 2.14: Three types of water invasion during water injection. (a) Piston-like advance (b) Snap-off (c) If the contact angle is greater than 45°, water in the corners start bulging out into a throat. (Blunt, 1997 [62])

The work of Payatakes et al. (2000, 1998, 1986) [63, 64, 65, 66] was particularly focused on the steady-state flow of isolated ganglia. By introducing the concept of ganglion population balance equations into a mechanistic simulator, variables related to the ganglia (such as mean ganglion size, fraction of oil in the form of moving ganglia) were simulated under different circumstances. They also showed the effect of these variables on flow behaviour, especially the oil relative permeability. Despite the predictive power of this model claimed by the authors, the steady-state assumptions under which the pressure solution in the network was computed would have precluded the emergence of some important flow regime patterns (like viscous fingering), which would have impacted the results shown in the study.

Øren (1998) [25] used extracted sandstone networks from micro-CT images to predict

transport properties of the underlying rock. By assuming irregular pores with shape factors assigned from image analysis, he derived the entry capillary pressure for piston-like, snap-off and pore body filling displacements using the Mayer-Stowe-Princen (MS-P) method (1965, 1969, 1970 [67, 68, 69]) (the MS-P method relies on the Young's equation to describe the force balance at arc meniscii (AM) and allows the calculation of the capillary pressure thresholds required to invade a capillary element with an arbitrary geometry by equating the curvature of the AM to the curvature of the invading interface). Wettability alteration was also considered by modelling the advancing (during primary drainage) and receding (during imbibition) contact angles, and tracking the meniscus movement along the walls of capillaries. The simulated results – capillary pressure and relative permeability curves – were claimed to be in a good agreement with the experimental curves (Figure 2.15). Similar success in reproducing experimental data was reported by Patzek (2001)[70], Valvatne et al. (2004, 2005) [71, 27] and Dong (2007) [72] who implemented an improved version of the Øren formulation.

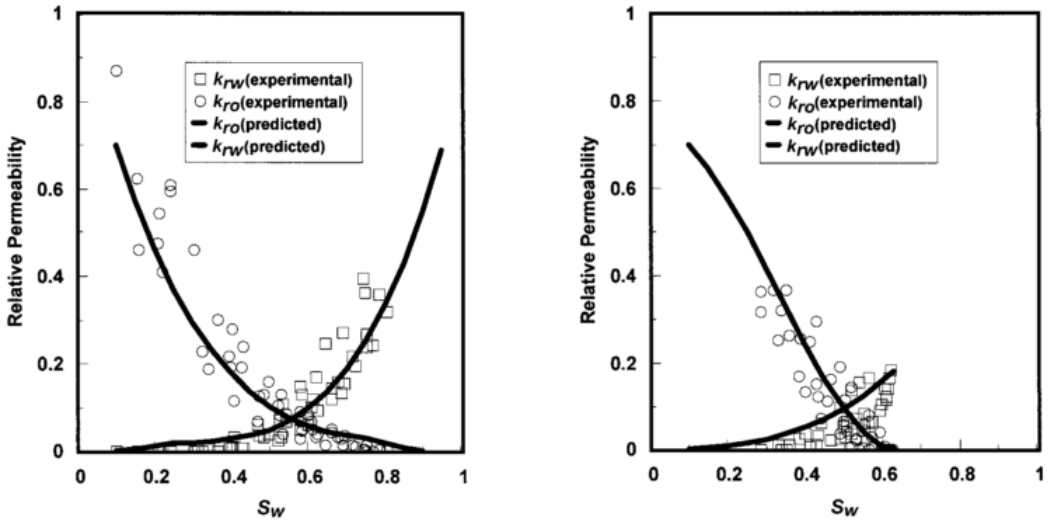

Figure 2.15: Comparison between predicted and simulated relative permeability curves during: primary drainage (left) and initial waterflood (right) for a water-wet Bentheimer sandstone. (Øren, 1998 [25])

The residual oil structure was studied for mixed-wet systems using a network model by Ryazanov et al. (2014) [73] applied to a reconstructed Berea sandstone. A thermodynamic criterion for oil layer formation (Van Dijke and Sorbie, 2006 [74]) was used to study the effect of spreading oil on final recovery. Whilst residual oil is usually reached after few pore volumes of injected water, their simulations showed that larger volumes must be injected to displace all the available oil in the system. This is due to the role played by oil layers in updating the oil connectivity, which might lead to a continuous slow recovery after water breakthrough.

Despite their differences, most of the aforementioned models assumed the presence

of only two phases in the porous media under investigation. Considering a third phase (usually in gas-oil-water systems) adds additional complexity that should be taken into account, and appropriate models need to be conceived to simulate the corresponding three-phase flow. This will be discussed in the next section.

2.8 Three-Phase Quasi-Static Flow in Porous Media

Three-phase flow is relevant in various oil recovery processes. Situations where gas, water and oil interact occur mostly during Water-Alternating-Gas (WAG) injection or depletion in water-flooded reservoirs. The pore-scale mechanisms associated with three-phase flow are, however, more complex than those in two-phase flow, and several key parameters play a role – for example, spreading phenomena, three-phase contact angles between the various phases, multi-chain displacements between the different clusters and wetting layers.

The complexity of three-phase flow makes experimental studies more challenging. Although few works exist in the literature to derive properties such as three-phase capillary pressure and three-phase relative permeability (Sohrabi et al., 2004 [75]; Element et al. 2003 [76]; Soll et al., 1993 [77]; Oak, 1990 [78]), it is well-recognised that such experiments are hard to achieve in the laboratory, and results are often difficult to interpret. The development of three-phase pore-network models has therefore been an important, cost effective alternative to simulate three-phase phenomena. These models have not only given insights into the underlying three-phase mechanisms, but have also been a great tool for investigating the sensitivity of three-phase systems to various parameters and have even proved useful for generating quantitative predictions (i.e. final saturations and relative permeabilities).

One of the first three-phase pore-network models was implemented by Heiba et al. (1984) [79] who extended the statistical model and percolation theory of capillary pressure to three-phase capillary-controlled displacements. Using a regular lattice, and considering six possible basic displacement events (one phase displacing another) in a spreading system, relative permeability curves were generated, although limited comparisons with experimental data were presented.

Øren et al. (1994) [80] designed micromodel experiments of tertiary gas floods in strongly water-wet, oil-water systems and the experimental data suggested the existence of important three-phase mechanisms, such as double drainage events (where a gas-oil interface advance is associated with an oil-water interface movement) and

the presence of oil layers when the oil spreading coefficient is positive. A network model was also implemented by extending invasion percolation concepts to include double drainage mechanisms and oil spreading. Simulated results and oil recovery curves were reported to be in good qualitative agreement with those observed in micromodel experiments. Furthermore, the model confirmed the important role of oil spreading films in improving tertiary gas flood efficiency in positive spreading systems (Figure 2.16). Improved versions of this model were developed in later works (Mani and Mohanty, 1997 [81]; Pereira, 1999 [82]) and similar results were reported.

Figure 2.16: Gas distribution in a square network at gas breakthrough in: a positive spreading system (left) a negative spreading system (right). (Øren et al., 1994)[80]

Fenwick et al. (1998) [83] developed a three-phase network model which introduced more complex mechanisms. Geometrical conditions were derived to check the stability of oil layers in triangular pores, and it was demonstrated that layers can be present even for negative spreading coefficients. Using a 30x15x15 water-wet network, it was shown that saturation paths and relative permeabilities were highly influenced by the layer stability. The simulated results were also reported to be self-consistent and in good qualitative agreement with experimental data.

Laroche et al. (1999) [84] studied the effect of wettability heterogeneities during three-phase gas injection. Micromodel experiments were carried out for various wettability configurations. A pore network simulator was also developed and three-phase displacements were simulated. Results showed that residual oil and irreducible water saturation could be largely affected by initial wettability. Highest recovery rates were achieved in oil-wet systems, as oil could escape via film flow. The networks used in the study were, however, not large enough (54 nodes x 12 nodes) to capture flow regimes or make even qualitative comparisons.

A sophisticated model has been developed by Van Dijke and co-workers in the past fifteen years [85, 86, 87, 88, 89, 90, 74, 91, 92]. The model was used initially to study saturation dependencies of relative permeabilities in three-phase flow, where allowed pore occupancies were classified based on the network wettability (Van Dijke

et al., 2001 [85]). As a concluding observation, the model pointed to the importance of interfacial tensions and the smallest and largest pores of water-wet and oil-wet clusters, as well as the degree of wettability.

In subsequent works, appropriate three-phase contact angles were derived based on Young's equations for each of the three pairs of fluids (oil-water, oil-gas, gas-water) residing on a solid which are given by:

$$\begin{cases} \sigma_{os} = \sigma_{ws} + \sigma_{ow} cos\theta_{ow} \\ \sigma_{gs} = \sigma_{ws} + \sigma_{gw} cos\theta_{gw} \\ \sigma_{go} = \sigma_{os} + \sigma_{go} cos\theta_{go} \end{cases} \tag{2.9}$$

where σ_{ij} and θ_{ij} are respectively the interfacial tension and the contact angle between phase i and phase j.

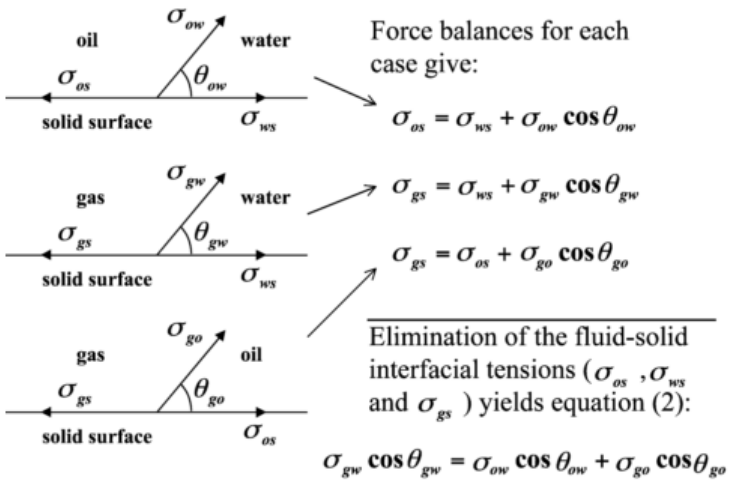

Figure 2.17: Force balance of three-phase fluid–solid combinations. (Van Dijke and Sorbie, 2002 [88])

Bartell and Osterhof (1927) [93] (Figure 2.17) had used these 3 equations to derive the relationship between contact angles between each pair of fluids, which is given by:

$$\sigma_{gw} cos\theta_{gw} = \sigma_{go} cos\theta_{go} + \sigma_{ow} cos\theta_{ow} \tag{2.10}$$

Van Dijke and Sorbie (2002) [88] adopted the following linear relationships to derive values of θ_{go} and θ_{gw} for a given θ_{ow} and which satisfy Equation 2.10:

$$\begin{cases} cos\theta_{go} = 0.5((-1 + \frac{\sigma_{gw}-\sigma_{ow}}{\sigma_{go}})cos\theta_{ow} + 1 + \frac{\sigma_{gw}-\sigma_{ow}}{\sigma_{go}}) \\ cos\theta_{gw} = 0.5((-1 + \frac{\sigma_{go}-\sigma_{ow}}{\sigma_{gw}})cos\theta_{ow} + 1 + \frac{\sigma_{go}-\sigma_{ow}}{\sigma_{gw}}) \end{cases} \tag{2.11}$$

The relationships given by the equations above are only valid for a spreading system. When oil is non spreading, the following relationships were used.

$$\begin{cases} cos\theta_{go} = 1 \\ cos\theta_{gw} = \frac{\sigma_{ow}}{\sigma_{gw}} cos\theta_{ow} + \frac{\sigma_{go}}{\sigma_{gw}}) \end{cases} \tag{2.12}$$

Three-phase displacements were also modelled in a novel way. Instead of considering simple and double displacement events, multi displacement chains were considered by associating the existing phase clusters into a graph of nodes where each pair of nodes is linked by the minimum capillary pressure required to trigger a displacement (Figure 2.18). Although the initial algorithm (Van Dijke and Sorbie, 2002 [87]) was restricted to up to five chain displacements due to computational limitations, the model was improved by solving the corresponding shortest path problem using Bellman-Ford-Moore algorithm combined with Tarjan's subtree disassembly algorithm (Van Dijke et al., 2008 [94]).

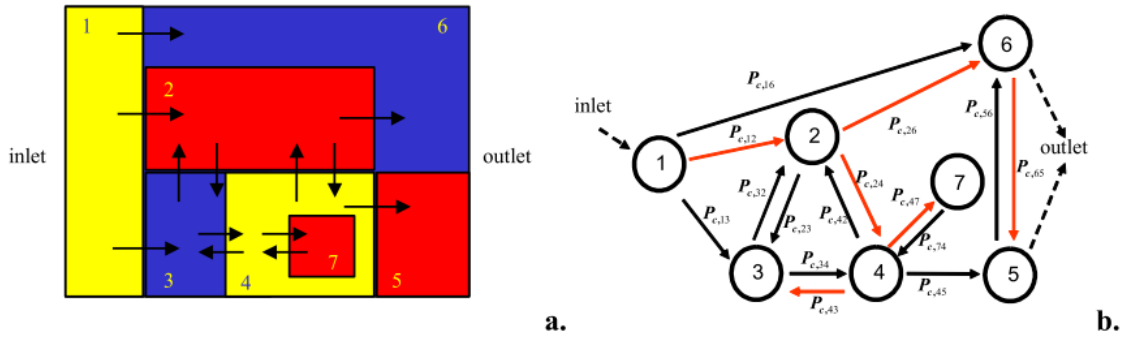

Figure 2.18: a. Map of network clusters with cluster-cluster connections and b. the equivalent graph. The capillary entry pressures are shown as costs for each direction of each connection. (Van Dijke et al., 2008 [94])

The model simulations developed by Van Dijke and co-workers were compared to WAG micromodel experiments. WAG simulations were shown to be in good qualitative agreement (Figure 2.19) with the experimental micromodel snapshots in water-wet (Van Dijke et al., 2002 [87]), oil-wet (Van Dijke et al., 2006 [90]) and mixed-wet systems (Van Dijke et al., 2010[91]).

Piri and Blunt (2005) [28, 29] implemented a similar model where more attention was given to phase occupancies and menisci fluctuations inside the capillary elements. By establishing all the possible phase combinations inside a pore corner and taking into

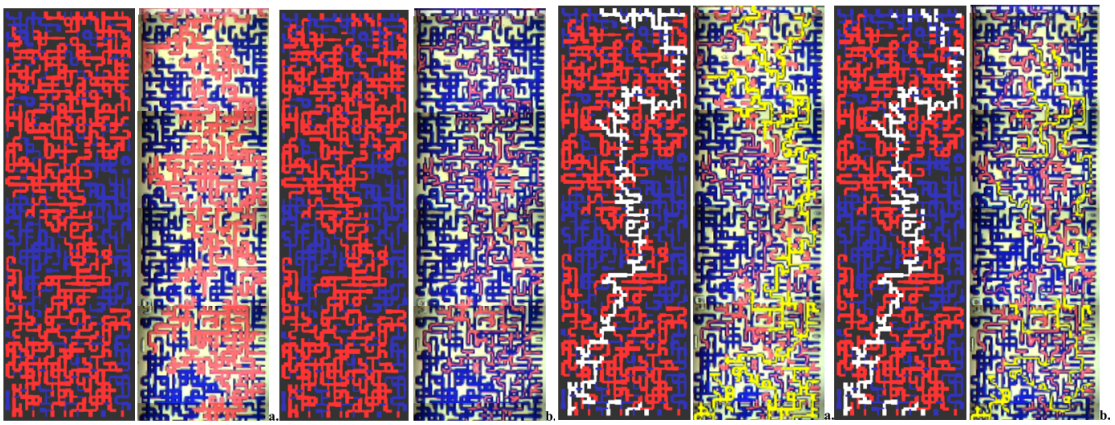

Figure 2.19: Simulated (left) and experimental (right) micromodel fluid configurations after -from left to right- primary drainage, initial water flood, first gas flood, first water flood. Oil has been coloured red and water blue. (Van Dijke et al., 2002 [87])

account the hysteresis effect, appropriate contact angles and entry capillary pressures were derived. Conditions for the formation and collapse of spreading layers were also established for square and triangular sections. The simulated saturations paths for three-phase flow in Berea sandstone network were reported to be consistent with those from experiments. Long chain displacements were not considered, however, and only double displacements were taken into account.

A thermodynamic criterion for oil layer formation in star-shaped pores was developed by Van Dijke and Sorbie (2006) based on "the balance of virtual work and change of surface free energy for a small displacement of a three-phase fluid configuration at capillary equilibrium in a pore with angular cross sections". The criterion was compared with the existing geometrical criterion (Fenwick and Blunt 1998), and the authors claimed the latter criterion is insufficient as it can lead to overestimation of the number of layers (and thus oil connectivity). Although initially derived for two-phase systems, the criterion was extended in a later work by Al Dhahli et al. (2013) to study oil layer stability between water and gas. Multi chain displacements were also taken into account in their model, and the three-phase simulator was applied on 3D networks extracted from micro-CT images. A good agreement with experimental data for various wettability scenarios was claimed, and the importance of chain displacements on residual oil was highlighted.

Despite the complex mechanisms implemented in the aforementioned works, these three-phase pore network models are usually quasi-static and are only valid when the flow is capillary dominated. When viscous forces are present, however, the steady-state flow hypothesis is violated, and appropriate dynamic modelling approaches must be adopted to capture the flow behaviour emerging from the competition between capillary and viscous forces. An overview of some of these unsteady-state

models will be discussed in the next section.

2.9 Unsteady-State Flow in Porous Media

Unsteady-state flow can be observed in a wide range of oil recovery processes (e.g. high rate waterflooding, high rate gas injection, high rate depletion and ganglia mobilisation). The main difference with steady-state flow lies in the existence of non-negligible viscous forces that can affect the regime behaviour and make the system state not totally dependent on the phase saturations but rather on the interplay between viscous forces and capillarity. Indeed, the capillary number – a measure used to highlight the competition between these forces – is usually referred to when determining whether the system is capillary or viscous dominated. The most common definition of capillary number is given by (Lenormand, 1984 [60]):

$$C_a = \frac{\mu V}{\sigma} \tag{2.13}$$

where μ refers to the viscosity of the invading phase, V the Darcy velocity, and σ the interfacial tension. Although this formulation has been widely used, several works have adapted it to include other key parameters that can affect the flow regime, such as the rock porosity and the viscosity of the defending phase.

Larson et al. (1977) [95] established a relationship between residual non-wetting phase saturation and the capillary number in a two-phase displacement. Flow conditions required to mobilise a single blob were first derived using concepts from percolation theory alongside the mechanics of blob mobilisation. Residual oil volume was then estimated, although the blob size distribution considered did not take into account the flow regimes that could be affected by the viscous forces as the capillary number was varied.

Koplik and Lasseter (1985) [96] implemented one of the first dynamic models in a 2D network with two fluids of the same viscosity. In their model, the pressure gradient across every capillary element was determined by solving the mass conservation equation in each node and including a capillary term in Poiseuille's law between node i and node j as follows:

$$q_{ij} = \frac{\pi r^4}{8\mu} \frac{(p_i - p_j - P_{ij}^{\pm})}{L} \tag{2.14}$$

where q_{ij} is the flow into the pore between node i and node j, p_i is the pressure

in node i, p_j is the pressure in node j, and $P_{ij}^{\pm} = \pm\frac{2\sigma cos\theta}{r}$ is the capillary pressure between node i and node j. The sign of $P_{ij}^{\pm}$ depends on the arrangement of the wetting and the non-wetting phase inside the capillary element. In the case of a drainage event, the capillary pressure term would resist the flow whilst the opposite would be true for an imbibition event. Positions of the menisci between the wetting and the non-wetting phase were updated using a time step that conserves the mass in each pore (this approach has been used in several subsequent works). The simulations were performed on a relatively small 2D network, however, due to the limited computational power available at the time.

Lenormand and Zarcone (1984) [60] designed glass micromodel experiments to study the effect of capillary number during unsteady state imbibition in gas-oil systems. Results showed that, for low capillary numbers, films can flow along the roughness of the square capillary walls (and so snap-off is the main displacement mechanism) whilst piston like displacements are predominant at higher capillary numbers. This study was extended later by Lenormand et al (1988) [97] where drainage processes were investigated and the viscous ratio impact was studied alongside the capillary number. The viscous ratio is defined as

$$M = \frac{\mu_{Defending}}{\mu_{Invading}} \tag{2.15}$$

where $\mu_{Invading}$ and $\mu_{Defending}$ are respectively the viscosity of the invading and the viscosity of the defending phase.

An unsteady-state network simulator was then implemented by following a similar approach to that described by Koplik and Lasseter. Depending on the flow rate, three main regimes were observed :

- **Stable displacement**: Observed at high capillary numbers and small viscous ratios (<1). Due to the high viscous forces of the invading phase, the capillary resistance is negligible and a flat frontal advance is observed accompanied by small clusters trapped behind. This usually yields a low final residual saturation.
- **Viscous fingering**: Observed at high capillary numbers and large viscous ratios. The viscosity of the defending phase is important whilst the capillary effects are negligible for the invading phase. This results in tree-like fingers spreading through the network towards the outlet and eventually leads to a high residual saturation. Viscous fingering has been investigated in various research works, and numerous mathematical formulations have been developed in the past to capture this growth process (i.e. Kessler et al., 1988 [98]).

- **Capillary fingering**: Observed at medium to low capillary numbers. The capillarity is dominant compared to viscous forces. Large fingers grow in all directions and can eventually connect to each other leaving large clusters of defending fluid behind.

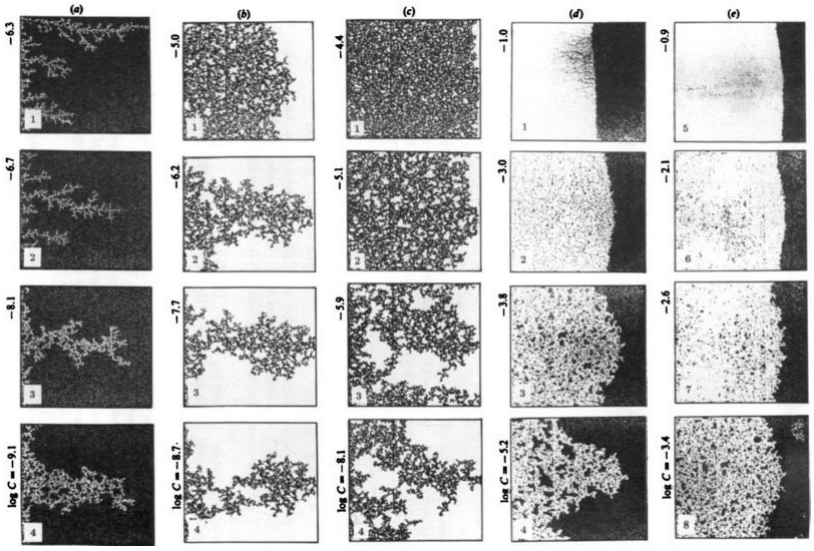

Figure 2.20: (a) Air displacing a very viscous Oil – from viscous fingering to capillary fingering (b) Mercury displacing Hexane – from viscous fingering to capillary fingering (c) Mercury displacing Air (d) Glucose solution displacing Oil (e) Glucose solution displacing Oil – from stable displacement to capillary fingering. (Lenormand, 1988 [97])

The simulations were complemented by several micromodel experiments in Air-Oil, Glucose water-Oil, Hexane-Mercury, and Air-Mercury systems (Figure 2.20). Various capillary numbers and viscous ratios were used, and the same regimes were observed. A phase diagram was also constructed to determine the boundaries of each regime based on the capillary number and the viscous ratio. The simulated diagram was shown to be in a good agreement with the micromodel experiments. A similar study was carried out later by Zhang et al. (2011) [99] using different micro-model experiments. The same three regimes were observed and the stability diagrams were plotted and compared to the one reported by Lenormand (Figure 2.21).

McDougall and Sorbie (1993) [100] developed a dynamic pore-network simulator to study the viscous/capillary force balance during waterflooding in laminated structures. A 2D 40x40 distorted network of cylindrical bonds was constructed and a global pressure solution for different capillary numbers was computed to take into account the effect of viscous forces. The entry capillary pressure required to invade a single pore was then given by:

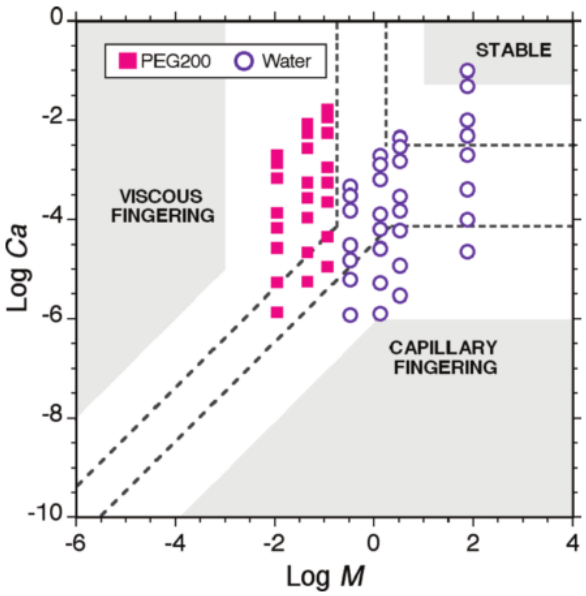

Figure 2.21: Stability diagram showing three stability domains (dashed lines). The stability areas reported by Lenormand et al. are denoted by the gray zones. (Zhang, 2011 [99])

$$P_{entry} = \frac{2\sigma cos\theta}{r} + \Delta P \tag{2.16}$$

where ΔP was the pressure gradient across the pore. Six layered systems were then studied by changing the permeability of blocks inside the network. Sensitivity to both lamina orientation and wettability configuration was examined. Results showed more residual oil in the laminae in both oil-wet and water-wet cases for low capillary numbers, and better efficiency of waterflooding was observed when viscous forces were dominant, although less recovery was achieved in the water-wet case.

Blunt and Scher (1995) [101] also studied unsteady-state displacement in a cubic lattice. In their model, rather than solving the pressure field inside the network, percolation theory was used to account for the global flow rate and gravity forces as a perturbation to the threshold capillary pressure required to invade a pore. The flow regime change as a function of the capillary number was captured although viscous fingering was not observed. Results showed that dramatically lower residual saturations could be achieved by increasing the flow rate. Such an effect was reported as emerging as the capillary number exceeded 10^{-8}.

Aker et al. (1998) [102] developed a similar pore network model to that implemented by Lenormand to study the dynamics of drainage on a 2D 40x60 lattice of tubes. The pressure field was solved after including the capillary pressure in the mass conservation equation. A constant injection rate was simulated by assuming the following relationship:

$$Q = A\Delta P + B \tag{2.17}$$

where Q is the flow rate, ΔP is the pressure gradient across the network, and A and B are parameters depending on the network geometry and the fluid configuration. Whilst $Q = A\Delta P$ refers simply to Darcy's law, the term B takes into account the existence of capillary forces. Solving equation 2.17 for two different constant rates yields the values of A and B, and the appropriate ΔP for any flow rate can then be applied across the network. The menisci positions are then updated in every pore, and new menisci are created whenever the non-wetting phase reaches a node (Figure 2.22). Several rules were adopted to take care of the different scenarios that could emerge when different menisci meet one another. The model allowed two menisci at most in the same pore by merging any third meniscus entering a pore with the others. For situations where both the non-wetting and the wetting phase flow toward a node, both fluids are mixed, and two menisci are created instead.

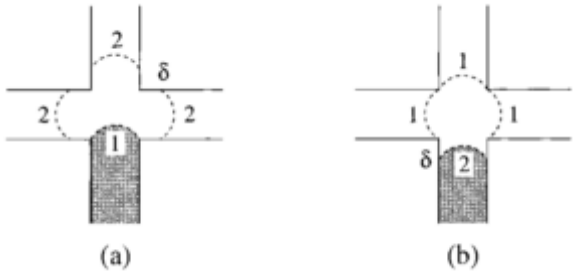

Figure 2.22: The motion of the menisci at the nodes. (a) The non-wetting fluid (grey) reaches the end of the tube (position 1) and is moved a distance δ into the neighbor tubes (position 2). (b) The wetting fluid (white) reaches the end of the tubes (position 1) and the non-wetting fluid retreats to position 2. (Aker, 1998 [102])

The same three flow regimes were observed as in Lenormand's work and the temporal evolution of the global pressure gradient was simulated for different capillary numbers and viscous ratios. The pressure across the lattice tends to decrease during viscous fingering as the saturation of the less viscous phase increases, and it rapidly decreases once the invading phase breaks through the network. Similarly, the pressure across the network increases during stable displacement and it fluctuates during capillary fingering. Singh and Mohanty (2003) [103] developed an improved version of this model by (i) including film flow in 3D networks with cubic bodies and square cross-section throats, and (ii) substituting the dynamic filling by a pseudo-percolation approach when the flow is capillary-dominated.

A similar approach was implemented by Mogensen and Stenby (1998) [104] to model dynamic imbibition in a 3D network of triangular pores with a focus on the effect of flow rate on the competition between snap-off and frontal displacement. The

modelling of the wetting phase in the corners of the pores was achieved in a similar fashion as described by Blunt and Øren. Sensitivity to contact angle, aspect ratio and capillary number on the distribution of residual oil was examined. Results showed that snap-off could be suppressed after a certain capillary number threshold (10^{-7} – 10^{-8}). At higher capillary numbers, the trapped ganglia could be mobilised and therefore lower residual non-wetting phase could be achieved.

Al-Gharbi and Blunt (2005) [105] implemented a two-phase dynamic model of drainage where the cross section of each pore and throat is represented as a scalene triangle. Both phases are allowed to exist in a single capillary, and the configuration of fluids is determined based on the contact angle. The conductance of each capillary was computed by creating an equivalent resistor network to the hydraulic resistance of the various fluids in the capillary (Figure 2.23).

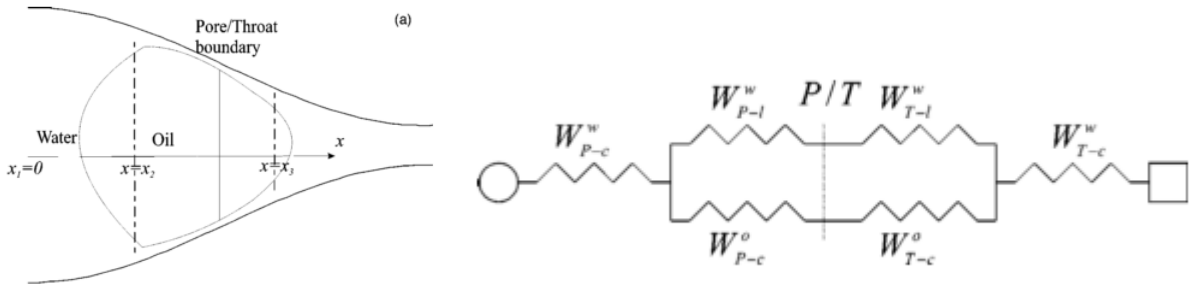

Figure 2.23: Illustration of a fluid configuration: oil occupies the pore/throat boundary (left). The equivalent electrical resistors diagram used to compute hydraulic resistance W (right). (Al-Gharbi and Blunt, 2005 [105])

A pressure value was assigned to each pore and throat center. This resulted in a system of (n+m) unknowns that could be solved by applying the mass conservation equation for every pore. Once the pressure field is solved, a phase flow, Q_w(flow of water) and Q_o (flow of oil) is attributed to each capillary based on the configuration of fluids in it. The fluid volumes are updated according to:

$$V^n_{fluid} = V^{n-1}_{fluid} + (Q^{in}_{fluid} - Q^{out}_{fluid}) \times \Delta t \tag{2.18}$$

where V^n_{fluid} and V^{n-1}_{fluid} are the volumes of one fluid in a capillary in iteration n and $n-1$, and Δt is the time between both iterations. Both piston-like and pore body filling dynamics were implemented, and an additional drainage snap-off mechanism was added. Sensitivities to the capillary number and viscous ratio were done. A quasi-static flow was reported for low capillary numbers, and more ganglia were observed as the capillary number increases due to snap-off events. The network models were however too small (9 nodes x 9 nodes) to capture clear flow regimes.

Joekar-Niasar and Hassanizadeh (2011) [106] developed an unsteady-state two-phase

model to examine the theory of non-equilibrium capillarity, which relates the difference in fluids pressure to their corresponding saturation according to:

$$P^n - P^w = P^c - \tau \frac{\partial S^w}{\partial t} \tag{2.19}$$

where P_n and P_w are the non-wetting and wetting fluid pressures, respectively, P_c is the capillary pressure, S_w is the saturation of the wetting fluid, and τ is a non-equilibrium capillarity coefficient. The novelty in the model lies in the use of two separate pressure fields for each fluid in the network. This was achieved by attributing a separate conductance to each fluid in each capillary element, and then combining the two mass conservation equations for both fluids and expressing the total pressure in a capillary as a function of the local pressure in each fluid. Once the global pressure field is solved (using similar techniques to those discussed earlier), the pressure of each fluid, P_i^n and P_i^w,in each capillary element i, is given by:

$$\begin{cases} P_i^w = P_i - s_i^n P_i^c \\ P_i^n = P_i + s_i^w P_i^c \end{cases} \tag{2.20}$$

where s_i^n and s_i^w are the non-wetting and wetting fluid saturations in the capillary, and P_i^c is the capillary pressure between two phases. The saturation of each phase is updated then according to equation 2.18. For low capillary numbers, a pseudo quasi-static model was applied to model the displacement events. Several sensitivities were done to examine the effect of various parameters on the wetting phase saturation, and curves correlating τ to $S_w$were plotted for drainage and imbibition processes.

Regaieg et al. (2013) [107] implemented a fully-dynamic pore network model to investigate viscous finger thickening during waterfooding. This phenomenon was observed during viscous fingering regimes, where the fingers start to swell after breakthrough, increasing significantly the recovery. The porous medium was modelled as a distorted regular lattice of capillary elements. The implemented model determined the pressure field by fixing a flow rate and including capillary forces in the solver. An iterative approach was used to block any counter current imbibition flow until a consistent pressure field was achieved. Saturations were updated according to equation 2.18. The model was validated against the experimental study of Lenormand (1988) [97] and was successful in reproducing all observed regimes. Finger thickening was also reproduced in 2D and 3D simulations, and was explained by the high pressure gradient at the tip of the upstream fingers after breakthrough (Figure 2.24).

The model also predicted that finger thickening would occur only if the pressure

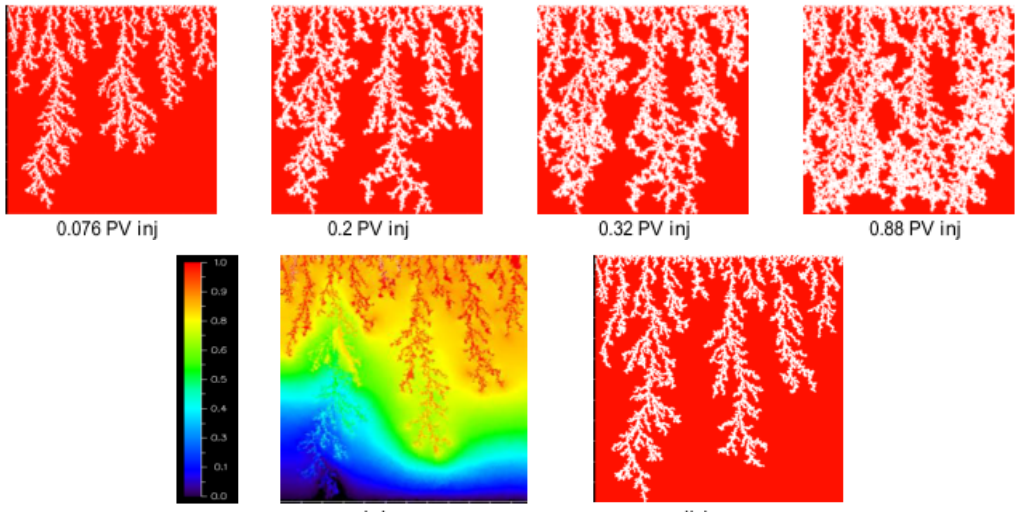

Figure 2.24: Simulations of viscous thinckening in 30cmx30cm 2D network (top) and pressure visualisation of the resident fluid in each pore (bottom). (Regaieg, 2013 [107])

drop plateau after breakthrough was higher than the mean capillary entry pressure of the network. This model has been improved computationally in a later work by Regaieg and Moncorge (2016) [108]. One of the main features implemented was the division of the network grid into several blocks, classified into dynamic, quasi-static and inactive. The classification is based upon one global pressure solution. Dynamic simulation is then applied only on dynamic blocks, whilst a fast quasi static model is used to simulate flow in quasi-static blocks. This approach was reported to improve the speed of the original dynamic code by a factor of 16000 in some 2D cases.

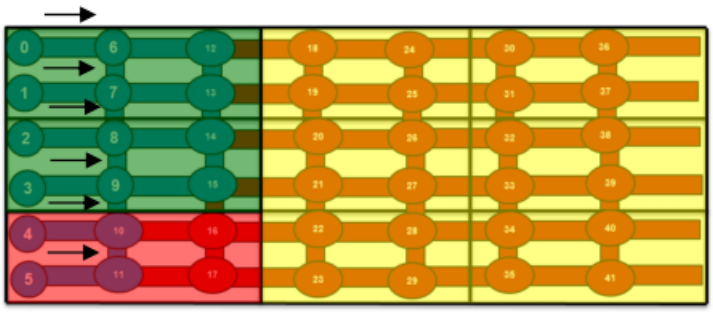

Figure 2.25: A pore network with grid blocks having different states: dynamic gridblocks (green), quasi-static grid blocks (red) and inactive gridblocks (yellow). (Regaieg and Moncorge, 2016 [108])

2.10 Modelling Depletion in Porous Media

Reservoir depletion (often referred to as depressurisation in the literature) is one of the oldest processes in the oil industry. As its name suggests, depletion involves

simply withdrawing the oil from the production wells which results into a continuous decline of the reservoir pressure.

As the pressure decreases, some of the dissolved gaseous molecules eventually reach a point - called the bubble point - where the thermodynamic stability conditions under which they had remained dissolved in oil are no longer satisfied. At this stage, the oil is termed "supersaturated", as it contains more dissolved gas than would be the case under equilibrium conditions. This eventually results in a phase change and the "nucleation" of the first gas bubbles in the reservoir. Additional dissolved gas molecules begin diffusing into the nucleated bubbles, and gas clusters grow and displace additional oil toward the production wells. This mechanism is also known as solution gas drive.

The high mobility of gas clusters usually results in the upward migration of gas, where it is eventually produced alongside oil from the production wells (increasing the gas/oil ratio (GOR) and decreasing oil production). As it is difficult to control the gas/oil ratio, solution gas drive is therefore considered to be a highly inefficient process, and is generally associated with relatively low oil recovery.

Hence, a common strategy is to maintain the pressure of the reservoir above the bubble point by employing water or gas flooding. When reservoirs are sufficiently mature and oil recovery is no longer economically viable, depletion is considered as a cheap and natural process to displace some of the remaining oil left behind. Depletion in water-flooded reservoirs has therefore become a well-recognised technique that yields potential additional recovery (Ligthelm et al., 1997 [109]; Peteresen and al., 2004 [110]) and has also proved to be more efficient in some heavy oil scenarios (Sheng, 1999 [111]), which has revived interest in this process in recent years.

We discuss in this section some of the major experimental works related to depletion, and we discuss the theoretical models developed in the literature to simulate the mechanisms of this recovery process.

2.10.1 Experimental Observations

One of the first depletion experimental works was carried out by Kennedy and Olson (1952) [112], who investigated the formation of methane bubbles in kerosene. Their study showed a dependency between the number of bubbles formed and the supersaturation within the rock. For high supersaturation (around 770 psi) a rapid release of bubbles was reported, whilst no bubbles where observed below 30 psi supersaturation. Initial water saturation was shown to have no effect on nucleation frequency (Figure 2.26). The authors concluded that only few bubbles nucleate under reser-

voir conditions and that solution gas drive is mainly due to the enlargement of gas clusters via diffusion rather than frequent nucleation events. This study was extended in a later work by Wieland and Kennedy (1957) [113] to include measurements from East Texas field cores and similar results were reported.

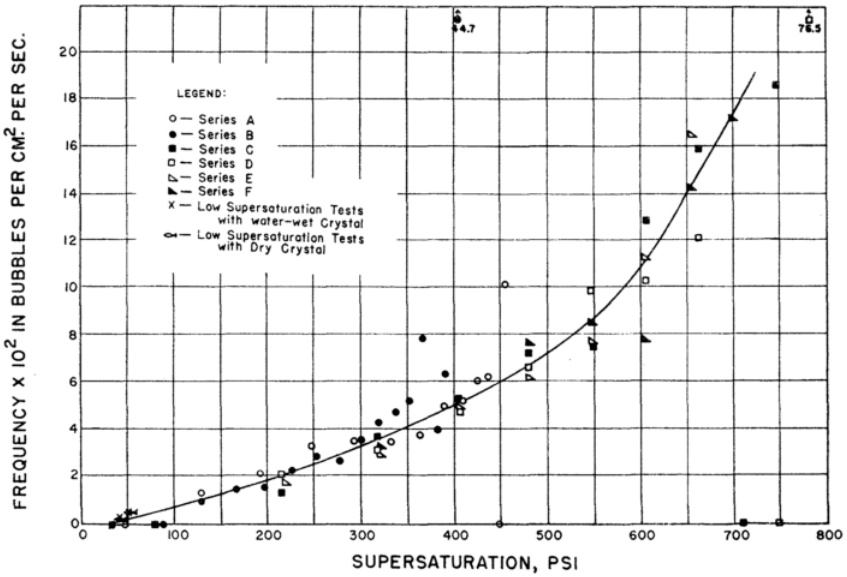

Figure 2.26: Relationship between the frequency of bubbles and kerosene supersaturation. (Kennedy and Olson, 1952 [112])

Stewart et al. (1954) [114] presented an experimental study where the number of bubbles was measured for different depletion rates. A high number of bubbles appeared to form at high depletion rates due to the corresponding high supersaturation (Figure 2.27), although the laboratory rates reported in their study are far from realistic field rates. The authors postulated however that their findings suggested that depleting the reservoir over a short time frame could eventually yield better recovery. Similar results were reported by Hunt and Berry (1956) [115] who also highlighted the important role played by depletion rate on the number of bubbles formed. An exponential probability distribution was also proposed to predict the nucleation times, which was in good agreement with the experiments.

The experiments of Handy (1958) [116] also suggested increased oil recovery using high depletion rates on Bandera sandstone cores. The recovery was reported to increase with increased oil viscosity for a given depletion rate. Supersaturation was calculated as the difference between the equilibrium pressure at the corresponding GOR and the observed pressure. The supersaturation curves were plotted and reached a maximum shortly after the first bubbles had nucleated followed by a slow decline. This was explained by the competition between nucleation and diffusion mechanisms. In fact, as gas diffuses into the nucleated bubbles, the oil becomes less supersaturated and the likelihood of new bubbles to form decreases. The author suggested three main factors affecting nucleation potential:

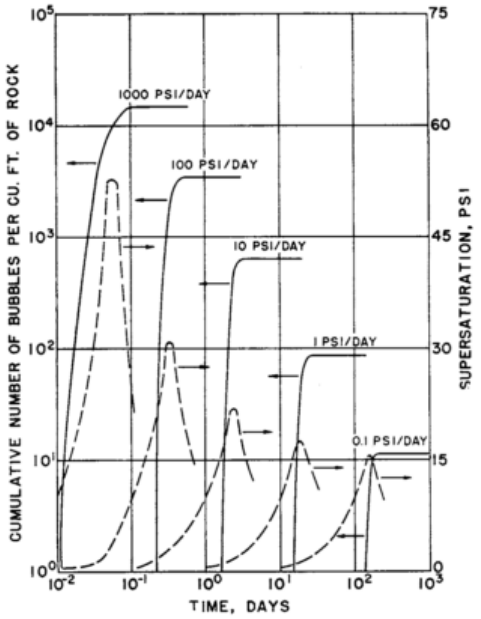

Figure 2.27: Relationship between number of bubbles and depletion rate. (Stewart, 1954 [114])

- Depletion rate
- Diffusion coefficient of the dissolved gas
- The supersaturation threshold of nucleation

Chatenever et al. (1959) [117] confirmed the observations of Kennedy and Olson (1952) [112] regarding the influence of gas nucleation on oil recovery. The authors reported a low density of nucleated bubbles under laboratory conditions and concluded that gas cluster growth is the main mechanism behind oil displacement. The experimental visualization of solution gas drive processes showed elongated gas structures, and pores with larger radii seemed to be preferentially displaced by gas.

The experiments of Dumoré (1970) [118] shed light on the role played by gravity on the upward migration of gas clusters during solution gas drive. The author injected gas at very slow rate into two packs of glass grains with different permeabilities. The experimental images exhibited a "dispersive" conically shaped regime in the high permeability networks compared to a channeled non-dispersive migration for low permeability samples (Figure 2.28).

The author also reported the effect of depletion rate on final gas distribution. For the samples with low permeability, the depletion rate seemed to have no impact on the final gas saturation, and disconnected gas agglomerations filling the entire network were observed. However, a network of channels was seen for low permeability samples, and low depletion rates resulted into low final gas saturations. These experiments highlighted the importance of the pore size distribution and the balance

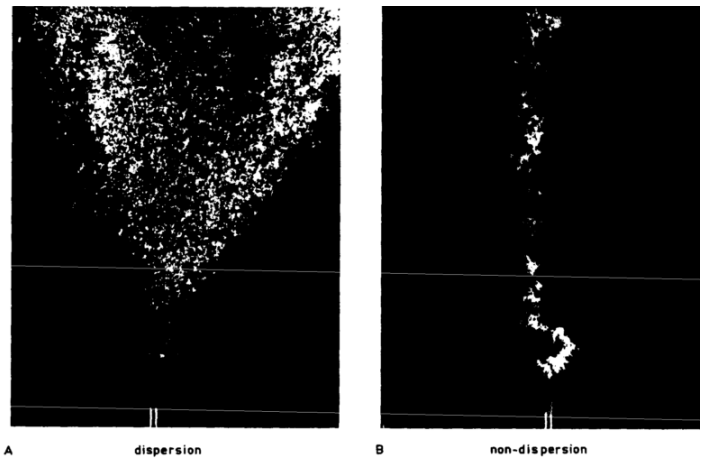

Figure 2.28: Dispersive flow (high permeability sample) vs Channeled flow (low permeability sample). (Dumoré, 1970 [118])

between capillary forces and gravitational forces on the gas growth pattern and final recovery.

Danesh et al. (1987) [119] studied the mechanisms of depletion based on experimental observations and classified them into three main components:

- Bubble nucleation: Once the bubble point is reached, the oil becomes supersaturated and the first bubble emerges. The authors observed that the first bubbles always nucleate in large pores. The presence of connate water was reported to delay bubble formation.
- Bubble growth: Gas diffuses into the bubble which starts to grow in a capillary controlled manner and to invade the largest surrounding oil-filled pores once its internal pressure exceeds the entry capillary pressure threshold $\frac{2\sigma}{r}$ of the neighbouring pore. The formed gas clusters are long and narrow and could eventually result in trapped oil clusters being left behind.
- Gas flow: Snap-off events result in the breakup of gas clusters into small bubbles that jump slowly upwards - both gas and oil start to flow into the production wells.

These observations were also consistent with the work of Li and Yortsos (1991) [120] and Dominguez et al. (2000) [121] who observed nucleation events in glass micromodels. Bubbles were shown to nucleate at different sites and they tended to grow in a ramified pattern (Figure 2.29).

The sensitivity of the critical gas saturation to depletion parameters has been investigated in several experimental works. The critical gas saturation, S_{gc}, is an important measurement in the depletion process as it usually refers to the saturation that

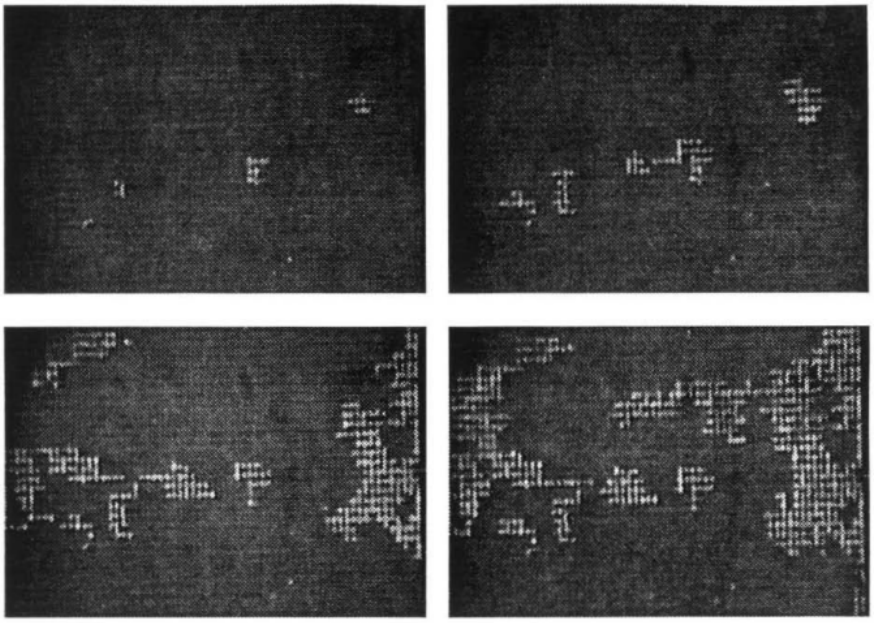

Figure 2.29: Growth pattern during depletion experiments in glass micromodels. (Li and Yortsos, 1991 [120])

signals the start of gas flow. However, various definitions have been adopted in the literature leading to different interpretations and results. Yortsos and Parlar (1989) and Li and Yortsos (1993) [122] defined S_{gc} as the saturation at which a spanning cluster forms. This definition might be consistent when studying depletion on small scales or when gravity gradients are not high enough to trigger gas fragmentation and upward-migration. However, the definition is usually impractical in laboratory experiments, and spanning gas clusters might not even form under high viscous or gravity forces. In these conditions, S_{gc} could be defined as the saturation at which the gas starts to be mobilised (Moulu, 1989 [123]). Firoozabadi and al. (1992) [124] also defined S_{gc} as the minimum gas saturation at which gas production commences. These definitions can lead to low estimation of S_{gc}, however, as gas bubbles could nucleate near the system outlet. A more general definition considers S_{gc} as the saturation at the onset of bulk gas flow (Tsimpanogiannis and Yortsos, 2004 [125]; Kortekaas and van Poelgeest, 1991 [126]).

Moulu (1989) [123] studied the impact of depletion rate on recovery and critical gas saturation S_{gc} during gas solution drive. Experimental results showed S_{gc} increases as the depletion rate increases. Similar observations were also reported by other researchers although various values were suggested in each work (Petereson et al., 2004 [110]; Kumar et al., 2000 [127]; Firoozabadi and al. (1992) [124]; Li and Yortsos (1993) [122]; Kortekaas amd van Poelgeest, 1991 [126]). Some cases suggested, however, a non-monotonic response of S_{gc} to the depletion rate. Kamath and Boyer (1995) [128] reported that changing the depletion rate from 100psi/day to 20psi/day had no effect on S_{gc} for the depletion experiment they carried out.

The effect of interfacial tension (IFT) on critical gas saturation was investigated in the work of Kortekaas and van Poelgeest (1991) [126]. The experiments carried out on two cores from a North Sea reservoir showed that early formation of bubbles was observed for lower IFT values as a low energy threshold (and lower supersaturation) was needed for the the bubbles to nucleate. A non linear relationships was observed between IFT and S_{gc} as shown by Figure 2.30. The increase of S_{gc} for high IFT was explained by the increase of supersaturation which made the number of nucleated bubbles close to that observed for low IFT values.

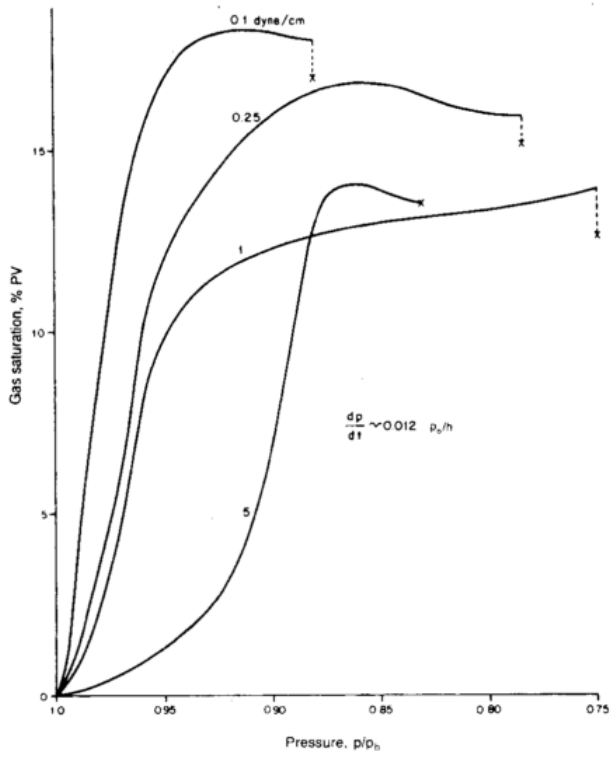

Figure 2.30: Effect of IFT on gas saturation buildup and S_{gc}. (Kortekaas and van Poelgeest, 1991 [126])

Phase distribution also seems to impact depletion results. The experiments of Mackay et al. (1998) [129] on both virgin and waterflooded micro-models showed that bubbles nucleated only in the oleic phase. Gas clusters were seen to grow into larger clusters that could eventually migrate upwards when no water was present. In waterflooded cases, water could hinder bubble coalescence, however, reducing the diffusion of dissolved gas and increasing the local supersaturation and bubble density (Figure 2.31).

Multi-displacement chains were also observed, and the authors reported increased water production in water-wet networks as the water was pushed towards the outlet when the gas was displacing oil ganglia (Figure 2.32).

The wettability effect on nucleation events was investigated by Dominguez et al. (2000) [121]. Depletion experiments were carried out on micromodels with different

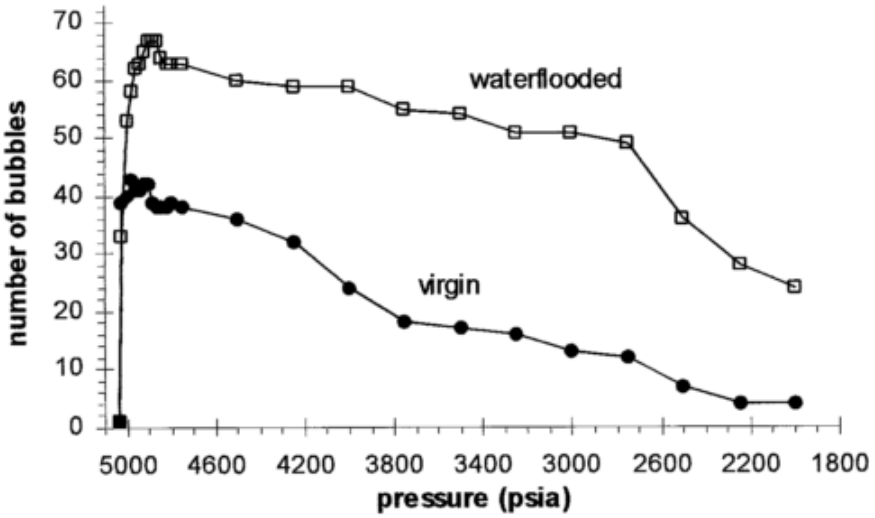

Figure 2.31: Bubble density in virgin and waterflooded micromodels. (Mackay et al., 1998 [129])

Figure 2.32: Phase distribution before and after depletion. Water saturation decreased due to multi-displacement chains. (Mackay, 1998 [129])

contact angles between the nuclating liquid and the rock surface. Results showed higher bubble density for the weakly-wet cases (Figure 2.33). The authors explained this behaviour by the presence of impurities in the less wetting configurations that would become the main nucleation sites as the pressure drops. These results suggested that nucleation could be a reproducible process rather than a random phenomena as claimed by Moulu (1989) [123] and Firoozabadi and Kashchiev (1996) [130].

The viscosity of oil appears to play an important role in the solution gas drive process. Depletion experiments in heavy oil showed uncommon behaviours including low GOR ratios and the formation of foamy oil (Sheikha, 2012 [131]; Sheng et al., 1999 [111]). The experiments of Lago et al (2002) [132] showed higher bubble density for highly viscous oils during depletion experiments on glass micro models (Figure 2.34). Maini et al. (2010) [133] reported, however, insignificant change on the recovery factor when oil viscosity changes.

The aforementioned experimental works make it clear that depletion is a complicated process, and several mechanisms seem to interact in a complex way - as highlighted

Figure 2.33: Bubble density for three wettability configurations. θ= 0 (left), θ= 0.66 rad (middle), θ= 0.82 rad (left). (Dominguez, 2000 [121])

by the different results and the various explanations presented in the literature. Indeed, it is well recognised that every depletion experiment is unique and needs to be interpreted separately from previous experiments. This also explains the development of several numerical models in the literature that try to simulate depletion processes in porous media to gain more insights into the interaction between the underlying mechanisms and to analyse their sensitivity to various parameters. These models will be discussed in the next section.

2.10.2 Theoretical Work

Bubble nucleation and growth are common phenomena that consist of a phase change in response to a shift of the thermodynamic equilibrium. It can be observed in various processes, such as the release of CO2 bubbles in soft drinks, the formation of nitrogen bubbles in the blood of divers as they rise to the surface, and naturally the problem under investigation in this work which is reservoir depletion.

The nucleation process has been extensively studied in the literature (Jones et al, 1999 [134]; Blander et al. 1979 [135]). The formation of a gas bubbles occurs when the partial pressure of the dissolved gas become sufficiently higher than the liquid pressure. Henry's law states that the partial gas pressure in a liquid is directly proportional to its concentration and therefore the supersaturation of a liquid can be defined as the difference between the liquid pressure P_l and the gas pressure P_g which is given by:

$$P_g - P_l = KC(t) - P_l(t) \tag{2.21}$$

where K is the solubility constant. When the system is in equilibrium, $P_g = P_l$. However, as the oil pressure drops in the context of depletion, the oil becomes supersaturated, and the first bubbles emerge to shift the system towards its equilibrium

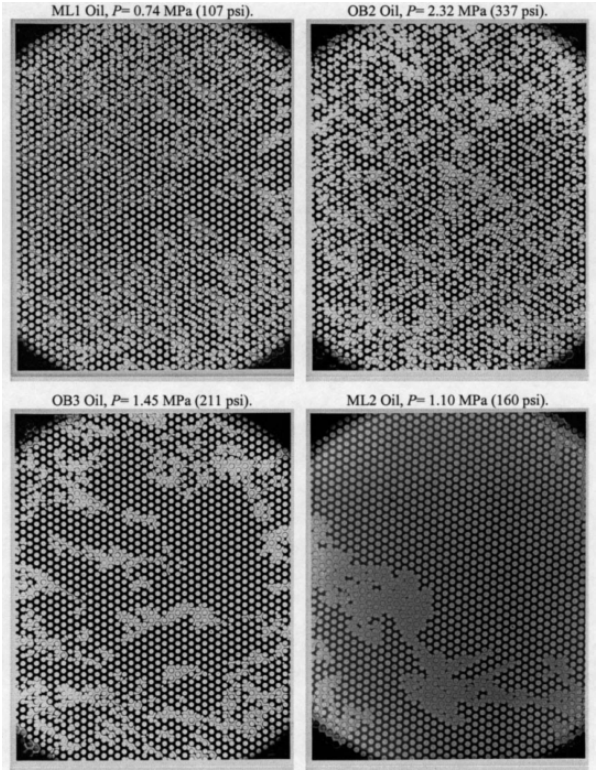

Figure 2.34: Bubble density in glass micromodels for four oil viscosities. ML1: 1000mPa.s; OB2: 1700mPa.s; OB3: 680mPa.s; ML2:0.6mPa.s (Lago et al, 2002[132])

state. A spherical bubble in thermodynamic equilibrium with the surrounding liquid would satisfy the following equation:

$$KC - P_l = \frac{2\sigma}{r} \tag{2.22}$$

where σ is the interfacial tension between the gas and the liquid and r is the bubble radius.

Depending on the location of the nucleation event, two mechanisms have been suggested (Figure 2.35):

- Homogeneous nucleation: This occurs when the bubbles emerge in the *bulk* of the host liquid once a supersaturation threshold is reached.
- Heterogeneous nucleation: Pre-existing cavities, micro bubbles, or liquid impurities are needed for a bubble to nucleate. It is believed that most surface irregularity and wall roughness of porous media makes nucleation most likely to be heterogeneous in nature.

Following the nucleation event, the formed bubbles begin to expand spherically. This

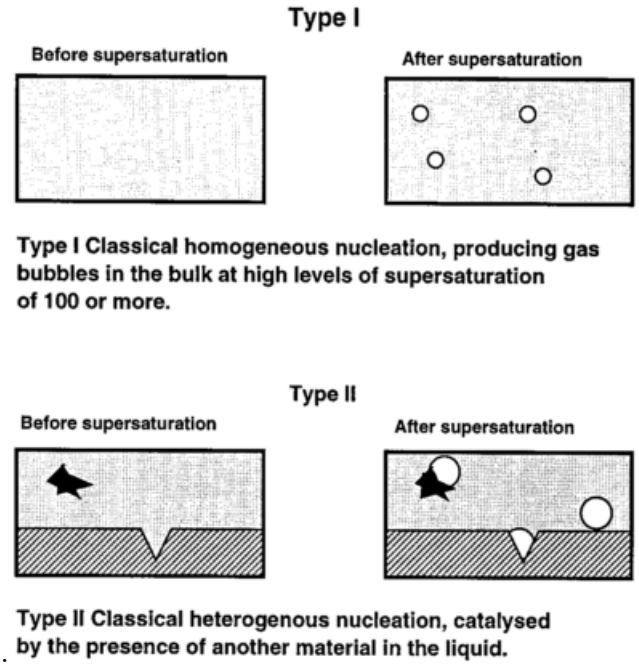

Figure 2.35: Types of nucleation events. (Jones, 1993[134])

was modelled in the work of Scriven (1959) [136] and the evolution of the bubble radius was calculated as:

$$R = 2\beta\sqrt{Dt} \tag{2.23}$$

where β is a dimensionless parameter related to the local supersaturation, D is the diffusion coefficient and t is the growth time.

The dissolved gas diffuses towards the nucleated bubbles enabling them to grow larger and to fill the surrounding space. This is due to the concentration gradient of the dissolved gas across the bubble interface and the resulting flux dictated by Fick's first law:

$$J = -D\nabla C \tag{2.24}$$

where J denotes the diffusive flux of the dissolved gas, D is the diffusion coefficient, and C is the dissolved gas concentration. The ideal gas law can then be applied to update the bubble pressure P and the bubble volume V according to:

$$PV = nRT \tag{2.25}$$

where n is the bubble mole content, R is the ideal gas constant and T is the tem-

perature.

Moulu (1989) [123] considered a homogeneous nucleation model to estimate the rate of bubble nucleation. He calculated the the number of bubbles formed per unit time per unit volume, B_n, using the formulation of Blander and Katz (1975) [137] given by:

$$B_n = Zexp(\frac{-16\pi\sigma^3}{3kT(P_g - P_o)^2}) \tag{2.26}$$

where σ is the gas-oil interfacial tension, kT is the translation energy of an average gas molecule, P_o and P_g are respectively the the oil and gas pressure, and Z is a fitting parameter. The growth of bubbles was modelled using Fick's first law and ideal gas law. The numerical estimations of Sgc, PV relationship, and bubble pressure were in agreement with the experimental data.

Firoozabadi and Kashchiev (1996) [130] studied two models of nucleation:

- Instantaneous nucleation (IN): Once a supersaturation threshold is reached, all bubbles form at once at random sites and they start growing simultaneously.
- Progressive nucleation (PN): New bubbles are continuously nucleating and growing at different time intervals.

The gas volume V_g was calculated for each case according to :

$$\begin{cases} V_g = V_o \int_0^t J(t')v_b(t,t')dt' & PN \\ V_g = V_o N_0 v_b(t,0) & IN \end{cases} \tag{2.27}$$

where J is the bubble formation rate,V_o is the initial liquid volume, N_0 is the number of nucleus bubbles per unit volume formed instantaneously at time $t = 0$, and $v_b(t,t')$ is the volume at time t of a bubble nucleated at time $t' < t$. Gas volume and supersaturation were measured later during depletion experiments for two depletion rates and compared to the IN and PN model predictions. The authors reported better agreement with the IN model and theorised, therefore, that nucleation in porous media is mainly instantaneous, and therefore the experiments are inherently non reproducible. These observations were contradictory with the experiments and models of Li and Parlar (1989) [138] and El Yousfi et al. (1997) [139] who reported that nucleation is heterogeneous and progressive and reproducible.

Yortsos and co-workers (Tsimpanogiannis and Yortsos, 2002 [140]; Du and Yortsos, 1999; Li and Yortsos, 1993 [122]) built a pore network model of depletion, where

conical crevices were modelled in the network and assigned a radius W (Figure 2.36). A bubble would then nucleate in the crevice if the local supersaturation exceeded a critical value given by:

$$KC - P_l > \frac{2\sigma}{W} cos\theta \tag{2.28}$$

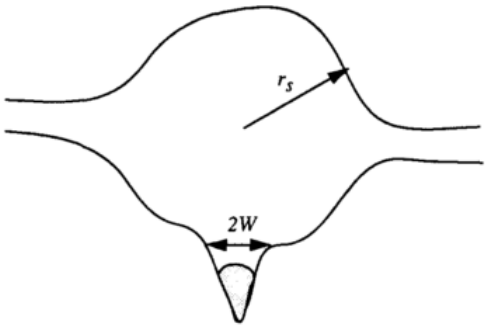

Figure 2.36: Schematic of a crevice of a radius W in a pore. (Li and Yortsos, 1993 [122])

The mass transfer of the dissolved gas molecules was modelled using the diffusion-convection equation, and the pressure P of the gas bubble filling a pore of volume V was updated according to the ideal gas law as dictated by:

$$V\frac{dP}{dt} = RT\frac{dn}{dt} \tag{2.29}$$

Once the pressure is higher than the entry capillary pressure of a neighbouring oil-filled pore, the bubble invades the corresponding pore and both the pressure and the volume of the new gas cluster are recalculated according to:

$$P\frac{dV}{dt} + V\frac{dP}{dt} = RT\frac{dn}{dt} \tag{2.30}$$

The simulations were shown to be in reasonable agreement with the experimental results, although only binary systems were considered in the examined scenarios.

McDougall and co-workers developed various pore network models using similar techniques to investigate the influence of key parameters on depletion such as IFT (McDougall and Mackay, 1998 [141]), initial water saturation (McDougall and Sorbie, 1999 [142]), the impact of heavy oil (Bondino et al., 2005 [143]), gravitational forces (Ezeuko et al., 2010 [144]), and viscous effects (Bondino et al., 2011 [145]). The depletion simulator developed in this work builds on those models by adding new approaches to handle more complex mechanisms and to implement a better pore space description. This is discussed in more detail in Chapter 4.

2.11 Conclusions

In this chapter, we introduced the major concepts of pore network modelling as reported in the literature. We started by discussing the different approaches regarding the modelling of the pore space using equivalent idealistic networks. These could be classified into: (1) statistically generated networks, where a simplistic lattice with statistically-equivalent geometrical properties is used to simulate the underlying rock, and (2) Micro-CT networks which focus on capturing the exact topology of the rock by extracting a digital reconstruction of the pore elements from Micro-CT scans. Several ways have been adopted to model a single capillary element. Whilst some researchers have adopted simplistic approaches by modelling the network as a lattice of cylindrical ducts, others have adopted more complex methodologies by classifying capillary elements into pores and throats and dealing with circular, square or scalene cross sections. The latter approach could, however, result in computationally-expensive simulations and limited network sizes (i.e. El-Gharbi, 2005 [105]).

We also discussed how various flow models have been implemented in the literature to simulate fluid flow in porous media. We started by introducing quasi-static flow models where capillary forces are predominant during drainage or imbibition. Pore network models were shown to be a valuable tool to understand underlying pore-scale mechanisms, and several pore network simulations claimed a successful prediction of experimental data such as capillary pressure and relative permeability curves. The models in the literature were also capable of studying the sensitivity of macroscopic measures (such as oil recovery or residual oil) to a range of key parameters, such as the rock wettability. Some key three-phase models in the literature were also discussed. Some important three-phase mechanisms such as spreading and multi-displacement chains have been modelled in various ways, and several models were capable of reproducing qualitative experimental behaviours. We then presented some of the dynamic multiphase models where viscous forces are no longer negligible. Some of these models were capable of reproducing experimentally observed flow regimes and various sensitivities were carried out to investigate the impact of capillary number and viscous ratio on oil recovery. These models are computationally challenging, however, as they require frequent solving of the pressure field in the host network. We finally discussed depletion experiments and solution gas drive mechanisms. This particular process was shown to be a source of conflicting interpretations and experimental results. Complex mechanisms, such as nucleation and bubble growth, seem to interact in intricate ways, and this makes depletion a challenging process to examine experimentally. Few numerical frameworks, including pore network models, have been developed to investigate the key factors that

could affect depletion outcomes.

Although several authors have claimed quantitative agreement between numerical pore network simulations and experimental data, it is well-recognised that making predictions using pore network modelling often requires tuning various input parameters to match experiments - an aspect that has led some researchers to question their predictive potential. This was shown in the work Bondino et al. (2012) [146], where pore-scale flow during drainage and imbibition have been studied separately by four third-party contractors using pore network modelling techniques. Although the examined networks were extracted from the same core sample, the relative permeability results showed large variations between the different studies.

Despite their limited predictive power at present, pore network models are powerful tools for (1) understanding the physical mechanisms governing pore-scale flow by investigating phenomena observed in experiments, (2) studying the sensitivity of macro-flow properties to various parameters, and (3) examining the interaction and synergies between those parameters and their impact on oil recovery. Such aspects have been explored in this work through the implementation of a novel pore network simulator that incorporates various pore-scale modelling approaches and this will be discussed in detail in the next chapter.

Chapter 3

An Overview of *numSCAL*: an Advanced C++ Pore Network Simulator

3.1 Introduction

The simulator implemented in this work follows on from a Fortran pore-scale depletion simulator developed by McDougall and Sorbie (1999) [142], McDougall and Mackay (1998) [141], Bondino et al. (2005) [143], and Ezeuko et al. (2010) [144]. That simulator modelled the depletion process using a simple invasion percolation process coupled to a multiphase diffusion model whereby, after bubbles had nucleated, the evolution of gas into the surrounding pores depended primarily upon their relative capillary entry criteria. The porous medium was modelled using a simple three-dimensional network of interconnected cylindrical capillary elements, anchored to experimental samples using the "3Rs" approach.

In this work, a radically new simulator has been developed *ab initio* using the C++ programming language and Qt framework. The objective of this change was not only to improve the speed and the structure of the earlier simulator, but also to take advantage of the object oriented structure of C++ that allows us to easily add new features to both the network model construction and the flow algorithms. Indeed, what started initially as a modest depletion simulator has evolved into a full suite of software comprised of several modules and capable of simulating a wide variety of flow phenomena at the pore-scale. We call this simulator *numSCAL* – a numerical Special Core Analysis Laboratory. A basic open source version of numSCAL is available online and can be downloaded from the public GitHub repository: `https://github.com/ahboujelben/numSCAL_basic`.

We start this chapter by presenting the features and flow models supported by *numSCAL* (Figure 3.1) – each model is discussed thoroughly in the subsequent chapters. We also present the formulation adapted in this work to model the pore space, together with details of a novel methodology for upscaling irregular pore networks extracted from microCT images. Finally, we describe the networks that have been used in this work and present their properties.

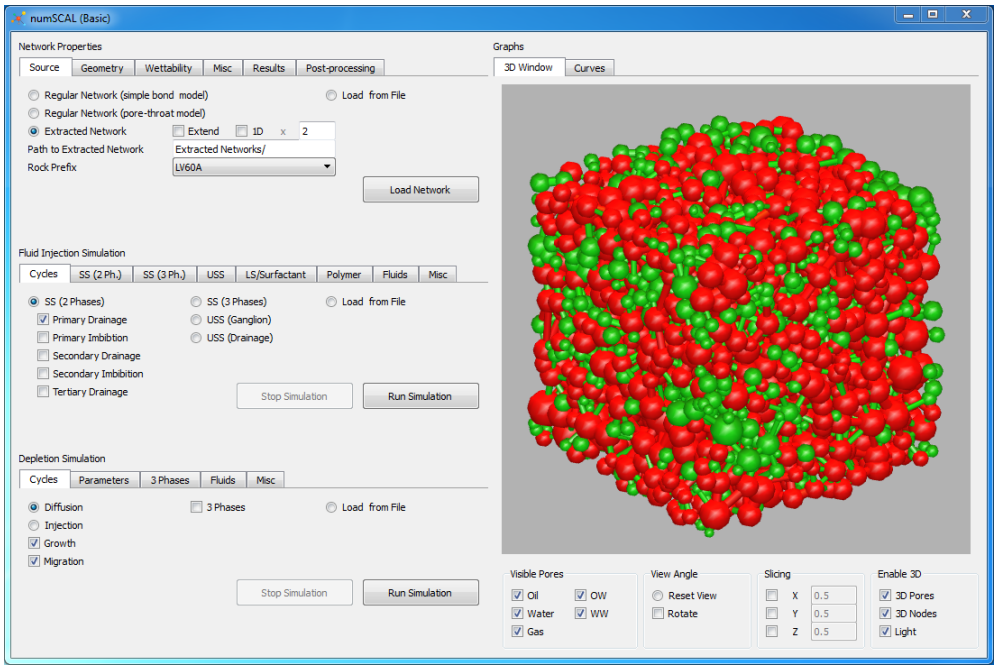

Figure 3.1: A screenshot of numSCAL software.

3.2 numSCAL Features

3.2.1 Pore space modelling

We model the porous medium in *numSCAL* as a network of capillary elements, partitioned into nodes (pore bodies) and bonds (pore throats), with the nodes being linked by the bonds (Figure 3.2). To each network element (a node or bond) we attach a range of geometric attributes (inscribed radius, length, volume, *inter alia*) that enables us to consider a range of different network modelling philosophies. At its most simplistic, we can use the framework to model the pore space as a simple 3D scaffold of interconnected cylindrical bonds; an approach that is useful for obtaining rapid, qualitative results, as fewer pore-scale entities need to be considered. At the other extreme, we can also use the methodology to model multi-phase flow through networks that are topologically and geometrically complex, where the pore space is comprised of irregular pore elements with distributed connectivity.

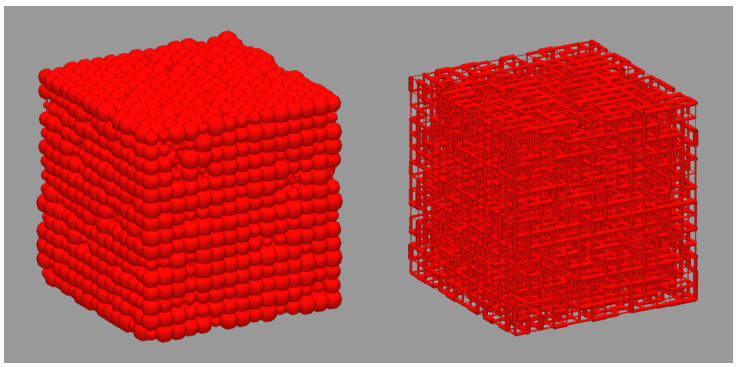

Figure 3.2: 15x15x15 regular networks (left) nodes and throats (right) simple bonds.

Although our network elements can be assigned arbitrary geometries, we will focus initially on elements with circular, triangular or square cross-sections. A shape factor (G) associated with any given pore element can be defined as:

$$G = \frac{A}{P^2} \tag{3.1}$$

where A is its cross-sectional area and P its perimeter. As examples, a circle and a square have shape factors of $\frac{1}{16}$ and $\frac{1}{4\pi}$, respectively. For a triangle, the shape factor will range from ~ 0 for a highly skewed scalene triangle to $\frac{\sqrt{3}}{36}$ for an equilateral triangle.

Regular Networks

Regular networks are assigned pre-determined dimensions $N_x \times N_y \times N_z$, where N_x, N_y, N_z are the number of nodes in the x, y and z directions, and their structure is somewhat idealized. However, capillary entry radii can be assigned randomly to the constitutive elements from a realistic pore size distribution in order to reconstruct the porous medium under investigation.

Several pore size distributions are supported in *numSCAL* to sample pore radii once the minimum radius R_{min} and the maximum radius R_{max} are provided:

- Uniform distribution

$$f(r) = \begin{cases} \frac{1}{R_{max} - R_{min}} & R_{min} \leq r \leq R_{max} \\ 0 & otherwise \end{cases} \tag{3.2}$$

- Triangular distribution

$$f(r) = \begin{cases} \alpha(r - R_{min}) & R_{min} \leq r \leq c \\ \beta(R_{max} - r) & c \leq r \leq R_{max} \\ 0 & otherwise \end{cases} \tag{3.3}$$

where $c = \frac{\alpha R_{min} + \beta R_{max}}{R_{min} + R_{max}}$

- Rayleigh distribution

$$f(r) = \begin{cases} \frac{2(r-R_{min})e^{\frac{-(r-R_{min})^2}{\beta}}}{\beta(1-e^{\frac{-(R_{max}-R_{min})^2}{\beta}})} & R_{min} \leq r \leq R_{max} \\ 0 & otherwise \end{cases} \tag{3.4}$$

where β is the Rayleigh parameter.

- Truncated Normal distribution

$$f(r) = \begin{cases} N(R_{max} - r)(r - R_{min})e^{\frac{-(r-\mu)^2}{2\sigma^2}} & R_{min} \leq r \leq R_{max} \\ 0 & otherwise \end{cases} \tag{3.5}$$

where N is a normalisation factor, and μ and σ are the parameters of the normal distribution.

- Truncated Weibull distribution

$$f(r) = \begin{cases} (R_{max} - R_{min})(-\kappa ln(x(1 - e^{-\frac{1}{\kappa}}) + e^{\frac{1}{\kappa}}))^{\frac{1}{\gamma}} + R_{min} & R_{min} \leq r \leq R_{max} \\ 0 & otherwise \end{cases} \tag{3.6}$$

where κ and γ are the parameters of the Weibull distribution.

Less connected systems can be considered by simply randomly removing a fraction of the capillary elements until a desired coordination number Z is reached. The underlying network can also be distorted to mimic the irregular topology of real rocks. This can be achieved by displacing the coordinates of nodes according to a chosen distortion factor δ (Figure 3.3). The coordinates x_i, y_i, and z_i can then be calculated as follows:

$$\begin{cases} x_{i,new} = & x_{i,old} + L.\delta.(2\eta_x - 1) \\ y_{i,new} = & y_{i,old} + L.\delta.(2\eta_y - 1) \\ z_{i,new} = & z_{i,old} + L.\delta.(2\eta_z - 1) \end{cases} \tag{3.7}$$

where L is the average pore length in the network and η_x, η_y and η_z are random generated numbers between zero and one.

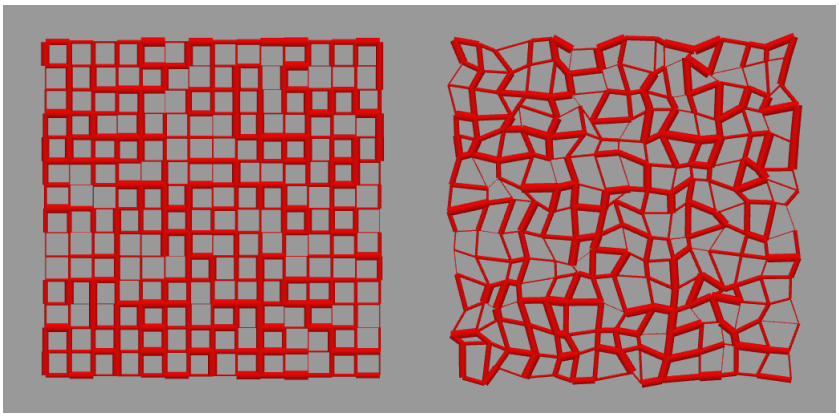

Figure 3.3: Left: regular non-distorted 15x15 network. Right: distorted 15x15 network; distortion factor $\delta = 0.4$.

Networks extracted from MicroCT images

A more realistic network can be generated through the use of a series of image processing operations conducted on 3D images taken from real rock samples. A topologically equivalent network of capillary elements can then be built with properties (radius, volume, shape factor) extracted from the original Micro-CT data. The extracted networks reported as part of this work are based on Micro-CT data obtained from the Imperial College database (Figure 3.4) (Ref, `https://goo.gl/dccvF9`).

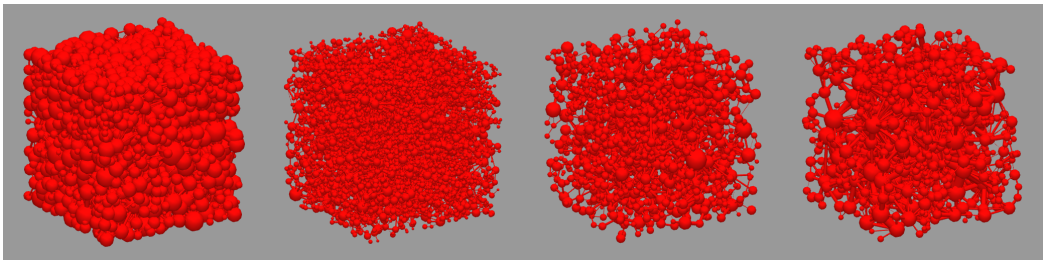

Figure 3.4: Extracted networks from microCT images. From left to right: Synthetic Silica A1, Berea, Sandstone S1 and Sandstone S7.

3.2.2 Wettability configurations

The initial wettability of the network is usually set before running any flow simulation (although it is also possible to alter it during a simulation – see Low Salinity section later in Chapter 8). We therefore assign to each capillary element a contact angle according to a chosen wettability configuration:

- Water-Wet network

All the elements are assigned a contact angle randomly selected between θ_{WWmin} and θ_{WWmax} where $0 \leq \theta_{WWmin} \leq \theta \leq \theta_{WWmax} < 90°$.

- Oil-Wet network

All the elements are assigned a contact angle randomly selected between θ_{OWmin} and θ_{OWmax} where $90° \leq \theta_{OWmin} \leq \theta \leq \theta_{OWmax} < 180°$.

- Fractional-Wet network

The wettability of each capillary element is chosen randomly (water-wet or oil-wet). A contact angle is assigned accordingly within the bounds of θ_{WWmin} and θ_{WWmax} (if the element is water-wet) or θ_{OWmin} and θ_{OWmax}(if the element is oil-wet).

- Mixed-Wet Small network

The smallest capillary elements are assigned an oil-wet contact angle, whilst the largest are considered water-wet. The fraction of oil-wet pores is provided as an input parameter. The contact angles are assigned according to the minimum and maximum values of θ for each wettability case.

- Mixed-Wet Large

The largest capillary elements are assigned an oil-wet contact angle, whilst the smallest are considered water-wet. The fraction of oil-wet pores is provided as an input parameter.

It is also possible to build custom wettability configurations. For instance, it is common to consider some initial water saturation Swi at the start of the simulation. We thus run a primary drainage (where oil is displacing water in a water-wet network) until the desired Swi is reached. We then set all the water-filled capillary elements as water-wet (usually the smallest ones) whilst we assign to the oil-filled pores oil-wet contact angles (assuming that aging altered the initial wettability of the rock).

3.2.3 Flow Models

Several flow models have been developed within the scope of this work and have been implemented into the *numSCAL* simulator (Table 3.1). These models cover a wide range of pore-scale phenomena and will be briefly discussed below.

Simulations	Steady/Unsteady state	Supported Networks
Virgin depletion	Steady-state/Unsteady-state	regular/microCT networks
Gas injection with gravity	Steady-state/Unsteady-state	regular/microCT networks
Tertiary depletion	Steady-state	regular/microCT networks
WAG injection	Steady-state	regular/microCT networks
Waterflooding	Steady-state/Unsteady-state	regular/microCT networks
Unsteady-state drainage	Unsteady-state	regular/microCT networks
Ganglia mobilisation	Unsteady-state	regular networks
Low Salinity injection	Unsteady-state	regular/microCT networks
Polymer injection	Unsteady-state	regular/microCT networks
Surfactant injection	Unsteady-state	regular/microCT networks

Table 3.1: List of simulations supported by numSCAL simulator

Quasi-steady state two-phase and three-phase flow

This model simulates quasi-steady state multiphase flow in both regular and microCT digital networks. By quasi steady-state we mean that phase saturations are assumed to be invariant with time at each fixed capillary pressure value and only change if the controlling capillary pressure changes. A full cycle of displacements can be simulated: primary drainage, primary imbibition, secondary drainage, secondary imbibition and tertiary drainage. Snap-off mechanisms, cooperative pore body filling and film flow are supported in triangular capillaries. A single contact angle is considered and no distinction is made between the advancing and receding contact angles (although this should be addressed in future work).

When three phases are present, a graph-theory-based approach has been implemented to simulate the multi-displacement chains occurring at the pore-scale. Three-phase contact angles are used and spreading phenomena have been incorporated using geometrical conditions corresponding to triangular cross-sections. This model can be used to simulate quasi-static flow in any three-phase configuration, and three-phase saturation and relative permeability curves can be generated. WAG simulations are also supported. Both regular networks and networks extracted from microCT images are supported.

Unsteady-state drainage model

This model is appropriate when the balance between capillary and viscous forces is under investigation in two-phase systems. A dynamic approach is implemented to simulate fluid injection into a porous medium under either constant flow rate or constant differential pressure conditions. The algorithm solves the pressure field in the underlying network and updates phase saturations accordingly. Both regular networks and networks extracted from microCT images are supported.

Unsteady-state ganglion model

This model provides valuable insights into the conditions under which it is likely to observe ganglia displacements during a flood. The model extends the dynamic approach to solve the pressure field and update phase saturations in the network. Two fluids can simultaneously flow through a capillary element and no distinction is made between the invading and the defending phase. The model is appropriate when investigating high rate injection scenarios or scenarios characterised by low capillarity and can estimate the additional hydrocarbon recovery due to ganglia mobilisation. Only regular bond models are supported at the time of writing.

Unsteady-state EOR model

This model is based on the unsteady-state drainage model and is useful for simulating EOR processes at the pore-scale and their manifestations at the core-scale. Low salinity water, surfactant and polymer injection protocols are supported. The model is useful for investigating the efficiency of EOR techniques and estimate the additional recovery they could eventually yield. Both regular networks and networks extracted from microCT images are supported.

Two-phase and three-phase depletion

This model is used to simulate depletion experiments and supports both regular and micro-CT digital networks. All the stages of the depletion are implemented – this includes nucleation, diffusion, gas growth and gas migration. When depletion is simulated in a water-flooded system, an alternative three-phase model based on graph theory is used to simulate the interactions and chain-displacements between gas, oil and water. Oil spreading and film flow are also considered in this model.

3.2.4 Graphical engine

A new graphical engine based on OpenGL has been developed in this work to provide real-time visualisation of the running simulations (Figure 3.5). Several options are available to display the underlying network:

- Visualisation of a single phase.
- Visualisation of only oil-wet or water-wet elements.
- Visualisation of one or multiple tracers during EOR processes (i.e. low salinity water, polymer, etc.).
- Slicing the underlying network to uncover obstructed elements.
- Real-time generation of capillary pressure, saturation and relative permeability data.

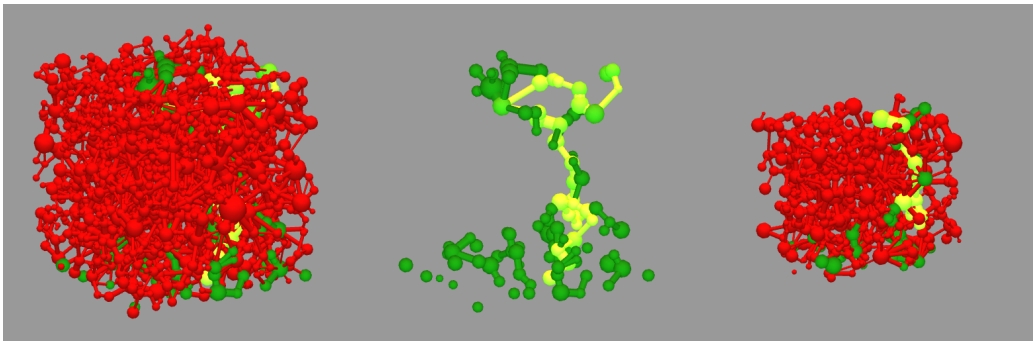

Figure 3.5: Three screenshots generated by the graphical engine of *numSCAL* during a simulation of low salinity water injection into an oil-filled sandstone (S1) network. Red: oil ; Green: water ; Light Green: Low Salinity water concentration. Left: the entire network. Middle: only the water phase. Right: a slice of the network.

3.3 From the Pore Scale To The Core Scale

Building a network that faithfully represents the geometric characteristics of a real rock is one of the main challenges of pore network modelling. The rock geometry has a great impact on the flow of fluids inside the network and an erroneous representation of the physical rock characteristics could lead to inaccurate results.

Simple calibration of regular networks against rock samples is the most basic approach to represent rock topology: an anchored regular network can be obtained by adjusting various network parameters (such as the pore size distribution, coordination number, the degree of distortion) in order to match a limited set of

experimental data from the studied rock. Usually, the calibration process aims to match the absolute permeability, the porosity, the capillary pressure curve, and relative permeability curves. Various tuning parameters can be used to achieve an acceptable match to these data but such a match is non-unique.

Calibrated regular models are undeniably very useful to get an insight into pore-scale displacement mechanisms. However, they do not accurately describe the real complex topology of the pore space (such as the irregularity of pore space geometry, the distribution of coordination number and the possible existence of short range pore size correlations). As a result, a high level of uncertainty can be expected from this kind of anchoring procedure.

A more complex approach has been developed recently through the construction of geologically realistic networks that incorporate the realistic geometry of porous media. Micro Computed Tomography (Micro CT) is a direct method that can be used to achieve this goal. By analysing the spatial variations in attenuation coefficients recorded from a series of X-rays directed at a sample from multiple directions, the distribution of grains and void space can be distinguished and mapped. A skeleton of the reconstructed 3D image that carries the essential geometric and topological information in a condensed form can then be extracted and used as the simulation network.

Micro CT is a very expensive process and it is currently able to resolve rock images down to a few microns. Therefore, the extracted networks from the Micro-CT images are usually not large enough to capture many of the important phenomena associated with flow simulation, especially those dealing with gravity and viscous forces. Extending a small extracted network to the core-scale would be a very useful development, as it would allow us not only to realise a large network model that has the same geometrical properties of the real rock, but also to mimic flow experiments at the core-scale.

Stitching Approach

A new approach has been implemented to build larger networks from the initial networks extracted from microCT images. The idea is to build a modular network from the original small-scale data (Figure 3.6-a). We begin by reflecting the initial network across one plane of symmetry – the plane perpendicular to the X direction – and then "stitch" the two networks together by creating new common throats at the plane of symmetry. This produces a network twice as large as the original (Figure 3.6-b). We next apply the same approach to this stitched network, choosing this time another plane of symmetry – the plane perpendicular to the Y direction.

This produces a network four times larger than the original (Figure 3.6-c). Applying the approach one last time – using the plane perpendicular to the Z direction – a network eight times larger than the original will be created (Figure 3.6-d).

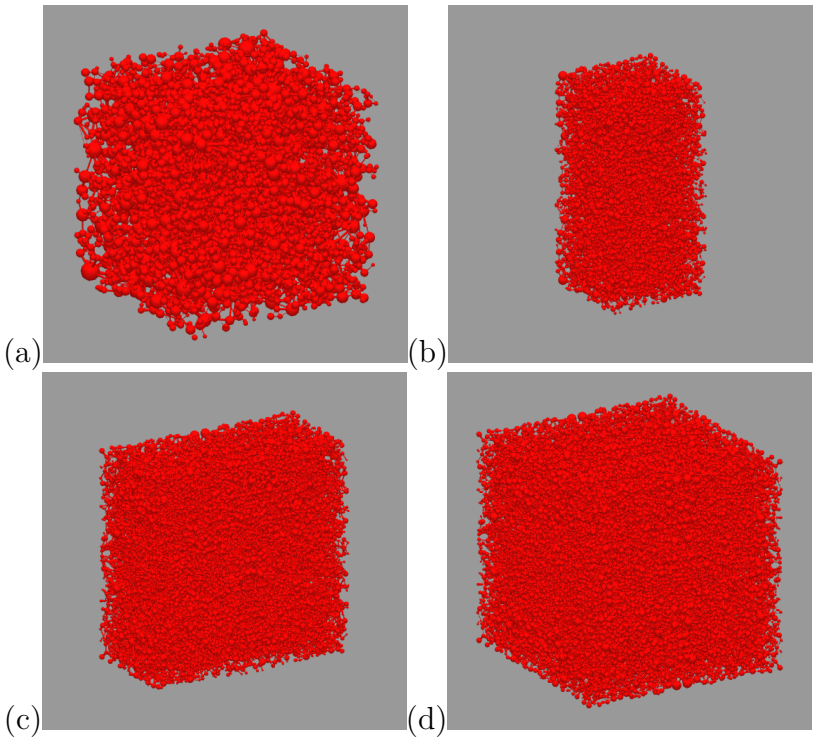

Figure 3.6: Stitching approach (a) original sandstone network (b) extension of network a. in the X direction (c) extension of network b. in the Y direction (d) extension of network c. in the Z direction

To validate this approach, we built extended networks from small networks extracted from micro CT images, and we compared the properties of the original networks to those of the larger models. We adopted three stitching approaches:

- extension (1D) x2: The original network is duplicated in the X direction.
- extension (1D) x4: The original network is repeated four times in the X direction.
- extension (3D) x2: The original network is duplicated sequentially in each direction resulting into a network eight times bigger.

Results show that the absolute permeability and the porosity for the original and their extended counterparts are very similar (Table 3.2).

We next carried out steady state primary drainage simulations to compare the capillary pressure from the original and extended networks. Results show a good match for both curves (Figures 3.7).

Rock	Size	Permeability (mD)	Porosity (%)	Total nodes	Total throats
Berea	original	1,111	20	6,004	12
	extended (1D) x 2	1,028	20	12,008	24,751
	extended (1D) x 4	1,013	20	24,016	49,307
	extended (3D) x 2	1,028	20	48,032	100,720
A1	original	8,077	43	3,366	11,469
	extended (1D) x 2	7,018	43	6,732	22,739
	extended (1D) x 4	6,714	43	13,464	45,281
	extended (3D) x 2	7,018	43	26,928	92,548
S1	original	1,481	14	1,717	3,011
	extended (1D) x 2	1,419	14	3,434	5,913
	extended (1D) x 4	1,406	14	6,868	11,748
	extended (3D) x 2	1,406	14	13,736	24,432
S7	original	7,926	25	982	2,728
	extended (1D) x 2	6,280	25	1,964	5,365
	extended (1D) x 4	5,957	25	3,928	10,660
	extended (3D) x 2	5,957	25	7,856	22,116

Table 3.2: Rock properties of four original microCT digital networks and their equivalent extended reconstructions

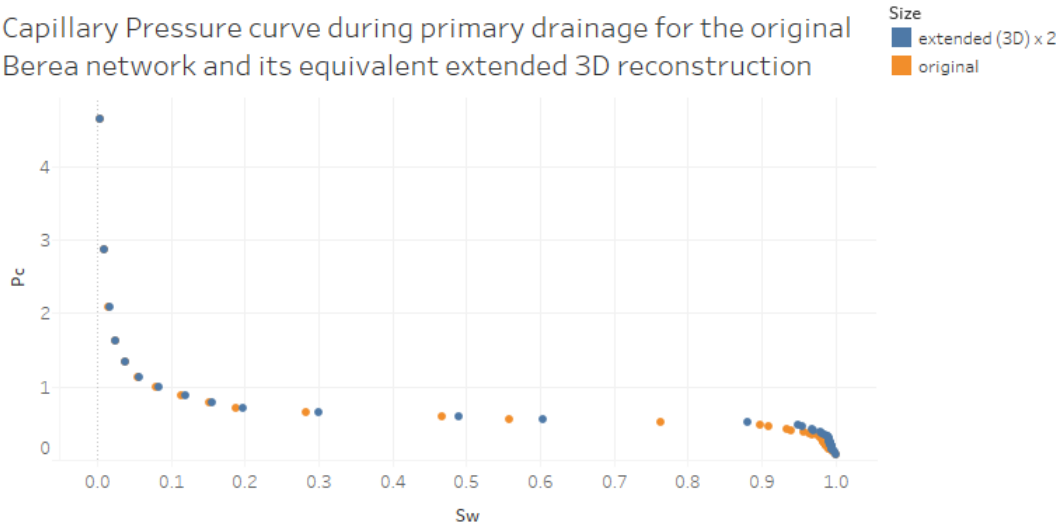

Figure 3.7: Capillary pressure curve during primary drainage for original Berea network and and its equivalent extended 3D reconstructionk

The gas saturation curves during depletion simulations are also found to be in good agreement between the original networks and their extended equivalent reconstructions (Figure 3.8).

From these comparisons we can conclude that the stitching method is a useful initial attempt to build digital core-scale porous media that capture the same properties as the the original small networks extracted from micro-CT images. Another alternative approach that can be easily implemented in future work, is to reconstruct large stochastically-generated irregular networks with the same connectivity and geometrical properties of the original micro-CT rocks (Idowu, 2009 [147]). Note, however, that these large extended networks require significantly higher computational pro-

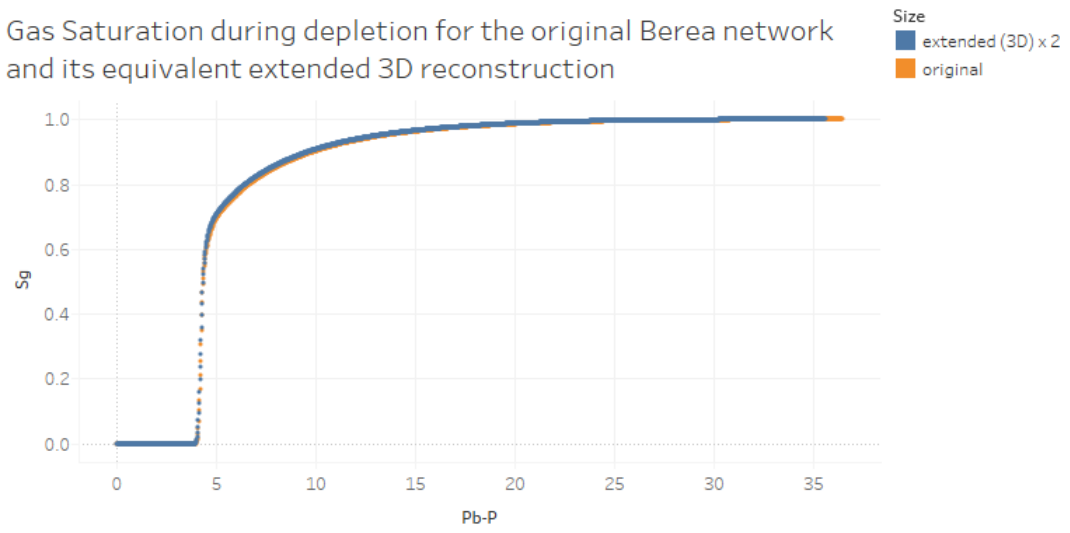

Figure 3.8: Gas Saturation during depletion for original Berea network and its equivalent extended 3D reconstruction

cessing, which makes their use only possible with optimised numerical solvers.

3.4 Studied Networks

In the following chapters, several networks are used to run flow simulations to study various pore-scale phenomena. Both statistically generated networks and networks extracted from micro-CT images are simulated and we are particularly interested in the impact of key parameters on hydrocarbon recovery. We note that statistically generated 2D networks are particularly useful in this context, as they allow better visualisation of a displacement process than their 3D counterparts. Consequently, we will often provide 2D simulation results to better highlight the governing pore-scale mechanisms.

3.4.1 Regular 2D Networks

The 2D statistically generated networks used in this study are regular bond networks, and pore radii are sampled from a predefined pore size distribution. During the sampling operation, it is important to be able to reconstruct exactly the same network again to make valid comparisons between different simulations. We therefore apply a unique random seed when we statistically generate a network.

The random seed can be seen as a parameter that ensures that every time we sample a sequence of numbers from a random distribution, we always end up with the same sequence. Therefore, two networks generated with the same seed would

share identical micro and macro properties. Two statistically generated networks built from two *different* seeds, however, would share the same macro properties (i.e. average coordination number, pore size distribution) but they would have completely different spatial distributions of pores (e.g. in Figure 3.9, the radii of both networks are sampled from the same uniform distribution, but evolve different phase structures due to their different seed numbers).

It is well-recognised that statistically generated networks need to be large enough to be capable of capturing the overall flow behaviour and to prevent statistical variations due to different seeds affecting the simulation outcomes. In fact, two small 2D networks with the same geometrical properties and statistically sampled from the same pore size distribution using two different seeds could yield completely different results, as the the number of possible pathways open to the flow is limited (Figure 3.9).

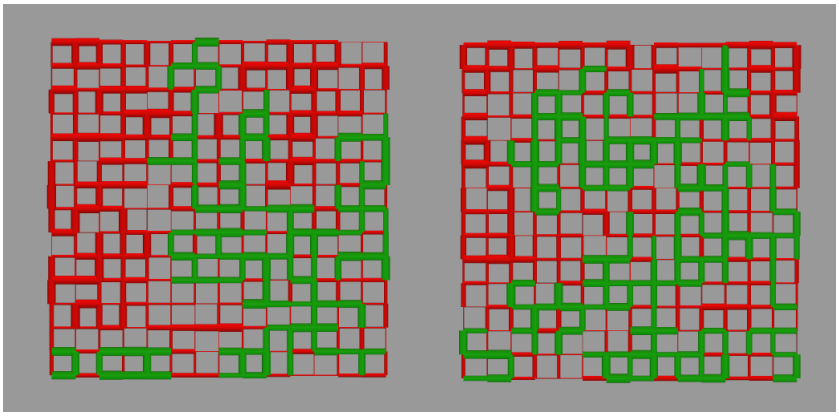

Figure 3.9: Fluid configuration at water breakthrough during quasi-static water injection into two 15x15 statistically networks with the same properties and different seeds. Water flows into the network from the inlet pores at the bottom. Left: water saturation at breakthrough: 48%. Right: water saturation at breakthrough: 62%.

However, large network would require greater CPU power, and so, a compromise is needed between large statistically reliable sizes and reasonable processing times. A sensitivity to network size has been carried out in this context to examine the implication of seed variation on the critical saturation and supersaturation during depletion simulations for different network sizes. The chosen sizes cover the range of networks which could be simulated in less than three days using the unsteady-state model.

Figure 3.10 and 3.11 show, respectively, the statistical variation in critical gas saturation and supersaturation for different network sizes and seeds. The grey area refers to the Interquartile Range (IQR), which corresponds to the middle 50% of the results. As expected, dispersion decreases as the network size increases – 200x100 2D networks yield an acceptable variation to seed and they can be run in a reasonable time. 3D networks are far less sensitive to seed, although they can be CPU-

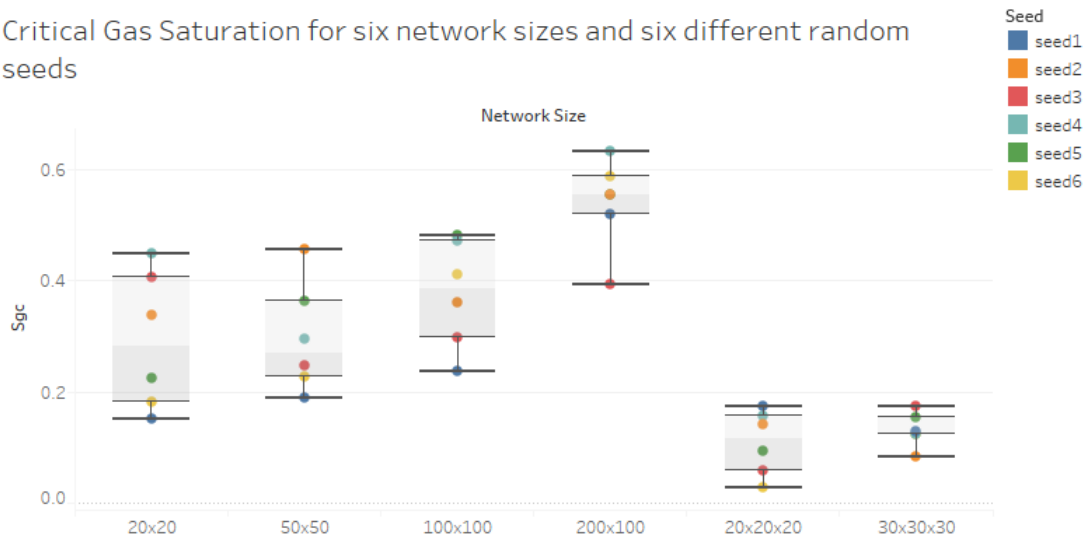

Figure 3.10: Statistical dispersion of critical gas saturation for six network sizes and six different random seed.

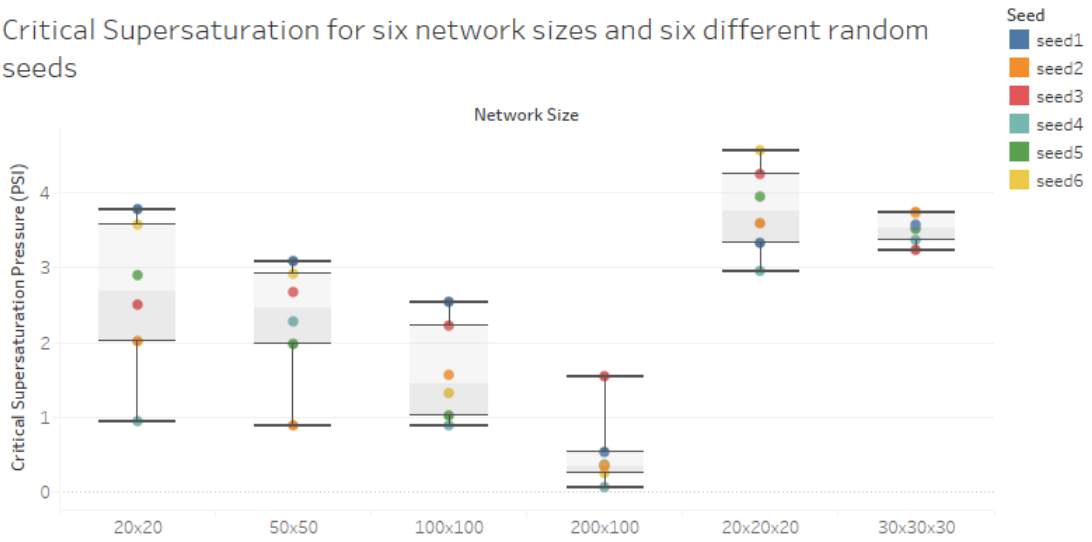

Figure 3.11: Statistical dispersion of critical supersaturation for six network sizes and six different random seed.

expensive, and a 30x30x30 system provides satisfactory convergence.

In the following chapters, 200x100 statistically generated networks are mainly used to examine sensitivities and study various pore-scale related mechanisms. When the third dimension is a key parameter (i.e. relative permeability calculation, three phase flow), digital micro-CT or 30x30x30 networks are used. The properties of these networks were calibrated in previous research works to represent a typical Berea sandstone. The inscribed radii are sampled from a Truncated Normal distribution (Figure 3.12) and the pore volumes and conductivities, V and G, are calculated using the 3Rs approach (see Chapter 2, Section 2.3) as follows:

$$\begin{cases} V = & \bar{C}\pi r^{\nu} L 10^{6\upsilon-12} \\ G = & \bar{A}\pi r^{\lambda} \frac{10^{6\lambda-24}}{8\mu L} \end{cases} \tag{3.8}$$

where $\bar{C}$ and $\bar{A}$ are respectively the volume and conductance constants, ν and λ are respectively the volume and conductance exponents, r is the bond inscribed radius, L is the bond length and μ is the viscosity of the fluid inside the pore.

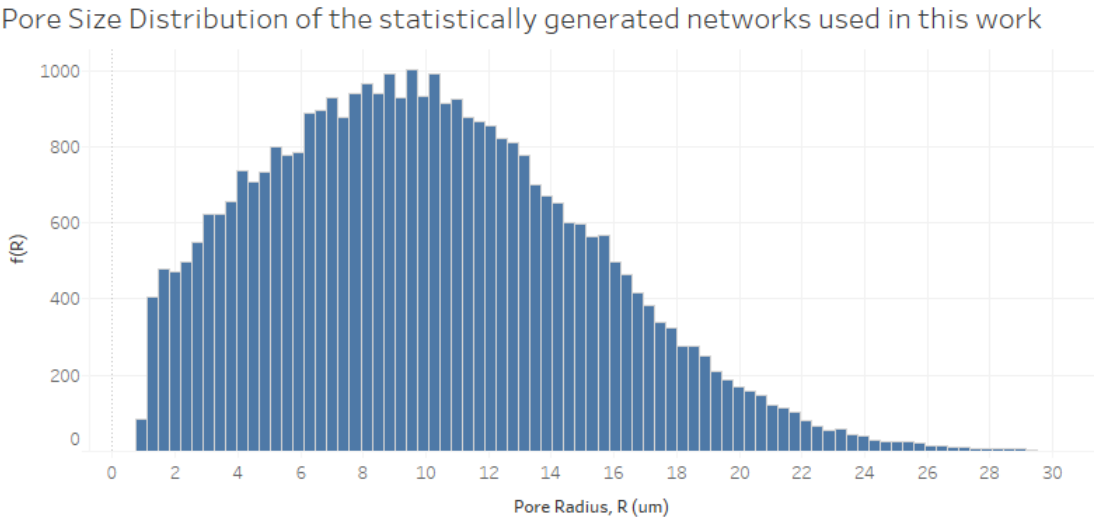

Figure 3.12: Pore size distribution of the statistically generated networks used in the thesis: Truncated Normal($\mu = 9$,$\sigma = 6$).

The geometrical properties of the statistically generated networks are given by Table 3.3. These parameters result in network porosities and permeabilities of $\Phi = 7.56\%\,(2D)$; $9.46\%\,(3D)$ and $\kappa = 208mD\,(both\,2D\,and\,3D)$.

Coordination number	3.65 (2D), 4.55 (3D)
Degree of Distortion	0.3
Average Pore Length	100 μm
Maximum Inscribed Radius	30 μm
Minimum Inscribed Radius	1 μm
Pore Size Distribution	Truncated Normal($\mu = 9$,$\sigma = 6$)
3R coefficients ($\bar{C}$,$\bar{A}$, ν, λ)	$(12, 1, 0.5, 4)$

Table 3.3: Geometrical properties of the statistically generated networks used in the scope of this work.

3.4.2 MicroCT Networks

Most of the simulations carried out in this study use 2D statistically generated networks as they can provide better visualisation and understanding of the underlying pore-scale mechanisms. Networks extracted from microCT images are nevertheless

examined in some sections, especially when the rock geometry and connectivity are under investigation. The four main microCT digital networks used in this study are listed in Table 3.2 and correspond to Berea, 2 sandstones (S1 and S7) and a synthetic silica (A1).

3.5 Conclusions

In this chapter we introduced *numSCAL*: the pore network simulator developed within the scope of this work. The software has been developed using C++ and can be used to investigate a wide range of pore-scale phenomena. Several models have been implemented into *numSCAL* to simulate quasi-static two and three phase flow, unsteady state flow, ganglia mobilisation, EOR processes and depletion experiments.

Three formulations have been also used to model the pore space: statistically generated bond networks, statistically generated pore-throat networks, and networks extracted from microCT images. Various pore size distributions have been implemented to build regular networks, and the simulator has been adapted to read in the digital networks provided by the Imperial College database (Ref, `https://goo.gl/dccvF9`).

A new methodology has also been introduced to upscale the small microCT networks and reconstruct larger networks that have the same properties as the originals. Drainage and depletion simulations showed a good agreement between the original networks and their stitched expanded equivalents.

Finally, we described the regular Berea analogues used in much of this research and discussed their properties. The importance of random number seed has been illustrated, and the selected network sizes have been chosen based on their seed sensitivity and the computational time they would require to run to completion.

In the following chapters, we present the main components of the different models implemented in *numSCAL*. Most of these model descriptions are followed by sensitivity analyses to investigate the impact of key system variables. We begin with a discussion of our modelling framework for depletion in two-phase systems.

Chapter 4

numSCAL Steady-State Two-Phase Depletion Module

4.1 Introduction

Depletion is a complex process that involves the displacement of oil by newly formed gas bubbles once the reservoir pressure drops below a critical threshold. Investigating depletion experimentally has proved to be challenging, and contradictory conclusions have been reached in the past regarding the mechanisms underlying depletion experiments (see Chapter 2, Section 2.10). Mathematical modelling of depletion seems therefore a reasonable and cheap option to investigate this process and help explain inconsistencies in the literature. This approach requires the implementation of a complete solution gas drive workflow, from the early apparition of the first bubbles in the reservoir, to the growth and migration of gas towards the top of the underlying network.

As discussed in the previous chapter, the simulator developed in this work covers a wide range of processes related to oil extraction. One of the main components implemented in *numSCAL* incorporates the mechanisms of depletion and solution gas drive, and builds upon previous theoretical and numerical studies by McDougall and co-workers (Bondino et al., 2011 [145]; Ezeuko et al., 2010 [144]; Bondino et al., 2005; McDougall and Sorbie, 1999 [142], McDougall and Mackay, 1998 [141]).

In this chapter, we begin by introducing an overview of the various components that constitute the *numSCAL* depletion module, including bubble nucleation, diffusion of dissolved gas, gas growth and gas migration. We then move on to discuss the limitations of the current approach and suggest methods to improve its predictive potential. Finally, we apply the model to numerous pore networks to analyse the

sensitivity of gas growth during depletion to some key field parameters, such as the depletion rate, the rock connectivity and the interfacial tension.

4.2 Depletion Model Description

The depletion model implemented in *numSCAL* divides the depletion process into four main steps:

1. Bubble nucleation
2. Gas diffusion
3. Gas growth
4. Gas migration

Although the four mechanisms occur simultaneously in reality, the model discretises the process into separate subroutines at every time step (Algorithm 4.1). The simulation begins when the first bubbles could potentially nucleate (i.e bubble point pressure PB) and proceeds until the local supersaturation exceeds a critical value. At this point, the first bubbles begin to nucleate and dissolved gas diffuses into the gas bubbles according to Fick's laws. The rise of the internal pressure in the bubbles triggers the invasion of the surrounding oil-filled pores and the growth of gas clusters. When gravitational and/or viscous forces are large enough, the clusters may begin to migrate upwards as a result of an alternating drainage-imbibition process. Each mechanism is simulated over the course of the chosen timestep to ensure the consistency of the process.

Additionally, the model works under the following assumptions:

- The flow inside the capillary elements is considered to be laminar – the meniscus between two fluids is assumed to be perpendicular to the axis of the pore.
- The fluids inside the capillaries are immiscible, and the fluid phases are considered incompressible.
- The gas behaves according to the ideal gas law (although Z-factors can be readily included).

The workflow of the depletion module is described by Figure 4.1.

Algorithm 4.1 Depletion algorithm

1. Initialise network
   - Fill network with oil
   - Assign cavities according to selected cavity size distribution
2. Decrease pressure according to selected depletion time step
   - Update fluid properties according to the new pressure value
3. Check nucleation events
   - For every pore i, check if nucleation threshold is reached
   - If true, create a gas bubble in i (volume: host pore volume; mass: dissolved gas concentration $\times$ volume; pressure: derived from ideal gas law)
4. Diffuse gas
   - Choose initial diffusion time step
   - While (diffusion time < depletion time step)
     - For every pore i
       - Calculate the inflow and outflow of dissolved gas (Fick's laws)
       - Update gas concentration in i
     - Check if mass of gas is conserved in the system
       - If not: diffusion time step /=2 and repeat the iteration step
     - diffusion time += diffusion time step
5. Grow gas bubbles
   - Cluster gas-filled pores
   - Calculate the pressure in every gas cluster according to ideal gas law
   - Determine trapped oil-filled pores
   - Loop over all the non-trapped oil-filled pores adjacent to a gas cluster
     - Find the pore j with the minimum capillary entry pressure Pc
   - If the internal pressure of the gas cluster > Pc
     - Fill j with gas
     - Calculate growth time step according to Poisseuille's law
     - growth time += growth time step
   - Repeat, until no more oil-filled pores can be invaded or growth time > depletion time step
6. Migrate gas bubbles
   - Loop over all the non-trapped oil-filled pores adjacent to a gas cluster
     - Find the pore j with the minimum capillary entry pressure Pc
   - If the capillary entry pressure is negative
     - Fill i with gas
     - Calculate migration time step according to Poisseuille's law
     - Loop over all the gas-filled pores of to the invading gas cluster
       - Find the pore j with the maximum entry pressure
       - Re-imbibe j with oil
       - Repeat, until re-imbibed volume=originally displaced volume
     - migration time+= migration time step
   - Repeat, until no more oil-filled pores can be spontaneously invaded or migration time > depletion time step
7. Repeat 2 - 6, until no more oil-filled pores can be invaded or the selected number of depletion steps is reached

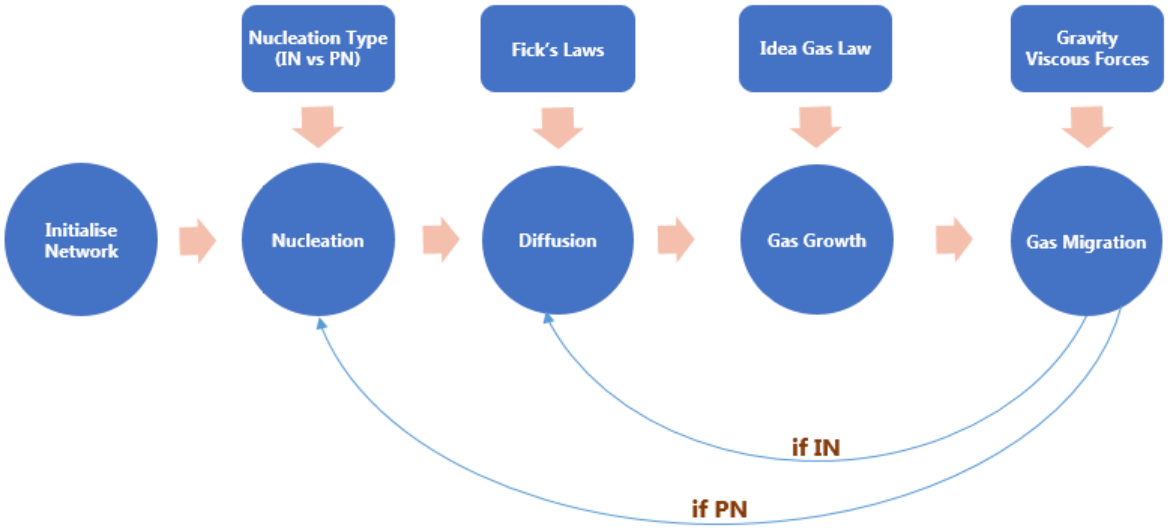

Figure 4.1: numSCAL Depletion Module workflow

4.2.1 Nucleation Module

Intra-pore nucleation is the first step modelled in our depletion simulations, where local supersaturation is monitored to determine if an embryonic bubble should form at a potential nucleation site. Two approaches are included in the simulator: an instantaneous nucleation model (IN), and a progressive nucleation model (PN).

Instantaneous nucleation is implemented by forming a fixed number of bubbles in randomly chosen capillary elements once a predefined critical supersaturation has been reached (Figure 4.2-top). Whilst this approach is somewhat idealised, it is nevertheless useful when investigating straightforward issues such as the effect of bubble density during solution gas drive.

The nucleation algorithm used in the IN model is based upon a single critical supersaturation threshold and this is somewhat limiting. A more realistic model has consequently been included in the simulator to reproduce the physics of the progressive nucleation process: in particular, its intrinsic random nature. In the PN model, the local supersaturation is continuously computed (element by element) and the nucleation of a new bubble is more *likely* to occur in highly supersaturated elements containing an active site (Figure 4.2-bottom). Active sites are considered to be pre-existing vapour-filled crevices - believed to be present on pore walls - which act as catalysts for nucleation (although randomly-distributed "impurities" could also be invoked as potential nucleation sites). Here, an explicit crevice size distribution is input to the simulator and the activation of a crevice (of radius W) occurs when the local supersaturation exceeds the capillary entry pressure of the crevice, viz:

$$KC - P_l \geq \frac{2\sigma cos\theta}{W} \tag{4.1}$$

where C is the local dissolved gas concentration, P_l the liquid pressure, K the gas equilibrium constant, σ the gas-liquid interfacial tension and θ the contact angle. Hence, with this nucleation model, crevices with the largest radii should nucleate first. However, the number of activated cavities at any stage of depressurisation depends not only on the crevice size distribution itself but also on the local degree of supersaturation (a function of other factors including coordination number, depletion rate, and diffusivity). The simulator is coded in such a way as to allow nucleation to emerge naturally as these parameters are varied.

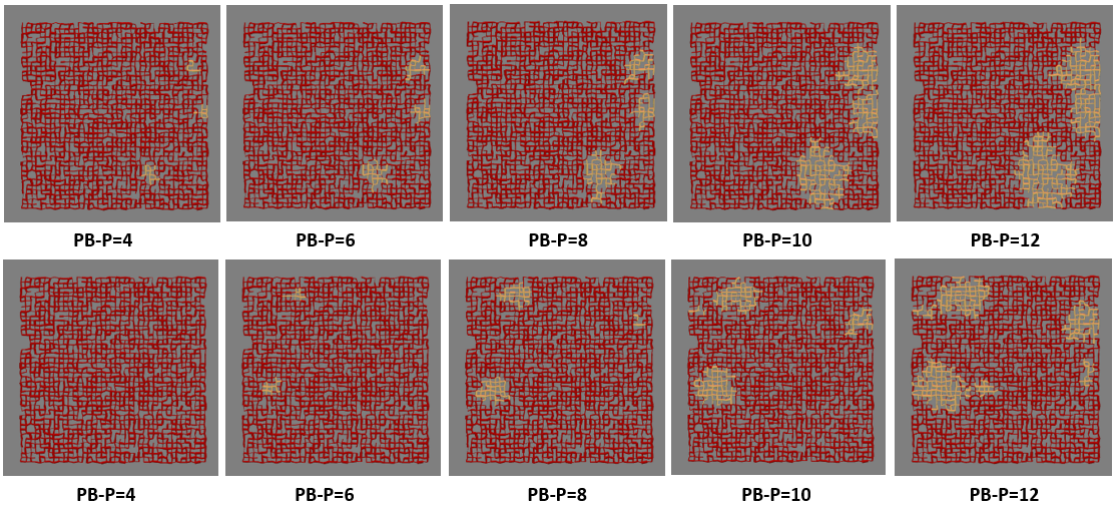

Figure 4.2: IN vs PN nucleation. Top: IN model: three bubbles are nucleated simultaneously and begin growing simultaneously through the entire depletion simulation with no additional nucleation events. Bottom: PN model: As the pressure drops, new bubbles are nucleated. For $P_b - P = 6$, only two bubbles exist. For $Pb - P = 12$, six bubbles are growing in the network.

4.2.2 Diffusion Module

Following nucleation, gas immediately starts to diffuse from pore-to-pore and across new gas-liquid interfaces (Figure 4.3). Gas fluxes between two fluid-filled elements with different gas concentrations are given by Fick's first law:

$$J_{ij} = \frac{D(C_j - C_i)}{L} \tag{4.2}$$

where J_{ij} is the mass flux from element i to element j, C_i and C_j are the dissolved gas concentrations in element i and j respectively, D is the diffusion coefficient, and L is the effective diffusion length, which equals the distance between two element

centres. For an element containing a bubble, the dissolved gas concentration C_i is considered to be that of the nearby bubble interface, and is given by:

$$C_i = \frac{GOR}{VF}\rho_g \tag{4.3}$$

where GOR is the gas oil ratio, VF the volume factor (the ratio of the volume of oil at reservoir conditions to that at surface condition), and ρ_g the gas density. As dissolved GOR is an increasing function of pressure, the dissolved gas concentration near bubbles will decrease during depletion, which results in a continuous mass transfer of gas molecules from the surrounding liquid to the bubble.

For each element, gas concentrations are updated at each time step by applying the discrete form of Fick's second law:

$$C_i^{new} = C_i^{old} + \frac{(mass_{in}(\Delta t) - mass_{out}(\Delta t))}{V} \tag{4.4}$$

where $mass_{in}(\Delta t) - mass_{out}(\Delta t)$ is the net sum of diffusive fluxes across the ends of the element, and V is the element volume. The flux between two elements is assumed to take place across the minimum cross sectional surface between them. Therefore, considering an element with a cross section equal to A, the mass diffusing into it in time Δt is given by:

$$mass_{in}(\Delta t) - mass_{out}(\Delta t) = \sum_{i \in \aleph} J_i \times Min(A, A_i) \times \Delta t \tag{4.5}$$

where $\aleph$ is the set of the neighbouring capillary elements, and A_i the cross section area of neighbouring element i.

One of the many improvements that have been made to the earlier model relates to the choice of the diffusion time Δt. After each time step, the dissolved gas concentration in each element should neither exceed the maximum dissolved gas concentration in any element in the network before the start of diffusion, nor fall below the dissolved gas concentration near bubble interfaces. If the diffusion time is selected above a certain threshold, however, this condition could be violated and the resulting concentration field would become discontinuous.

A rather time-consuming manual tuning procedure was required in the earlier model in order to obtain an estimate of the diffusion time that would guarantee continuity of the concentration field. That method generally led to the selection of a very small diffusion time – consequently, the diffusion module during a depletion simulation

could take a prohibitively long time to run.

That approach has now been replaced by a new dynamic algorithm, where an automatic check of the continuity of the concentration field is performed after each diffusion step. In case of discontinuity, the previous step is cancelled, and the diffusion timestep is halved. The process is repeated until the continuity of the concentration field is achieved – this approach guarantees an optimal choice of the diffusion timestep, and the diffusion routine no longer represents a bottleneck to simulation efficacy.

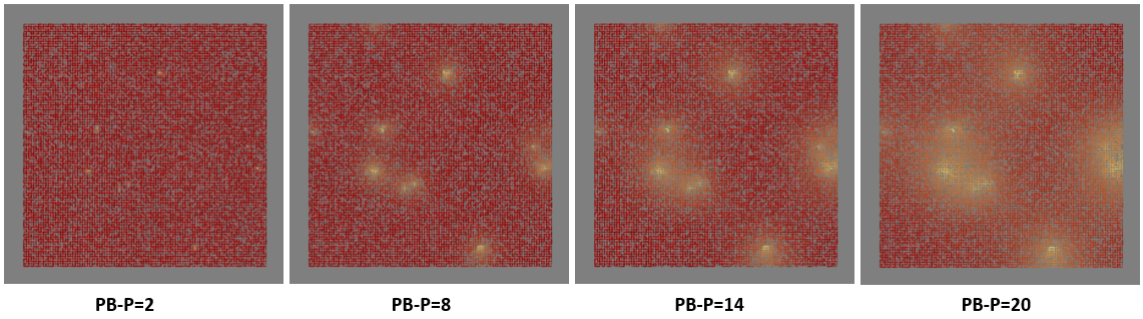

Figure 4.3: Illustration of diffusion phenomenon during depletion simulation. After nucleating 10 bubbles instantaneously, dissolved gas in the oil starts to diffuse through the gas-liquid interface. The pores are painted according to the dissolved gas concentration in oil (red: high concentration, yellow: low concentration). As the simulation evolves, the areas around the nucleated bubbles become yellowish as the dissolved gas in those areas had already been transferred to the bubbles according to Fick's first and second law.

4.2.3 Growth Module

At each step of the depletion simulation, the number of moles of gas transferred into each bubble via diffusion is monitored and the increase of gas mass inside each bubble leads to its growth inside the pore. When the bubble volume is smaller than the volume of its host cylindrical pore, the local gas pressure is a given by the Young-Laplace equation:

$$P_{bub} - P_o = \frac{2\sigma}{r} \tag{4.6}$$

where P_{bub} is the pressure in the bubble is, P_o is the oil pressure, σ is the gas-liquid interfacial tension and r the current bubble radius.

The bubble volume V_{bub} increases according to ideal gas law:

$$V_{bub} = \frac{n_{bub} RT}{P_{bub}} \tag{4.7}$$

where n_{bub} is the number of moles in the bubble, R and T are the gas constant and temperature, respectively. It is important to notice that the increase of bubble volume is not only due to the increase of n_{bub} through diffusion, but also to the reduction of the external pressure field P_o – hence gas expansion emerges naturally from the model.

Once the bubble volume becomes equal to the volume of the pore where it first nucleated, the pressure of the bubble starts to increase, and eventually exceeds the capillary entry pressure requirements of the neighbouring pore(s), which drives the gas expansion. The capillary entry pressure P_C of a cylindrical oil-filled neighboor of radius r is given by:

$$P_C = \frac{2\sigma}{r} cos\theta \tag{4.8}$$

where θ is the oil-gas contact angle, whilst, if an extracted network with angular pores is simulated, the capillary pressure is calculated following the formulation of Øren (1998) [25]:

$$P_C = \frac{\sigma(1 + 2\sqrt{\pi G})cos\theta}{r} F_d(\theta, G) \tag{4.9}$$

where G is the shape factor of the capillary element, and $F_d(\theta, G)$ is given by;

$$F_d(\theta, G) = \frac{1 + \sqrt{1 + 4GD/cos^2\theta}}{1 + 2\sqrt{\pi G}} \; , \; D = \pi(1 - \frac{\theta}{\pi/3}) + 3sin\theta cos\theta - \frac{cos^2\theta}{4G} \tag{4.10}$$

Gravitational Forces

Gravitational forces are also accounted for at the pore-scale. Oil-filled pores near the bottom of the gaseous structure are at higher pressure compared to those adjacent to its upper surface. Therefore, with the bottom of the network acting as the datum level, the net incremental change in capillary entry pressure associated with the invasion of a neighbouring pore at height H from the bottom of the network is given by:

$$-P_{inc,gravity} = -\rho_o gH + \rho_g gH = -\Delta\rho gH \tag{4.11}$$

where ρ_o and ρ_g are respectively the oil and gas density, and g is the gravitational constant (Figure 4.4). Therefore, if all other parameters are kept constant, gas bubbles at higher vertical elevations can be expected to expand more readily compared to those at the bottom of the network, due to the decreasing hydrostatic liquid pressure towards the top of the system.

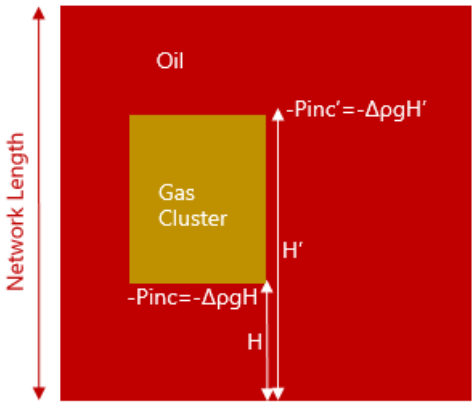

Figure 4.4: A schematic of the incremental gravitational force at the top and the bottom of a gas cluster.

Viscous Forces

Viscous forces are also approximated in this model – a constant pressure is set at the network inlet and a null pressure at the outlet and these are used as boundary conditions to determine the nodal pressure distribution in the system at each time step.

For a single element of inscribed radius r and length L, the flow q is given by a Poiseuille-type law:

$$q = \frac{1}{2}\frac{A^2 G}{\mu L}\Delta P \tag{4.12}$$

where μ is the viscosity of the fluid inside the capillary element, G the element shape factor, L its length, A its cross section, and ΔP the pressure difference acting across it (note that equation 4.12 is reduced to Poiseuille's law when G is substituted by the shape factor of a cylindrical element). Now, when both oil and gas are present in an element, μ is considered to be the average viscosity and calculated as:

$$\mu_{avg} = F_o \mu_o + F_g \mu_g \tag{4.13}$$

where F_o and F_w are the oil and gas fractions in the capillary, and μ_o and μ_g are the oil and gas viscosities, respectively.

[As an aside, when a pore body-throat model is considered, the conductance g_{ij} between two pore bodies i and j connected by a throat is the harmonic mean of each individual conductance. The flow rate q_{ij} is then given by:

$$\begin{cases} q_{ij} = g_{ij} \Delta P \\ \frac{1}{g_{ij}} = \frac{1}{g_i} + \frac{1}{g_t} + \frac{1}{g_j} \end{cases} \tag{4.14}$$

]

Our usual single-phase solution procedure is then used (see Chapter 2, Section 2.6.5) to calculate an approximate viscous pressure field (but now, the fluid viscosity varies from pore to pore through Equation 4.13). The obtained solution can then be used to calculate the pressure gradient across every capillary element, which is then considered as a perturbation to the capillary entry pressure associated with the invasion of a neighbouring pore.

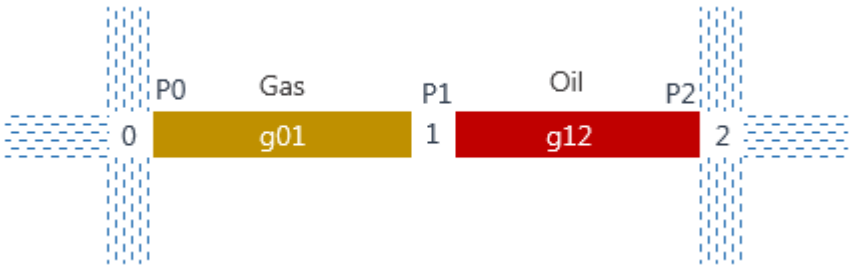

Figure 4.5: Phase configuration where gas is located in the pore on the left whilst oil is filling the pore on the right. P_i refers to the pressure at node i. g_{ij} refers to the conductivity of the pore connecting nodes i and j.

If we consider the configuration depicted by Figure 4.5, this perturbation due to viscous forces is given by:

$$-P_{inc,viscous} = P_1 - P_2 \tag{4.15}$$

Note that the sign of $(P_1 - P_2)$ determines whether the viscous force would reduce or increase the entry capillary pressure required to invade the pore on the right.

Gas Expansion

Now, as the bubble expands, the bubble pressure is updated according to the ideal gas law:

$$P_{bub}(t) = \frac{n_{bub}(t)RT}{V_{bub}} \tag{4.16}$$

This takes into account the bubble expansion due to the continuous mass flux into it. When multiple bubble nucleate, the model accounts for the individual growth of each and re-calculates internal gas pressure if coalescence occurs.

In the old version of the depletion simulator, a simple approach was used to simulate the filling of neighbouring pores. If the pressure difference between gas and oil was less than all entry pressures of neighbouring pores, then the gas cluster was considered to be constrained and the interface did not advance until additional gas diffusion or additional depletion of the oil had occurred. Once unconstrained, the gas began to invade the neighbouring oil pore with the lowest capillary entry pressure. This meant that only a single pore was invaded each timestep, which is equivalent to an invasion percolation mechanism.

In this work we use a new dynamic approach, where gas clusters grow by partially filling *all* the surrounding pores that have a capillary entry pressure lower than the pressure difference between the gas and oil. This is accomplished by calculating the minimum filling time for each of those surrounding pores and updating the gas interface positions in all other partially-invaded pores after the invasion.

For each neighbouring oil-filled pore i that could be invaded by a gas cluster, the relative filling time t_i is given by:

$$t_i = \frac{V_i(1 - f_i)}{\Delta P_i g_i} \tag{4.17}$$

where f_i is the fractional saturation of gas filling of the pore i ($f_i = 1$ if the pore is entirely filled with gas), V_i is the pore volume, g_i is the pore conductance and ΔP_i is the pressure across the pore which is calculated from:

$$\Delta P_i = P_{bub} - P_o - (P_{entry} - P_{inc}) \tag{4.18}$$

where P_{inc} is given by the sum of Equation 4.11 and 4.15. The pore with the minimum filling time t_{min} is filled with gas, and the positions for all the other

interfaces are updated according to:

$$\begin{cases} f_i^{new} & = \frac{V_{g,old}+V_{g,inc}}{V_i} \\ & = f_i^{old} + \frac{t_{min}\Delta P_i g_i}{V_i} \\ & = f_i^{old} + \frac{t_{min}}{t_i}(1 - f_i^{old}) \end{cases} \tag{4.19}$$

The growth proceeds until all the oil-filled pores that satisfy the entry pressure condition are invaded with gas, or once the growth time reaches the depletion timestep, or once the gas cluster reaches the maximum volume allowed by PVT. In the latter case, the gas cluster requires additional moles of gas to enter it via diffusion and/or an additional drop in system pressure to keep growing.

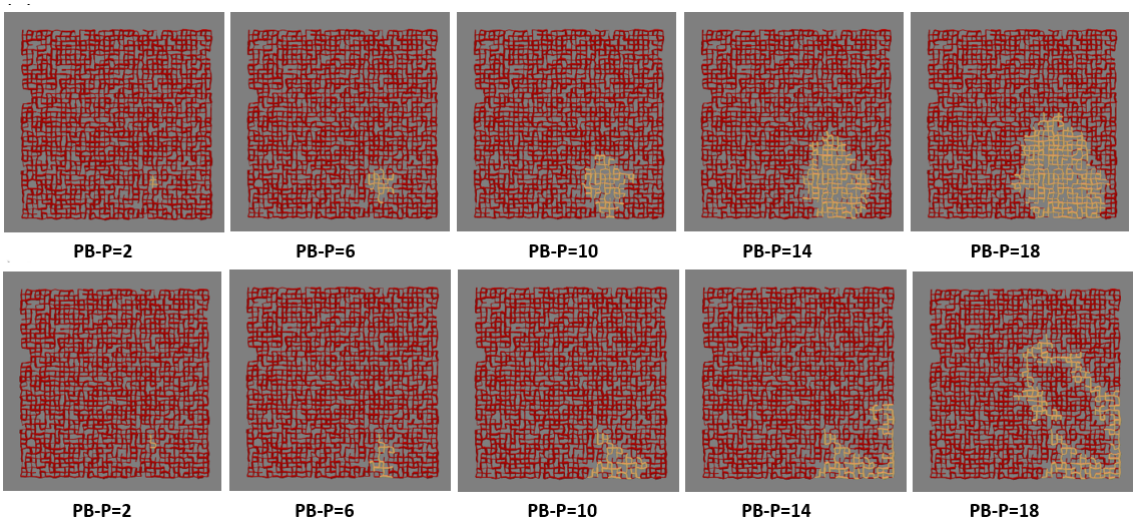

Figure 4.6: Illustration of gas growth using the dynamic growth module (top) and the invasion percolation module (bottom).

Figure 4.6 shows the difference between the new dynamic approach and the old approach based on invasion percolation mechanism. The figure shows the growth of one bubble in a 100x100 regular network (uniform PSD between $1\mu m$ and $20\mu m$) where pressure decreases from 750 psi to 730 psi during one day. As multiple pores are filled simultaneously using the dynamic approach, the nucleated bubble grows in a compact fashion, and less oil trapping is obtained by the end of the depletion simulation (Figure 4.6-top). In contrast, the invasion percolation approach leads to a capillary expansion where gas fingers grow in different directions (Figure 4.6-bottom). This would eventually lead to early breakthrough and increased oil trapping.

Impact of Depletion Discretisation on Gas Growth

It is important to highlight the fact that the number of steps used to discretise the depletion simulation has a great impact on the growth behaviour. The amount of dissolved gas that goes into a bubble is mainly determined by the diffusion area (the area between the gas cluster and the surrounding oil) and, in order to obtain realistic growth, it is necessary to update the interfacial area at each step of the depletion simulation. Using a small number of steps can lead to an underestimate of diffused gas. Consider the extreme example when we nucleate one bubble and diffuse all the available dissolved gas during one day in one single step (remember, diffusion occurs prior to growth in the model): under this unrealistic assumption, the bubble would remain contained in one single pore, and when the growth module is called, it would grow suddenly according to the quantity of gas diffused into it. However, in reality, the bubble would have expanded progressively throughout the day. The liquid-gas area would expand accordingly, which would attract more dissolved gas toward the bubble.

To address this issue, we discretise the depletion simulation sufficiently finely whilst keeping the gas-liquid interfacial area consistent with the amount of gas in each bubble. Figure 4.7 shows the growth of one bubble under the same assumptions described in the previous depletion simulation shown in Figure 4.6. The depletion steps are increased here from 10 (the number of steps used previously in both cases) to 10000. Now, both the invasion percolation approach and the dynamic approach result in the same growth pattern at every pressure value. Using this solution leads to the unification of both approaches described previously when simulating the bubble growth.

For the simulations carried out in this work, we discretise each day of depletion into 10000 steps to allow a real-time adaptation of the liquid-gas interface. Hence, we obtain the same growth pattern independent of the growth module deployed during the simulation. However, it should be noted that this new approach can handle steep pressure decline that can be observed near fractures or during very high depletion rates, where compact growth is likely to occur.

4.2.4 Migration Module

In some cases, when buoyancy forces are very large, capillary entry thresholds are spontaneously overcome, resulting in upward mobilization of gas clusters (Figure 4.9). The buoyancy forces are modelled in a similar way as the hydrostatic oil pressure was included in the formulation of the net entry pressure. We consider that

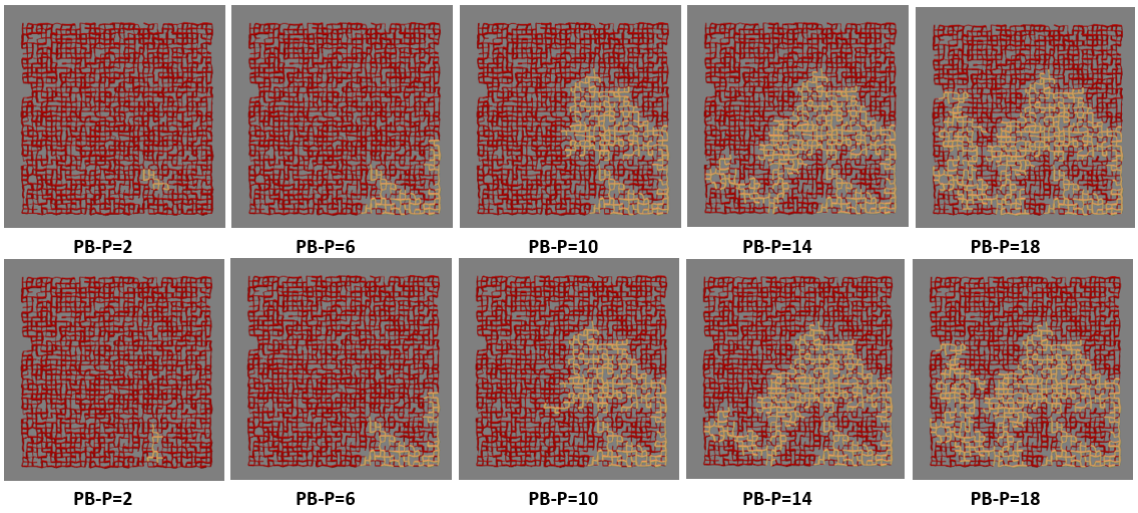

Figure 4.7: Illustration of gas growth using (a) the dynamic growth module and (b) the invasion percolation module. The simulation is carried out on a regular network 100x100 network. The pressure has been decreased from 750psi to 730psi during one day. The depletion simulation is discretised into 10000 steps.

the bottom of the *bubble* acts as the datum level; thus, the net incremental change in capillary entry pressure P_{inc} associated with the invasion of a neighbouring pore at height h from the bottom of the bubble is now given by:

$$-P_{inc} = -\rho_o gh + \rho_g gh = -\Delta\rho gh \tag{4.20}$$

During gas migration, volume conservation has to be maintained, and re-imbibition of the oil has to be modelled. The approach that we use in this work is as follows: once an oil-filled element has been invaded with gas due to migration, we imbibe gas-filled elements with oil until both volumes of the invaded and the imbibed elements are equal. Imbibition occurs in the gas-filled elements characterised by the *maximum* entry pressure thresholds, a discussion of which now follows.

We assume that oil can imbibe into a pore or a throat filled with gas via snap off at a capillary pressure of $\frac{\sigma cos\theta}{r}$. In addition to this mechanism, imbibition via piston like displacement is also allowed. This occurs at a capillary pressure of $\frac{2\sigma cos\theta}{r}$ for a throat. However, the capillary entry pressure for filling a capillary element during spontaneous imbibition is affected by the largest radius of curvature that can be obtained, which is directly linked to the number of adjacent oil-filled throats as shown in Figure 4.8.

We use a linear relation to link the capillary entry pressure for re-imbibition into a gas-filled element as a function of the number of neighbouring elements filled with gas. When no adjacent throats are filled with gas the process is similar to piston-like displacement and the capillary entry pressure is given by $\frac{2\sigma cos\theta}{r}$. For a pore with

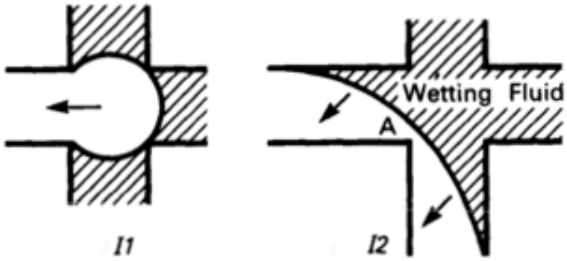

Figure 4.8: Cooperative pore filling mechanisms: (I1) the nonwetting fluid is only in one duct. An instability appears when the meniscus no longer touches the walls. (I2) The nonwetting fluid is in two adjacent ducts and the collapse occurs when the meniscus reaches point A. (Lenormand, 1984 [60])

coordination number z and $z-1$ adjacent throats filled with gas, we assume that the entry pressure is equal to $\frac{\sigma cos\theta}{r}$. For a pore with n adjacent elements filled with gas, the capillary entry pressure is given by:

$$P_{entry} = \frac{2\sigma cos\theta}{r} - \frac{n}{z-1}\frac{\sigma cos\theta}{r} \tag{4.21}$$

which approaches the correct limits for $n = 0$ and $n = z - 1$.

This approach follows the observations of Lenormand and Zarcone (1983) [59], where piston-like events occur at higher capillary pressures than snap-off. This also mimics observations in micro-model experiments, where oil re-imbibes preferentially into gas-filled pores lying at the extremities of the gas structure. The net incremental change in capillary entry pressure due to the gravitational forces is also accounted for during imbibition.

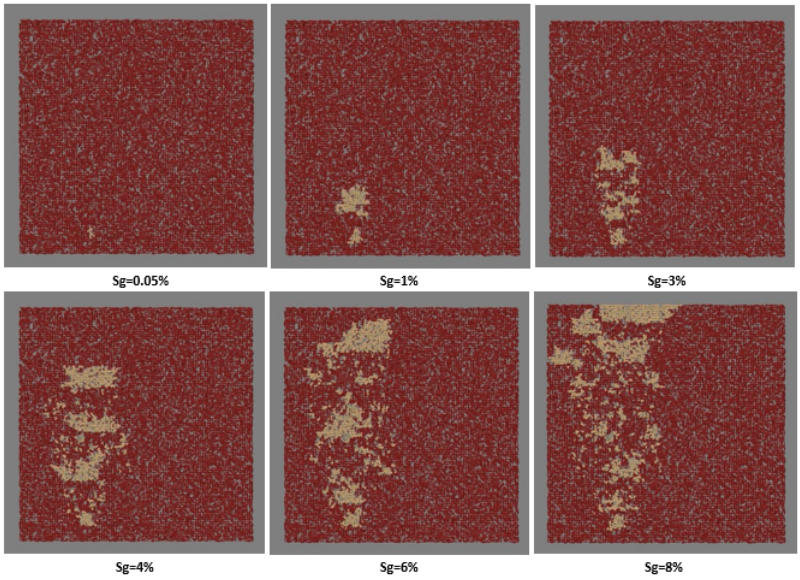

Figure 4.9: Illustration of gas migration during gas injection simulation in a 100x100 regular network. Gas is injected into one single pore with 1g/min rate. When gravity module is activated, and buoyancy forces are high enough to allow spontaneous migration, imbibition events start to occur resulting in the migration of the gas toward the top of the network.

4.2.5 Trapping and Oil Films

Trapping rules are implemented in the depletion module to prevent gas structures from invading inaccessible oil pores. An oil-filled pore is considered trapped if two conditions are simultaneously satisfied:

1. The pore has no bulk connection to the outlet of the network, and
2. The pore is not connected via an oil-wet pathway to the outlet of the network (i.e. no escape path via films is available).

If we consider the configuration shown in Figure 4.10, oil cluster 1 is directly connected to the outlet, hence, the associated oil-filled pores with an interface with the gas cluster could be invaded. Oil cluster 2 is topologically trapped (no bulk connection to the outlet), but it belongs to large spanning cluster of oil-wet pores. This allows the associated pores to escape via film flow and therefore they are accessible to the invading gas cluster. Oil cluster 3, is topologically trapped and belongs to a water-wet spanning cluster, and therefore, is considered as trapped and the gas is not allowed to invade the corresponding pores.

The identification of separate phase clusters alongside wetting clusters requires the application of efficient clustering algorithms every time the network configuration

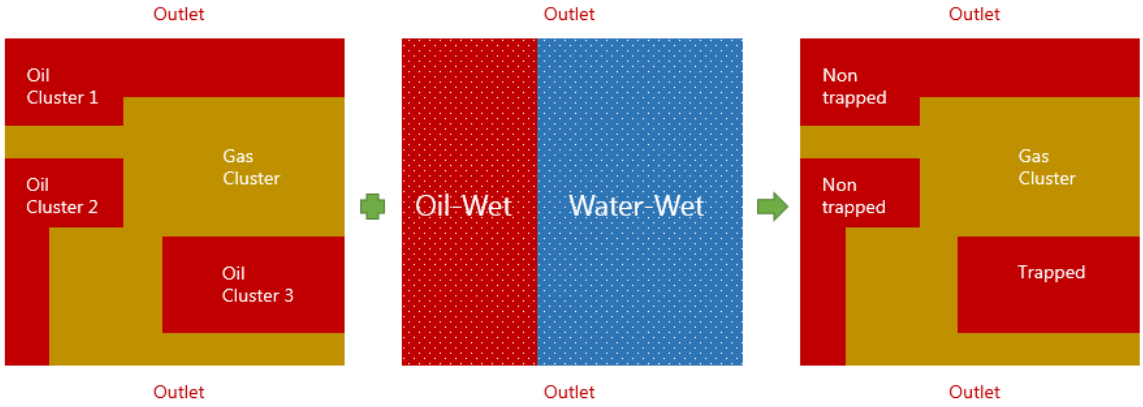

Figure 4.10: A schematic of the trapping rules. Oil cluster 3 is trapped as it has neither a bulk connection nor an oil-wet pathway to the outlet.

changes. This has been addressed in this work by adapting a Hoshen-Kopelman algorithm [148]. Although originally intended to be applied on two-dimensional lattices, the algorithm has been extended to support three-dimensional lattices, as well as irregular networks with bonds and nodes. By using this method, the network has only to be fully examined once, and each capillary element is assigned an incremental cluster label according to the cluster labels of its surrounding neighbours. At the end of the process, a final sweep is required to update cluster labels in accordance with a cluster connectivity matrix.

Films in Angular Pores

When angular pores are under investigation (this will be the case when networks extracted from microCT images are used), the assigned wettability based on the contact angle θ is no longer sufficient to decide whether oil can escape via film flow or not. In fact, films can only flow through a corner of an angular pore (Figure 4.11) if stable arc menisci (AM) can form.

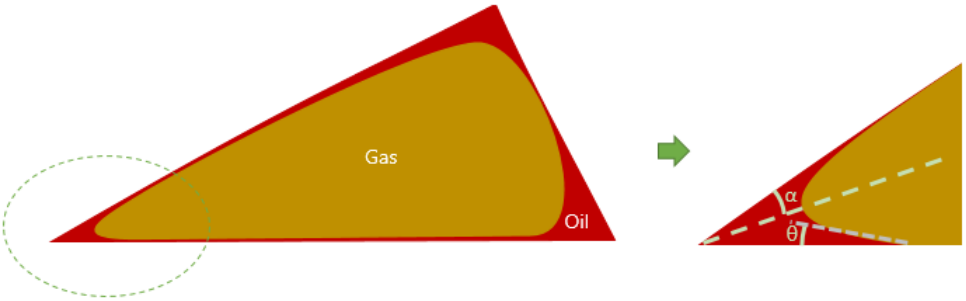

Figure 4.11: A schematic of oil film in the corner of a gas-filled angular pore.

If we consider Figure 4.11, where oil films are present in a corner of half angle α, the necessary geometrical condition for AM stability is given by:

$$\theta < 90^\circ - \alpha \tag{4.22}$$

The stability of at least one AM is required for a pore to be assigned a flag reflecting the potential for oil to escape via film flow. The clustering algorithm uses this flag to determine the set of pores with film pathways connected to the outlet.

Film volumes are also taken into account, and are calculated based on the formulation of Øren (1998) [25]. The volume $V_{film,corner}$ occupied by oil in a corner of half angle α is given by:

$$V_{film,corner} = Lr_c^2[\frac{cos\theta cos(\theta+\alpha)}{sin\alpha} - \frac{1}{2}(\pi - 2(\theta+\alpha))] \tag{4.23}$$

where $r_c = \frac{\sigma}{P_C}$ is the radius of curvature of the AM., and L is the length of the capillary element. Similarly, the conductance $g_{film,corner}$ of an oil film present in a corner is calculated as:

$$g_{film,corner} = \frac{r_c^4}{L\mu}[\frac{cos\theta cos(\theta+\alpha)}{sin\alpha} - \frac{1}{2}(\pi - 2(\theta+\alpha))] \tag{4.24}$$

where μ is the oil viscosity.

4.2.6 Model Limitations

How to Deal with a Third Phase

In previous implementations of the depletion simulator, the presence of water as a third phase was modelled in a simple way: similar trapping rules were applied to identify non trapped water clusters (those which are connected to the outlet via bulk or water-wet pathways) and the gas was allowed to invade oil-filled pores which belonged to an oil cluster adjacent to a non-trapped water cluster. The invaded oil cluster would in turn displace the non-trapped water cluster by invading the water-filled pore corresponding to the minimum oil-water capillary entry pressure.

Whilst this approach was convenient for simple configurations, where only a few phase clusters existed in the system, the limited chain displacement events (the longest chain would be gas-oil-water) could result in an underestimate in the volume of oil that could be really displaced if longer chains were allowed.

Three phase models presented in the literature have reported how considerably

longer displacement chains can occur – van Dijke et al (2006) [90] registered up to eight chain long displacement events during WAG simulations (Figure 4.12). In a subsequent paper (Van Dijke et al., 2008 [94]), fifteen chained displacement events were simulated.

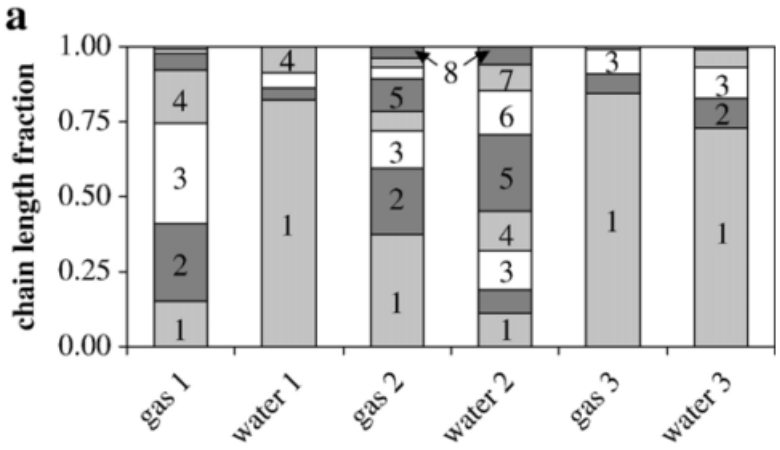

Figure 4.12: Displacement statistics for WAG simulations. Fraction of the total number of displacement chains with the indicated length. (Van Dijke, 2006 [90])

Hence, a consistent model of depletion when three phases are present (i.e. depletion in water-flooded cores) requires the implementation of physics specific to three-phase flow. Moreover, multi-displacement chain events need to be modelled to achieve realistic estimates of the oil quantities that could be displaced by solution gas drive. Such mechanisms have been implemented in the new *numSCAL* three phase module, and will be discussed in detail in Chapter 5.

Dealing with the Issue of Viscous Forces

As discussed in Section 4.2.3, viscous forces are modelled using a pseudo-single phase approach, where the pressure field is solved in the network by taking into account spatial variations in viscosity but ignoring capillary pressure terms. The pressure gradient across each pore is then used as an incremental perturbation to the associated capillary entry pressure. Although the approach can affect the gas growth regime and result in elongated gas structures when a pressure gradient is applied across the network (Figure 4.13), it is important to highlight an inconsistency associated with this approach.

When the nodal pressure field is solved across the network, the capillary pressure terms acting across oil-gas interfaces are not taken into account. This can result in a pressure solution inconsistent with the pressure drops that exist across oil-gas interfaces.

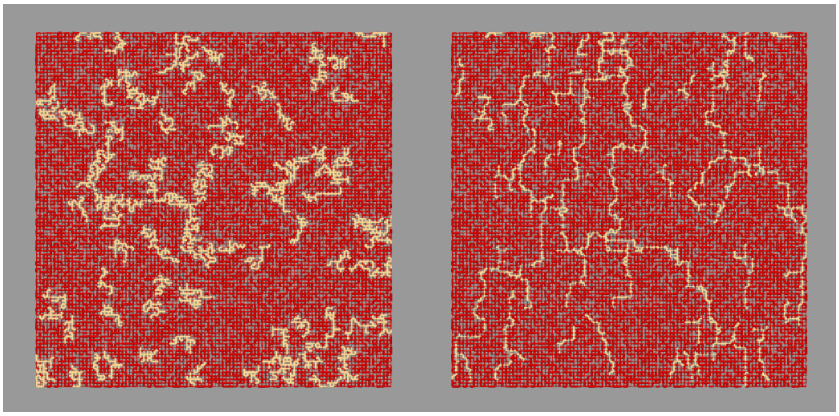

Figure 4.13: Effect of viscous forces during depletion. When capillary forces are predominant, gas bubbles grow in a compact fahion (left). Setting a pressure gradient across the network result into elongated gas structures that grow towards the low pressure boundary – the top of the network in this case (right)

To illustrate this point, consider the configuration described in Figure 4.14 where gas is flowing through two identical connected pores. 0, 1 and 2 refer to the nodes at the ends of the pores, and P_0, P_1 and P_2 are the associated pressures respectively. An oil-gas interface is present in the pore $(1, 2)$ associated with a capillary pressure P_C.

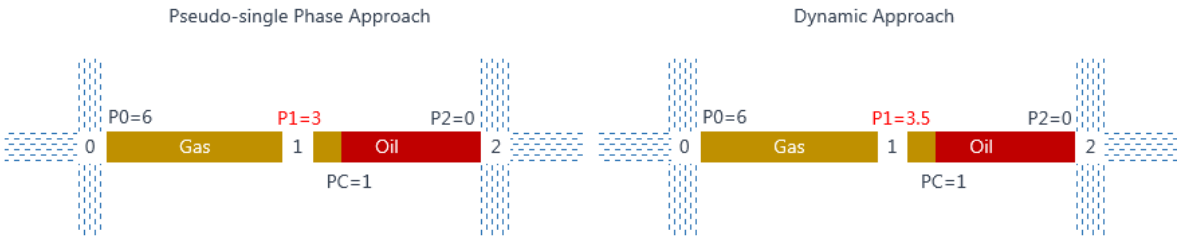

Figure 4.14: Pressure calculation using a pseudo-single phase approach (left) and a dynamic approach (right)

For the sake of simplicity, let us assume that gas and oil have the same viscosity, P_0 and P_2 are predefined pressures assigned 6 and 0, respectively, and P_1 is unknown. Conservation of mass implies that the flows in both pores are equal. As the pseudo-single phase approach ignores the capillary pressure associated with the interface in the pore $(1, 2)$, we can write $P_0 - P_1 = P_1 - P_2$, and thus $P_1 = 3$. However, a consistent approach would include the term P_C in the flow conservation equation (which we assume for simplicity equal to 1), and therefore, $P_0 - P_1 = P_1 - P_2 - P_C$. Thus, $P_1 = 3.5$.

This simple example shows that a pseudo-single phase approach can lead to erroneous calculations of the pressure field in the network. To study the effect of viscous forces on gas growth, a more consistent dynamic approach needs to be considered.

Two unsteady-state models have been implemented in this work to tackle this problem. The first is related to dynamic drainage whilst the second involves ganglia mobilisation mechanics. These models will be discussed in Chapter 6 and Chapter 7, respectively. Consequently, large viscous forces will not be considered further in this chapter.

4.3 Application: Analysis of Steady-State Gas Evolution during Depletion in Porous Media

Numerous simulations have been carried out using the *numSCAL* depletion module to examine sensitivities to a wide range of parameters that affect the depletion process – some of these parameters are related to the experimental protocol (depletion rate, bubble density, fluids properties…), others are related to the underlying rock properties (rock type, connectivity).

For the sensitivity analyses we use both idealised 2D and 3D oil-wet networks described in Chapter 3 Section 3.4.1, as well as real networks extracted from Micro-CT images. Typical base-case depletion experiment parameters are shown in Table 4.1.

Bubble point pressure	750 psi
Depletion Rate	2 psi/day
Initial GOR (pressure dependent)	15 sm^3/sm^3
Initial gas density (pressure dependent)	40 Kg/m^3
Oil Volume Factor (constant)	1 sm^3/sm^3
Gas-Oil Interfacial tension (constant)	30 dyn/cm
Oil Viscosity (constant)	300 cP
Gas viscosity (constant)	0.02 cP
Diffusion Coefficient	0.3 $10^{-5}cm2/s$
Default Nucleation Module	PN $1cavity/200pores$

Table 4.1: Default parameters used for the sensitivity analysis

The computational time required to run these simulations depends on the network size, depletion rate, depletion steps, pore size distribution, network connectivity and various other flow parameters. Most of the simulations carried out in this study took less than two days to complete. Table 4.2 shows the running time of a depletion simulation (10000 steps) for different configurations using an i7-3770 processor.

Network	Number of capillaries	Depletion Rate	Time (seconds)
200x100	$\backsimeq$ 37000	1psi/day	111838
200x100	$\backsimeq$ 37000	2psi/day	66800
200x100	$\backsimeq$ 37000	5psi/day	39187
200x100	$\backsimeq$ 37000	10psi/day	36016
200x100	$\backsimeq$ 37000	50psi/day	24221
Berea	$\backsimeq$ 19000	2psi/day	207056
A1	$\backsimeq$ 15000	2psi/day	314957
S1	$\backsimeq$ 5000	2psi/day	13023
S7	$\backsimeq$ 4000	2psi/day	18674

Table 4.2: Computational performance of the two-phase depletion module

4.3.1 Effect of Depletion Rate

Instantaneous Nucleation (IN)

In this section, we are interested in the effect of depletion rate on gas cluster growth and, consequently, oil recovery. We start the analysis using the IN nucleation module, where 10 bubbles are nucleated instantaneously and allowed to grow. We consider 4 different depletion rates, 1 psi/day, 5 psi/day, 10 psi/day and 50 psi/day, in an oil wet 200x100 regular network. Note that by assuming an oil-wet model, all oil will be allowed to drain from the network via film flow.

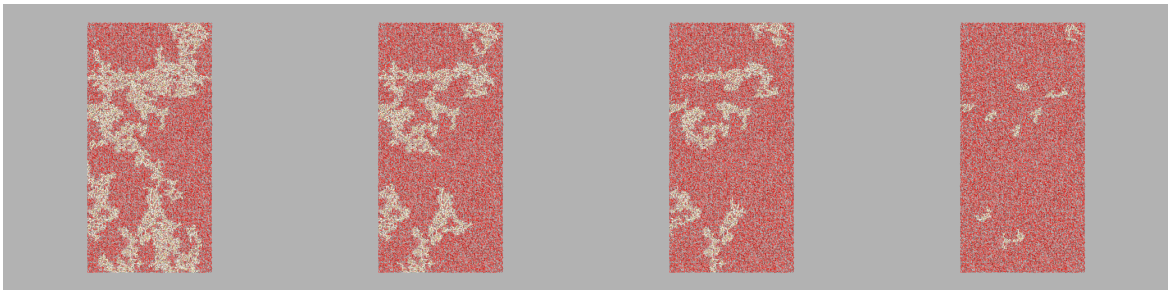

Figure 4.15: Gas distribution at PB-P=10psi for 4 depletion rates using IN nucleation module. From left to right: 1psi/day, 5 psi/day, 10psi/day, 50psi/day.

It can be seen from these initial results that, at any given pressure, low depletion rates result in greater gas expansion (Figure 4.15). This is primarily due to the fact that when the depletion is fast, gas has less time to diffuse from the oil to the bubbles - this is well illustrated by Figure 4.16, where it is shown that when Pb-P is equal to 20, gas reached a saturation of 45% for 1psi/day depletion rate, while it was only 20% for 50psi/day depletion rate. Higher rates cause the oil to become more supersaturated, and more gas tends to be maintained in the dissolved state (Figure 4.17). This is in agreement with the experiments of Moulu and Longeron (1989) [123] and Li and Yortsos (1995) [149] that showed more gas liberated - and better oil production - at lower depletion rates at a given pressure.

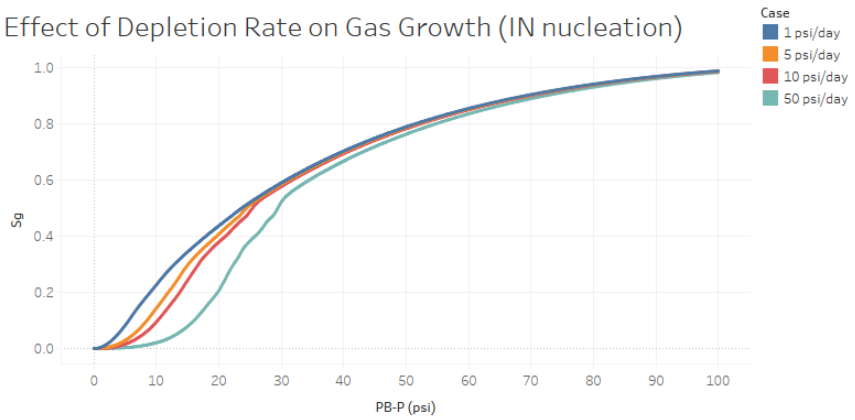

Figure 4.16: Effect of depletion rate on gas growth using IN nucleation module.

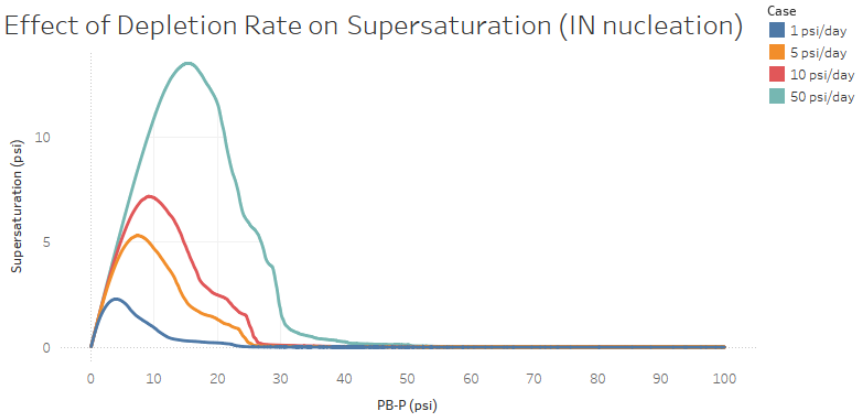

Figure 4.17: Effect of depletion rate on average supersaturation using IN nucleation module.

However, it is often the case that higher depletion rates can be responsible for higher critical gas saturations. This has been observed in the experiments of Kortekaas and Van Poelgeest (1991) [126], and Ligthelm et al (1997) [109], who confirmed that larger gas saturations are obtained at faster rates.

The results that we obtained from our IN simulations exhibit the converse behaviour, however, and this is due to the fact that we assumed a fixed number of bubbles to be nucleated regardless of depletion rate. This simple (and unrealistic) approach of the IN formulation explains why, at a given pressure, more gas could develop at lower rates. In reality, a faster depletion rate may also give rise to high local supersaturation, leading to an increasing number of bubbles being progressively nucleated. We investigate this in the following section.

Progressive Nucleation (PN)

The effect of depletion rate is now investigated under the assumption of progressive nucleation, which is believed to be a more realistic model of the actual nucleation

mechanism in porous media. We run four simulations corresponding to the same four depletion rates used in the previous section: 1 psi/day, 5 psi/day, 10 psi/day and 50 psi/day.

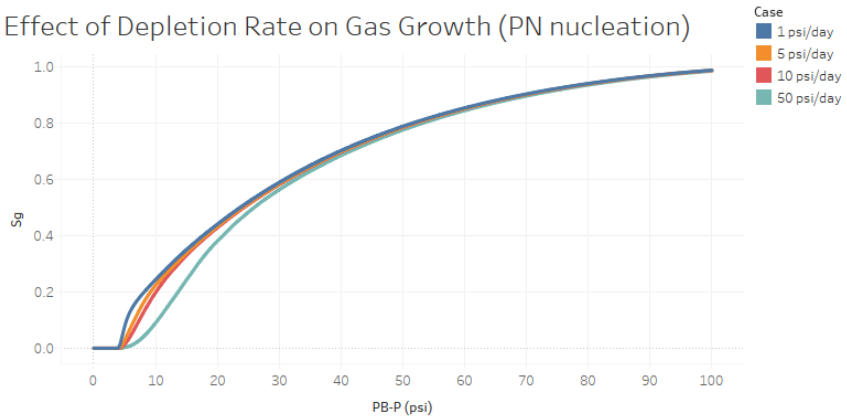

Figure 4.18: Effect of depletion rate on gas growth using PN nucleation module.

From Figure 4.18, it is seen that more gas expansion is achieved for low depletion rates during the early stages of depletion (which is similar to the results obtained with IN nucleation). As the simulation progresses, the profiles rapidly asymptote to the same gas saturation for any particular pressure for all depletion rates. Again, as explained in the IN section, for low depletion rates, dissolved gas has more time to diffuse into the nucleated bubbles, which explains the high gas saturation at the beginning of the simulation. However, this effect is counteracted later by another phenomenon observed for high rate depletion, in which more bubbles are nucleated due to high local supersaturations. This is well illustrated by Figure 4.19 where the correlation between the depletion rate and the number of gas clusters is clearly visible.

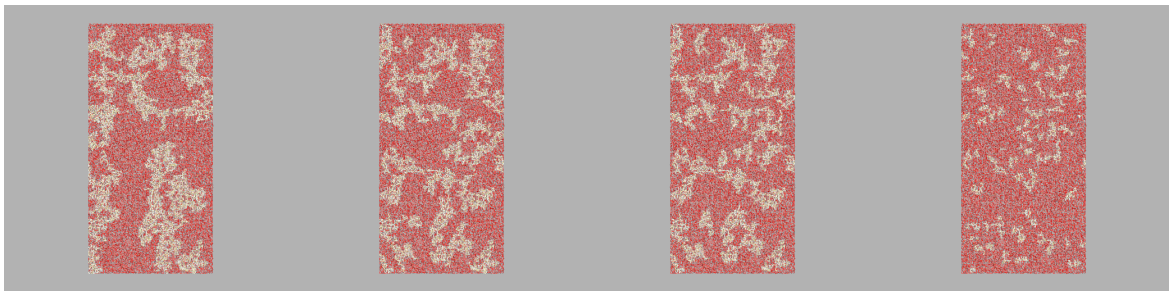

Figure 4.19: Gas distribution at PB-P=10psi for 4 depletion rates using PN nucleation module. From left to right: 1psi/day, 5 psi/day, 10psi/day, 50psi/day.

The high local supersaturations achieved for high depletion rates can result in a rapid increase in gas saturation and the formation of foamy oil. This is validated by Figures 4.20 and 4.21, where we can see the effect of depletion rate on both supersaturation and bubble number. For PB-P=10, the number of gas cluster for 50psi/day depletion rate was four times higher compared to 1psi/day.

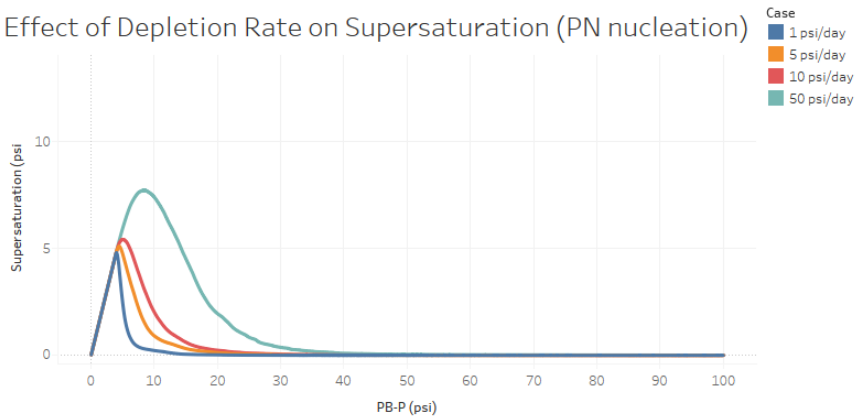

Figure 4.20: Effect of depletion rate on average supersaturation using PN nucleation module.

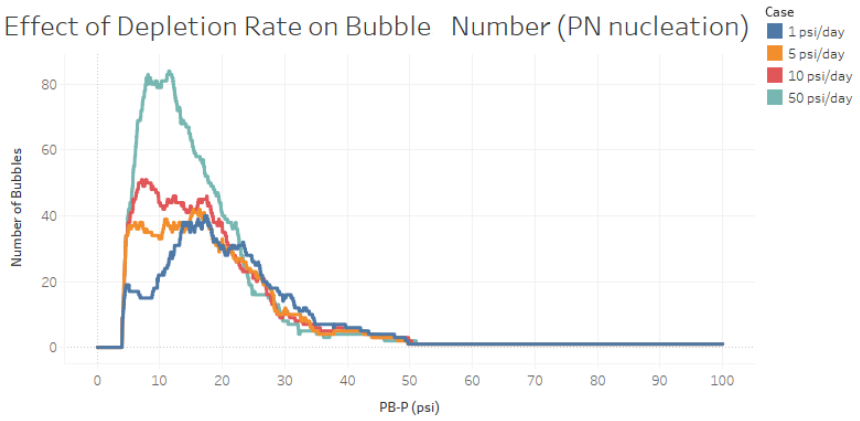

Figure 4.21: Effect of depletion rate on bubble number using PN nucleation module.

Such behaviour also leads to higher critical gas saturations (Sgc) for high rate depletion experiments (Table 4.3). As Sgc marks the beginning of gas production (and the formation of a spanning gas cluster in this case), this measure can be correlated to the efficiency of the depletion process. In fact, at gas breakthrough, it is expected that gas growth would be negligible afterwards as the gas pressure would decline significantly, and thus Sgc would be the maximum gas saturation that could be eventually reached. Hence, the fact that high rates appear to yield higher Sgc values compared to slower rates is consistent with the experimental observations that demonstrate better recovery for high depletion rates.

Case	Sgc	Critica lPressure (psi)
1 psi/day	0.52	725.3
5 psi/day	0.55	722.6
10 psi/day	0.55	722.3
50 psi/day	0.56	720.4

Table 4.3: The effect of depletion rate on critical gas saturation.

We run the same simulations on 3D 30x30x30 networks to derive relative permeabil-

ity curves and results are in agreement with the 2D observations. Figure 4.22 shows an early breakthrough and higher gas permeability for low depletion rates. The effect on oil permeability is negligible.

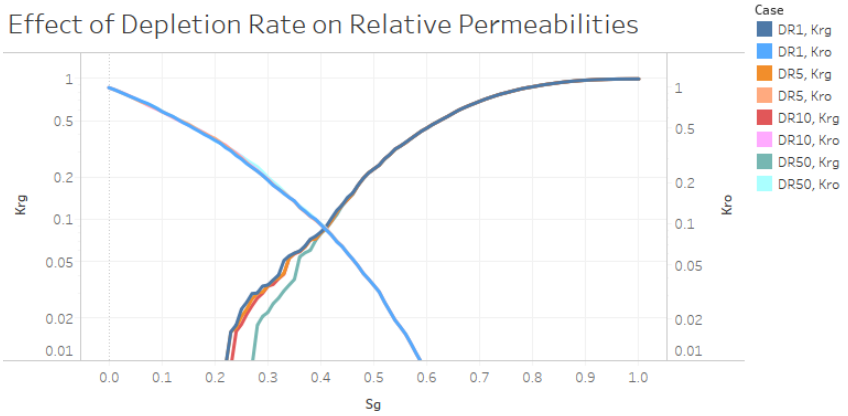

Figure 4.22: Effect of depletion rate on relative permeability curves using PN nucleation module.

Effect of Oil Trapping

It is worth noting that gas saturation curves displayed in this study are affected by the trapping rules applied in the model. In fact, oil-filled pores are allowed to be invaded instantaneously if they are connected to the outlet via oil-wet pathways. This explains the fact that gas saturations asymptote to 1 in all cases as every oil-filled capillary element in an oil-wet system can be notionally invaded once its corresponding capillary entry pressure is overcome. In fact, if we run the same depletion rate sensitivity simulations on a water-wet network - where film flow does not occur - gas stops growing when all the non-trapped pores are invaded (Figure 4.23).

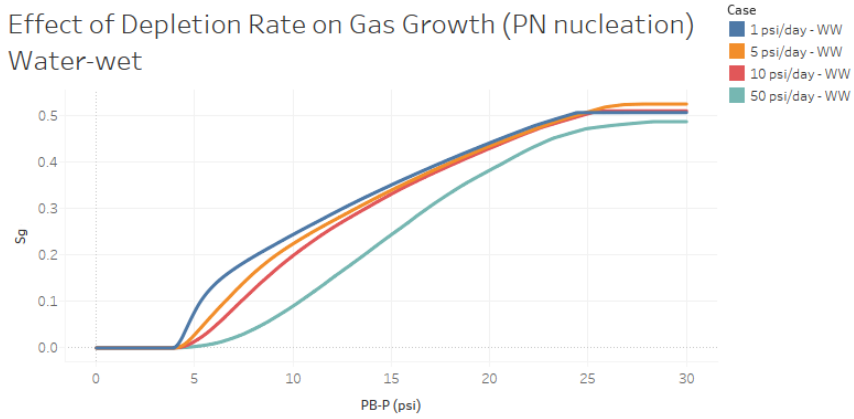

Figure 4.23: Effect of depletion rate on gas growth using PN nucleation module.

Only oil-wet scenarios will be considered further in this chapter although wettability effects on depletion will be discussed in Chapter 5. [As an aside, the film draining

process should be ideally tracked as a function of time - this is beyond the scope of this work but could be implemented in future work as part of a dynamic depletion model].

Another important factor that needs to be noted here is the fact that we keep running the simulation until all the available oil is displaced (another reason that explains the convergence of gas saturations towards 1 in oil-wet systems). In reality, gas expansion is expected to slow down significantly after breakthrough as discussed earlier. Therefore, the gas saturation curves are relevant only at early stages of depletion and should not be considered in isolation from the critical gas saturation which represents a better indication of the depletion performance.

4.3.2 Effect of Bubble Density

The previous simulations showed a strong correlation between depletion rate and bubble density. Here, we examine the effect of the latter independently.

Instantaneous Nucleation (IN)

We begin by using the IN module to simulate nucleation. We run 4 simulations where a predetermined number of bubbles are nucleated instantaneously at the beginning of the depletion simulation. Figure 4.25 shows the evolution of gas saturation for the 4 studied scenarios.

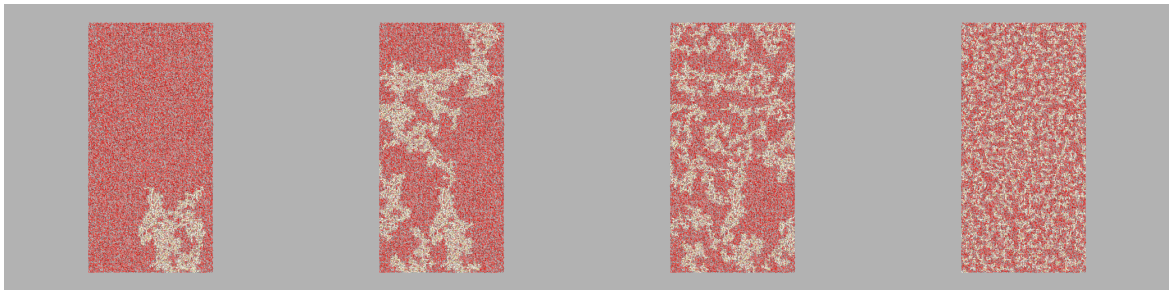

Figure 4.24: Gas distribution at PB-P=10psi for 4 bubble densities using IN nucleation module. From left to right: 1 bubble, 10 bubbles, 100 bubbles, 1000 bubbles.

As expected, higher gas saturations are achieved when more bubbles are nucleated. For instance, at PB-P=10, the gas saturation was around 28% when 1000 bubbles were nucleated, whilst less than 10% gas saturation was achieved when only one bubble grew in the network. The curves asymptote towards the same saturation at very low pressure values due to the fact that no oil is trapped in these simulations. Because of the reduced supersaturation of the oleic phase when large numbers of bubbles are nucleated (Figure 4.26), the nucleated bubbles are expected to reach

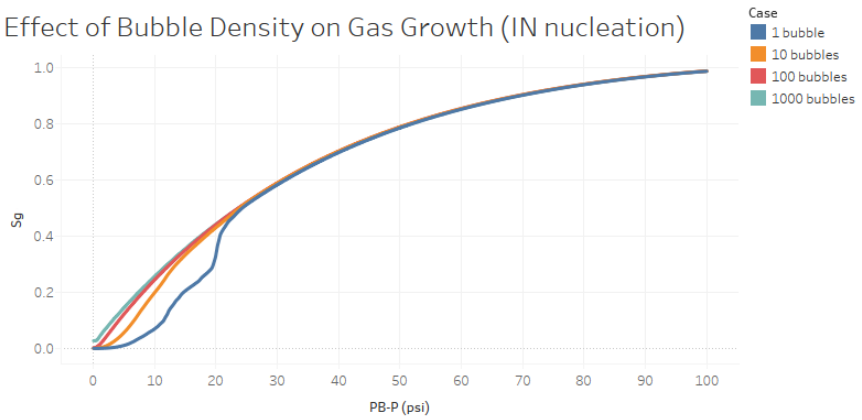

Figure 4.25: Effect of bubble density on gas growth using IN nucleation module.

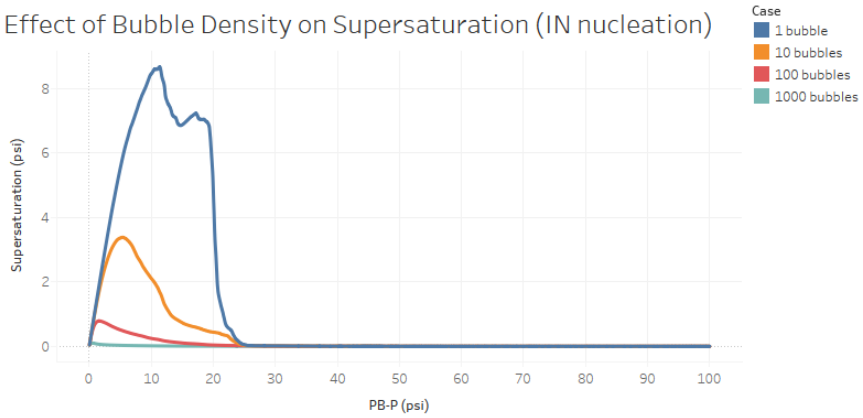

Figure 4.26: Effect of bubble density on average supersaturation using IN nucleation module.

smaller size compared to the case where only a few bubbles are growing in the network (Figure 4.24). This delays breakthrough and so higher Sgc values are expected for higher bubble densities (Table 4.4), which points towards better recovery for processes inducing a high number of gas bubbles (i.e. deploying high depletion rates).

Case	Sgc	Critical Pressure (psi)
1 bubble	0.33	730.00
10 bubbles	0.47	728.04
100 bubbles	0.55	722.72
1000 bubbles	0.64	715.72

Table 4.4: The effect of bubble density on critical gas saturation.

Progressive Nucleation (PN)

We now examine the impact of bubble density using the more realistic PN nucleation module. We consider 4 cavity densities: 1 cavity per 50 pores, 1 cavity per 200 pores,

1 cavity per 500 pores, and 1 cavity per 1000 pores. Figure 4.27 exhibits the same pattern observed using the IN nucleation, where higher gas saturations are achieved at early stages for the networks with higher numbers of cavities. The difference between the four scenarios is smaller than that of the IN case. In fact, the system here is more self equilibrating as the bubble nucleation events are correlated to the local supersaturation.

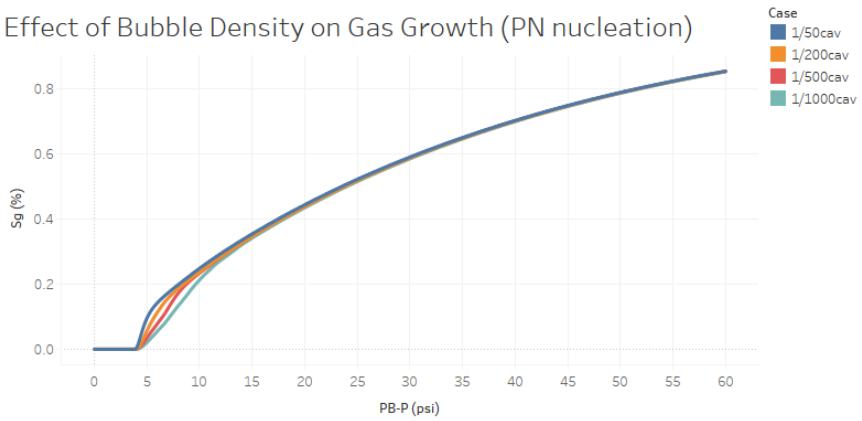

Figure 4.27: Effect of bubble density on gas growth using PN nucleation module.

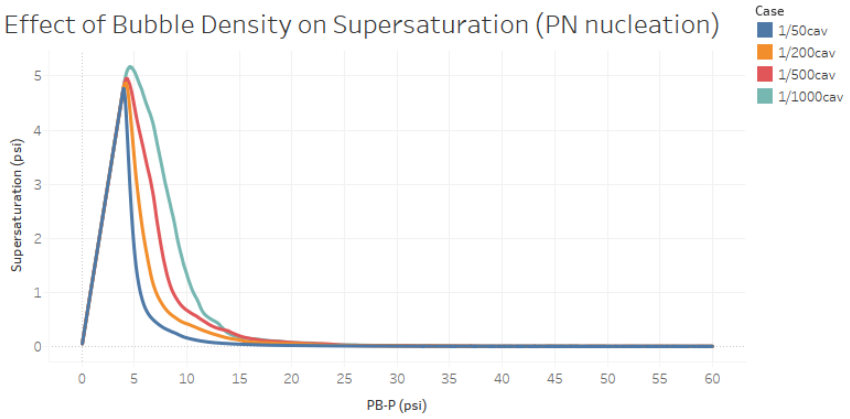

Figure 4.28: Effect of bubble density on average supersaturation using PN nucleation module.

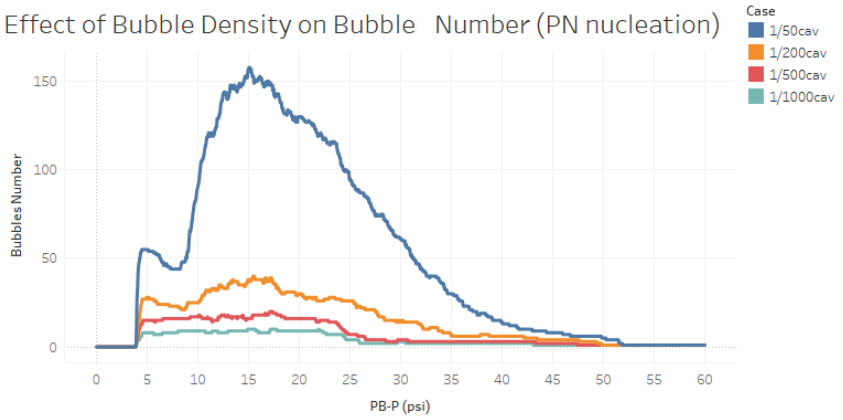

Figure 4.29: Effect of bubble density on bubble number using PN nucleation module.

Figure 4.28 shows that lower supersaturations are achieved for high cavity densities. Indeed, despite the competition for the dissolved gas, the large number of nucleated bubbles appears to bring down the local supersaturation in the network and yields faster equilibration of the gas-oil system (Figure 4.29). Also, the increase of cavity density is accompanied by delayed gas breakthrough and higher critical gas saturations (Table 4.5). This observation is consistent with the previous simulations, and suggests that the production of foamy oil - which might be the consequence of a highly heterogeneous network with numerous cavities - can lead to better recovery.

Case	Sgc	Critical Pressure (psi)
1/50cav	0.60	719.48
1/200cav	0.54	723.48
1/500cav	0.53	724.24
1/1000cav	0.51	725.48

Table 4.5: The effect of bubble density on critical gas saturation.

The relative permeability curves obtained by running the same simulations on 3D equivalent networks confirm early gas breakthrough and higher gas saturations during the early stages of the depletion for low bubble densities (Figure 4.30).

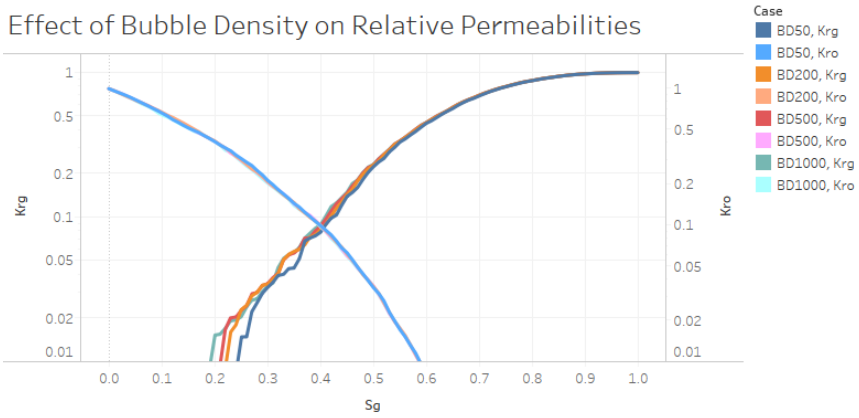

Figure 4.30: Effect of bubble density on relative permeability curves.

4.3.3 Effect of Diffusion Coefficient

The effect of diffusion on gas growth is now investigated inside a porous medium. We run several simulations on a 2D 200x100 oil wet network for five values of diffusion coefficient D/Do (where $Do = 10^{-5}cm2/s$) : 0.01, 0.1, 0.3, 0.9 and 3. We use the default nucleation module (PN module) and its default parameters stated in Table 4.1 (unless mentioned, we will be using the PN module for all future sensitivity analyses).

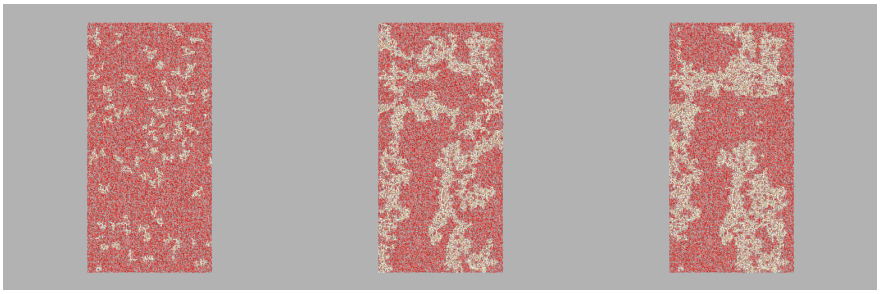

Figure 4.31: Gas distribution at PB-P=10psi for 3 diffusion coefficients. From left to right (unit: $D/D0$): 0.01, 0.3, 3.

Figure 4.32 shows that gas evolves more rapidly during the early depletion stages as the diffusion coefficient increases. Gas diffusion into the nucleated bubbles is directly proportional to the diffusion coefficient and therefore a higher diffusion coefficient results in higher gas saturations in the network. This is, of course, to be expected.

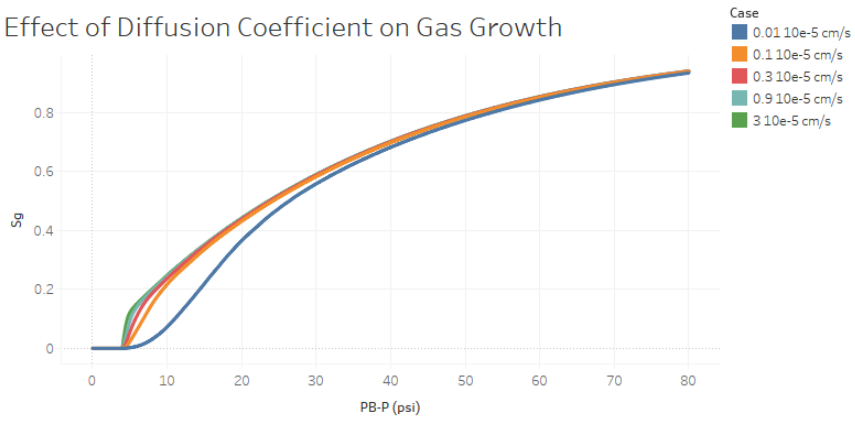

Figure 4.32: Effect of diffusion coefficient on gas growth using IN nucleation module.

However, it should be noted that low diffusion coefficients also result in higher local supersaturations (Figure 4.33) and thus more nucleated bubbles may appear in the network due to the progressive nature of the nucleation. For instance, at PB-P=10, the number of gas clusters for $D/Do = 0.01$ is almost four times higher that that for $D/Do = 3$ (Figure 4.34). This explains why the gas saturation curves asymptote at late stages of depletion. The increase in the number of bubbles will intensify the competition between the various gas clusters for the dissolved gas, which can actually *delay* gas breakthrough (Table 4.6) and lead to higher critical gas saturations for lower diffusion coefficients (as gas clusters have more time to expand and grow before breakthrough).

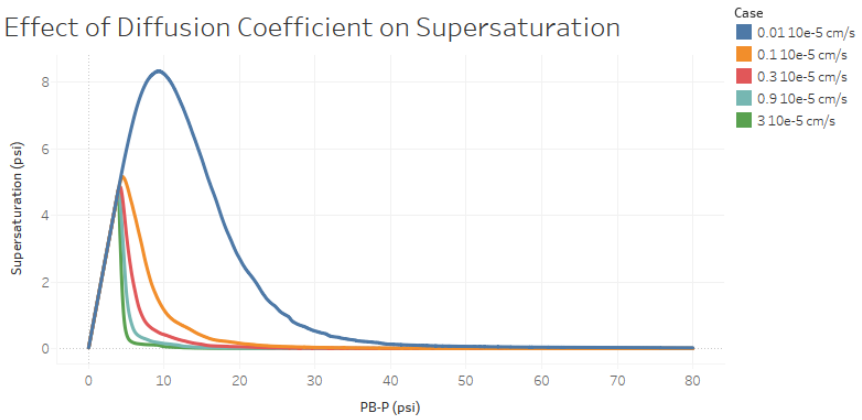

Figure 4.33: Effect of diffusion coefficient on average supersaturation using PN nucleation module.

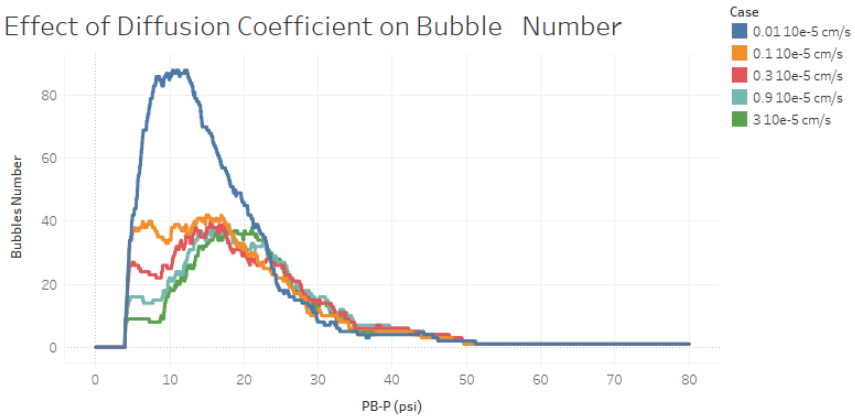

Figure 4.34: Effect of diffusion coefficient on bubble number using PN nucleation module.

Case	Sgc	Critical Pressure (psi)
0.01 10e-5 cm/s	0.56	720.10
0.1 10e-5 cm/s	0.55	722.38
0.3 10e-5 cm/s	0.54	723.46
0.9 10e-5 cm/s	0.51	725.68
3 10e-5 cm/s	0.49	727.16

Table 4.6: The effect of diffusion coefficient on critical gas saturation.

The relative permeability curves have been obtained for the set of studied values applied on 3D networks as shown in Figure 4.35 and the early gas breakthrough is clearly highlighted for large diffusion coefficients.

4.3.4 Effect of Interfacial Tension

We examine now the effect of interfacial tension on solution gas drive during depletion. Five values have been considered using the 2D 200x100 oil-wet network:

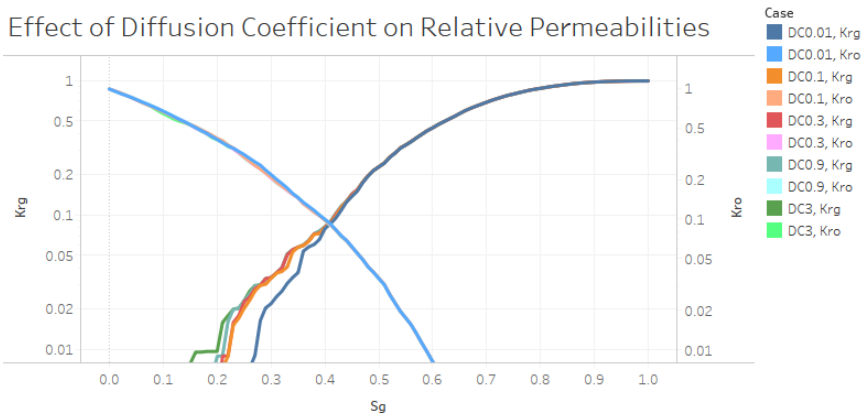

Figure 4.35: Effect of diffusion coefficient on relative permeability curves.

$10dyn/cm$, $20dyn/cm$, $25dyn/cm$, $30dyn/cm$ and $75dyn/cm$.

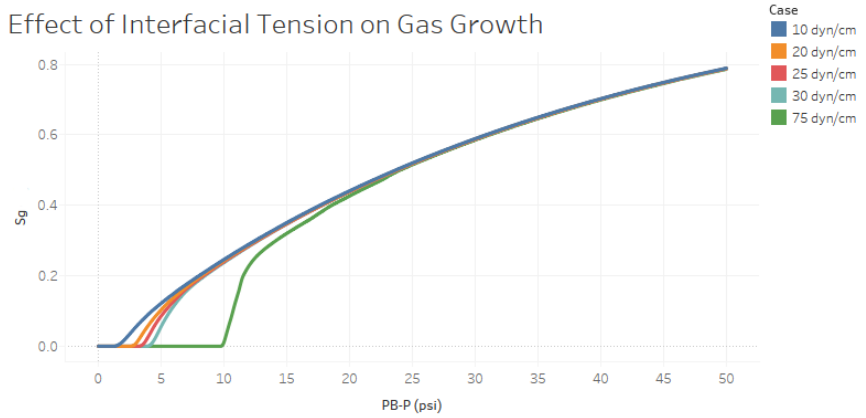

Figure 4.36: Effect of interfacial tension on gas growth.

Figure 4.36 shows that higher saturations were achieved for lower interfacial tensions at early stages of depletion. This can be explained by two factors. First, lowering the interfacial tension decreases the entry capillary pressure ($\frac{2\sigma cos\theta}{r}$) required to invade an oil-filled capillary element adjacent to growing gas clusters. This can result in enhanced gas expansion (and eventually early gas breakthrough). Second, low interfacial tension values yield a lower threshold for nucleation (see equation 4.1), hence, more bubbles are expected to nucleate (Figures 4.37 and 4.38). 80 gas clusters were observed at PB-P=10 for the lowest interfacial tension compared to only 10 gas clusters for the highest.

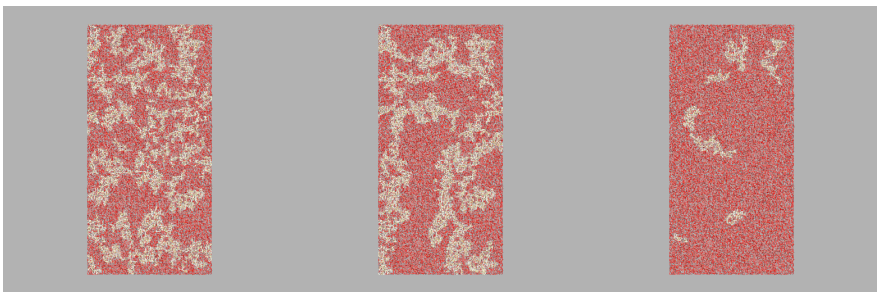

Figure 4.37: Gas distribution at PB-P=10psi for 3 interfacial tensions. From left to right (unit: dyn/cm): 10, 30, 75.

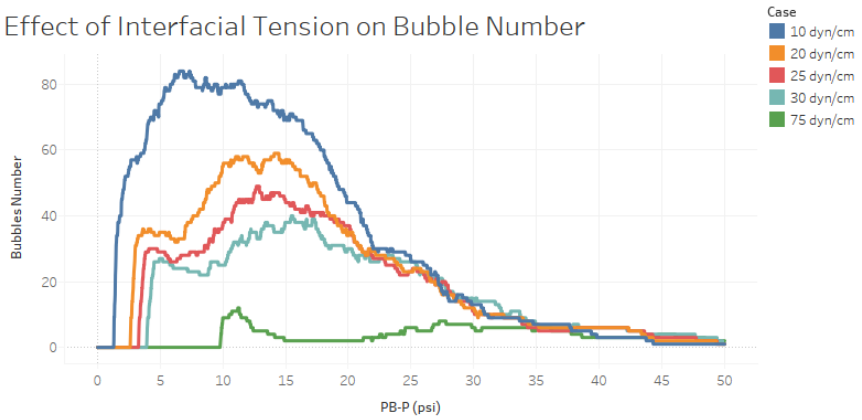

Figure 4.38: Effect of interfacial tension on bubble number.

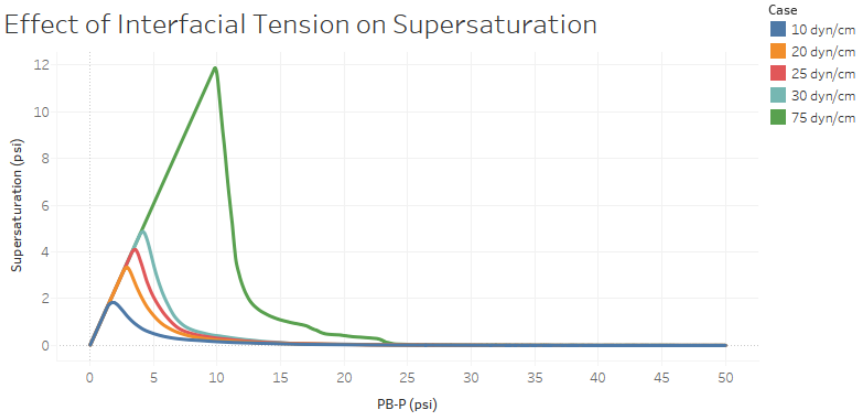

Figure 4.39: Effect of interfacial tension on average supersaturation.

Case	Sgc	Critical Pressure (psi)
10 dyn/cm	0.56	722.42
20 dyn/cm	0.55	722.72
25 dyn/cm	0.55	722.96
30 dyn/cm	0.54	723.46
75 dyn/cm	0.46	728.14

Table 4.7: The effect of interfacial tension on critical gas saturation.

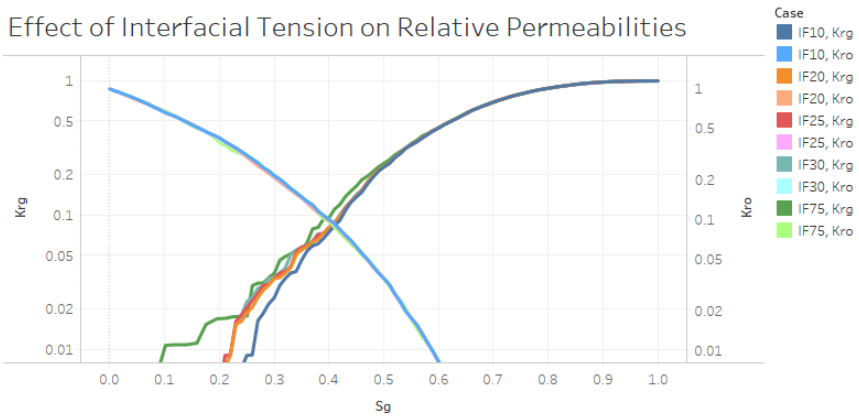

Figure 4.40: Effect of interfacial tension on relative permeability curves.

This effect is counteracted, however, by increased supersaturation for higher interfacial tensions due to the reduced number of nucleation events (Figure 4.39), and thus, the number of bubbles (and eventually the gas saturation) asymptote to similar values as the depletion simulation progresses. The difference in bubble density also leads to delayed gas breakthrough and higher critical gas saturations for low interfacial tension values (which suggest better depletion performance for these cases) as shown by Table 4.7. This is also confirmed by relative permeability curves when we ran the same simulations on the 3D equivalent networks (Figure 4.40).

4.3.5 Effect of Coordination Number

Pore-scale connectivity is investigated next to evaluate its effect on gas evolution during depletion experiments. We built four 3D networks with different coordination numbers: $Z = 3$, $Z = 4$, $Z = 5$ and $Z = 6$, and we monitor the growth of bubbles under the same depletion rate.

From Figures 4.41, we can see that gas expanded more readily in the well-connected network and lower gas saturations were obtained in the poorly-connected networks. In fact, low connectivity tends to slow down the bubble growth rate which leads to low gas saturation. This can be explained by the influence of connectivity on diffusive mass transport. The dissolved gas mass flux is affected by the length of diffusion path which is a function of the coordination number Z and so decreasing the latter leads to less gas transfer into the bubble and consequently less gas saturation at any given pressure.

However, the constrained diffusive flow of the dissolved gas in poorly-connected networks also leads to increased local supersaturation (Figure 4.42) and this, in turn, yields higher bubble densities in the networks (which explains the fact that

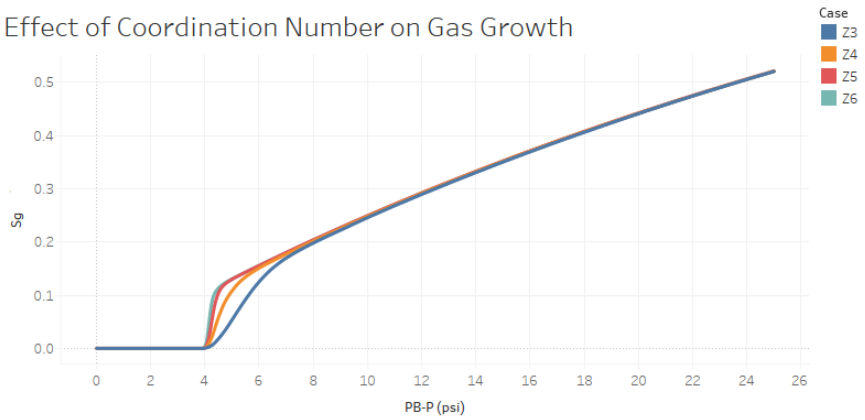

Figure 4.41: Effect of coordination number on gas growth.

gas saturation curves assymptote to the same saturation). This could be observed in Figure 4.43, where the bubble number for Z=3 is significantly higher compared to that of Z=6. Although this can lead to delayed breakthrough, higher values of Sgc are obtained for networks with low connectivity (Table 4.8). For instance, the value of Sgc for $Z = 3$ is twice that corresponding to $Z = 6$. This result is important, as connectivity effects could dominate during high-rate experiments and could lead to erroneous estimates of gas saturation and oil production.

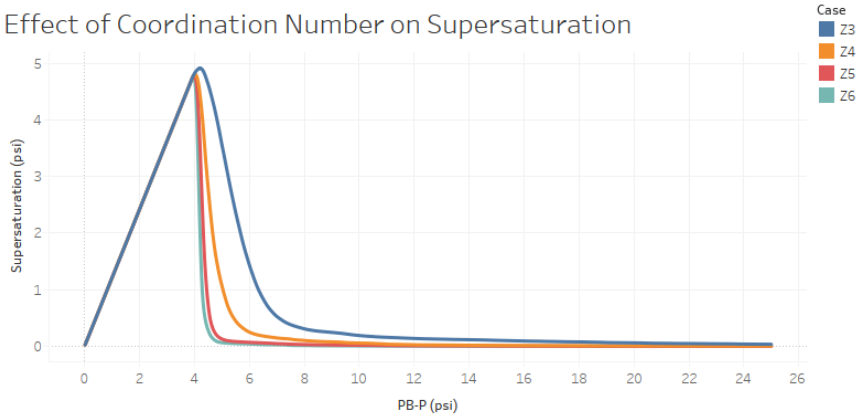

Figure 4.42: Effect of coordination number on average supersaturation.

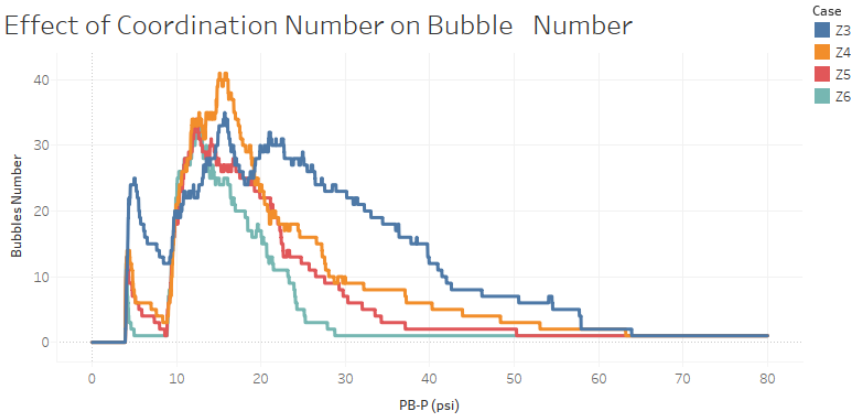

Figure 4.43: Effect of coordination number on bubble number.

Case	Sgc	Critical Pressure (psi)
Z3	0.20	742.08
Z4	0.13	744.48
Z5	0.14	744.46
Z6	0.11	745.58

Table 4.8: The effect of coordination number on critical gas saturation.

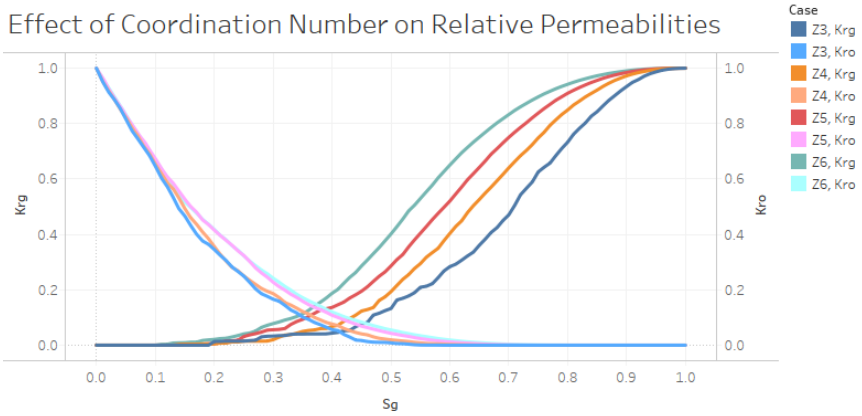

Figure 4.44: Effect of coordination number on relative permeability curves.

The impact of coordination number on relative permeability is shown in Figure 4.44. Gas relative permeability is significantly higher for well-connected networks compared to those with low coordination number. This is be explained by the rapid coalescence of bubbles in well connected networks whilst the limited number of available paths in poorly connected systems delays the coalescence of the the numerous bubbles. The emergence of a large connected and spanning gas cluster therefore occurs more quickly in networks with higher coordination numbers. These observations are also valid for oil relative permeability: the high number of bubbles in poorly-connected networks decreases the oil permeability to a greater extent compared to the case of well-connected networks, where oil can remain spanning for a long time despite the presence of several gas clusters.

4.3.6 Effect of Rock Type

We carried out further simulations using four extracted networks from real rocks to confirm the observations regarding the impact of connectivity on the depletion process (Figure 4.45). The deployed rocks have different average coordination numbers as illustrated by Table 4.9.

The curves of gas saturation as a function of pressure decline (Figure 4.46) confirm the conclusions obtained for the idealised networks. Gas expansion was found to be

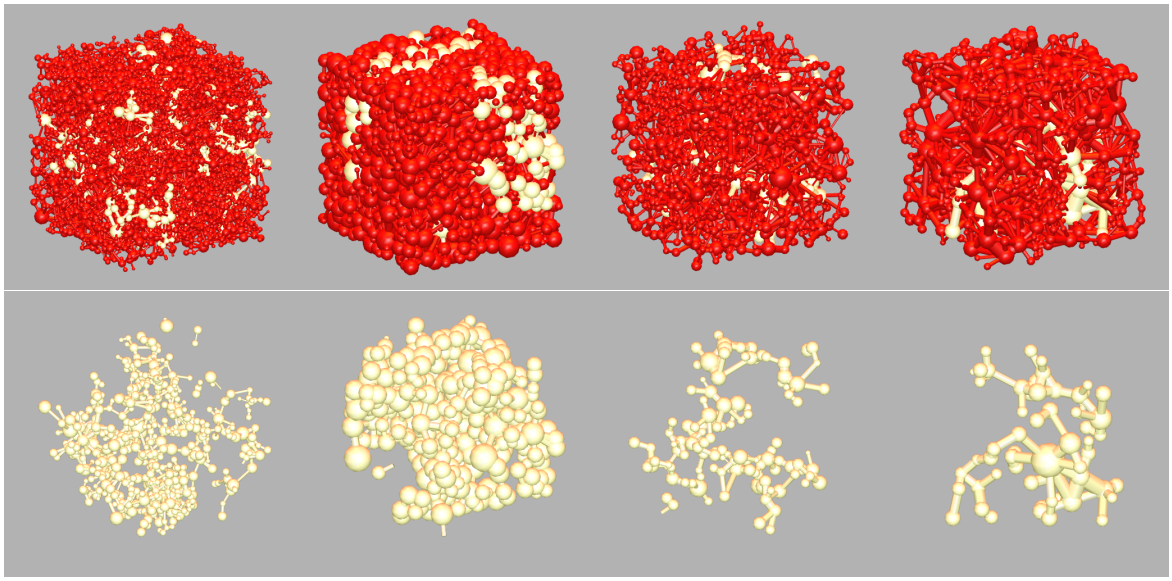

Figure 4.45: Gas distribution at PB-P=10psi for 4 microCT networks. From left to right: Berea, A1, S1, S7.

Rock Network	Average coordination number
Berea	3.91
A1	6.65
S1	3.15
S7	5.23

Table 4.9: Average coordination number of four networks extracted from microCT images.

highly efficient in the silica rock analogue due to its high connectivity. Relatively low gas saturations were achieved in the sandstone S1 model due to the lack of connection between the different capillary elements – this retarded the degree of gas transfer via diffusion. It should be noted that, in poorly connected networks, higher local supersaturations are expected to be achieved due to the longer diffusive pathways and this eventually leads to more nucleated bubbles (Figure 4.47). It is also worth mentioning that the two maximums shown by the supersaturation curves are a manifestation of the irregular topology of these networks extracted from MicroCT images - some of the nodes can be surrounded by narrow throats and remain, therefore, highly-supersaturated until late stages of the depletion (due to the slow diffusive flow of dissolved gas exiting these elements). As oil saturation decreases, the contribution of these highly-supersaturated nodes becomes significant to the overall network supersaturation, which results in a secondary pic in the total supersaturation curves observed at PB-P=45psi.

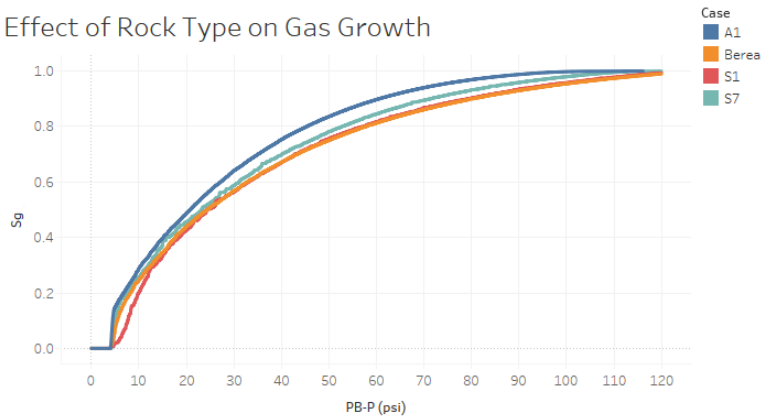

Figure 4.46: Effect of rock type on gas growth.

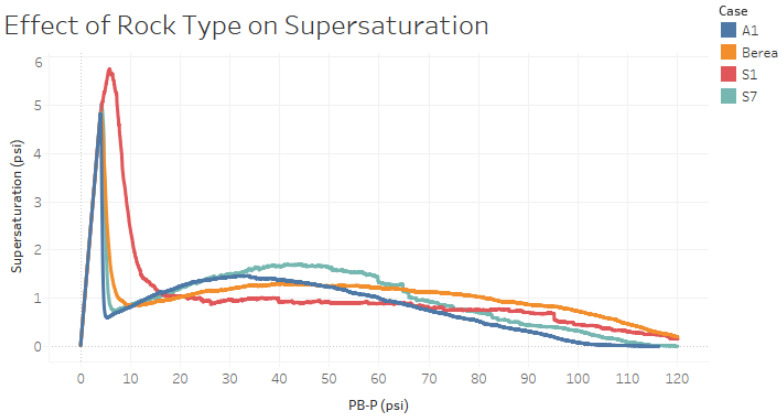

Figure 4.47: Effect of rock type on average supersaturation.

Although oil relative permeability curves are consistent with the results of the idealised network study, gas relative permeability curves show a non-linear correlation with average coordination number. For instance, the highest values of gas relative permeability are achieved for both Berea and S1 networks, which are the most poorly-connected networks. The critical gas saturations exhibit the same non-linear relationship with rock connectivity (Table 4.10): the earliest gas breakthrough occurs for the Berea sandstone although its corresponding network is poorly-connected. This can be explained by the irregular topology of these relatively small networks which can affect the simulated outcome: in fact, a short spanning path connecting both the inlet and the outlet in a large poorly-connected network can lead to early gas breakthrough – such a phenomenon is unlikely to happen in an idealised network.

These results emphasise the importance of using realistic networks in pore-scale modelling, as the irregularity of the porous media might have significant impact on the simulated results. However, it is also important to deploy large networks when investigating the sensitivity of flow parameters in order to minimise the statistical

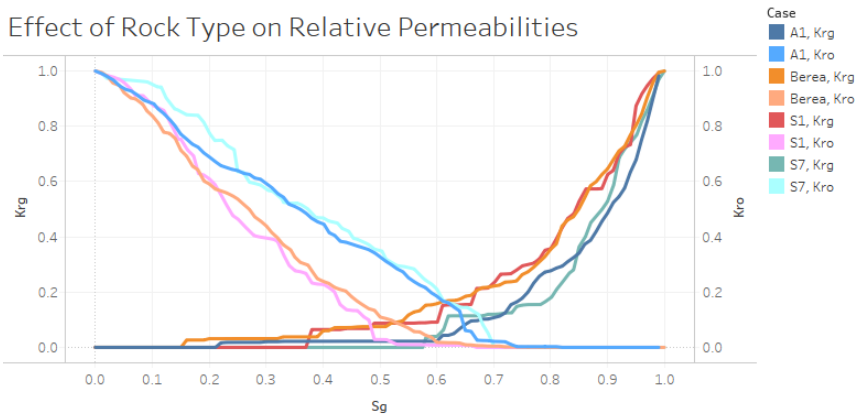

Figure 4.48: Effect of rock type on relative permeability curves.

Case	Sgc	Critical Pressure (psi)
A1	0.22	742.58
Berea	0.16	743.16
S1	0.38	732.76
S7	0.58	720.90

Table 4.10: The effect of rock type on critical gas saturation.

errors that could emerge from using small-sized irregular networks. Although building large 3D networks requires the application of sophisticated numerical solvers to simulate pore-scale processes in a reasonable CPU time (which is beyond the scope of this work), we believe large 2D networks are still a good compromise to gain meaningful insights into the most influential parameters that affect a specific phenomenon.

4.3.7 Effect of Pore Size Distribution

We finally examine the effect of pore size distribution (PSD) on gas growth during depletion. We consider here three PSDs (Figure 4.49): $TN(r_{min} = 0.1, r_{max} = 3, \mu = 1, \sigma = 2)$, $TN(r_{min} = 1, r_{max} = 2, \mu = 9, \sigma = 6)$ and $TN(r_{min} = 20, r_{max} = 20, \mu = 23, \sigma = 3)$, where $TN(r_{min}, r_{max}, \mu, \sigma)$ refers to the truncated normal distribution applied on the interval $[r_{min}, r_{max}]$; μ and σ are the distribution parameters (see Chapter 3, Section 3.2.1). For the remainder of this section, we will omit TN parameters when referring to one distribution, and thus, $TN(r_{min} = 0.1, r_{max} = 3, \mu = 1, \sigma = 2)$ will be refereed to as $TN(0.1, 3)$.

Figure 4.50 shows that gas expands more readily in networks containing large radii. At $PB - P = 10$, gas saturation for $TN(20, 30)$ is almost twice the value of that for $TN(0.1, 3)$. This result is expected, as large radii correspond to low capillary entry pressures, and thus gas clusters require less energy (and less diffused gas) to invade

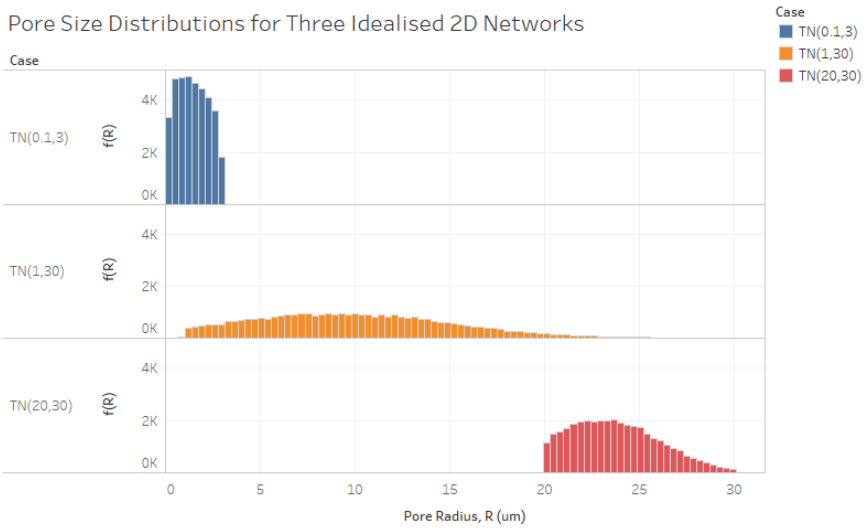

Figure 4.49: Pore size distributions used in the PSD sensitivity analysis.

the neighbouring oil-filled pores compared to networks containing a large proportion of small radii.

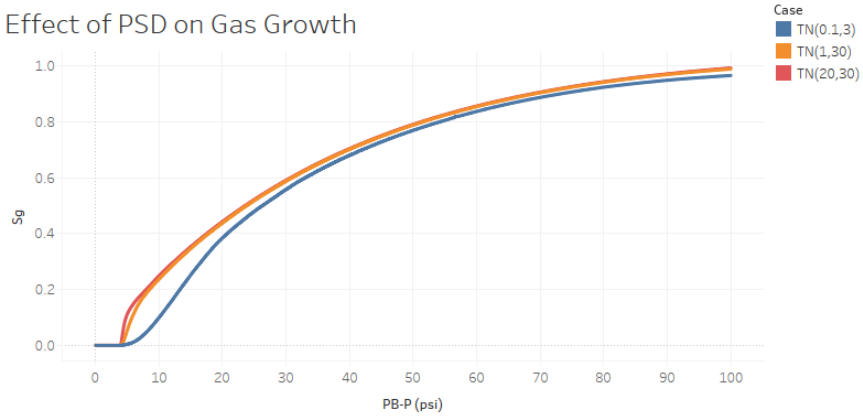

Figure 4.50: Effect of pore size distribution on gas growth.

Figure 4.51 shows very different growth patterns for the three PSDs. While gas growth is more compact for $TN(20, 30)$, the growth pattern looks more fingered for $TN(1, 30)$. For $TN(0.1, 3)$, numerous bubbles grow in a capillary fashion. These observations are explained by two factors. First, the range of the PSD is directly linked to the growth pattern: capillary-dominated growth means that gas fills sequentially the oil-filled pores from the larger ones to the smaller. As the PSD range narrows, similar capillary thresholds are required to invade all neighbouring pores, the invasion becomes less heterogeneous, and thus gas grows in a compact fashion. We can conclude, therefore, that the ratio R_{max}/R_{min} affects directly the gas growth pattern in porous media. However, another factor also plays an important role here: due to the high capillary entry pressures associated with $TN(0.1, 3)$, the gas expands slowly (as the internal gas pressure needs to reach high values before invading neighbouring elements), which results in increased supersaturation and thus

further progressive nucleation (Figures 4.52 and 4.53). The high bubble density affects the gas breakthrough that occurs at later stages of the depletion in this case (due to the competition between bubbles) but results in higher Sgc values compared to $TN(1, 30)$ and $TN(20, 30)$ (Table 4.11).

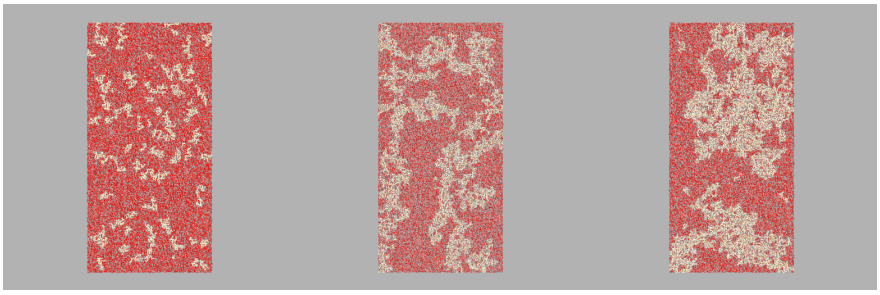

Figure 4.51: Gas distribution at PB-P=10psi for 3 pore size distributions. From left to right: TN(0.1,3), TN(1,30), TN(20,30).

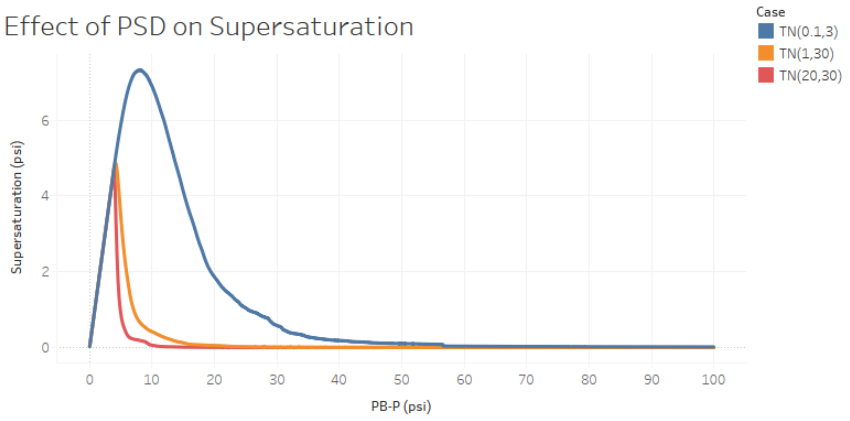

Figure 4.52: Effect of pore size distribution on average supersaturation.

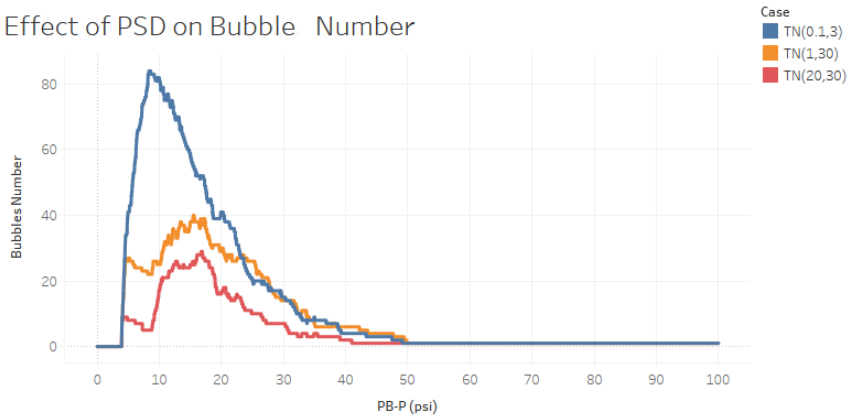

Figure 4.53: Effect of pore size distribution on bubble number using PN nucleation module.

Case	Sgc	Critical Pressure (psi)
TN(0.1,3)	0.59	717.34
TN(1,30)	0.54	723.46
TN(20,30)	0.42	731.42

Table 4.11: The effect of pore size distribution on critical gas saturation.

The impact of PSD on relative permeability curves is shown in Figure 4.54. Gas relative permeability is higher for networks that contain small pores (and vice versa for oil permeability): fingered capillary growth allows gas to have a greater spatial impact on flow paths. In contrast, compact growth, despite being fast, delays connectivity of individual gas clusters, which decreases its relative permeability.

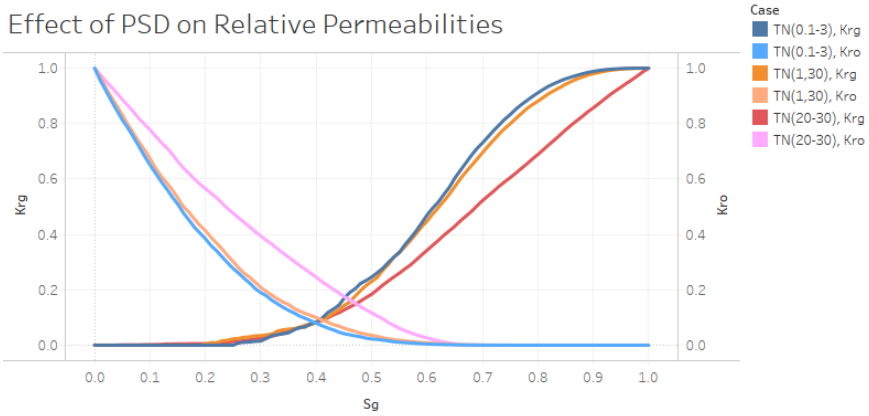

Figure 4.54: Effect of pore size distribution on relative permeability curves.

4.4 Conclusions

In this chapter, we have introduced the *numSCAL* depletion module and described the implementation of its main components. By adopting a robust mathematical model of the major phases of depletion, an entire depletion experiment could be investigated from the nucleation of the first bubble to the migration of large gas clusters. The module used several ideas implemented in an earlier Fortran simulator but numerous enhancements and additions have been made in the new C++ implementation (i.e. the support of digital networks extracted from microCT images, the dynamic calculation of the timestep for the diffusion module). These improvements have resulted in significant optimisation and speed up of the depletion simulation.

We have used this tool to study the impact of various parameters on gas evolution during depletion including: depletion rate, bubble density, diffusion coefficient, interfacial tension, network connectivity and pore size distribution. Simulations have

shown that all these parameters have a considerable impact on gas growth, bubble density, critical gas saturation and relative permeabilities. Of particular interest is the competition between nucleated bubbles for dissolved gas and the resulting gas growth and critical gas saturation; for most of the investigated parameters, we have observed that system shifts affecting the diffusion or the entry capillary pressure have a direct impact on the local supersaturation and bubble density (which are also correlated to the depletion efficiency). Such behaviour emerges as a consequence of the complex interaction between the different investigated parameters and makes it difficult to predict *a priori* the outcome of the simulation before actually running it. The schematic shown in Figure 4.55 demonstrates how the various parameters interact in a complex fashion during a depletion experiment. It is therefore not surprising that the associated literature is often confusing and contradictory. Thus, this tool represents a valuable addition to the reservoir software toolbox as it allows the examination of flow/rock parameters individually or collectively and helps to estimate the effect of shifting the system configuration towards a specific state.

Simulations using digital networks have also shown the impact of irregularities on gas growth and highlighted the importance of using realistic networks to make realistic estimations of recovery. Whilst the current size of these networks makes it difficult to generate predictive results, they can still be used to run useful sensitivities nonetheless. Although we have developed a methodology to extend the size of these networks (see Chapter 3, Section 3.6), computational challenges persist. This can constitute an important focus of the future work (i.e. code parallelisation, optimised numerical solver). Simulating large 3D networks would also allow the investigation of gravitational effects in 3D cores which, was examined previously using only 2D systems (Ezeuko et al, 2010 [144]).

As mentioned in Section 4.2.6, the current implementation requires further mechanisms necessary to examine more complex phenomena - the simulations we have considered so far assumed the presence of only two phases (i.e. oil and gas, or water and gas). The addition of water as a third phase adds another level of complexity due to the interaction between the three-phases. This problem is tackled by implementing a new generic three-phase module based on graph theory that we will discuss in the next chapter.

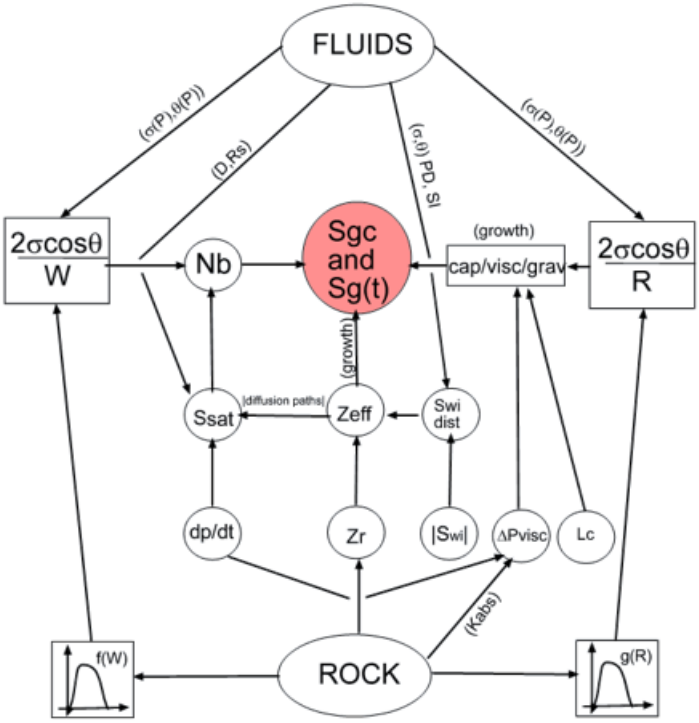

Figure 4.55: Schematic demonstrating the ways in which various fluid/rock properties interact during a depletion process: changing one single parameter can impact several phenomena simultaneously. Both gas saturation *Sg(t)* and critical gas saturation *Sgc* are directly affected by: (1) the forces acting at the pore scale (*cap/visc/grav*), (2) the number of nucleated bubbles *Nb* and (3) the rock connectivity *Zr*. The bubble number *Nb* depends on the local supersaturation Ssat and the nucleation threshold $\frac{2\sigma cos\theta}{W}$ which is a function of the cavity size distribution *f(W)* and the underlying fluid properties ($\theta(P)$: contact angle value; $\sigma(P)$: surface tension value). Fluid properties also have a direct effect on the capillary entry pressures $\frac{2\sigma cos\theta}{R}$ which are also dependent on the pore size distribution *g(R)*. Viscous forces are affected by the pressure gradient across the network $\Delta Pvisc$ and the core length *Lc*. Finally, rock connectivity can be affected by the initial water saturation */Swi/* and the initial water distribution *Swi dist* obtained after primary drainage (PD) and spontaneous imbibition (SI) resulting in an effective connectivity *Zeff* which has a direct impact on gas diffusion paths and, consequently, local supersaturation *Ssat* in the network. The latter is directly affected by the depletion rate *dP/dt*, gas diffusion coefficient *D* and dissolved gas concentration *Rs*.

Chapter 5

numSCAL Steady-State Three-Phase Flow Module

5.1 Introduction

Three-phase displacements at the pore scale can be observed in a wide range of processes related to oil recovery. For instance, Water Alternating Gas injection (WAG) is a common procedure where both water and gas are injected alternatively to displace the oil originally in place and decrease the residual oil saturation. Depletion in water-flooded reservoirs is another process where the nucleated gas bubbles grow and displace both oil and water clusters. Under these conditions, the complex mechanisms that govern the interaction between the various phases need to be incorporated into any simulator that aims to model three-phase flow at the pore-scale. Although several models have been implemented in the literature to simulate WAG experiments (see Chapter 2, Section 2.8), depletion has been simulated mostly under two-phase conditions (see Chapter 2, Section 2.10).

The depletion model described in the previous chapter is only suitable for gas-oil, or gas-water systems. Introducing a third phase requires an expanded modelling approach where three phase mechanisms are considered, such as oil spreading on water, and multiple chain displacements. The latter occur due to the mobilisation of several clusters containing various phases that stretch from the growing gas clusters to the outlets of the system. Such displacements tend to follow the lowest energy paths, and so a shortest path algorithm needs to be developed.

In this chapter, we introduce a new method to model gas growth in pore networks initially filled with both oil and water. We first discuss the additional mechanisms incorporated into the model, such as spreading and three-phase contact angles. We

then explain the methodology we used to reconstruct mathematical graphs based on the fluid configuration in the underlying pore networks. We also present the details of solving the shortest path problem and updating the phase saturations in capillary elements accordingly. Finally, we apply the model to study the impact of parameters relevant to three-phase depletion experiments, such as initial water saturation and spreading coefficient.

5.2 Model Description

The *numSCAL* three-phase module is called when simulating depletion in oil-water systems. While nucleation and diffusion modules remain the same, the growth of gas clusters is now modelled by applying concepts from graph theory, where the most favourable paths towards the outlet are calculated using a short path algorithm inspired by Djikstra [150]. The algorithm is capable of updating the network status throughout a simulation through the calculation of various costs, such as the capillary pressures between different phase clusters. As the capillary entry pressures amongst the various clusters depend essentially on the wettability configuration of the network, our model is easily generalizable to mixed-wet systems. Spreading layers and fluid films are also considered in our modelling approach.

The model starts by identifying all the phase clusters present in the network – these clusters constitute the nodes of the underlying mathematical graph. A loop over all interfaces in the capillary elements of each phase cluster is then performed to compute the minimum entry pressure required to displace an adjacent cluster. These represent the costs in our graph model. Once all the costs are calculated, a variant of the Dijkstra algorithm is applied to determine the least energetic path from each growing bubble to the outlet. The obtained solution is then used to trigger the corresponding multi-displacement chain at the pore scale whilst conserving the mass in the system. The new fluid configuration is used to build a new graph, and the procedure is repeated until no more displacements are possible.

The model works under the following assumptions:

- The flow inside the capillary elements is considered to be laminar and the meniscus between two fluids is assumed to remain perpendicular to the axis of the pore.
- The fluids inside the capillaries are immiscible.
- The gas expands according to the ideal gas law (although Z-factors can be included if necessary).

- The graphs are considered acyclic when solving the shortest path problem: a cluster cannot appear more than once in a displacement chain (the reason behind this assumption is to avoid issues related to so-called negative cycles, as we shall see in the next section).

The workflow of the *numSCAL* three-phase chain displacement module is described by Figure 5.1

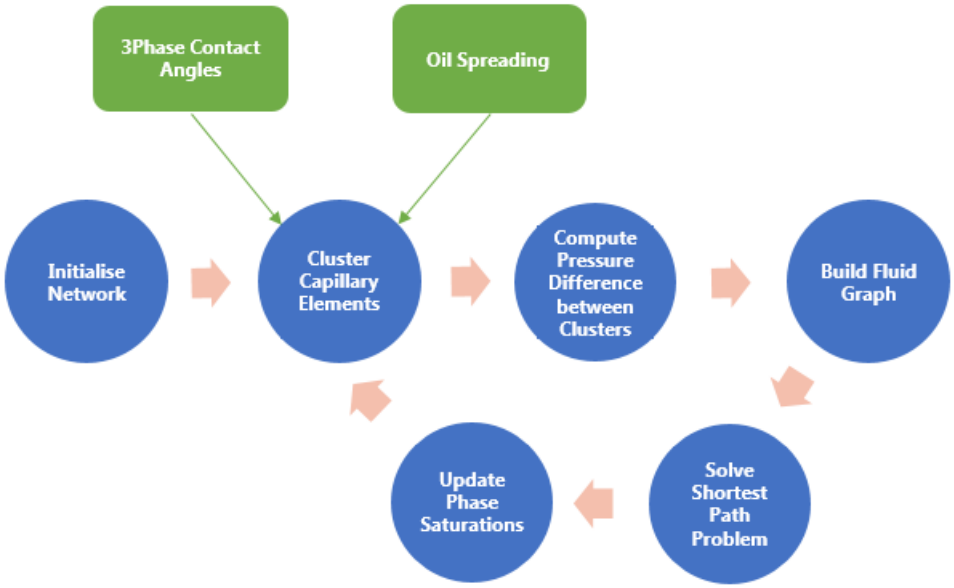

Figure 5.1: numSCAL Three-Phase Module Workflow

A displacement event in a two-phase steady state depletion process occurs when the pressure of a gas cluster overcomes the entry pressure of one of its adjacent non-trapped fluid-filled neighbours. When the network is filled with both water and oil, the displacement event usually consists of a chain of displacements involving many clusters, the first being the expanding gas cluster and the last being a cluster connected to the outlet. The most favourable displacement corresponds to the chain requiring the least energy expenditure and this requires knowledge of the pressure differences between the various clusters.

5.2.1 Computing the Capillary Entry Pressure between Two Clusters

To determine the entry pressure required for one cluster to displace another, both bulk-to-bulk connections and bulk-to-film/layer connections need to be taken into account. Consider for instance the situation depicted in Figure 5.2.

The figure represents a schematic of two neighbouring clusters connected to one an-

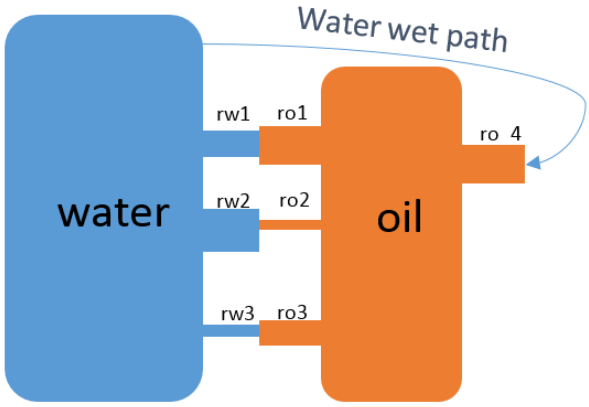

Figure 5.2: Bulk-bulk and bulk-film connections between an oil cluster and a water cluster

other via 3 pairs of pores (with radii $ro1$,$rw1$; $ro2$, $rw2$; $ro3$, $rw3$). If we consider an *oil-wet* network, and we assume the pores to be cylindrical, then the entry pressure that water needs to overcome to displace oil (a drainage process) is given by:

$$P_{entry} = MIN(\frac{2\sigma}{ro1}, \frac{2\sigma}{ro2}, \frac{2\sigma}{ro3}) \tag{5.1}$$

If a displacement occurs, then the largest pore would be invaded first.

If we consider the case when water is displacing oil via piston-like displacement in a *water-wet* network (an imbibition process), then the entry pressure takes a negative value and so:

$$P_{entry} = MIN(-\frac{2\sigma}{rw1}, -\frac{2\sigma}{rw2}, -\frac{2\sigma}{rw3}) \tag{5.2}$$

and the pore with the smallest radius would be displaced first.

If we now consider water displacing oil in a generalised *mixed-wet* network, and if we enable film flow in our model, then it is also possible for the water to displace an oil-filled pore via snap off. This can occur if the oil-filled pore resides on a water wet pathway connected to the invading water cluster or the system inlet. In such a case, the entry pressure becomes:

$$P_{entry} = MIN(\frac{2\sigma}{ro1}, \frac{2\sigma}{ro2}, \frac{2\sigma}{ro3}, -\frac{\sigma}{ro4}) \tag{5.3}$$

Note that the snap off event is more favourable in this case (an imbibition process) compared to bulk invasion (a drainage process).

5.2.2 Computing the Capillary Entry Pressure between Gas Clusters and the Network Outlet

Overcoming the relative entry pressure of one cluster is not the only condition to satisfy when modelling multi chain displacements in three-phase flow (Figure 5.3). In this case, the displacement only occurs when the pressure difference between the growing gas cluster and the pressure at the outlet is greater than the sum of relative entry pressures between each pair of neighbouring clusters. We will use the configuration of Figure 5.3 to describe how this is handled in our simulator.

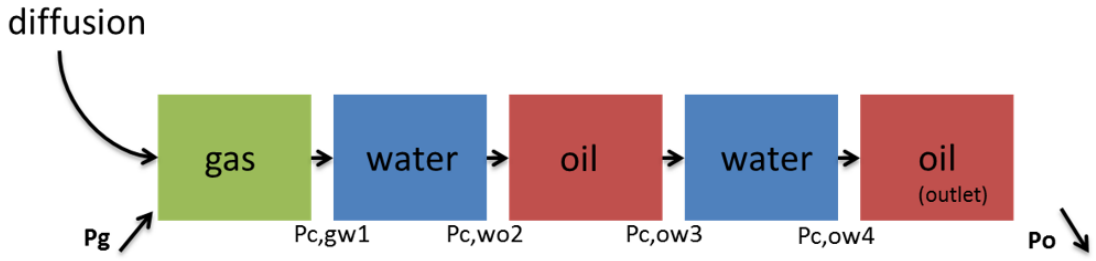

Figure 5.3: Chain displacement during a depletion experiment: Pg increases due to diffusion, while Po decreases due to the depressurisation of the reservoir. When Pg-Po overcomes the sum of relative entry pressures between the neighbouring clusters, the displacement occurs.

During a depletion experiment, the pressure in the gas cluster P_g will increase due to diffusive mass transport, whilst the pressure at the outlet of the network will decrease due to continuous oil production – hence, $P_g - P_o$ increases throughout a simulation (if the outlet phase is water, then $P_g - P_w$ increases in a similar way). A displacement event will occur when $P_g - P_o$ exceeds the effective capillary entry pressure of the ganglion train that is defined by:

$$P_{entry} = Pc, gw1 + Pc, wo2 + Pc, ow3 + Pc, ow4 \tag{5.4}$$

5.2.3 Solving the Shortest Path Problem

The example discussed above represents an ideal configuration, where only one chain of displacements is available. In a real network, however, many chains of displacements are possible topologically. As we discretise the simulation into many steps, only one chain displacement is permitted for each time increment, and this corresponds to the chain that involves the lowest effective entry pressure. In other words, among all the possible multi chain displacements that could occur, we need to find the least energetic event that does occur. This is clearly a rather involved situation

to model efficiently.

One way of solving the problem is to reconstruct the entire cluster-cluster connection map by checking all pores and their surrounding neighbours. This leads to a graph where the vertices correspond to the phase clusters and the edges represent the capillary entry pressures between each pair of clusters. Finding the most favourable chain of displacements to the outlet is reduced to solving the shortest path problem in the reconstructed graph for every growing gas cluster (Figure 5.4).

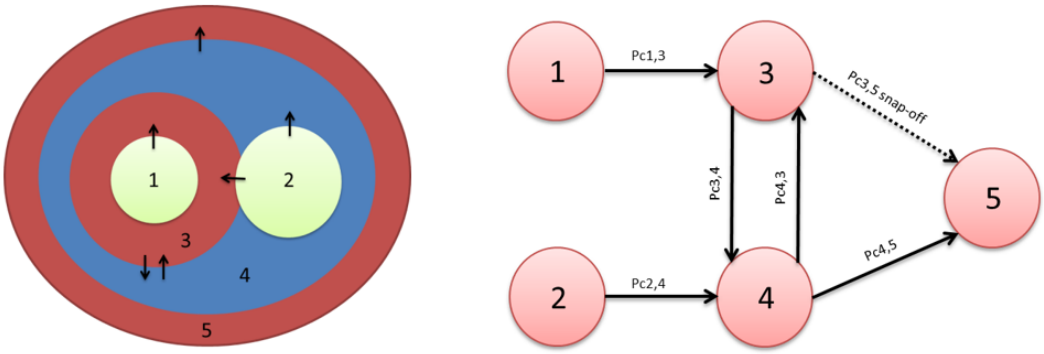

Figure 5.4: A cluster configuration and its associated graph. If the network is oil-wet, two oil clusters (3 and 5) could be connected via films, and could therefore be connected in the graph (Pc3,5 snap-off)

Van Dijke et al. (2008) [94] simulated WAG experiments by building the graph that describes the different clusters in the network and calculating the cost (the relative entry capillary pressure) between each pair. The Bellman-Ford algorithm was then applied to find the shortest path between the outlet and the inlet [151].The choice of this algorithm was due to the fact that some costs can be negative, and so more widely used graph search algorithms, such as that proposed by Djikstra (1959) [150] could not be applied. One limitation of the algorithm was the inability to converge when there is a closed internal chain of displacements for which the effective pressure is negative. Such a situation results in what is termed a "negative cycle". In order to circumvent this difficulty, a subtree disassembly algorithm was used to detect these negative cycles and delete them from the pathway search.

The method we implement in this work improves upon that described above: instead of constructing the whole graph of relationships between clusters and then identifying the shortest path, we combine both steps into a single algorithm. The main idea is to begin exploring the graph partially from a growing gas cluster, ensuring that for each step we are following the lowest energy path available to the expanding gas cluster.

Consider the situation where we have a single gas cluster growing in the network. To identify the most favourable chain of displacements we carry out the following

procedure:

1. We assign a target pressure $P_g = 0$ to the gas cluster and a target pressure $P_i = \infty$ to all the clusters in the network (by the end of this algorithm, P_i will represent the effective relative pressure between the gas cluster and cluster i).

2. We then check the relative entry pressure between the gas cluster and all its surrounding clusters, and we set $P_{i,current}$ for these clusters, according to $P_{i,current} = P_g + P_{c,gi}$ where$P_{c,gi}$ denotes the capillary entry pressure between the gas cluster and fluid cluster i. If $P_{i,current} < P_i$ (which is true for the first iteration as $P_i = \infty$), then we attribute to P_i the value of $P_{i,current}$.

3. We choose the cluster i with the minimum target pressure P_i, and we check the entry pressure of each of its surrounding clusters. For each cluster j of the neighbouring clusters, we again compute the target pressure $P_{j,current} = P_i + P_{c,ij}$, where $P_{c,ij}$ denotes the capillary entry pressure between the cluster i and cluster j. If $P_{j,current} < P_j$, then we attribute to P_j the value of $P_{j,current}$. [Note that P_j denotes here the *sum* of capillary pressures that gas needs to overcome to displace cluster j.]

4. We repeat step 3. until we encounter an outlet cluster (or a cluster connected to the outlet via film flow or a wetting phase layer). Once the outlet has been reached, the effective chain capillary pressure to overcome is given by P_f, where f denotes the outlet cluster.

During the search for the outlet cluster, we assume that once a cluster is already associated with the current shortest path, it cannot be visited a second time. This is a necessary condition to obtain an acyclic partial graph and prevents any possible negative cycle from occurring. The scan is interrupted if no outlet cluster is detected (this could happen if the gas cluster has already invaded all the outlet pores and all the oil/water pores that have connection to the outlet via film or layers; in that case, all the remaining oil or water would be trapped).

To construct the graph of phase clusters, we use the open source "Fibonacci Heap" container provided by boost C++ library (`http://www.boost.org/`) to store the network clusters and their corresponding properties (Fredman et al., 1986 [152]). This allows a quick access to the cluster with the minimum cost (i.e. capillary entry pressure) which result in better computational performance when solving the shortest path problem.

5.2.4 Updating Phase Saturations

Once a chain displacement is identified, it is possible to backtrack through the tree of clusters belonging to the final chain of displacements and to construct a list of all the pores involved in the displacement. The maximum volume of fluid that we allow to be displaced over a time step corresponds to the smallest pore volume change in the chain that results in a pore becoming completely filled with a moving phase (Figure 5.5). We update the fraction of each phase in all participating pores accordingly – this ensures the conservation of mass through the full simulation.

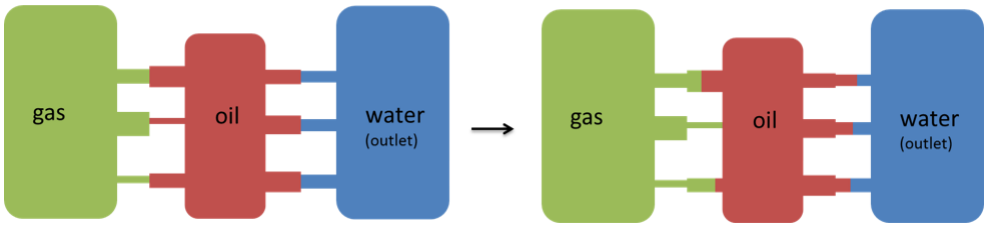

Figure 5.5: Chain displacements at the pore level between three clusters. The displacement always corresponds to the smallest pore volume change in the chain that results in a pore becoming completely filled with a moving phase.

When there are multiple gas clusters growing simultaneously in the network, we determine the most favourable chain displacement for each gas cluster to the outlet. We then perform the displacement that requires the least effective entry pressure to overcome.

The approach used in this work is similar to that proposed by Djikstra (1956) [150] and this may appear to be inappropriate at first glance, as some of the costs in the graph can be negative. However, we make the assumption that chain displacements happen sequentially; the gas cluster starts to grow progressively and displaces its neighbouring cluster, which in turn starts to move and displace another cluster in a sequential fashion. For this reason, we believe that our algorithm is physically appropriate for simulating three phase depletion. Although this approach does not enable us to calculate the pressure in every cluster in the network, the pressure in the clusters involved in the displacements *can* be calculated. The speed of the algorithm adopted here is also a big advantage over other models, as we do not need to explore the whole graph (a computationally expensive task). The fact that we do not have negative cycles in our implementation also improves the efficiency of our method, as no subtree disassembly algorithm needs to be applied.

5.2.5 Modelling Spreading Phenomena

Spreading is an important phenomenon that may occur at the pore scale if the force balance between the three interfacial tensions becomes unstable (see Chapter 2, Section 2.6.3). This is reflected in this model by associating the ability of oil to spread between water and gas to the oil spreading coefficient defined as:

$$C_s = \sigma_{gw} - \sigma_{go} - \sigma_{ow} \tag{5.5}$$

Oil spreading occurs when C_s is positive, and in that case, an oil-filled capillary element could become non-trapped if it belongs to an oil cluster adjacent to a gas cluster connected to the outlet.

Spreading not only affects phase trapping criteria but also the capillary entry pressures during gas growth. For instance, under oil spreading conditions in a water wet system where gas is adjacent to an oil cluster, the capillary entry pressure that gas needs to overcome to invade an adjacent cylindrical water-filled pore is given by:

$$P_c = \frac{2(\sigma_{og} + \sigma_{ow})}{r} \tag{5.6}$$

Under non-oil spreading condition, the criterion for expansion becomes:

$$P_c = \frac{2\sigma_{gw}}{r} \tag{5.7}$$

When angular pores are examined, equation 4.22 related to the geometrical stability of arc menisci (AM) is verified for both water-oil and oil-gas AMs. Moreover, an additional geometrical condition for layer stability in a corner with half angle α is checked based on the formulation of Fenwick and Blunt (1998) [153], and is given by:

$$\frac{r_{ow}}{r_{go}} \leq \begin{cases} \frac{cos(\theta_{go}+\alpha)}{cos(\theta_{ow}+\alpha)} & if\ \theta_{ow} \leq \theta_{go} \\ \frac{cos\theta_{go}-sin\alpha}{\theta_{ow}-sin\alpha} & if\ \theta_{go} \leq \theta_{ow} \end{cases} \tag{5.8}$$

where r_{ij} is the curvature radius of the AM between phase i and j.

Currently, we assume that oil layers are volumeless, although this feature can be added in future work. Their impact on oil connectivity is, however, considered. In fact, the formed layers in angular corners are used as part of the clustering

algorithm to determine the connectedness of oil clusters to the outlet, which may be an important factor that affects displacement chains.

5.2.6 Modelling Three Phase Contact Angles

For pressure depletion in a system containing gas and a single fluid phase, only one type of interface can exist (either gas-oil or gas-water), and so we need only to account for the contact angle between the two phases in the system. This approach cannot be applied for the case of three phase depletion, where we have three contact angles related to one another through the force balance between the three phases (Figure 2.17).

In our model we use the linear relationships proposed by van Dijke and Sorbie (2002) [88] to find θ_{go} and θ_{gw} for a given θ_{ow} and given values of interfacial tension as follows:

$$\begin{cases} cos\theta_{go} = 0.5((-1 + \frac{\sigma_{gw}-\sigma_{ow}}{\sigma_{go}})cos\theta_{ow} + 1 + \frac{\sigma_{gw}-\sigma_{ow}}{\sigma_{go}}) \\ cos\theta_{gw} = 0.5((-1 + \frac{\sigma_{go}-\sigma_{ow}}{\sigma_{gw}})cos\theta_{ow} + 1 + \frac{\sigma_{go}-\sigma_{ow}}{\sigma_{gw}}) \end{cases} \tag{5.9}$$

where σ_{ij} and θ_{ij} are respectively the interfacial tension and the contact angle between phase i and phase j.

5.2.7 Clustering Algorithm

Clustering capillary elements with similar properties is essential to determine the possible chain of displacements that could occur within the network, and to construct the graph of relationships between the various phases (as described in the following sections). We apply the Hoshen-Kopelmann algorithm [148] (see Chapter 4, Section 4.2.5) to associate to each capillary element three properties corresponding to (1) the major phase it contains (to determine whether it is topologically connected to the outlet), (2) its wettability (to determine whether it has a wetting path to the outlet) and (3) whether it has a spreading oil layer (to determine whether oil is connected to the outlet via spreading layers).

5.3 Application: Analysis of Capillary-dominated Gas Evolution in Three-Phase Systems

Numerous simulations have been carried out to investigate the keys parameters that can affect primary depletion in oil reservoirs with initial water saturation. As the connectivity of pore space is a key factor in determining the displacements between various phase clusters, we run sensitivity simulations on a 3D Berea sandstone network extracted from microCT images (corresponding properties are listed in Table 3.2).

To initialise the network with a preset initial water saturation Swi, we start by filling the entire network with water. Then, we run a steady state primary drainage (where oil invades the network in a percolation invasion fashion) until the desired Swi value is reached (Figure 5.6). We assign to the water-filled capillary elements an oil-water contact angle θ_{OW} equal to 30° (i.e. the initial water-filled capillary elements are assumed to be water-wet). The oil-filled capillary elements are selected to be either oil-wet (base case: $\theta_{OW} = 140°$) or water-wet ($\theta_{OW} = 40°$).

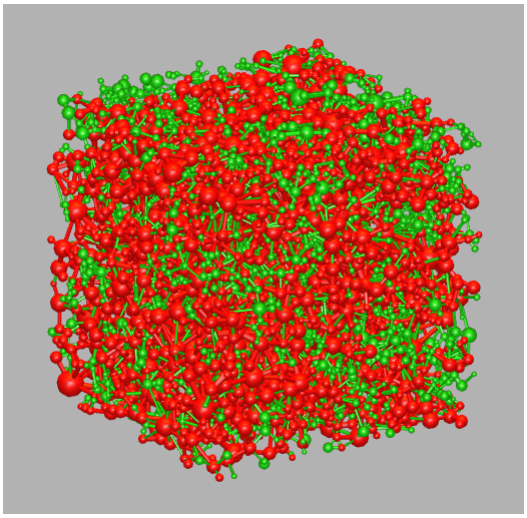

Figure 5.6: Berea network filled with water and oil (Swi=10%) after a primary drainage simulation. Oil (red) occupies the largest capillary elements whilst water (green) fills the smallest ones. Water-filled pores are considered water-wet.

The depletion parameters for a base case depletion scenario are listed in Table 5.1:

Table 5.2 shows the running time of a three-phase depletion simulation (10000 steps) for different configurations using an i7-3770 processor. Again, the running time is affected by various factors including the initial water saturation and initial wettability. For instance, higher Swi values seem to yield slower simulations in the case of A1 networks (which is in contrast with the trend observed in other rock samples). This can be explained by the high connectivity of A1 samples that might eventually

Bubble point pressure	750 psi
Depletion Rate	2 psi/day
Initial GOR (pressure dependent)	15 sm^3/sm^3
Initial GWR (pressure dependent)	1 sm^3/sm^3
Initial gas density (pressure dependent)	40 Kg/m^3
Oil Volume Factor (constant)	1 sm^3/sm^3
Water Volume Factor (constant)	1 sm^3/sm^3
Gas-Oil Interfacial tension (constant)	30 dyn/cm
Gas-Water Interfacial tension (constant)	30 dyn/cm
Oil-Water Interfacial tension (constant)	30 dyn/cm
Oil Viscosity (constant)	300 cP
water Viscosity (constant)	1cP
Gas viscosity (constant)	0.02 cP
Gas-Oil Diffusion Coefficient	0.3 $10^{-5}cm2/s$
Gas-Water Diffusion Coefficient	0.3 $10^{-5}cm2/s$
Initial Water Saturation	10%
Wettability	Oil-Wet
Default Nucleation Module	PN $1cavity/200pores$

Table 5.1: Default parameters used for the sensitivity analysis

result in numerous trapped clusters as Swi value increases and, thus, higher number of simulated multi-chained displacements.

Network	Number of capillaries	Wettability	Swi	Time (seconds)
Berea	$\backsimeq$ 19000	Oil Wet	10%	210633
Berea	$\backsimeq$ 19000	Oil Wet	20%	407173
Berea	$\backsimeq$ 19000	Water Wet	10%	538755
Berea	$\backsimeq$ 19000	Water Wet	20%	384837
A1	$\backsimeq$ 15000	Water Wet	10%	158504
A1	$\backsimeq$ 15000	Water Wet	20%	489129
S1	$\backsimeq$ 5000	Water Wet	10%	24044
S1	$\backsimeq$ 5000	Water Wet	20%	22029
S7	$\backsimeq$ 4000	Water Wet	10%	30725
S7	$\backsimeq$ 4000	Water Wet	20%	10617

Table 5.2: Computational performance of the three-phase depletion module

5.3.1 Base case

We start the sensitivity analysis study by running a depletion simulation on the Berea network using the base case scenario parameters. Figure 5.7 shows the network configuration at $PB - P = 60psi$.

Here, gas grows into the oil-wet capillary elements originally filled with oil. Hence, oil is preferentially displaced compared to water which occupies the water-wet capillary elements. The phase saturation curves confirm this observation. Figure 5.8

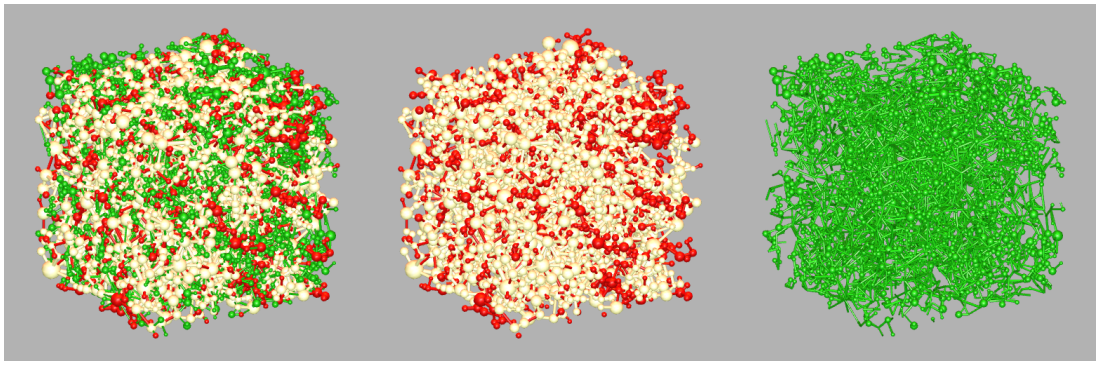

Figure 5.7: Left: Network configuration at PB-P=60psi. Middle: oil-wet capillary elements. Right: water-wet capillary elements. (Oil: red; Water: green; Gas: white)

shows that oil saturation drops as the first bubbles start to grow inside the network. Water saturation remains constant meanwhile. This can be explained by the phase distribution initially in place. In fact, oil occupies the largest pores after primary drainage, thus, low capillary entry pressures are needed for gas to invade these pores. Higher capillary entry pressures are required, however, to displace water from the smaller pores.

Another factor that explains this behaviour is due to the wettability of the network. Oil occupies the oil-wet pores, and thus, it can be readily displaced from the network as it is connected to the outlet via oil-wet pathways. Water-wet pathways to the outlet are unlikely to exist in this configuration (due to the low Swi value), however, and displacing water would involve the more costly multi-chained displacements. Therefore oil is more accessible to gas in this particular case. Note that after most of the oil is displaced, water saturation drops slightly due to the invasion of the non-trapped water-filled capillary elements, then reaches a threshold that marks the irreducible water saturation (7% in this case).

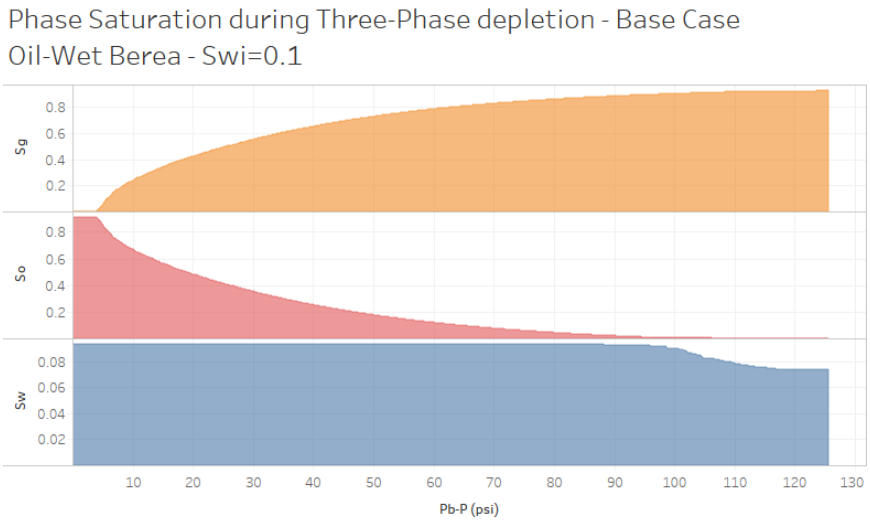

Figure 5.8: Evolution of phase saturation for gas, oil and water during the depletion simulation.

Figure 5.9 shows the the number of clusters for each phase. The number of gas bubbles goes up as they progressively nucleate in the network then drops when gas clusters start to coalesce. This is accompanied by the fragmentation of existing oil clusters whose number grows initially then drops again when most of the oil clusters are removed from the network. The number of water clusters stays largely unchanged, however, and only slightly fluctuates at the end of the depletion when a fraction of it is displaced by gas.

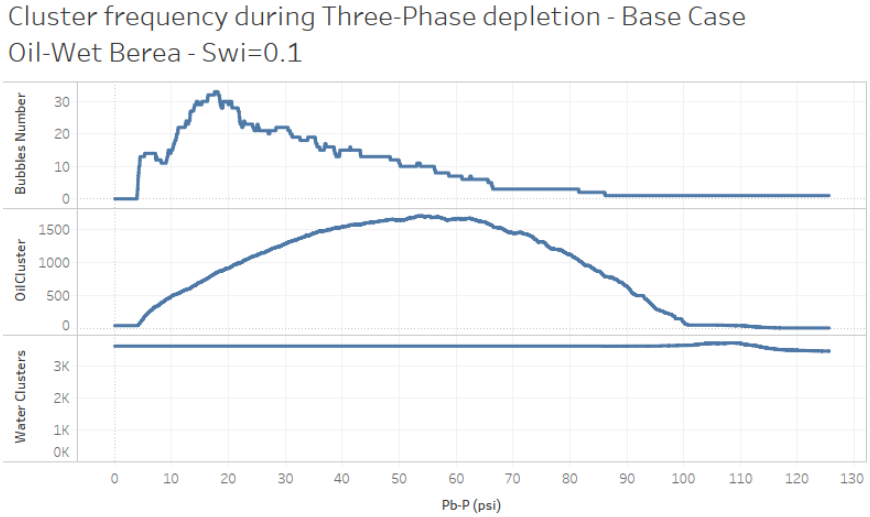

Figure 5.9: Evolution of cluster number for each phase during the depletion simulation.

These observations suggest that depletion in water-flooded oil-wet networks is highly efficient, as gas displaces mainly oil clusters whilst water remains trapped in the smallest pores. This conclusion remains valid only under the assumption that gas has enough internal pressure to expand into the entire network. Hence, it appears that the critical gas saturation can be an alternative indicator of depletion efficiency, which we will investigate in the next section for different initial configurations.

5.3.2 Effect of Initial Water Saturation

We examine now the effect of initial water saturation Swi on gas evolution during three-phase depletion simulations. We consider four Swi values: 5%, 10%, 15% and 20% and we maintain the same wettability as the base case (oil-wet for oil-filled pores and water-wet for water-filled).

Figure 5.10 shows that gas expands more readily in networks with low initial water saturations. At $PB - P = 60psi$, gas saturation is equal to 83% for Swi=5% compared to 65% for Swi=20%. This is consistent with the fact that as more dissolved gas is available under such conditions (GOR is significantly higher than GWR) and

so more can diffuse into the nucleated bubbles. Moreover, as oil is preferentially displaced (due to lower capillary entry pressures), gas has more accessible sites to invade compared to configurations with high Swi, where it can be momentarily constrained by water blocking the smallest pores.

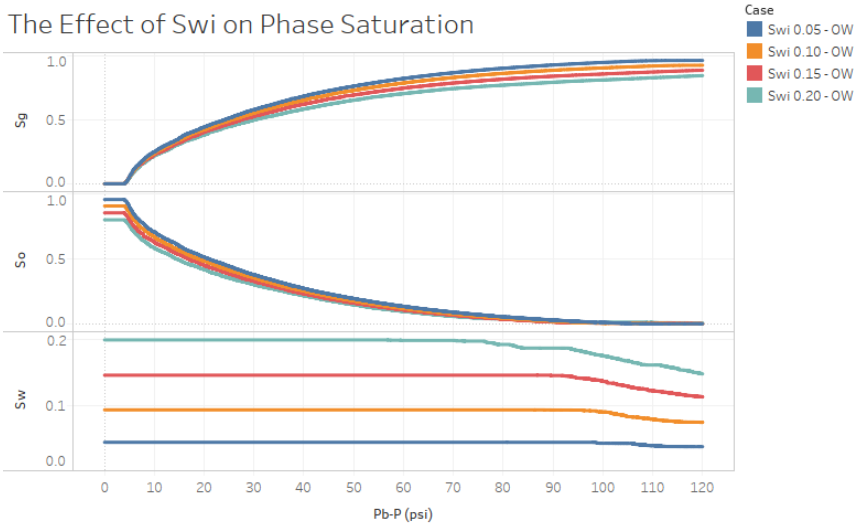

Figure 5.10: Evolution of phase saturation for gas, oil and water during the depletion simulation for 4 Swi values.

Although Figure 5.11 does not show a clear correlation between Swi and the number of nucleated bubbles, the number of oil clusters is greatly affected by the amount of initial water in the network. More oil clusters can be observed in networks with low Swi - around 5000 oil clusters were registered at PB-P=60psi for Swi=5% compared to only 500 for Swi=20%. This is a direct effect of the water distribution in the network: larger clusters of oil are found for low Swi values and bubble nucleation events result in their frequent fragmentation. For high Swi values, however, the clusters of oil remain relatively small in size at the end of primary drainage, and thus once a bubble nucleates in one of them the corresponding oil will be quickly removed (remember we are dealing with an oil-wet case where oil is connected to the outlet via film pathways). In addition these small clusters are more likely to be constrained by water in narrow throats, which can delay their displacement by the growing gas.

Figure 5.12, which compares the phase distribution in two networks with two different Swi values (5% and 20%) at PB-P=60psi, illustrates this effect well. For Swi=5%, most of the largest pores are already invaded by gas (they are more accessible to the growing gas). On the other hand, we can still see large pores belonging to relatively small oil clusters in the network with Swi=20% . These clusters are likely to be surrounded by small throats and, thus, will be only accessible at later stages of the depletion process (or if a bubble randomly nucleates inside them).

The effect of initial water saturation on relative permeability and critical gas satur-

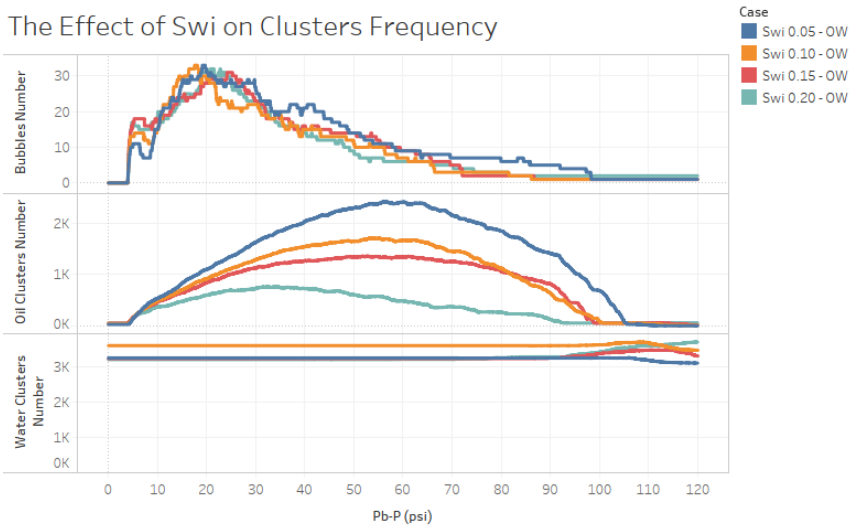

Figure 5.11: Evolution of cluster number for each phase during the depletion simulation for for 4 Swi values.

ations (Sgc) can be shown by Figure 5.13 and Table 5.3. Oil relative permeability is seen to decrease monotonically with an increase in Swi. Gas relative permeability is found to be less affected by the change of initial water saturation, although it is clear that gas breakthrough occurs earlier for low Swi. This early gas production is accompanied by a low Sgc value (14% for Swi=15%) compared to significantly higher critical gas saturations at high Swi (38% for Swi=20%) and appears to be a direct consequence of the difference in initial phase distribution for different Swi prior to depletion. For Swi=5%, for instance, gas has more space to grow and bubbles coalescence occurs quickly, resulting in the early formation of a spanning gas cluster. As more water occupies the network, delayed coalescence is expected and bubbles have more time to grow separately; by the time the bubbles form a spanning cluster, several parts of the networks have already been reached by the gas, which explains the corresponding high Sgc values.

As gas is unlikely to expand further after breakthrough (due to the drop of pressure in the spanning cluster), these observations suggest that the existence of initial water in the initial configuration might increase the critical gas saturation during tertiary depletion, which is in agreement with experimental observations (where depletion proved to yield good recovery in water-flooded reservoirs). Note, however, that some oil might remain in the biggest capillary elements for high Swi values, as we have shown in the previous paragraph. This oil can be the target of tertiary drainage processes or other EOR methods that could be deployed at the end of depletion.

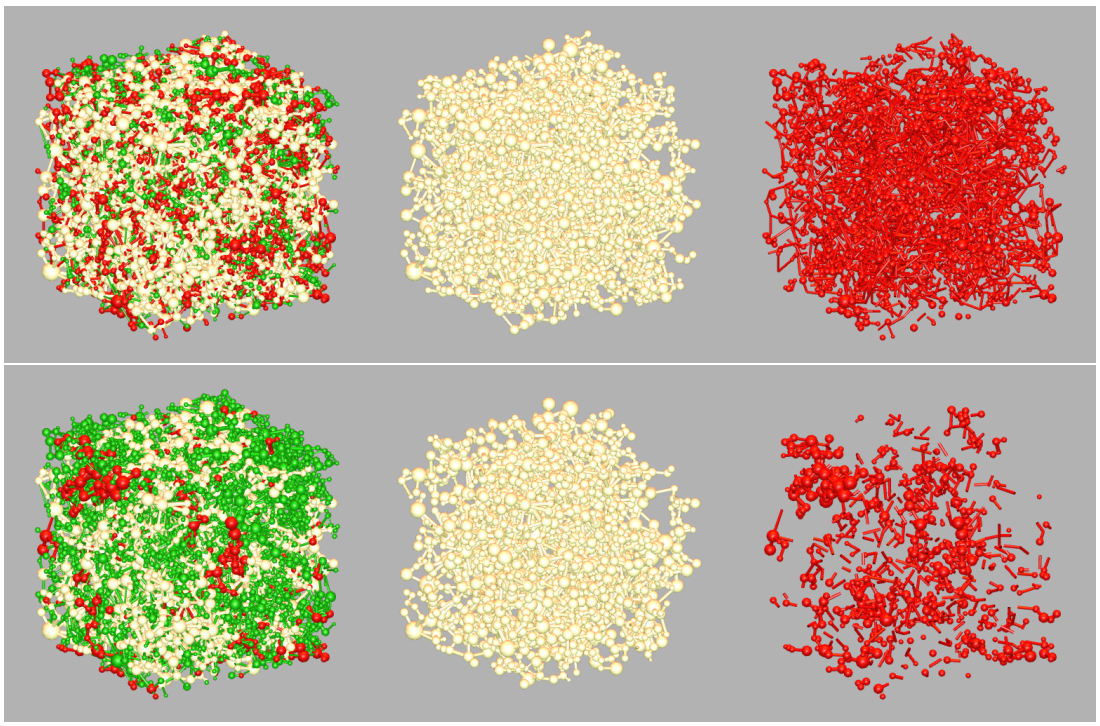

Figure 5.12: Network configuration at PB-P=60psi. Each row shows the full configuration as well as each individual phase distribution. Top: Swi=5%. Bottom: Swi=20%. (Oil: red; Water: green; Gas: white)

Case	Sgc	Critical Pressure (psi)
Swi 0.05 - OW	0.14	743.54
Swi 0.10 - OW	0.17	742.74
Swi 0.15 - OW	0.33	734.42
Swi 0.20 - OW	0.38	729.84

Table 5.3: The effect of initial water saturation on critical gas saturation.

5.3.3 Effect of Wettability

The results presented in the last section are only valid for the oil-wet configuration, where the oil-filled capillary elements have been assigned a contact angle $\theta_{OW} = 140°$. We now extend this analysis by investigating the effect of wettability change on gas growth in networks with initial water saturation. Two cases are considered:

- **OW**: water initially occupies 10% of the total network volume. Oil-filled capillary elements are assigned a contact angle $\theta_{ow} = 140°$; Water-filled capillary elements are assigned a contact angle $\theta_{ow} = 30°$;
- **WW**: water initially occupies 10% of the total network volume. Oil-filled capillary elements are assigned a contact angle $\theta_{ow} = 40°$; Water-filled capillary elements are assigned a contact angle $\theta_{ow} = 30°$.

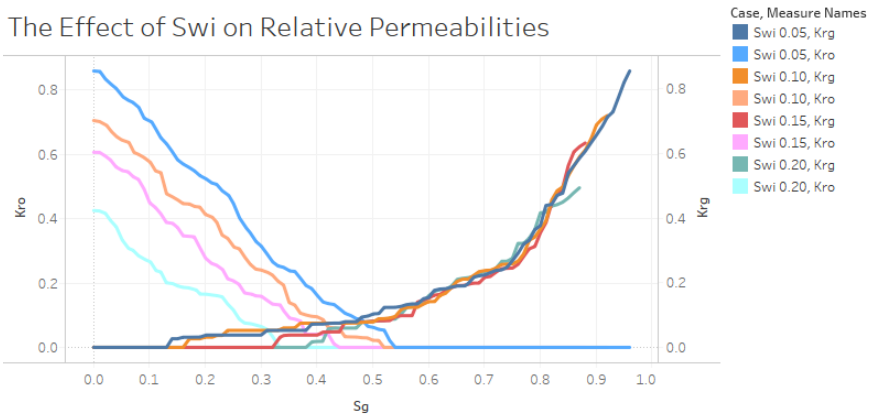

Figure 5.13: Oil and gas relative permeabilities during the depletion simulation for 4 Swi values.

Figures 5.14 and 5.15 show the different behaviours observed between the two configurations after 60psi depletion. Although the saturations of the three phases follow similar paths initially (oil is still preferentially displaced due to the associated low capillary entry pressure), water production starts very early stages in the WW case and is rapidly removed from the system; oil production, on the other hand, slows down once the water begins to be displaced and stops completely shortly thereafter, with more than 25% of the original oil in place left trapped. This results in gas filling almost the entire network for the OW case, whilst gas saturation reaches a maximum at approximately 73% for the WW case.

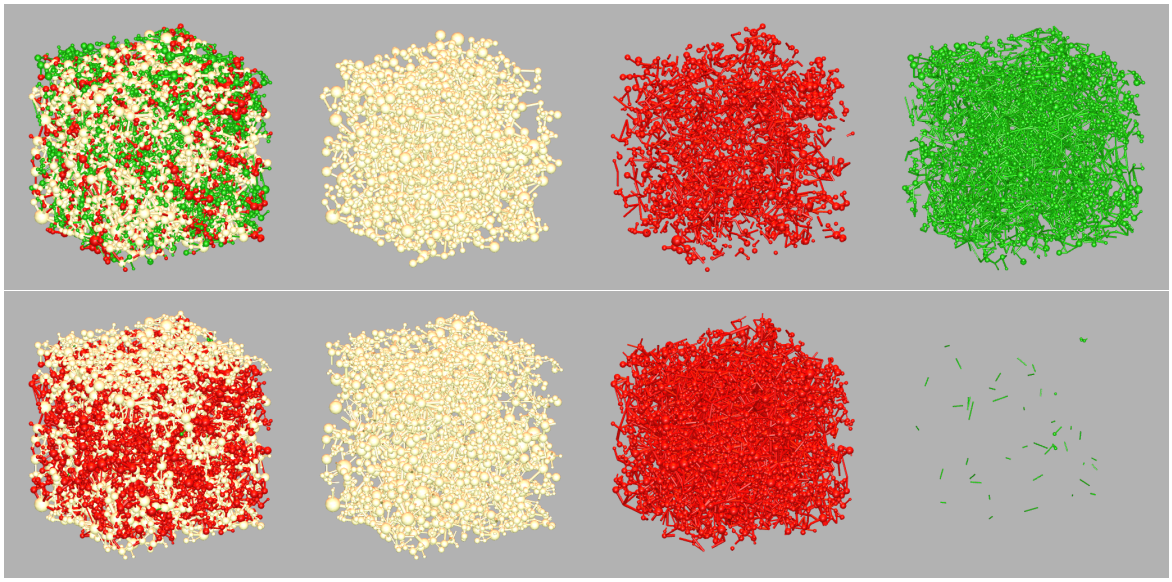

Figure 5.14: Network configuration at PB-P=60psi. Each row shows the full configuration as well as each individual phase distribution. Top: Oil-Wet configuration. Bottom: Water-wet configuration. (Oil: red; Water: green; Gas: white)

These observations clearly demonstrate the impact of wettability and film flow and how these can greatly impact recovery during three-phase depletion. For the WW case, the absence of oil-wet pathways towards the outlet resulted in more trapped

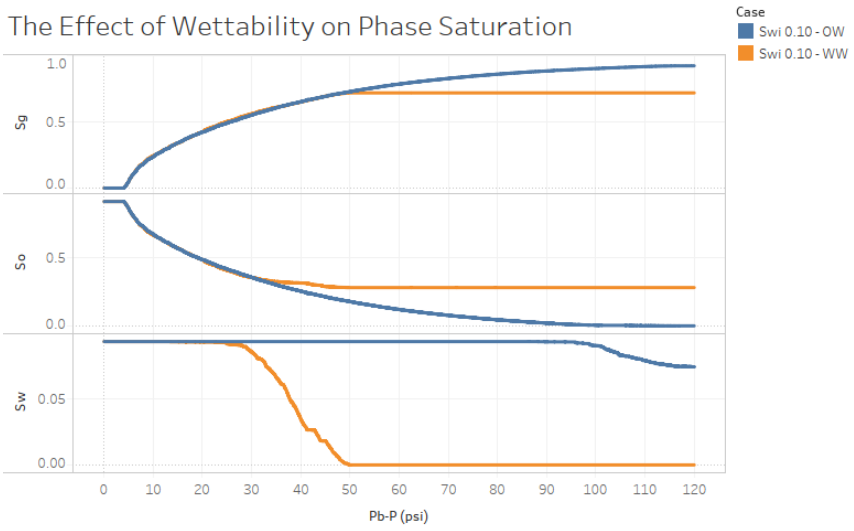

Figure 5.15: Evolution of phase saturation for gas, oil and water during the depletion simulation for two wettability configurations. Swi=10%..

oil. Although oil-filled pores can be notionally invaded by gas via multi-chain displacements, the required internal gas pressure to trigger those chains is higher than that needed to displace water, which is already connected to the outlet via film pathways. This explains the early water production and highlights two major stages of displacement during depletion in water-wet networks:

1. Gas initially invades oil-filled capillary elements topologically connected to the network outlet. At this stage oil is still preferentially displaced as it occupies the largest pores.

2. Once all the accessible oil is displaced, water is now preferentially displaced and oil production significantly drops (and eventually stops). Depletion continues until either all the water is removed or the internal gas pressure becomes insufficient to trigger more displacements.

Figure 5.16 shows another consequence of wettability change, where more bubbles are found to nucleate in the water-wet network. This can be explained by the three-phase contact angles derived using equation 5.9. Both oil-gas and water-gas contact angles (θ_{go} and θ_{gw}, respectively) are computed based on the three-phase surface tensions and the contact angle between oil and water, θ_{ow}. For the two wettability configurations used in this section and the surface tension values used ($\sigma_{go} = \sigma_{gw} = \sigma_{ow} = 30 dyn/cm$), the three-phase contact angles are given in Table 5.4.

Configuration	θ_{ow}	θ_{go}	θ_{gw}
OW (deg)	140	28	83
WW (deg)	40	83	28

Table 5.4: Three-Phase contact angles for two wettability configurations.

These values suggest that lower nucleation thresholds are expected for the WW case, as the the cosine of the contact angle between gas and oil is lower in the water-wet configuration and this results in a higher bubble density observed in the water-wet configuration. Another factor that affects this outcome is the rapid removal of oil clusters when the network is oil-wet (due to the existence of oil-wet film pathways), which accelerate bubble coalescence and reduce bubble density. This does not occur in the WW case, as oil is not preferentially displaced when not topologically connected to the outlet.

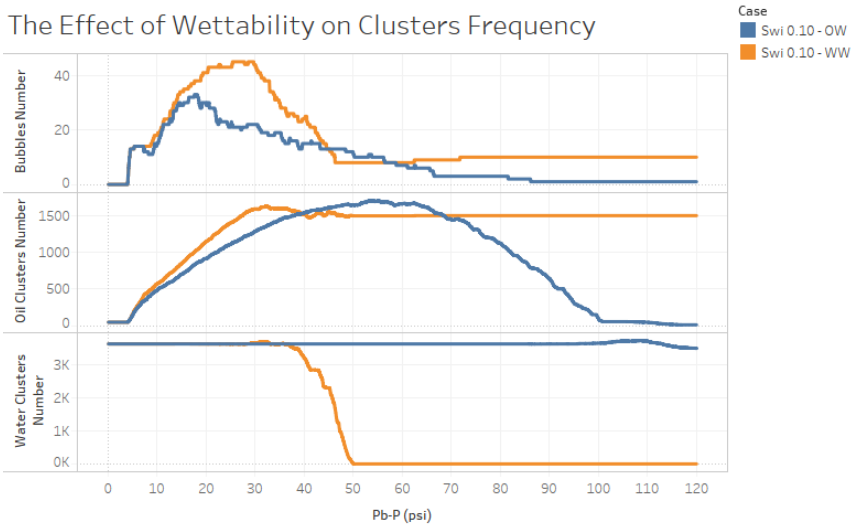

Figure 5.16: Evolution of cluster number for each phase during the depletion simulation for 4 Swi values.

The effect of wettability on relative permeabilities and critical gas saturation is shown in Figure 5.17 and Table 5.5. It is clear that the increased bubble density resulted in delayed breakthrough (due to delayed coalescence) and lower gas relative permeability for the water-wet configuration. The effect on oil permeability is small, however, as oil is preferentially displaced until it becomes disconnected. The delayed breakthrough of gas is also accompanied by significantly higher Sgc values for the WW case (63% for WW case compared to 14% for OW case; Swi=5%). Note, that as Swi is increased, the difference in Sgc values between the two wettability configurations decreases (45% for WW case compared to 38% for OW case; Swi=20%). This is explained by the abundance of film pathways to the outlet in both wettability configurations, which eventually facilitates the formation of a spanning gas cluster. This also suggests that – under the assumption that gas stops expanding after gas

breakthrough - water wetness might be expected to give greater recovery efficiency as more nucleation events are expected to occur and additional parts of the network are explored before a spanning gas cluster forms.

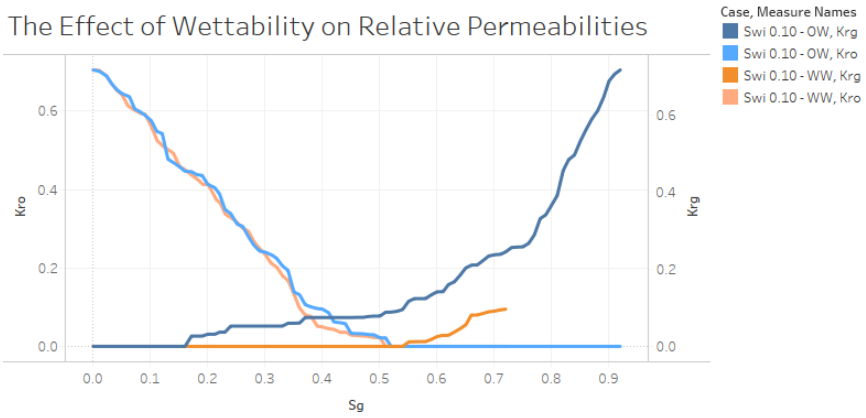

Figure 5.17: Oil and gas relative permeabilities during the depletion simulation for two wettability configurations. Swi=10%.

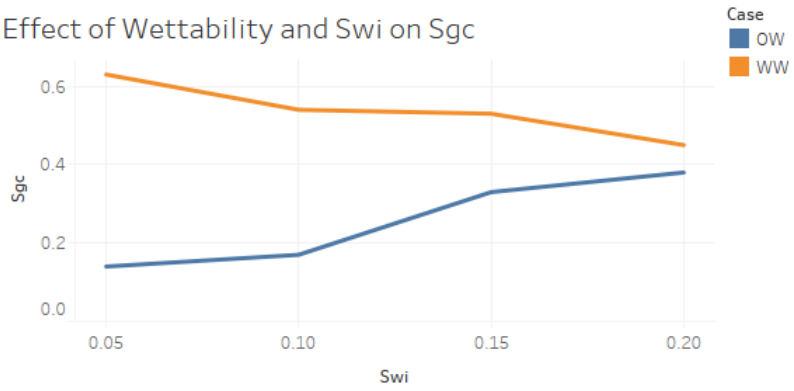

Case	Sgc	Critical Pressure (psi)
Swi 0.05 - OW	0.14	743.54
Swi 0.05 - WW	0.63	715.6
Swi 0.10 - OW	0.17	742.74
Swi 0.10 - WW	0.54	722.02
Swi 0.15 - OW	0.33	734.42
Swi 0.15 - WW	0.53	720.26
Swi 0.20 - OW	0.38	729.84
Swi 0.20 - WW	0.45	724.28

Table 5.5: The effect of initial water saturation and wettability on critical gas saturation.

5.3.4 Effect of spreading coefficient

We now examine the effect of spreading coefficient C_s on three-phase-depletion. Three scenarios are considered, where different interfacial tension configurations are

assigned to the capillary elements resulting in different spreading coefficients as shown in Table 5.6. We also consider the two wettability configurations described in the previous section.

Spreading Coefficient	σ_{gw}	σ_{go}	σ_{ow}
$C_s = 10$	30	10	10
$C_s = -10$	30	20	20
$C_s = -30$	30	30	30

Table 5.6: Spreading Coefficients for three surface tension configurations.

OW Networks

The spreading coefficient is predicted to have a small effect on phase saturations in oil-wet networks (Figure 5.18) - the only observation worth noting is the early gas production for $C_s = 10$, which can be explained by the low nucleation threshold in the corresponding configuration (i.e. low σ_{go} value). Moreover, as the oil can flow through films in oil-wet networks, the ability of oil-layers to form between water and gas is largely irrelevant under such conditions.

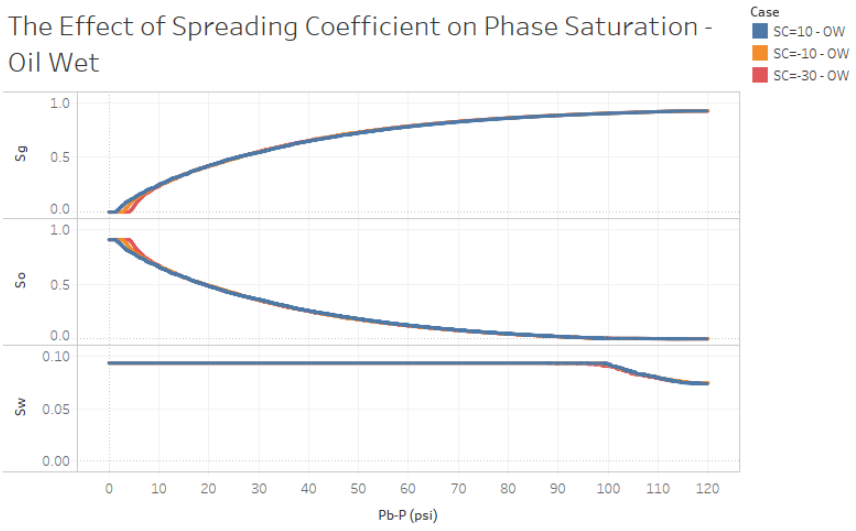

Figure 5.18: Evolution of phase saturation for gas, oil and water during the depletion simulation for three spreading coefficients. Swi=10%. Oil-wet network

Figure 5.19 shows higher bubble density for higher spreading coefficients in oil-wet networks which is again a manifestation of the low nucleation energy threshold under those conditions (i.e. lower interfacial tension). This delays gas breakthrough and affects both relative permeabilities and the critical gas saturation as shown by Figures 5.20 and Table 5.7 (Sgc almost tripled when the spreading coefficient shifted from -30 to 10).

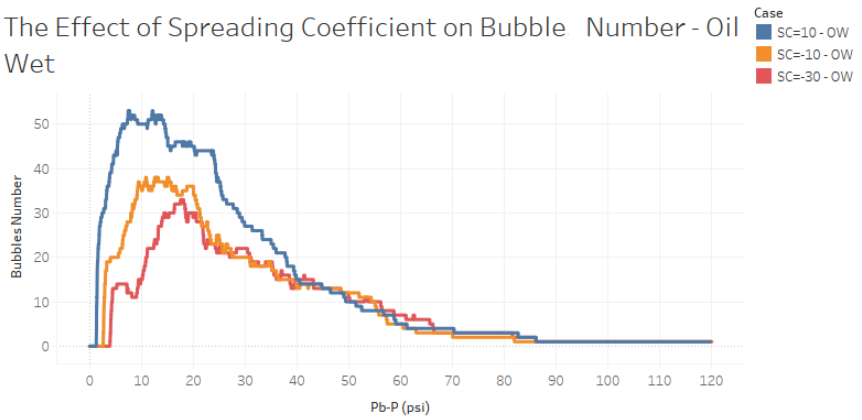

Figure 5.19: Evolution of bubble number during the depletion simulation for three spreading coefficients. Swi=10%. Oil-wet network.

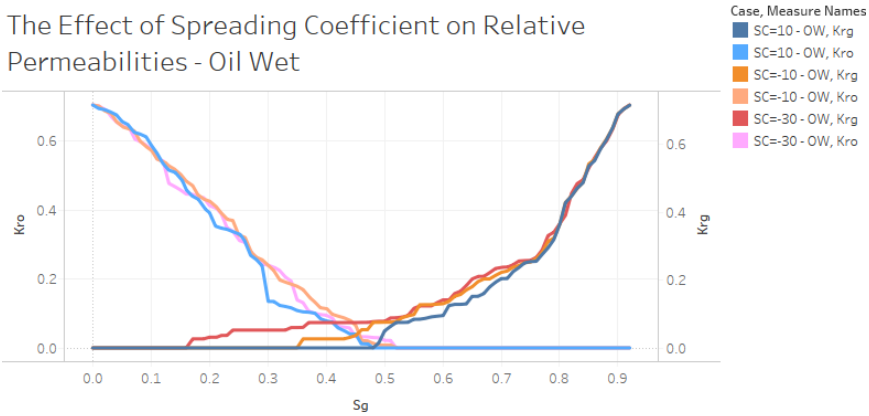

Figure 5.20: Oil and gas relative permeabilities during the depletion simulation for three spreading coefficients. Swi=10%. Oil-wet network.

WW Networks

For WW scenarios the impact of C_s is clearly different from that seen in the OW case as shown by Figure 5.21. When the spreading coefficient is negative water is produced at early stages and oil is left trapped until the end of the simulation. A positive value of Cs results in a complete removal of the oleic phase by the expanding bubbles, followed by further water displacement until the network is completely filled with gas. The formation of oil layers in this case shifts the network toward a configuration where oil is preferentially displaced for the entire process (as in the oil-wet case) which yields significantly improved recovery. This can be also shown in Figure 5.22 where the three phases are displayed for two spreading coefficients with opposite signs in the water-wet Berea network.

The number of bubbles under spreading conditions seems to be high initially but then drops quickly (due to the rapid removal of oil clusters which accelerates bubble

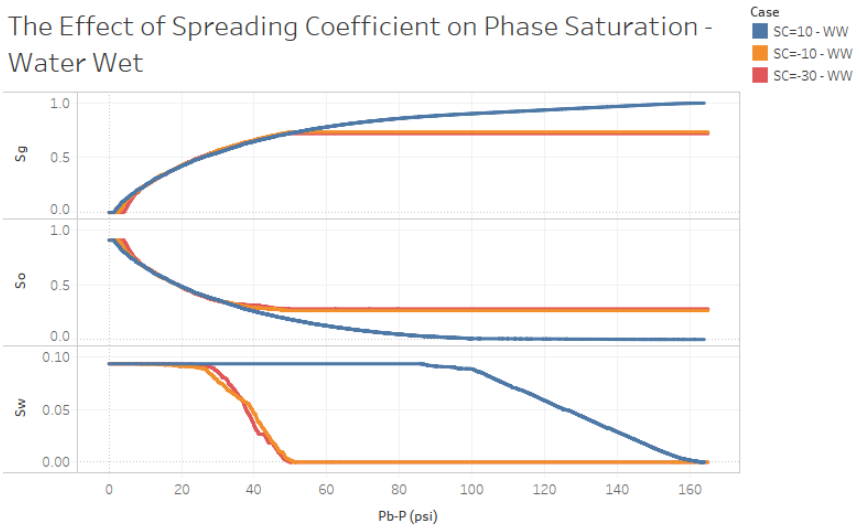

Figure 5.21: Evolution of phase saturation for gas, oil and water during the depletion simulation for three spreading coefficients. Swi=10%. Water-wet network.

coalescence) (Figure 5.23). This yields non-linearity in the Sgc values and the highest critical gas saturation corresponded to $C_s = -10$ (i.e. the case with the highest overall bubble density and the latest gas breakthrough as shown by the relative permeability curves in Figure 5.24).

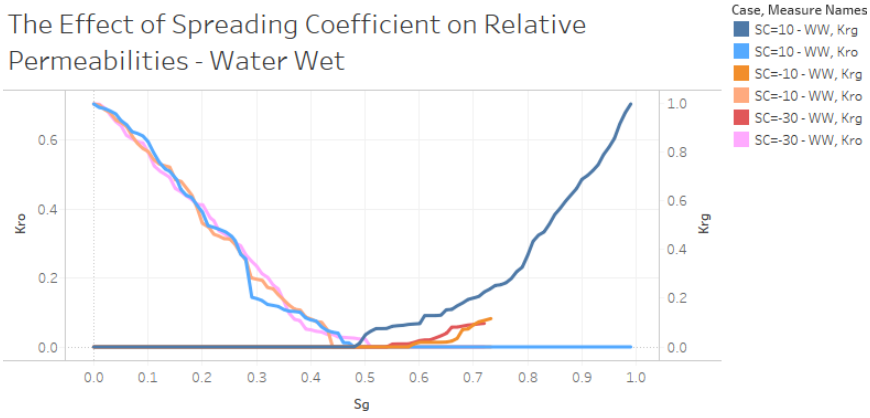

Figure 5.24: Oil and gas relative permeabilities during the depletion simulation for three spreading coefficients. Swi=10%. Water-wet network.

It is worth mentioning that these results only pertain to the particular scenarios we have set. A spreading coefficient might correspond to multiple interfacial tension configurations, which might in turn have different effects on other depletion properties (such as nucleation energy thresholds or capillary entry pressures). Hence, the spreading coefficient should not be considered separately from other related parameters and the aggregate effect on the depletion process must be considered rather than assigning a generic recovery factor for each spreading coefficient value.

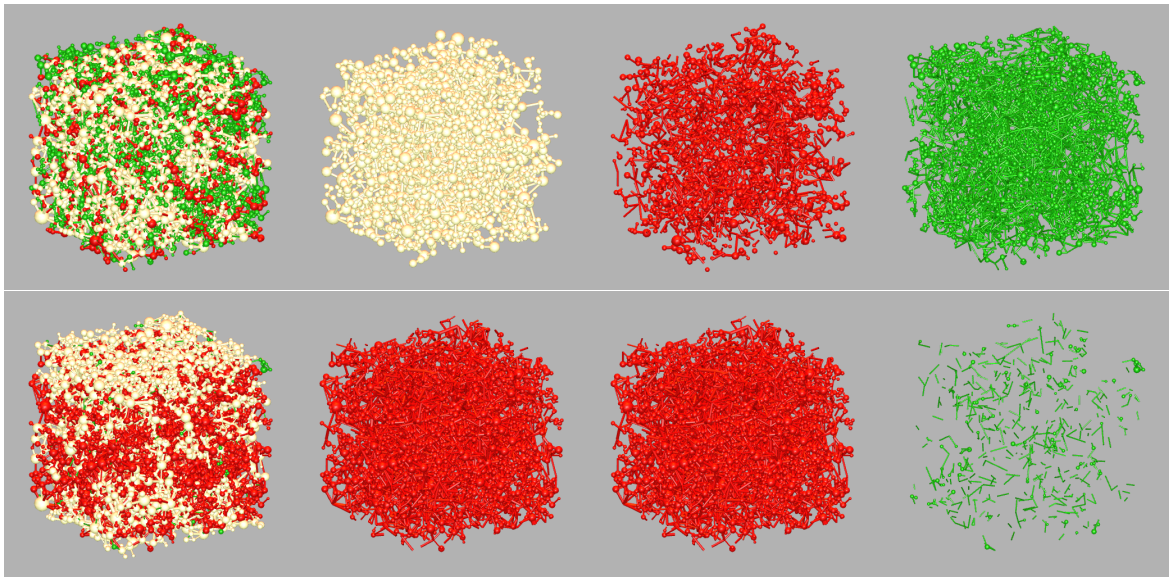

Figure 5.22: Network configuration at PB-P=60psi. Each row shows the full configuration as well as each individual phase distribution. Top: SC=10. Bottom: SC=-10. (Oil: red; Water: green; Gas: white)

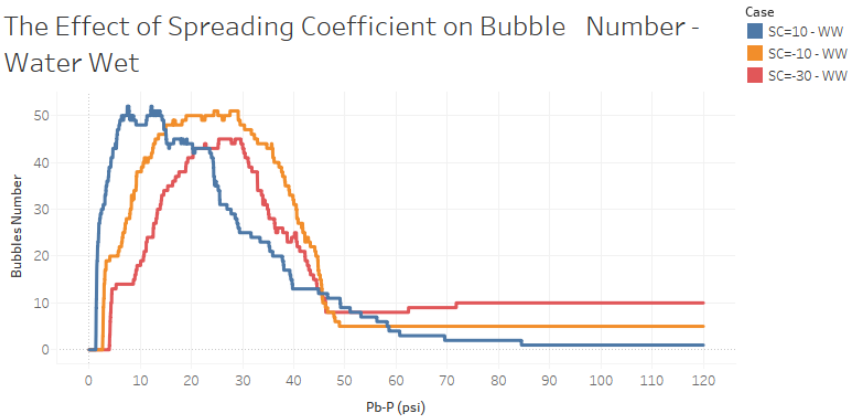

Figure 5.23: Evolution of bubble number during the depletion simulation for three spreading coefficients. Swi=10%. Water-wet network.

Case	Sgc	Critical Pressure (psi)
SC=10 - OW	0.49	725.46
SC=10 - WW	0.49	725.4
SC=-10 - OW	0.36	734.1
SC=-10 - WW	0.58	718.28
SC=-30 - OW	0.17	742.74
SC=-30 - WW	0.54	722.02

Table 5.7: The effect of spreading coefficient on critical gas saturation.

5.4 Conclusions

In this chapter we introduced the *numSCAL* three-phase module that has been implemented to simulate steady-state three-phase depletion in porous media. This has been achieved through employing concepts from graph theory to represent the different phase clusters inside a network as connected nodes, and entry capillary pressures as the associated costs. This approach has proved to be highly efficient in modelling multi-displacement chains that can occur during processes where gas, oil and water flow simultaneously. Three-phase angles and spreading oil layers have also been considered and both films and layers have been implemented to capture phase removal via oil-wet, water-wet and/or spreading layer pathways.

The module was used to investigate key parameters that affect depletion in a Berea sandstone network, where both oil and water are initially present. Of particular interest was the effect of initial water saturation, wettability and spreading coefficient on gas growth after primary drainage. In most cases, oil is preferentially displaced by gas when it is topologically connected to the outlet. The wettability of the network determines which phase is preferentially displaced subsequently, as films play an important role in the removal of trapped oil and water clusters. Thus, oil can eventually be completely displaced when the network is oil wet and/or when spreading oil layers exist. However, this requires continuous flux of gas entering the bubble to keep the internal gas pressure high enough to trigger additional invasion. In reality, it is possible that gas breakthrough would signal the end of depletion and, in that situation, water wet networks would result in better recovery (due to associated higher bubble densities that delay coalescence and yield higher critical gas saturations). Similarly, resident water can also affect nucleation events and delay the formation of a spanning gas cluster and this can indicate better recovery for high initial water saturations.

The simulated results also highlighted the complexity of three-phase depletion, as most of the parameters are tightly linked to one another - this makes prediction of the sensitivity to one parameter difficult to achieve without appropriate simulation tools. For instance, decreasing the gas-oil interfacial tension can reduce the entry capillary pressure between the growing gas and oil, but can also decrease the nucleation energy threshold (which can increase bubble density and delay their coalescence). In addition, changing the interfacial tension would directly impact the spreading coefficient and this could affect the connectivity of oil pathways towards the outlet (also correlated to the physical network connectivity), which could significantly affect the final recovery. This is where this module can be particularly useful, as most of the depletion mechanisms are implemented in a way that incorporates all these parameters in the underlying pore-scale physics. Thus, once fed with the appropriate

inputs from a particular core sample and fluid combination, it is possible to study the impact of different recovery protocols and to gain more informed insights about the effect of each flow parameter.

The predictive power of this tool is dependent upon accurate fluid and rock parameters. Hence, it is essential to acquire as much experimental data as possible to produce reliable simulations. In addition, more collaboration is needed with experimentalists to define the right efficiency indicators of the underlying process. We have already seen that higher gas saturations at the end of the simulation appear to correlate with low critical gas saturations. Thus it is important to know whether, in a specific core sample, gas continues to expand after breakthrough or not (which may have implications for field-scale predictions). The answer to this question would help to identify the potential of further recovery by continuing to decrease the reservoir pressure and to generate estimates of additional recovery. This can be used as a validation methodology to be used in the future.

So far, this module has only been applied to investigate three-phase depletion. However, other three-phase processes, such as WAG experiments, can be also examined. This is also a part of future work although the current implementation would likely require more additional features. One major assumption of the model is that viscous forces can be neglected. This makes the tool unsuitable to investigate scenarios where the flow velocity is sufficiently high to shift the network from the capillary-dominated regime (i.e. very high depletion rate, flow near the wellbore, medium/high rate gas or water injection). Unsteady-state approaches are needed in this case to capture the correct balance between capillary and viscous forces and to study the regimes that might emerge accordingly. Such methods will be discussed in the next two chapters as part of the *numSCAL* drainage and ganglion modules.

Chapter 6

numSCAL Unsteady State Drainage Module

6.1 Introduction

It is well recognised that flow behaviour at the pore-scale is mainly determined by the competition between capillary and viscous forces. Whilst quasi-static models can reproduce flow patterns and qualitative estimations of capillary pressure and relative permeability curves when capillary forces are predominant, they become inadequate when the effects of viscous forces become important. Viscous effects are usually observed when the fluids are displaced at high velocities – this could occur during high rate depletion or high rate waterflooding. In addition, some EOR processes target the capillary-viscous balance to achieve higher recoveries: for instance, polymer injection aims to reduce the viscous ratio by stabilising water fingers and shifting the flow pattern towards a more stable regime. Low salinity water injection aims to affect the chemical equilibrium between the hydrocarbon and water phase, opening up the possibility of displacing trapped ganglia of hydrocarbons or allowing water fingers to swell (Morrow and Buckley, 2011 [154]).

The investigation of dynamic processes requires the implementation of a dynamic model that captures both capillary and viscous forces. Sensitivity analysis to capillary number and viscous ratio can give valuable insights into the flow behaviours and the expected efficiency of high rate processes. This is not only relevant to high rate depletion experiments, but to any recovery process that involves competition between capillary and viscous forces. Such a model can also be useful for investigating some EOR techniques, such as low salinity water injection, polymer injection and surfactant injection.

Within this context, a fully unsteady-state drainage model (based upon an earlier model by Regaieg, 2013 [107]) has been developed as part of this work – we present in this chapter the various components that constitute the associated module of the *numSCAL* simulator. We discuss the pore space architectures handled by the framework and the way in which capillary forces are included when computing the pressure field in the network. We also show how the pressure solution is coupled to the flow rate under investigation and how phase saturations are updated accordingly. Finally, we validate the model by comparing some simulated results to the seminal experimental work of Lenormand (1988) [97] and we carry out a sensitivity analysis study to examine the effect of key flow parameters on drainage processes.

6.2 Model Description

Like any other pore network model, a number of underlying assumptions are made when implementing the basic unsteady-state drainage model.

- The flow inside the capillary elements is considered to be laminar – the meniscus between two fluids is assumed to be always perpendicular to the axis of the pore.
- The fluids inside the capillaries are incompressible and immiscible.
- Film flow is not modelled explicitly at this stage (although it *is* taken into account in the context of phase trapping).
- Counter-current imbibition is not considered.
- Ganglia mobilisation is neglected.
- Gravity forces are not considered significant.

To simplify the model description, we will consider a waterflooding simulation where water displaces oil in an oil-wet network. The workflow of the model is described by Figure 6.1. At each timestep, (1) the network is explored to look for trapped clusters; (2) a capillary pressure term is calculated in each capillary element containing an oil-water meniscus; (3) a pressure gradient is coupled to the chosen flow rate; (4) mass conservation is applied at every node, the pressure field in the network is calculated, and elementary flows in each capillary element are derived; (5) pores exhibiting counter-current imbibition behaviour are temporarily frozen, and the pressure solution is iterated (step 3), until a consistent pressure field with no

counter-current imbibition flow is attained; (6) phase saturations are updated according to mass conservation. This sequence is repeated until a desired number of pore volumes has been injected.

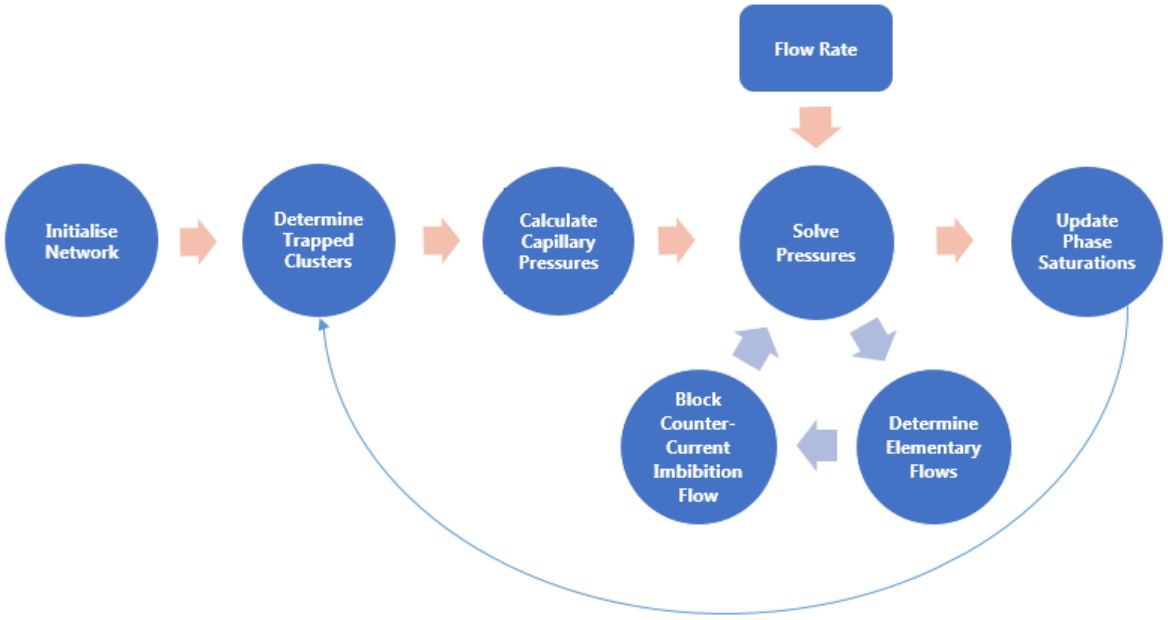

Figure 6.1: The Unsteady-state Fast Drainage model workflow

6.2.1 Pore Space Generation

The first step of the modelling approach consists of generating a network of capillary elements representing the porous medium. The supported networks include regular bond models (where the network is formed by interconnected cylindrical elements), node/throat regular networks (where the pore bodies are interconnected via narrow throats), and extracted networks from microCT images (see Chapter 3, Section 3.2.1). For the sake of simplicity, we use the regular bond architecture when describing the unsteady-state model components. This architecture will also be used in the sensitivity analyses that follow.

Inlet and outlet pores are assigned, and the network is filled with oil. Every pore is assigned two fluid flags at the end of its two extremities. These flags signal the existence of either oil or water at each end of the capillary element and determines whether a capillary pressure term should be included in the pressure solution. The simulation begins with water flowing into the inlet pores – the fluid flags on the upstream extremities of these pores are consequently instantaneously switched to "water" (Figure 6.2).

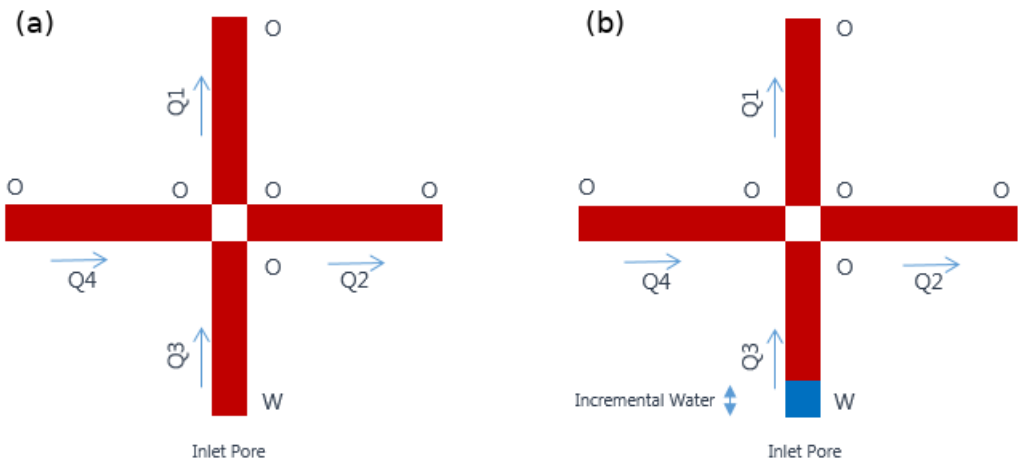

Figure 6.2: Fluid flags at the extremities of pores. Inlet pores are assigned a water flag at their inlet extremities to trigger the creation of a meniscus and a capillary pressure (a). Water starts to invade the network from the inlet pores (b).

6.2.2 Capillary Force Calculation

At every timestep during the simulation, the network is explored to look for menisci in capillary elements. A meniscus is taken into consideration when water is displacing oil from an oil-filled pore. This is reflected in the corresponding code by the presence of two different fluid flags (Figure 6.2). If the pore being considered is untrapped, we calculate the capillary pressure term corresponding to the meniscus separating the two fluids.

In the case of a cylindrical bond, the capillary pressure P_c is given by the Young-Laplace equation:

$$P_c = \frac{2\sigma cos\theta}{r} \tag{6.1}$$

where σ is the interfacial tension, r is the pore radius and θ is the oil/water contact angle.

If an extracted network with triangular pores is simulated, the capillary pressure is calculated following the formulation of Øren (1998) [25] using equations 4.9 and 4.10. However, here we choose to use the "3Rs" anchored 2D Berea networks, and so only cylindrical pores will be used in the simulations carried out in this chapter.

6.2.3 Computing the Pressure Field Across the Network

Computing the nodal pressure field throughout the simulation is an essential component of the simulation process and is used to update the network state at each time step. In this section, we describe the methodology used to determine the pressure field in the network under consideration.

We set a fixed injection rate for the flood (although constant pressure drop simulations can also be readily considered), which is effectively used as a boundary condition to determine the nodal pressure distribution and elementary flows within the system at each time step. We assume that for a single element of shape factor G, length L and cross section A, the flow Q is given by a Poiseuille-type law:

$$Q = g \times \Delta P \ , \ g = k\frac{A^2 G}{\mu} \tag{6.2}$$

where g is the element conductance, μ is the fluid viscosity in the element and ΔP the pressure difference acting across the element.

By applying a pressure gradient across the network (we choose to set a zero pressure at the inlet and a negative pressure at the outlet to ensure we have a phase flow towards to outlet), the pressure field inside the network can be obtained by applying the mass conservation law at each node i:

$$\sum_i Q_{i,j} = 0 \tag{6.3}$$

where $Q_{i,j}$ is the flow between node i and node j. When a capillary pressure is present across the curved interface between oil and water in a pore, a capillary pressure term should be included in the set of equations to obtain a consistent pressure solution. To do so, whenever a fluid-fluid interface is present in a capillary element, the elementary flow equation becomes:

$$Q = g \times (P_i - P_j \pm P_c) \tag{6.4}$$

The sign of P_c is determined based on the direction of flow from i to j. As we are treating a drainage case, the capillary pressure would always be resisting the advancing water flow. For instance if the water is flowing from i to j ($P_i > P_j$), the sign of P_c would be the opposite of $P_i - P_j$, and vice versa.

If we combine equations 6.3 and 6.4, and write it for a node, indexed 0, connected to

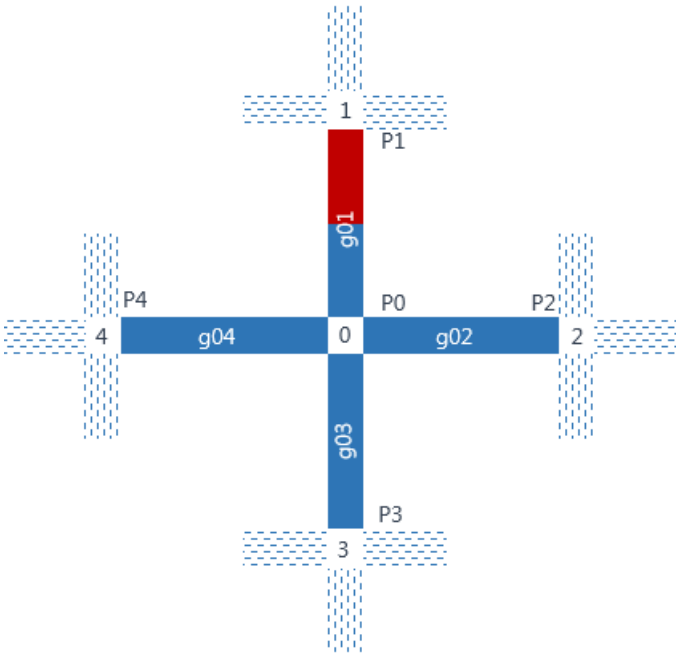

Figure 6.3: Four pores connected into node 0. P_i refer to the nodal pressures and g_i to the pores' conductivities.

four other nodes, indexed respectively 1, 2, 3 and 4 (Figure 6.3), we get the following expression:

$$\sum_{i=1}^{4} g_{0i} \times (P_0 - P_j \pm P_c) = 0 \tag{6.5}$$

and so:

$$(g_{01} + g_{02} + g_{03} + g_{04})P_0 - g_{01}P_1 - g_{02}P_2 - g_{03}P_3 - g_{04}P_4 = g_{01}P_c \tag{6.6}$$

Writing equation 6.6 for every node yields a system of linear equations where the nodal pressures constitute the unknowns. The system can be written schematically as:

$$G \times P = Q + C \tag{6.7}$$

where G is the conductivity matrix, P is the vector of unknown nodal pressures, Q is the vector describing the flow at the boundaries, and C is the vector capturing the capillary forces. The boundary conditions are provided by the pressure values in the inlet and the outlet pores.

We solve the system 6.7 using Cholesky factorisation when dealing with 2D networks. This method can become considerably slow for 3D networks, and the simulator switches automatically to the bi-conjugate gradient solution method in this case.

6.2.4 Coupling the Pressure Gradient Across the Network to the Flow Rate

To compute a consistent pressure field corresponding to the target flow rate, we need to apply the appropriate pressure gradient between inlet and outlet pores. To solve this problem, we begin with assigning a null pressure at the inlet, and an initial approximation to the outlet pressure resulting in an initial pressure gradient equal to ΔP_0 . We then compute the pressure field corresponding to ΔP_0, which then allows us to calculate the elementary flows. By summing flows from the outlet pores, we obtain the total outlet flow $Q(\Delta P_0)$ corresponding to the initial approximation ΔP_0. We then apply an iterative Secant Method to find a ΔP value satisfying the desired target flow. The computed pressure gradient at the $(k+1)^{th}$ iteration is given by:

$$\Delta P_{k+1} = \Delta P_k - (\Delta P_k - \Delta P_{k-1}) \frac{(Q(\Delta P_k) - Q_{target})}{(Q(\Delta P_k) - Q(\Delta P_{k-1}))} \tag{6.8}$$

Once the Secant method has converged, we apply the resulting pressure gradient to the network, finalise the pressure value at each node, and go on to determine the new flow in each capillary element.

6.2.5 Closing Pores with Counter-current Imbibition Flow

If we consider the configuration described by Figure 6.4, it is possible to conceive a scenario where the calculated elementary flow is directed from node 2 to node 0. This case would correspond to an imbibition process where oil displaces water in our oil-wet network. The model does not allow this in order to conserve the mass of the aqueous phase (although it *will* be modelled in the ganglion module described later), and thus, all the pores where an imbibition process is taking place become "closed" temporarily (this is achieved by assigning them a null conductivity). The pressure field is computed again until we reach a configuration where no imbibition flow is occurring (Figure 6.4, right). The pressure field is then consistent with all the elementary flows and mass is conserved when updating the phase fractions.

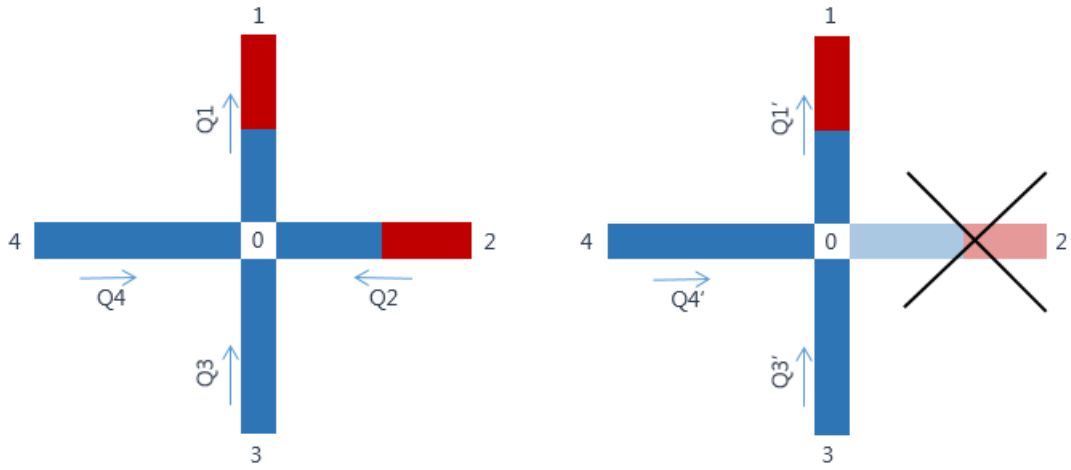

Figure 6.4: When the flow in a pore is directed from the defending phase to the invading phase, the pore is closed and the pressure field is solved calculated again. $Q_4 + Q_3 + Q_2 = Q_1$ (left) $Q'_4 + Q'_3 = Q'_1$ (right)

6.2.6 Multiple Pore Filling Algorithm

Once the elementary flows are known for all the capillary elements, we loop over all the untrapped pores where the water flow is positive, and we update the water fractions $F_{water,i}$ in *all* of these pores according to:

$$F_{water\_new,i} = F_{water\_old,i} + \frac{Q_i \times \Delta t}{V_i} \tag{6.9}$$

where V_i is the pore volume, Q_i is the pore elementary flow, and Δt is the time step used in the current iteration.

The time step is calculated at each iteration to ensure mass conservation when updating phase fractions. Thus, the timestep chosen corresponds to the shortest time required to fill entirely an oil-filled pore hosting an oil/water meniscus. Δt is therefore calculated as follows:

$$\Delta t = Min_{i \in \mathcal{F}} \frac{V_i}{Q_i} \times F_{water\_old,i} \tag{6.10}$$

where $\mathcal{F}$ is the set of untrapped pores with an oil/water interface.

6.2.7 Clustering Algorithm

The problem of clustering has been mainly addressed in this model by adapting a Hoshen-Kopelman algorithm [148] (see Chapter 4 Section 4.2.5). The trapped oil clusters are identified, and then removed from the pressure matrix in subsequent iterations.

Using this approach is sometimes problematic however – the aforementioned trapping rules mean that separate water clusters might not be able to coalesce if a single connecting oil pore is present (trapped between two water-filled pores belonging to different clusters (Figure 6.5)).

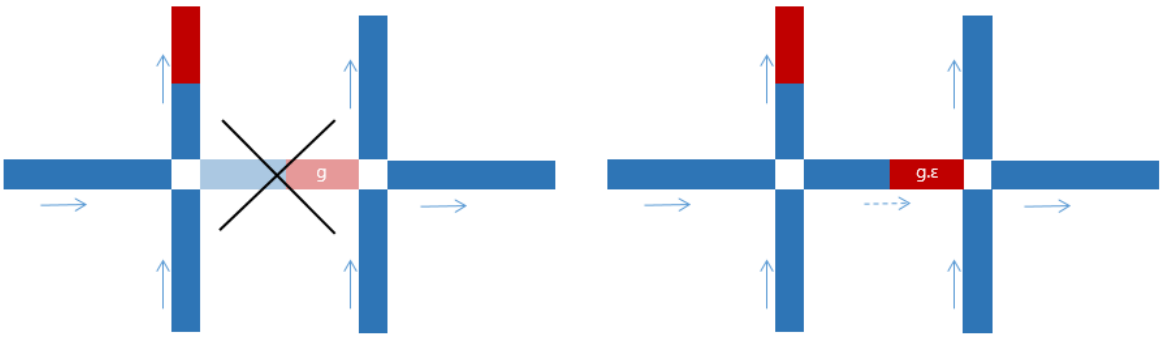

Figure 6.5: Blocking counter imbibtion can prevent water clusters from coalescing (left). We allow oil in this case to escape (via film flow). The pore is again open, and the pore conductivity is reduced to take into account the slow oil film flow (right).

This becomes especially important if we are tracking a dynamic tracer (low salinity water or polymer). For instance, in the case of a viscous fingering regime, the maintenance of disconnected water fingers without transverse interconnectivity would make the tracer flow preferentially through the spanning finger, and any EOR effect would be limited.

To address this unrealistic situation, single oil-filled pores trapped between two water clusters require special treatement. Although film flow is not modelled explicitly in this model, we assume that these pores would be filled over time by water, as oil would escape slowly via oil-wet pathways towards the outlet. These pores remain in the pressure matrix and their conductivity is multiplied by a dampening factor ε which reflects the slow nature of oil film flow.

6.2.8 Model Validation: Comparison with Lenormand Experiments

As a first application of the dynamic simulator, we use the model to simulate the drainage experiments of Lenormand from his seminal paper published in 1988 [97]. Although the experiments are almost three decades old, they still represent a solid database of experimental data that can be used to validate any unsteady state simulator. In these simulations, the main objective was to obtain the correct flow regime under different capillary numbers and viscous ratios. We generated random networks that were statistically equivalent to those used by Lenormand, and we used the same capillary numbers and viscous ratios. No history matching was carried out and so we do not expect to match the experimental patterns pore-by-pore but we do expect to reproduce the same flow regime. The results of our simulations show excellent qualitative agreement with the experimental regimes for all the simulations presented in the Lenormand papers. Figure 6.6 (viscous ratio greater than one) shows the transition from a viscous fingering pattern to invasion percolation by decreasing the flow rate of the invading phase. For a viscous ratio less than one, Figure 6.7 illustrates the transition from a frontal advance regime to a slightly less stable regime when the capillary number is decreased.

Note that it is possible to perform a quantitative comparison between simulated and experimental viscous fingering regimes based on various metrics such as the count of the total number of main, secondary and tertiary branches in the emerging structures (Kessler et al., 1988 [98]). Although this might be challenging in this particular case (as the generated networks do not match *pore by pore* those used by Lenormand), we note that both simulated and experimental figures exhibit similar counts of the number of main and secondary branches in the underlying networks shown in Figure 6.6 (i.e. three main branches can be seen in case 1 with two emerging secondary branches in average).

6.3 Application: Analysis of Unsteady State Drainage in Porous Media

In this section, we carry out numerous simulations to investigate the impact of various parameters on the dynamic evolution of two-phase flow; these parameters are related to both the applied flow protocol and the fluid properties in the underlying system. As the module targets essentially drainage processes, we consider the scenario where water is injected into an oil-wet network initially filled with oil (Figure

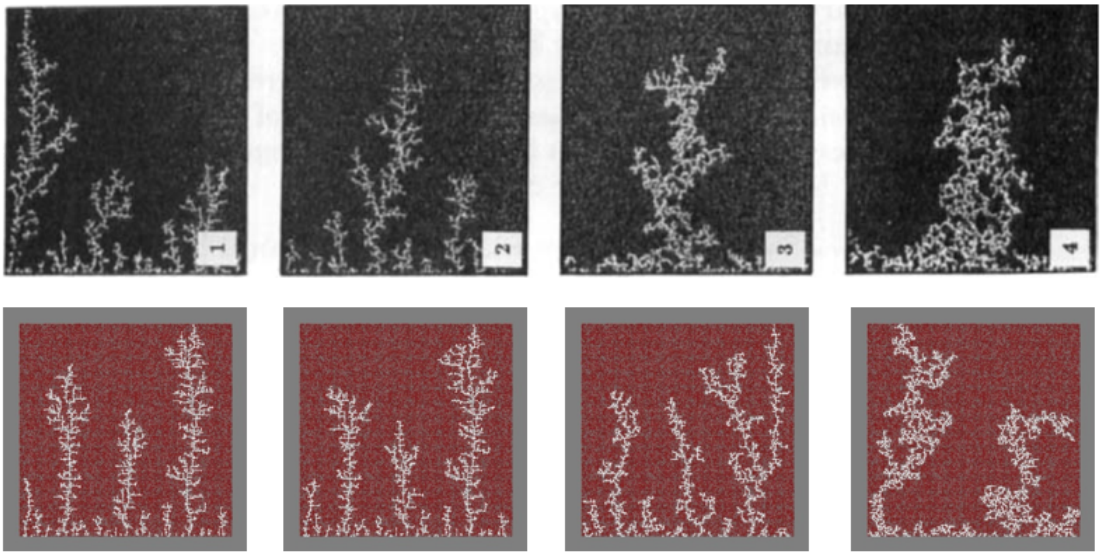

Figure 6.6: Lenormand experiments (Lenormand, 1988 [97]) vs Unsteady-state drainage model simulations (from viscous fingering to capillary fingering).

6.8). The same conclusions will be, however, valid for any two phase drainage system (i.e. gas injection into oil, gas injection into water). We also use the idealised 2D networks described in Chapter 3 Section 3.4.1 for this study. Typical base-case parameters are shown in Table 6.1.

[As an aside, the *numSCAL* unsteady-state drainage module will be extensively used in Chapter 8 to study the efficiency of various EOR processes. Thus, the simulations in this section will only partially cover the full range of applications where the module can be used]

Flow velocity	5 m/day
Oil viscosity (constant)	10 cP
Water viscosity (constant)	1 cP
interfacial tension	30 $10^{-3} dyn/cm$
Contact angle	140 deg

Table 6.1: Default parameters used for the sensitivity analysis of the unsteady-state drainage simulations

6.3.1 Effect of Flow Velocity

We begin this study by investigating the effect of Darcy (i.e frontal) velocity (V) on oil recovery; V is calculated as $\frac{Q}{\phi A}$, where Q is the volumetric flow rate ($m^3 s^{-1}$), ϕ is the network porosity, and A is the cross section area of the network along the flow direction. We consider three scenarios where four pore volumes of water are injected into a 2D 200x100 oil-wet network at three frontal advance rates: 1m/day, 5m/day and 10m/day. Fluid viscosities, interfacial tension and contact angles are

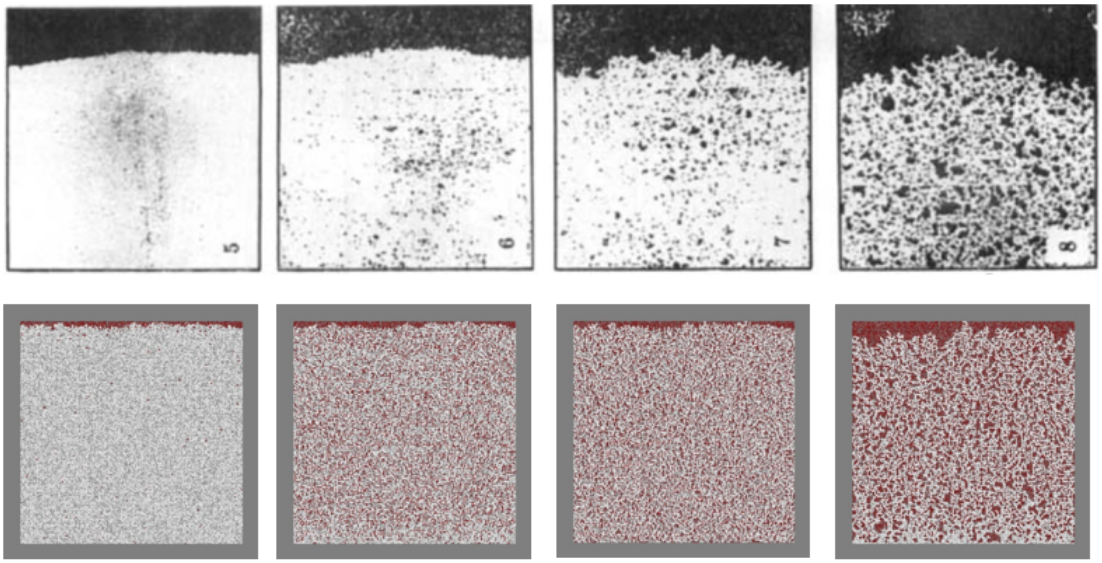

Figure 6.7: Lenormand experiments (Lenormand, 1988 [97]) vs Unsteady-state drainage model simulations (from a frontal advance regime to a slightly less stable regime).

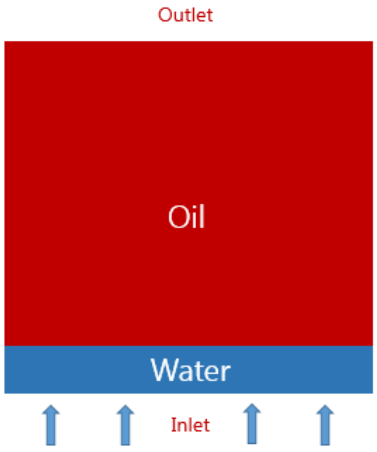

Figure 6.8: A schematic of the initial configuration of an unsteady-state simulation. Water invades the initially-oil-filled network from the inlet pores.

kept unchanged (Table 6.1). The viscosity ratio is 10 for these simulations.

Figure 6.9 shows the different phase distributions corresponding to each flow velocity. Whilst water invades the network in a capillary dominated fashion for V=1m/day, the flow becomes more directed for V=10m/day and an unstable finger emerges. This behaviour is explained by a shift of the regime (due to the increase of capillary number) from a capillary dominated invasion (where capillary forces are mostly dominant) to viscous fingering – where viscous forces are no longer negligible and affect the growth direction along the highest pressure gradients.

Figure 6.10 shows the evolution of water saturation as a function of injected pore volumes. Due to the shift of the invasion regime, greater recovery is achieved at

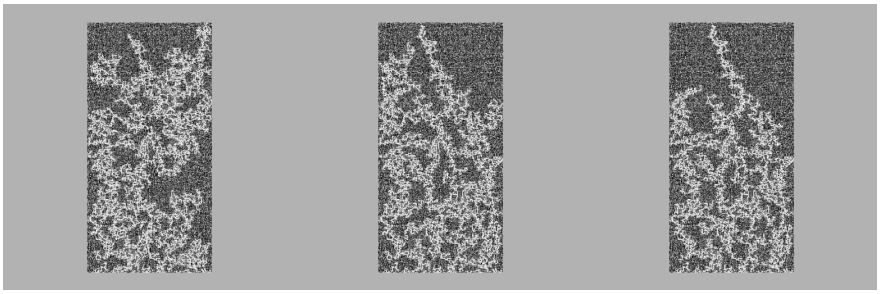

Figure 6.9: Effect of flow velocity V on final water distribution. From left to right: V=1m/s; V=5m/s; V=10m/s.

low flow velocities. At the end of water injection, 28% of the oil originally in place (OOIP) was displaced for V=1m/day compared to only 22% for V=10m/day. This behaviour might seem counter-intuitive, as water pressure is significantly higher for large flow velocities (Figure 6.11), and thus it might be expected that more pores would be open to the invading phase. However, in the capillary dominated regime, water can explore more of the network in comparison to the viscous fingering regime, where the invading phase is directed upwards by the high viscous forces and, thus, leaves more oil left behind. In addition, Figure 6.11 shows that the pressure across the network drops significantly after breakthrough. This usually signals the end of invasion: in most cases, water flow is maintained solely through the main spanning cluster and no further recovery is achieved.

[Note that under certain conditions, a phenomenon called "finger thickening" might occur after breakthrough, during which the spanning water fingers swell and thicken resulting in better recovery. See Regaieg et al., 2013 [107] for more details.]

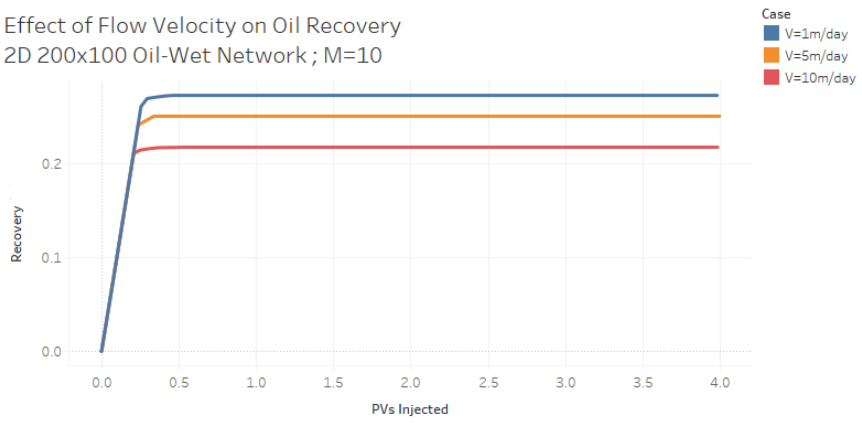

Figure 6.10: Effect of flow velocity on oil recovery.

The observations described above are only valid for the specific deployed viscous ratio (M=10). For values of M less than 1, increasing the flow rate is likely to switch the regime to a configuration that yields *better* recovery. The Lenormand experiments (1988) [97] showed that under such conditions, the capillary dominated growth is replaced by a steady frontal advance of the invading phase. In most

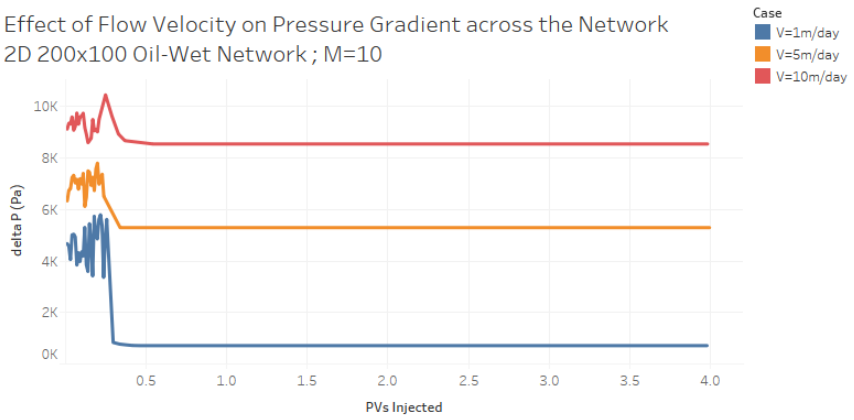

Figure 6.11: Effect of flow velocity on pressure gradient across the network.

reservoir scenarios, however, the unstable scenario is more likely to be the case, as oil is normally more viscous than the injected phase (whether it is gas or water). It is still possible, nonetheless, to invoke a perturbation to the capillary number to switch the regime to a favourable configuration. This can be targeted by affecting the fluid viscosities, the wettability of the reservoir or the underlying interfacial tensions. This will be explored later in this thesis.

6.3.2 Effect of Viscous ratio

The effect of viscous ratio M is investigated next. We consider four simulations where oil has different viscosities: 0.1cP (M=0.1), 1cP (M=1), 10cP (M=10) and 100cP (M=100). Water is injected with a constant flow velocity (5m/day), and all other fluid parameters are kept unchanged.

Figure 6.12 clearly shows a shift from a capillary dominated regime to a viscous fingering regime as the viscous ratio increases from 0.1 to 100. Here, the balance between the viscous forces of each phase plays an important role in determining the way in which water invades the capillary elements. When water viscosity is greater than or close to that of oil, capillary forces dominate the invasion pattern and water displaces oil from the elements with the lowest entry capillary pressure (i.e. the ones with the largest radii). Fluctuations in the pressure drop across the network for M=(0.1, 1, 10) are shown in Figure 6.13. The pressure gradient across the network is directly linked to the radii of the capillary elements which are being filled. As oil viscosity increases, the global pressure drop must be increased to maintain the injection rate, and so, the entry capillary pressures of the oil-filled pores become insignificant compared to the strong viscous forces, which limit the number of paths available to water. Consequently, the latter is directed through thin fingers towards the top of the network regardless of the entry capillary pressure of the adjacent

pores. The pressure gradient across the system decreases rapidly during the flood in this case (as a less viscous phase is filling the system), and stabilises following breakthrough.

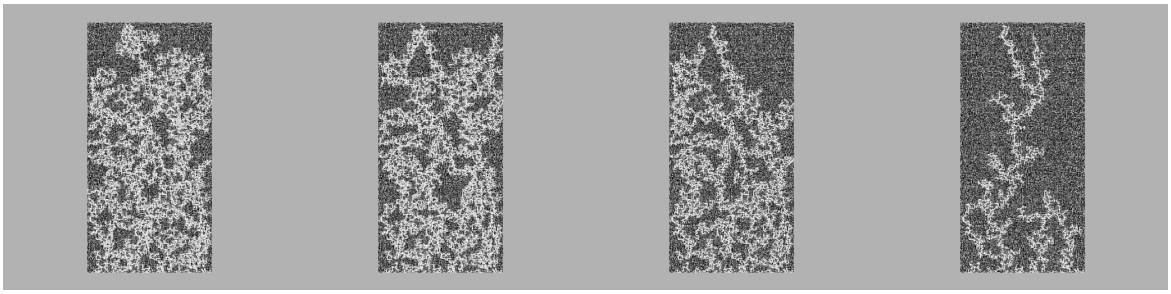

Figure 6.12: Effect of viscous ratio M on final water distribution. From left to right: M=0.1; M=1; M=10, M=100.

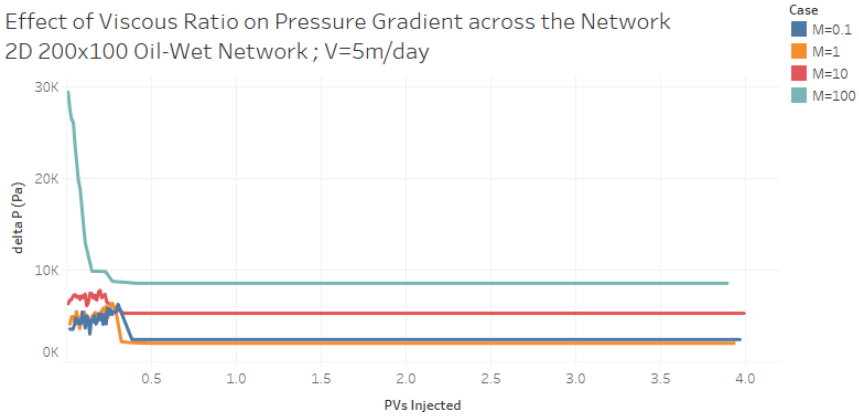

Figure 6.13: Effect of viscous ratio M on pressure gradient across the network.

Figure 6.14 shows that more oil is displaced for low values of the viscous ratio M. 35% of OOIP has been displaced for M=0.1 compared to a mere 11% for M=0.01. This significant difference is also explained by the capacity of water to reach more parts of the network when it is less directed by viscous forces. Some Enhanced Oil Recovery techniques attempt to make use of these mechanisms by inducing a viscosity change to improve oil recovery. Polymer injection aims, for instance, to increase water viscosity, shifting water invasion to a more stable flooding pattern. In contrast, thermal methods target decreasing oil viscosity (by injecting hot steam into the reservoir for example), and thus decreasing viscous instabilities by shifting the system towards a more stable regime.

6.3.3 Effect of Contact Angle

Now we examine the effect of contact angle θ on oil recovery. Although we keep the same wettabilty of the network (oil-wet), we consider four cases where all the capillary elements are assigned the same contact angle from the following list: 140°,

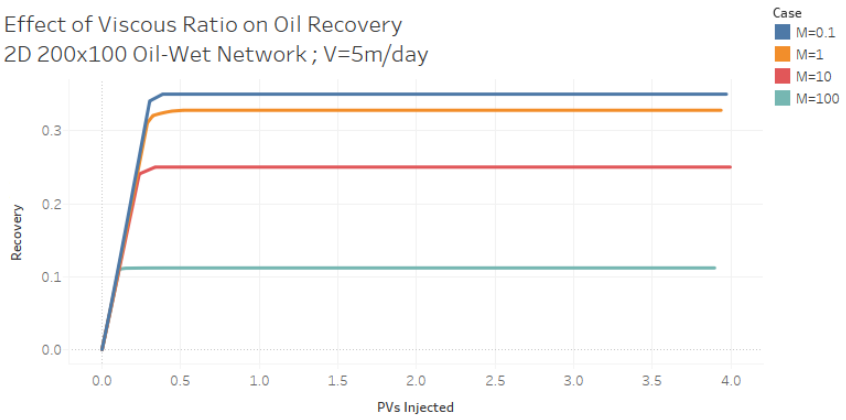

Figure 6.14: Effect of viscous ratio M on oil recovery.

110°, 100°, 95° and 91°. Flow velocity, viscous ratio and interfacial tensions are assigned the default values described in Table 6.1.

Figure 6.15 shows different phase distributions for each case. One noticeable observation is the fact that both the fingering regime and the degree of finger instability varies as the contact angle is decreased. This is due to the decrease of capillary entry pressure ($\frac{2\sigma cos\theta}{r}$) and pore-scale heterogeneity, which affect the fingering pattern and shift it towards a more fingered regime, where water flow is mostly directed along the pressure gradient. This can be also seen from the pressure history corresponding to each case (Figure 6.16). The fluctuations of the pressure drop before water breakthrough tend to disappear as the contact angle drops and capillary forces become progressively insignificant compared to the viscous effects.

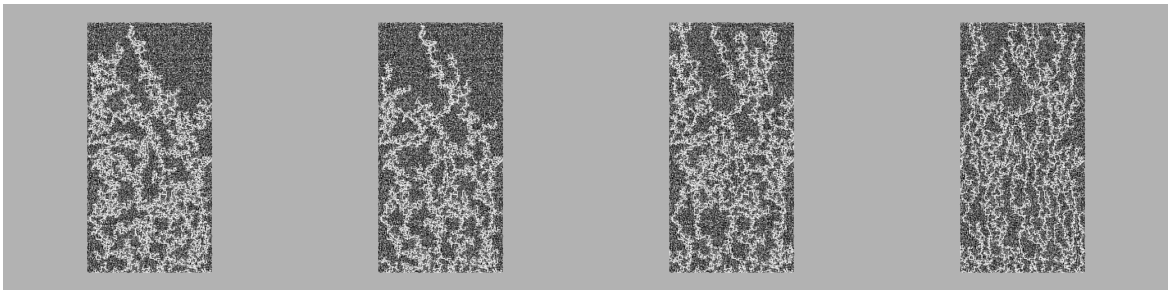

Figure 6.15: Effect of contact angle θ on final water distribution. From left to right: θ=140; θ=100, θ=95, θ=91.

The impact of this shift on oil recovery exhibits interesting behaviour (Figure 6.17 and 6.18). In fact, the final oil recovery is seen to be a non-linear function of the contact angle. As the contact angle decreases from 140°to 100°, the final water saturation drops from 25% to 22%. However, as the contact angle drops further towards 91%, the final oil recovery increases again to reach 25%. This non linearity can be explained by the effect of viscous forces on trapping. Firstly, a decrease in contact angle causes the fingers to narrow, and this should have a negative impact on final recovery. However, as the contact angle approaches 90°, the water fingers

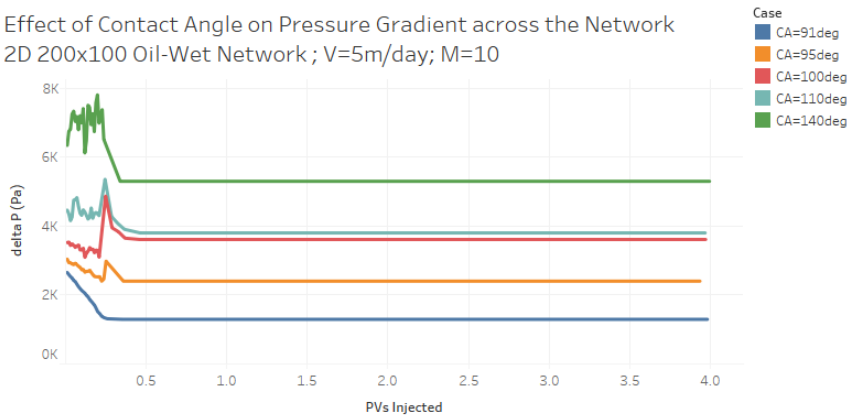

Figure 6.16: Effect of contact angle on pressure gradient across the network.

become thinner and acts more like a tracer, where heterogeneity in pore size becomes more influential. This decreases the number of trapped oil clusters left behind as the structure of the water phase minimises the emergence of large trapped oil clusters. The thin fingers permeate a greater extent of the network, and thus higher recovery is achieved.

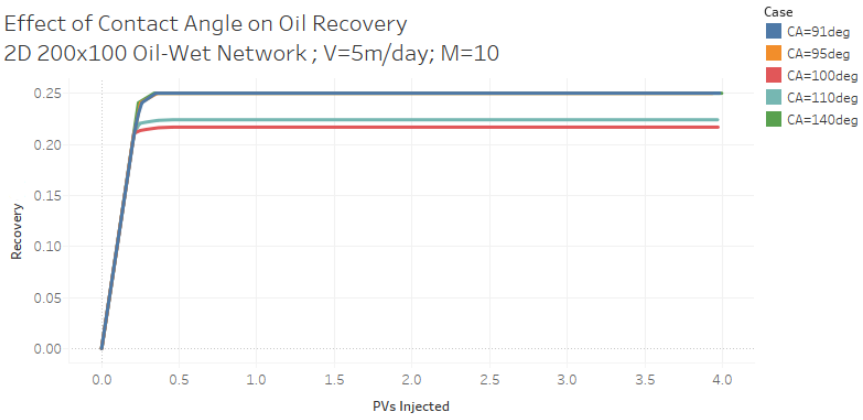

Figure 6.17: Effect of contact angle on oil recovery.

These observations give new insights into the application of enhanced recovery methods that target the reduction of oil-water contact angles in the reservoir (i.e. low salinity injection). These simulations show that the effects of such methods are not always beneficial and depend largely on additional important factors, such as the induced contact angle *variation*, the flow velocity and the viscous ratio. This will be discussed further in Chapter 8.

6.3.4 Effect of Interfacial Tension

The effect of interfacial tension (IFT) on dynamic displacement of oil by water is finally examined. We simulate six scenarios where the following values of interfacial tension are considered: $1 dyn/cm$, $5 dyn/cm$, $10 dyn/cm$, $20 dyn/cm$, $30 dyn/cm$ and

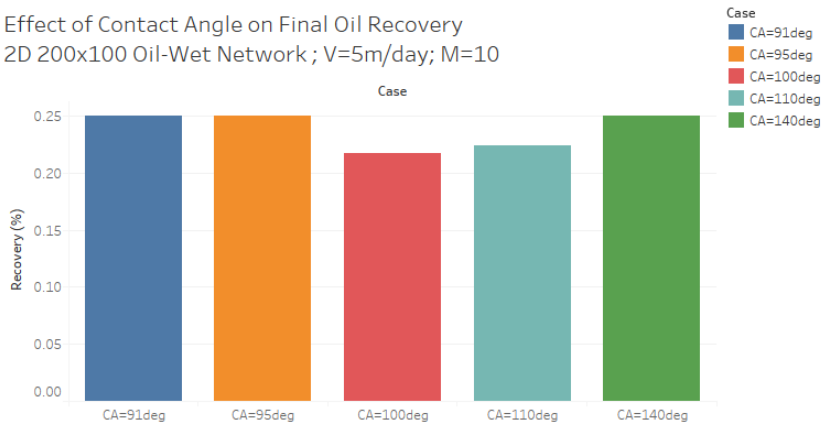

Figure 6.18: Effect of contact angle on final oil recovery.

$50 dyn/cm$. Default parameters from Table 6.1 are again used to set the flow velocity and the viscous ratio.

Figure 6.19 shows that patterns emerge that are similar to those observed in the sensitivity study of contact angle. The shift from a capillary dominated regime to viscous fingering when the interfacial tension decreases is clearly visible. This is an expected result, as the capillary entry pressure is proportional to the interfacial tension, and thus, decreasing the latter makes the viscous forces more dominant.

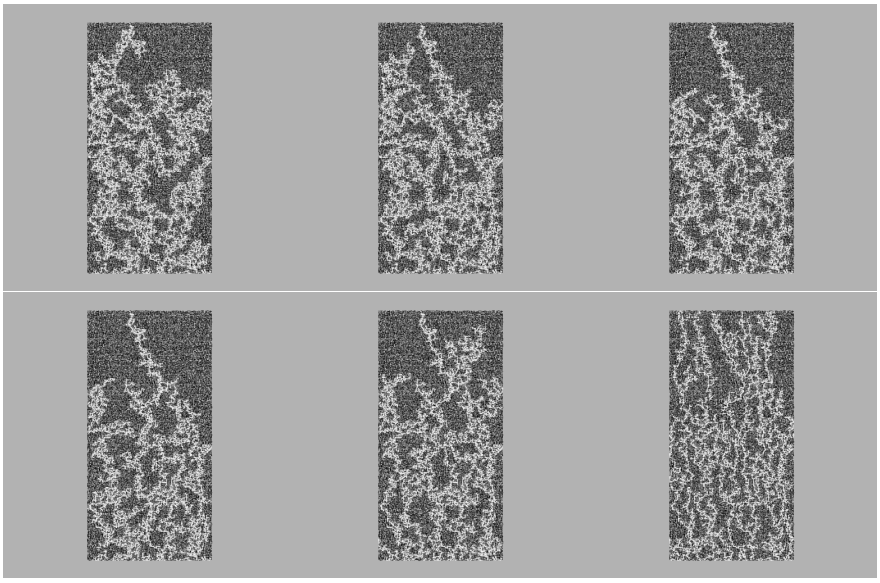

Figure 6.19: Effect of interfacial tension (IFT) on final water distribution. From left to right, and from top to bottom (unit: dyn/cm): IFT=50, IFT=30, IFT=20, IFT=10, IFT=5 IFT=1.

The oil recoveries also exhibit the same non-linearity observed in the previous section (Figure 6.20 and 6.21). Recovery is high (26%) when the regime is capillary-dominated (IFT=50dyn/cm). As the interfacial tension decreases, the fingers become thinner, the final recovery declines and eventually reaches 20 % for IFT=10dyn/cm. When the interfacial tension decreases further, the viscous forces become com-

pletely dominant (Figure 6.22 shows that capillary forces become insignificant for IFT=1dyn/cm), and thin vertical fingers fill the network resulting in high oil recovery (25% for IFT=1dyn/cm).

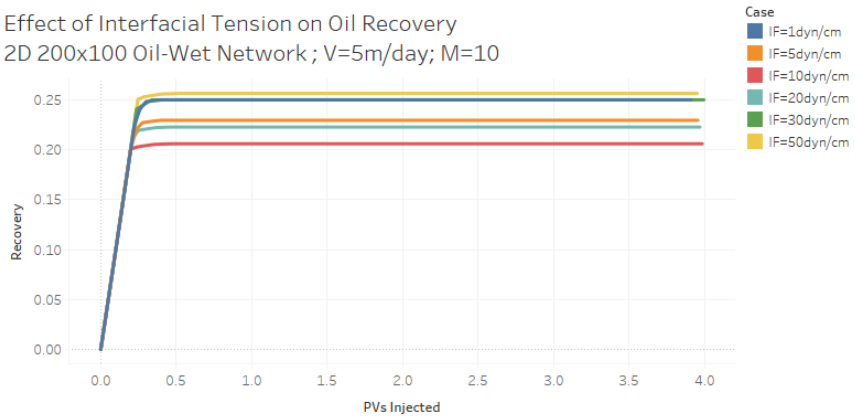

Figure 6.20: Effect of interfacial tension on oil recovery.

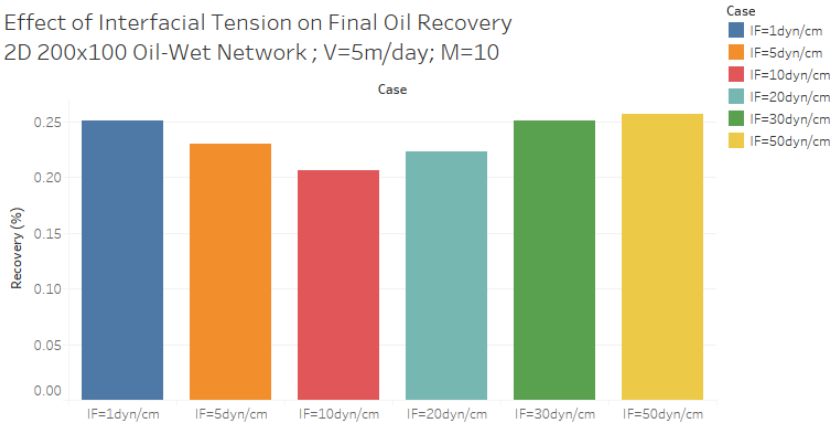

Figure 6.21: Effect of interfacial tension on final oil recovery.

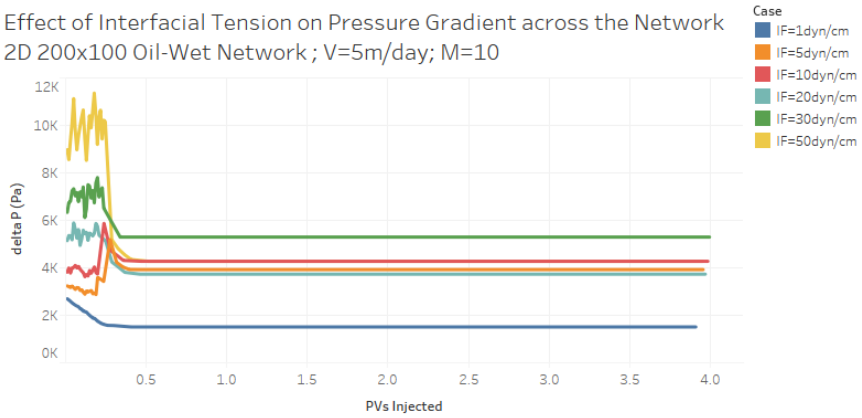

Figure 6.22: Effect of interfacial tension on pressure gradient across the network.

These observations again suggest that interfacial tension modification (i.e. when surfactant injection is deployed as an enhanced oil recovery method) might lead to contradictory conclusions, as the recovery outcome can be greatly affected not only

by the extent of induced IFT variation, but also by other key factors related to the flow protocol and the fluid configuration in the reservoir.

6.4 Conclusions

A fully dynamic pore-scale model has been described in this chapter. The model has been developed to simulate flow in porous media where viscous forces are not negligible. This has been achieved by adopting a dynamic solving of the pressure field in the underlying networks and updating the phase saturations accordingly. The capillary forces have been included in the pressure solution for pores hosting a meniscus and a consistent pressure field has been obtained. The model has proved to be capable of capturing a wide variety of flow regimes that depend on the capillary number and the viscous ratio. The experiments of Lenormand (1988) have been reproduced without using any data matching techniques.

The model has been applied to investigate the sensitivity of unsteady-state displacement of oil by water to key flow parameters. Results have shown that flow velocity and fluid viscosities play crucial roles in determining the invasion regime and the final oil recovery. Changing parameters such as contact angle and interfacial tension has also proved to be an effective strategy to switch the flow regime towards more favourable conditions, although final recovery curves exhibited a non-linear behaviour. This highlights the complexity of unsteady-state flow, which can be simultaneously affected by numerous factors (i.e. flow, fluid and rock properties) and makes the prediction of recovery outcomes challenging without investigating the underlying pore-scale mechanisms. Thus, the module implemented in this work represents a useful tool to examine the sensitivity of a specific parameter combination on oil recovery and helps to explain apparent inconsistencies that can emerge from core-scale experiments.

The current model is relatively fast for large 2D networks. Unsteady-state flow can be simulated on a 200x100 network within a few days. It is possible however to increase further the model efficiency by adopting more sophisticated linear solvers when computing the pressure field. A hybrid approach based on the work of Regaieg and Moncorge (2016) [108] will be considered in the future to solve the pressure only in regions of the system where viscous effects are predominant.

Several features can also be implemented in future work to improve the predictive potential of the model. For instance, counter-current imbibition flow is ignored at present although it could physically occur. Film flow has been also modelled in a simplistic way (only single pores separating water clusters can flow via films) and

dynamic tracking of the flow fraction through films may be an important mechanism to implement.

Ganglia mobilisation has not been considered in this model and this could have an impact on additional recovery and flow regime in rare cases where viscous forces are high enough to start displacing trapped hydrocarbon clusters. The ganglia mechanisms were not implemented in the unsteady state drainage model as they can significantly impact its computational speed. A fast drainage model that makes use of large networks, such as that developed here, has great potential to reproduce realistic flow regimes, and is unlikely to be affected by the randomness of the statistical generated networks (which can have a great effect is small networks). We chose to implement the ganglia mobilisation physics in a separate dynamic model, where algorithmic speed is not the main priority. This will be discussed in the next chapter.

The fast unsteady state drainage model will be used later to study various EOR processes. These will be discussed in Chapter 8, where low salinity water injection, polymer injection, and the synergies between the two will be examined.

Chapter 7

numSCAL Ganglion Migration Module

7.1 Introduction

The unsteady state drainage model described in Chapter 6 has clearly shown that viscous forces can have a significant effect on growth pattern. However, the model was unable to capture some important phenomena associated with strong viscous forces. For instance, simulation of water injection into water-wet networks would always result in some trapped oil being left behind and mobilisation of these trapped clusters is not possible using that approach, no matter how high the viscous forces involved (note that the unsteady-state drainage model uses a clustering algorithm to locate and freeze the trapped oil pores during water injection simulation).

Although the *numSCAL* depletion module *was* able to consider the movement of isolated phase structures, the approach used was limited to capillary-dominated displacements and could not capture the important phenomenon of fluid re-mobilisation due to viscous forces. Similarly, whilst the *numSCAL* three-phase module was capable of simulating multi-displacement chains and mobilising trapped clusters, the model worked under steady-state conditions, and viscous forces were not considered. Under certain conditions, it may be possible for viscous forces to overcome the capillary forces responsible for keeping isolated clusters trapped, and fluid mobilisation could eventually occur.

We present in this chapter a novel unsteady state model that has been implemented for examining multiphase ganglion transport in porous media. The inclusion of ganglia mobilisation mechanisms adds significant complexity to the code and specific routines to handle the related pore-scale physics have been developed and are dis-

cussed in detail. We conclude the chapter by showing simulation results that involve the displacement of trapped ganglia under various unsteady-state flow conditions.

7.2 Model Description

7.2.1 Background and Challenges

Simulating unsteady state flow in pore network models is not a new research field and several attempts have been undertaken previously to model flow behaviour in cases where viscous forces are no longer negligible in comparison to capillary forces. Although these studies have used different approaches to represent the pore space or to define expressions for the forces implicated during flow, most have used the same technique to update the network state during the simulation. This technique consists of measuring the minimum filling time that guarantees the complete filling of a single non-trapped pore by the invading phase. The minimum filling time, which also serves as the current time step Δt, is defined as:

$$\Delta t = Min_{i \in \mathcal{F}} t_i = Min_{i \in \mathcal{F}} \frac{V_i}{Q_i} \times (1 - f_i) \tag{7.1}$$

where $\mathcal{F}$ is the set of pores i with a meniscus, V_i is the pore volume of pore i, and f_i is the fraction of pore i that is already filled with the invading phase. Once the minimum filling time over all the capillary elements has been determined, the meniscus position in every pore containing both fluids is updated according to:

$$f_i^{new} = f_i^{old} + \frac{\Delta t}{t_i}(1 - f_i^{old}) \tag{7.2}$$

While models using this technique (including the *numSCAL* unsteady-state drainage model) are capable of generating convincing simulations of unsteady state flow (viscous fingering, steady displacement, capillary displacement), they are unable to simulate more complex phenomena, such as ganglion movement, counter-current flow, or the *simultaneous* injection of two phases. This is due to the fact that the technique assumes that, once a capillary element is filled with the invading phase, it cannot be refilled again with the defending phase for the rest of the simulation. This is not true when considering ganglion mobilisation, however, as a single element could be invaded by different phases on several different occasions during the flood and so the methodology breaks down.

An alternative approach is to treat ganglion movement as a separate mode of displacement (see Dias and Payatakes, 1986[64]). A clustering algorithm can be used to locate all ganglia of the same phase and a set of rules applied to individual ganglia to predict their movement. While such an approach can generate simulations that mimic the movement of trapped ganglia, it requires heavy computational effort and cannot be considered fully dynamic, as the movement is mostly controlled by a set of rules rather than counter-current imbibition flows – a crucial aspect of ganglion mobilisation.

Therefore, a new approach should be considered that allows ganglion movement to be part of a more general, holistic unsteady state formulation. The simplest idea is to adapt the previous unsteady state drainage model to allow the positions of menisci to vary according to flow direction (even if this means that the invading phase differs from that being injected at the inlet) and without considering explicit trapping rules.

To this end, let us consider the situation of a single-pore ganglion as shown in Figure 7.1 (the configuration could be considered as a part of a large network). For the sake of simplicity, we will consider here the capillary elements as simple connected bonds and we will be interested in modelling the mobilisation of oil in pore 2 surrounded by water in pore 1 and pore 3. Although we can assume any wettability distribution at this stage, we will assume for ease of explanation that the pores are all water-wet and that the oil is a non-wetting fluid.

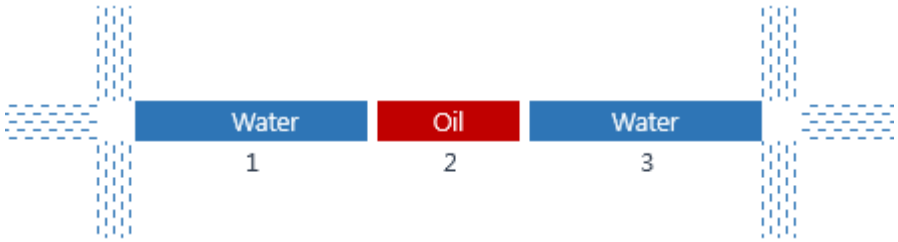

Figure 7.1: Three connected pores. Pore 1 and 3 are filled with water. Pore 2 is filled with oil.

If we compute the pressure solution for the network without the inclusion of capillary pressure terms, the flow direction in every pore can be determined. Figure 7.2 shows the updated state of the three capillary elements for two possible displacement outcomes (we assume that water is coming from the upstream pore in both cases).

In both cases, the oil is displaced into the neighbouring downstream pore and, while this is expected for high rate flow where capillary forces are relatively small, this should not occur if the viscous pressure gradient across the neighbouring pore is lower than its associated capillary entry pressure. However, because the elementary flows across the three elements are all non-zero once the pressure field has been

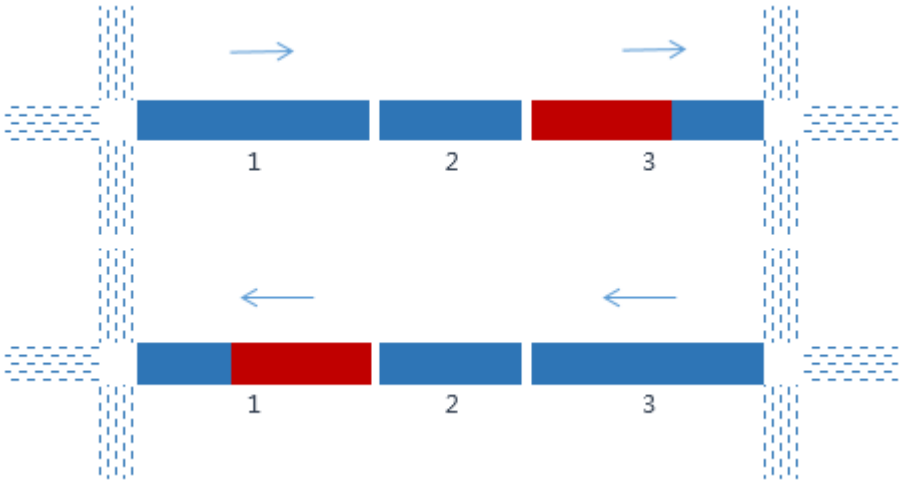

Figure 7.2: Phase distribution after updating the meniscus position for both possible flow directions.

solved, then one of the two cases depicted in Figure 7.2 must occur, and so the trapping of oil due to capillary forces cannot emerge naturally.

Now, capillary pressure terms have been ignored in this argument, so what would happen if these *were* included in the pressure equations? Including P_C terms *a priori* in the solver would lead to additional challenges (e.g. which P_C terms are used – those of the neighbouring pores about to be invaded or that of the host pore). However, even assuming this issue is resolved, we would again end up with a situation where the elementary flows will be non-zero and so one of the scenarios depicted by Figure 7.2 would again result and no natural trapping could emerge.

Therefore, the challenge for a general model for unsteady state flow is to enable ganglion movement when viscous forces are higher than capillary forces, whilst also making it possible for a ganglion to be trapped if capillary forces dominate – this is a non-trivial issue.

7.2.2 A New Approach to Model Ganglion Mobilisation

The model developed in this work aims to solve the aforementioned problem by adopting a new approach, where trapping due to capillary forces can emerge naturally as a consequence of the evolution of the pressure field inside the network. To illustrate this idea, consider again the initial configuration shown in Figure 7.1 and assume that the pressure solution has resulted in the flow direction being from pore 1 to pore 3. We do not include capillary pressure terms in the solver *at this stage* and simply allow a small fraction of the oil to be convected into pore 3. As time passes, and the pressure field is updated to account for intra-pore changes in phase viscosity due to the partial filling, oil continues to fill this pore. Only when

the fraction of oil in pore 3 exceeds a certain (very small) critical value (f_c) do we then include the capillary pressure term associated with a water-oil meniscus in pore 3 in the flow equation (Figure 7.3). *In effect, we are allowing the oil to assess its local environment and using this information to decide how the displacement should proceed.*

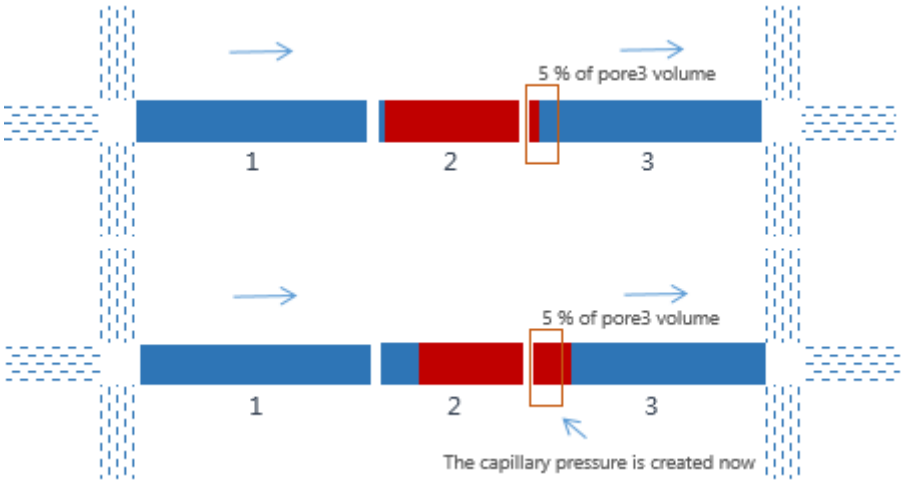

Figure 7.3: Phase distribution after displacing a small fraction of oil. Capillary pressure is created after oil fraction in pore 3 exceeds $f_c = 5\%$.

Now, two possibilities exist for the oil ganglion after we re-solve the pressure field with capillary pressure terms included:

Case1: The capillary pressure is not sufficiently high to stop the advance of the oil. In this case, the flow direction will be maintained and oil will continue to flow into pore 3 (Figure 7.4).

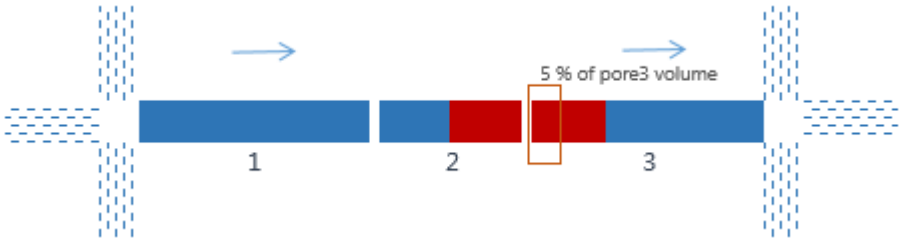

Figure 7.4: Phase distribution after the capillary pressure was created. The flow keeps the same direction and oil keeps filling pore 3.

Case2: The capillary pressure is high enough to stop the advance of oil. The flow direction will change after solving the pressure field in the network and oil will retreat back towards pore 2 (Figure 7.5). If the oil fraction ever falls below f_c, the capillary pressure is removed when solving the pressure field and the flow may change direction once again in the next time step. The outcome is that the oil volume in pore 3 will be unable to exceed f_c and water will be unable to completely re-invade pore 2. Consequently, oil will remain trapped predominantly inside pore

2 due to the perpetual reversal of flow direction from one time step to the next. We refer to this behaviour as "natural trapping", as water trapping is not defined by any set of topological rules but emerges naturally a consequence of the change in flow direction after solving the pressure field at each iteration. Moreover, this approach does not require any counter-current pores to be artificially closed to avoid numerical problems (as has been done in other studies)

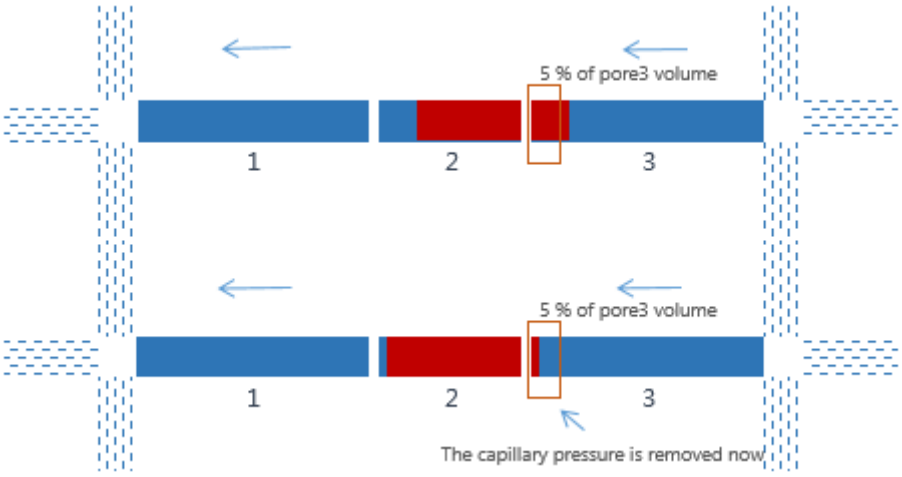

Figure 7.5: Phase distribution after the capillary pressure was created. The flow changes its direction and oil retreats back to pore 2.

Implication 1: Choice of time step

The choice of value for the small sensing fraction of fluid (f_c) has a large impact on the speed and the stability of the model: a large value would result in an unstable model and unrealistic behaviour, whilst a very small value (though guaranteeing smooth and realistic behaviour) would make the simulation prohibitively slow. After carrying out a number of sensitivity simulations, it was found that a value of f_c within the range $0.01 \leq f_c \leq 0.05$ gave an acceptable compromise between speed and precision. We refer to the fraction f_c as the "critical test fraction".

In order to ensure that, during each iteration, only a fraction f_c of fluid is moved (evaluated over the entire network), the choice of time step that we use in the simulation is re-defined:

$$\Delta t = Min_{i \in \mathcal{F}} \frac{V_i}{Q_i} \times f_{ci} \tag{7.3}$$

Note that $Min_{i \in \mathcal{F}} \frac{V_i}{Q_i}$ corresponds to the minimum time (calculated over the entire set of pores with an oil-water interface) required to fill a pore in the network. Multiplying this value by the critical test fraction gives the minimum time required to

fill a fraction f_c of this pore – this is the limiting control on timestep.

Implication 2: Inclusion of the capillary pressure in the solver

As mentioned earlier, the capillary pressure term is included in the elemental flow equation only when the fraction of each phase exceeds f_c – this is an important condition to ensure that trapping emerges naturally as a consequence of changes in flow direction.

Implication 3: Counter-current flow and simultaneous multiphase injection

Our new formulation provides the additional benefit that counter-current flow no longer needs to be treated as a special case (often handled by temporarily closing such pores to flow before iterating a consistent pressure solution – an approximation used in previous models that can lead to computational issues). Here, counter-current flow simply emerges depending upon local viscous pressure gradients and capillary pressures. In addition, we can easily extend our approach to consider the simultaneous injection of multiple phases at the network inlet, something that could prove highly beneficial when investigating certain relative permeability protocols.

7.2.3 Outflows and Inflows in Capillary Elements

When updating the network state, it is important to know the flow of each fluid coming in and out of each capillary element. It is also vital to build a formulation that describes the network status after each time step. In previous works on unsteady state models, when two phases coexist in the same capillary element, it is assumed that a single meniscus separates the two phases, and its frontal advance is monitored by updating its positionf_i^{new} as follows:

$$f_i^{new} = f_i^{old} + \frac{\Delta t}{t_i}(1 - f_i^{old}) \tag{7.4}$$

The approach we implement in this work no longer monitors the meniscus position in a capillary element – the simultaneous flow of two fluids inside a realistic pore geometry is considered too complex to be usefully modelled as a single meniscus advancing smoothly along the walls of an irregular capillary element (as highlighted by recent experimental works (see Rücker et al., 2015 [155]; Berg et al., 2015 [22];

Youssef et al., 2014 [156])). This is particularly true when isolated ganglia become mobilised. Thus, our model tracks the fraction of each fluid in each capillary element without focusing on modelling the explicit shape of the meniscus (or menisci) and we derive an appropriate expression for the corresponding capillary pressure(s). However, for our generalised pore-throat network, we do need to identify the phases situated at the entrance and exit of each throat – we will refer to these as "terminal flags" (Figure 7.6).

Figure 7.6: Terminal flags identify the phases situated at the entrance and exit of each throat.

The fraction of each phase within a capillary, together with its corresponding terminal flags, gives us sufficient information to decide whether or not a capillary pressure term should be included for that particular element. For a single throat, a capillary pressure term is included when: (1) its terminal flags are not the same, and (2) the fractions of the two fluids in it are both greater than the critical test fraction (f_c). Once a capillary pressure needs to be created, we use equation 4.9 in the corresponding flow equation.

To determine the phase leaving a throat via bulk flow, the model only needs to consider the terminal flag associated with its downstream end. In addition, if the downstream flag does not correspond to the wetting phase for a neighbouring downstream element, then the model will also allocate a fraction of the wetting phase as part of the total outflow. To illustrate this, consider the configuration in Figure 7.7. The pore is filled with water (with a fraction equal to f_w) and oil (with a fraction equal to f_o). The upstream terminal flag is oil, whilst the downstream terminal flag is water. As the flow direction is from right to left, the *bulk* phase that would be leaving the pore should be water.

Figure 7.7: A throat filled with oil and water. Water would be the main phase leaving the throat as the downstream terminal flag (where the flow arrow points to) is water.

Now, if water is the wetting phase, and the flow within the throat is given by q, then the flow of each fluid is given by:

$$\begin{cases} Water_{OutFlow} = q \\ Oil_{OutFlow} = 0 \end{cases} \tag{7.5}$$

However, if water is not the wetting phase, oil will also be allowed to leave the throat via films, and the phase outflows are consequently given by:

$$\begin{cases} Water_{OutFlow} = (1 - f_{film}) \times q \\ Oil_{OutFlow} = f_{film} \times q \end{cases} \tag{7.6}$$

The calculation of film fraction f_{film}will be described later.

7.2.4 Nodal flows

The previous section has described the way in which fluids are transported within throat elements. More generally, if we assign volume to both pores and throats, then we need to consider flow within nodal elements too. After calculating the flow of each phase leaving each throat in the network, these can be used to update the volume of each phase entering and leaving each node. The flow entering each node can be calculated by summing the outflows from all upstream throats. If we consider Figure 7.8 for instance, water and oil inflows at node n are given by:

$$\begin{cases} Water_{InFlow} = q_2 \\ Oil_{InFlow} = 0 \end{cases} \tag{7.7}$$

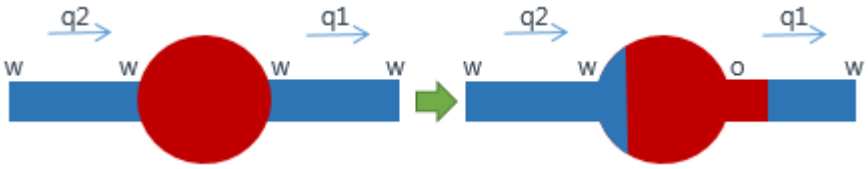

Figure 7.8: Phase distribution in a node connected to two throats, before and after updating the network state

To determine the phase leaving a node that contains both phases, we make the following simplifying assumption: if more than 50% of the total inflow is water, the outflow will be oil, and vice versa. The idea behind this assumption is that it is essentially impossible to take into account all the possible meniscus scenarios that could occur when two phases enter a complex 3D pore. Instead of trying to capture the complex mechanisms underlying such a situation, we assume that the dominant phase entering the node pushes the other phase out.

If we consider again the case described in Figure 7.8, water and oil outflows from the node would be calculated as:

$$\begin{cases} Water_{OutFlow} = 0 \\ Oil_{OutFlow} = q1 \end{cases} \tag{7.8}$$

Once the phase leaving a node has been determined (oil in the previous example), the corresponding terminal flag is assigned to the upstream end of pore 1.

If water is the wetting phase in the node, then the flow of each fluid is given by:

$$\begin{cases} Water_{OutFlow} = f_{film} \times q1 \\ Oil_{OutFlow} = (1 - f_{film}) \times q1 \end{cases} \tag{7.9}$$

7.2.5 Modelling Film Flow

We have stated previously that if the main phase flowing out of an element is the non-wetting phase, then we will also allow some volume of the wetting phase to leave that element (via film flow) as part of its total outflow. We now describe how that fraction of wetting phase is calculated.

Consider again the simple configuration shown in Figure 7.7 and we will assume that the pore and its downstream neighbour are oil-wet. We reason that the fraction of oil flowing out of the pore through films is a function of the local balance between viscous and capillary forces – when the flow is viscous dominated, the main outflow mechanism over a timestep would be through bulk convection of water and film flow of oil could be expected to be negligible. Conversely, when the flow is capillary dominated, a greater proportion of the outflow should correspond to film-flow of the wetting phase. To model such behaviour, we follow the approach of Li (2016) by introducing a control variable γ that reflects the approximate balance between capillary and viscous forces, calculated as follows:

$$\gamma = \frac{|\Delta P|}{|P_C| + |\Delta P|} \tag{7.10}$$

where ΔP is the pressure gradient across the element. The fraction of flow leaving the element via wetting films is then calculated using:

$$\begin{cases} f_{film} = (1-\gamma) \times f_{film}^{max} \\ f_{film}^{max} = 1 - 4\pi G \end{cases} \tag{7.11}$$

where G is the shape factor of the element. f_{film}^{max} refers to the maximum fraction of fluid that could leave the pore via films. We represent it as a function of the elemental geometry (which could be entirely general) that corresponds to the fraction of the pore cross section occupied by the wetting phase when the non-wetting phase fills the entire inscribed cylinder of the element (films would collapse beyond this point if capillary pressure were to decrease further).

7.2.6 Ganglion Flow

In situations where the wetting phase occupies both ends of a throat that still contains an amount of intra-pore non-wetting phase, we do not automatically assume that this non-wetting phase is trapped. At any subsequent stage of the simulation, an updated pressure field may result in this discrete ganglion becoming mobile and so we include such a possibility in our model. This allows us to track ganglion mobilisation (and possible production) throughout a flood.

In order to track the movement of a trapped ganglion inside a throat using our new flexible approach, all that is required is some straightforward book-keeping. We simply note the moment at which a phase becomes isolated within a throat (i.e. when neither the upstream terminal flag nor the downstream terminal flag matches the flag of the intrapore phase). Then, we simply replace the downstream terminal flag by the isolated phase flag once 50% of the non-ganglion volume has left the element (Figure 7.9). It is possible to track the quantity of the isolated non-wetting phase inside the pore and predict the moment when it reaches its downstream end. Note, that we found that taking an average estimate of half of a pore volume to determine the effect of intra-pore ganglia does not have a significant impact on the simulation and, most importantly, can save a great amount of computational time.

Figure 7.9: Modelling Ganglion flow.

7.2.7 Updating the Phase Fractions in Nodes and Throats

At each iteration, once the fractional flow of each phase has been calculated for each element, we apply mass conservation at nodes to update the new fluid fractions in both pores and throats. Let us consider Figure 7.10.

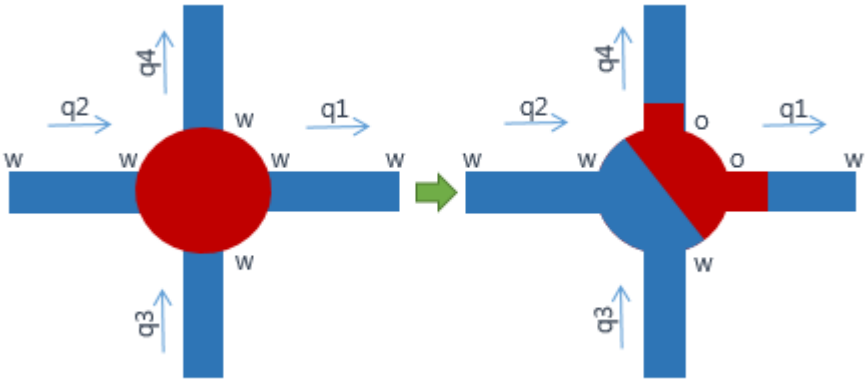

Figure 7.10: Phase distribution in a node connected to four throats before and after updating the network state.

Updating phase fractions in nodes

The updated oil fraction in a node (fn, o_{new}) is calculated as follows (the new water fraction is computed analogously):

$$\begin{cases} fn, o_{new} = fn, o_{old} + (Oil(n)_{InFlow} - Oil(n)_{OutFlow}) \times \frac{\Delta t}{Vn} \\ Oil(n)_{InFlow} = Oil(throat2)_{OutFraction} \times q_2 + Oil(throat3)_{OutFraction} \times q_3 \\ Oil(n)_{OutFlow} = Oil(n)_{OutFraction} \times (q_1 + q_4) \end{cases} \tag{7.12}$$

where V_n is the node volume, and $Oil(i)_{OutFraction}$ is the fraction of oil leaving element i and is calculated based on the terminal flags and film fractions as described previously.

Updating phase fractions in throats

Based on mass conservation, we use the following expression to compute the new oil fraction in throat 1 $(f1, o_{new})$ (the updated water fraction is computed analogously and the updated phase fractions in throat 4 are calculated in a similar fashion):

$$\begin{cases} f1, o_{new} = f1, o_{old} + (Oil(throat1)_{InFlow} - Oil(throat1)_{OutFlow}) \times \frac{\Delta t}{V_{th}} \\ Oil(throat1)_{InFlow} = Oil(n)_{OutFraction} \times q_1 \\ Oil(throat1)_{OutFlow} = Oil(throat1)_{OutFraction} \times q_1 \end{cases} \tag{7.13}$$

Note that the fact we use mass conservation to compute elementary flows implies that$fi, o_{new} + fi, w_{new}$ always sum to one. Also both fi, o_{new} and fi, w_{new} remain in the range [0-1] and adopting this formulation to update the network state guarantees a stable evolution throughout the entire simulation.

7.2.8 Computing the Pressure Field Across the Network

The pressure field is computed through the entire network on each occasion that the critical test fraction f_c has been exceeded in one throat. Capillary pressures are included in the mass conservation equation at every node and the resulting linear system is solved in the same fashion described in Chapter 6, Section 6.2.3. Similarly, the pressure gradient set across the network is also coupled to a fixed predefined flow rate using the Secant method (see Chapter 6, Section 6.2.4)

7.2.9 Simulation Procedure

Figure 7.11 illustrates the different components of the augmented unsteady state model (capable of simulating ganglion migration) developed in this work.

1. A target flow is fixed at the beginning of the simulation and we use the Secant method at each stage of the displacement to compute the pressure field required to maintain this value throughout the flood.

2. We determine an appropriate time step that optimises both the speed and stability of the model by allowing only a small fraction of fluid to move at each stage of the simulation. This approach allows phase trapping to emerge without recourse to time-consuming clustering algorithms and/or tree searches.

3. We next determine the inflow and outflow of each phase for each capillary element (throats and pores), based upon the terminal flags allocated in the previous iteration. Film flow is also modelled based on the local balance between capillary and viscous forces and local wettability conditions.

4. Finally, we use mass conservation to update the fraction of each phase in the capillary elements and resolve the new terminal flags. Capillary pressures are updated and the pressure solver is computed again for the next iteration.

Finally, we note that this approach is easily adapted for any network model architecture – we have already adapted it for use in regular bond networks, regular and irregular pore-throat networks, and off-lattice rock-derived networks.

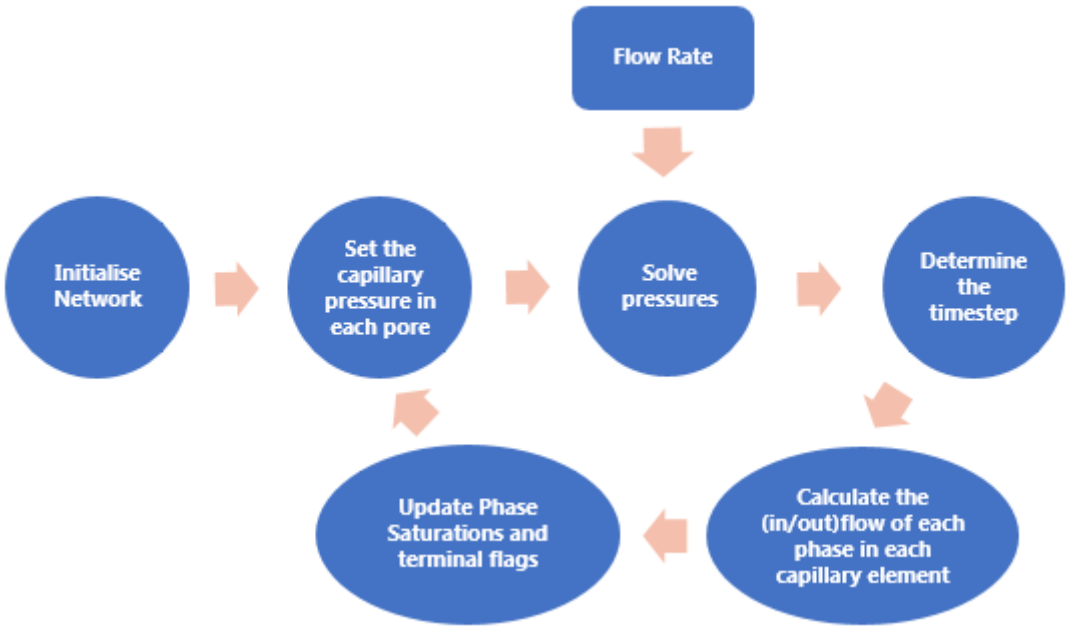

Figure 7.11: numSCAL Ganglia Model Workflow.

7.2.10 Model Validation

We again use the Lenormand experiments to check whether the same flow regimes emerge when applying the *numSCAL* ganglia module to simulate drainage experiments. Although no ganglia mobilisation was observed experimentally, the model is expected to reproduce the same behaviour as before, as ganglia mobilisation has been implemented in a way that allows it to occur as a natural consequence of the balance between capillary and viscous forces.

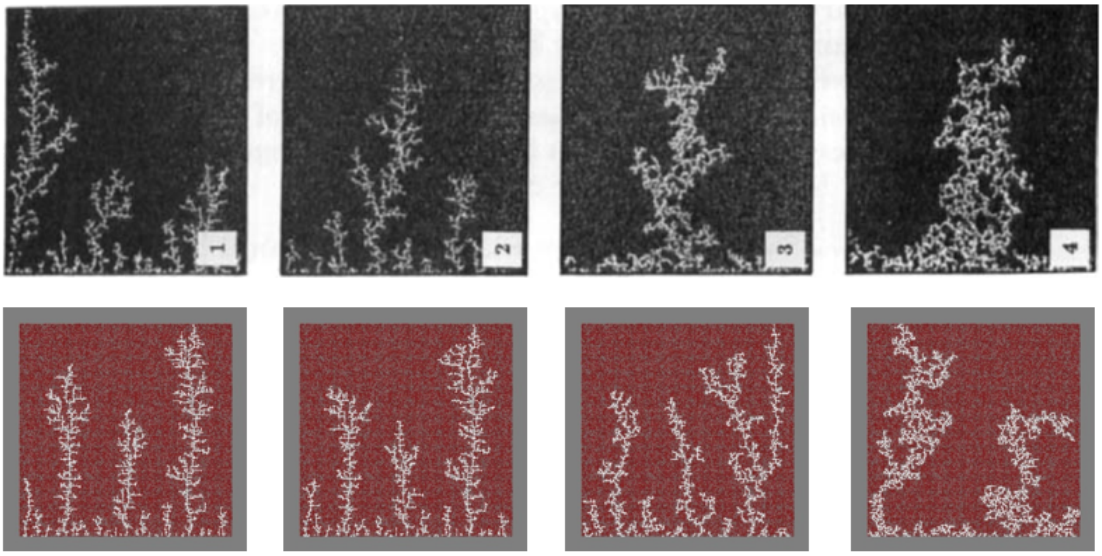

Figure 7.12: Lenormand experiments (Lenormand, 1988 [97]) vs numSCAL Ganglia model simulations (from viscous fingering to capillary fingering).

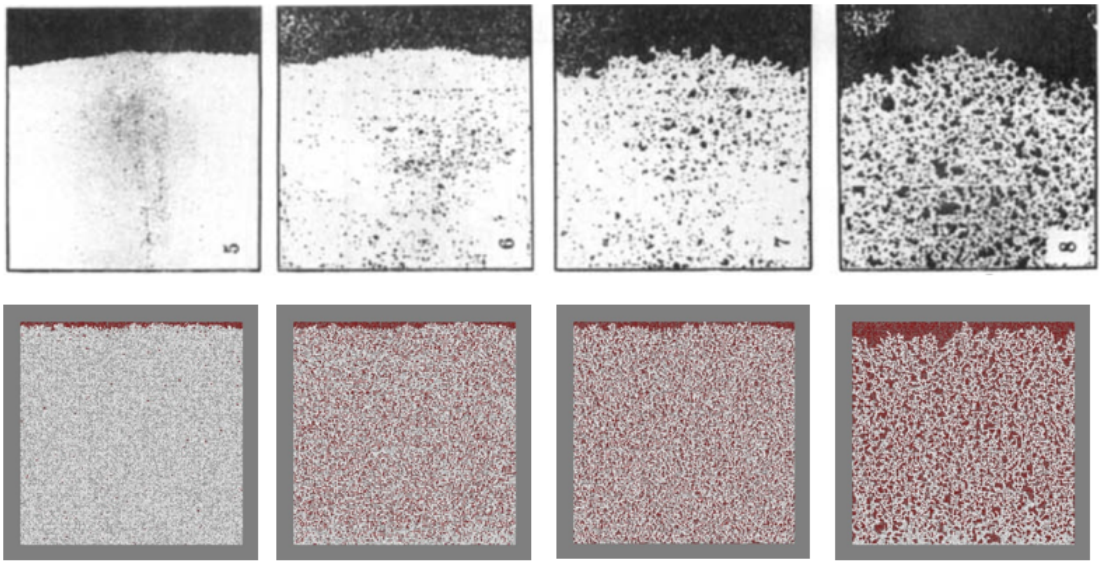

Figure 7.13: Lenormand experiments (Lenormand, 1988 [97]) vs numSCAL ganglia model simulations (from a frontal advance regime to a slightly less stable regime).

Simulation results (Figure 7.12 and 7.13) show that the final phase distributions are *exactly* the same as those obtained using the *numSCAL* unsteady-state drainage module. Our model is also capable of simulating flooding experiments on extracted networks from MicroCT images and we again obtain realistic flow regimes. Figure 7.14 shows a viscous fingering regime in a 3D sandstone analogue, Berea analogue and a synthetic silica system for high capillary numbers and low viscosity ratios.

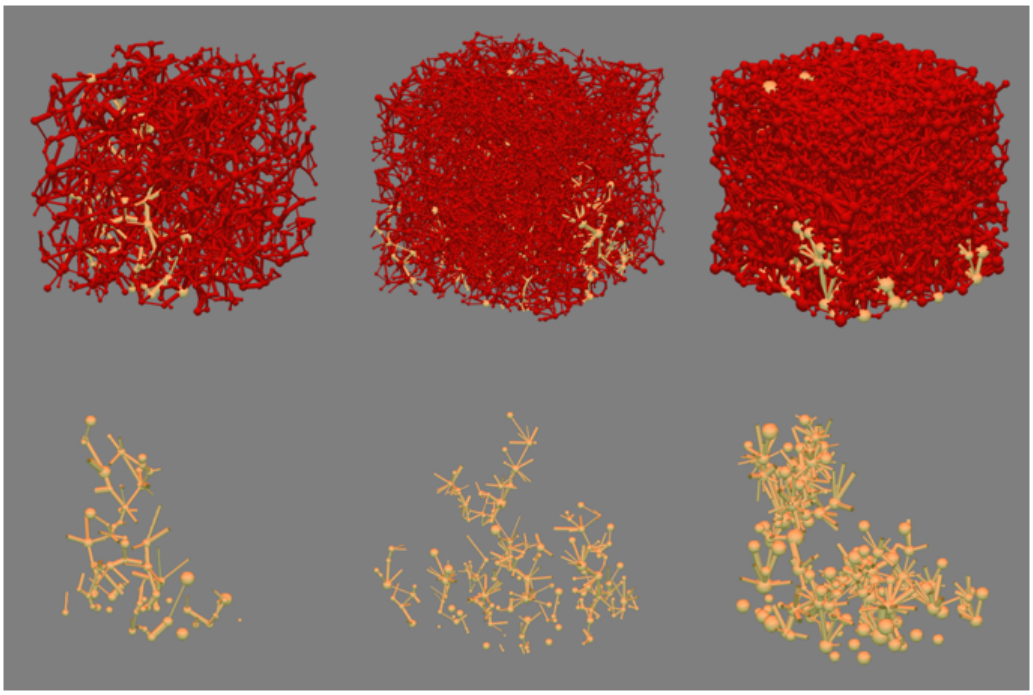

Figure 7.14: Simulation of high rate gas injection into oil networks using numSCAL ganglia model (from left to right: sandstone S1, Berea and Silica)

This agreement between both models gives us confidence in the capabilities of the model to correctly capture the balance between capillary and viscous forces. The model is deployed to study the onset of ganglia mobilisation under various unsteady-state conditions in the next section.

7.3 Application: The Onset of Ganglion Mobilisation under Unsteady-state Conditions

After water flooding or gas injection, numerous oil clusters remain trapped in the reservoir and these ganglia can yield significant additional recovery if successfully mobilised towards the production wells. Thus, it is of critical importance to determine the flow conditions that can trigger the onset of mobilisation, and to understand the impact of the key factors targeted by enhanced oil recovery (EOR) processes. In this section, we use the *numSCAL* ganglion module to examine scenarios where oil ganglia are initially trapped. As a preliminary study, we consider a simple scenario where the onset of a single ganglion mobilisation is investigated under different capillary numbers. Later, we apply the model to examine the effect of flow rate, viscous ratio, contact angle and interfacial tension on oil recovery during drainage. For the different scenarios, mobilisation of the trapped cluster(s) is expected to depend on the balance between the capillary and viscous forces. Unlike the unsteady-state

drainage model, which is unable to detect the onset of mobilisation, the *numSCAL* ganglion module allows us to determine when this phenomenon occurs.

7.3.1 Mobilisation of a Single Ganglion

We begin the sensitivity analysis by investigating the effect of flow rate on the mobilisation of a single ganglion. Here, we build a 40x20 water-wet network filled initially with water (contact angles are equal to 40°). The network shares the same properties as the generic 2D networks described in Chapter 3, Section 3.4.1. We also create an area (7x4 pores) in the middle of the network where capillaries are assigned large radii equal to $50\mu m$ (Figure 7.15) and are filled with oil. When the simulation starts, water is injected into the network from the inlet pores (the network bottom). Note that for this configuration, capillary forces are expected to resist the escape of oil through the small capillaries.

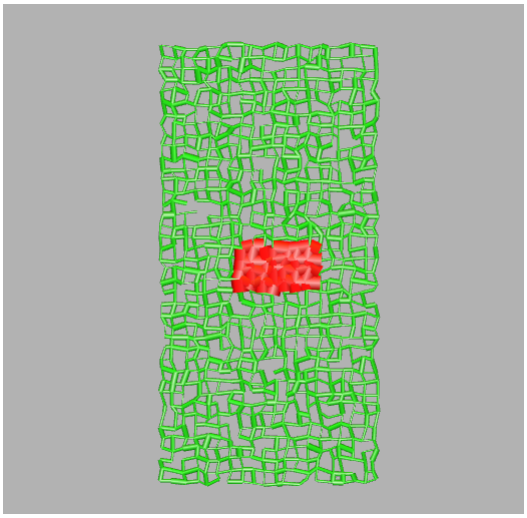

Figure 7.15: A custom network configuration: 40x20 2D water-wet network; the pores in the middle are assigned 50um radii and filled initially with oil. Oil: red; Water: green.

We start injecting water at a flow rate equal to $1.10^{-12}m^3s^{-1}$ (equivalent to a capillary number $Ca = 5.10^{-6}$, where $Ca = \frac{\mu V}{\sigma cos\theta}$; V: Darcy's velocity, μ: viscosity of the invading phase, σ: interfacial tension, θ: oil-water contact angle) for 4 pore volumes. Figure 7.16 shows the ganglion state after 1, 2, 3 and 4 pore volumes injected. At this flow rate, water flow completely bypasses the trapped oil which remains at its initial position due to strong capillary forces preventing it from entering the smaller pores. This behaviour is maintained as we keep gradually increasing the flow rate towards higher values up to $5.10^{-11}m^3s^{-1}$ ($Ca = 2.5.10^{-4}$).

When the the water is injected at a flow rate equal to $6.10^{-11}m^3s^{-1}$ ($Ca = 3.10^{-4}$),

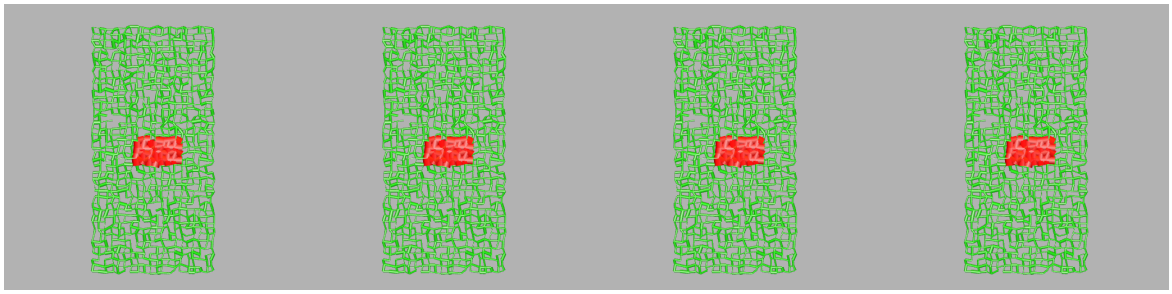

Figure 7.16: Phase distribution at different injection steps for any flow rate inferior to 6.10^{-11} ($Ca = 3.10^{-4}$). Pore volumes injected From left to right: 1, 2, 3 and 4. Oil: red; Water: green.

an interesting observation can be seen. Oil slowly starts to move upwards invading preferentially the largest pores above the central areal whilst water penetrates the oil cluster from beneath. The ganglion quickly becomes stable again once the viscous forces become insufficient to trigger more mobilisation and the oil-water configuration remains static until the end of water injection as shown by Figure 7.17.

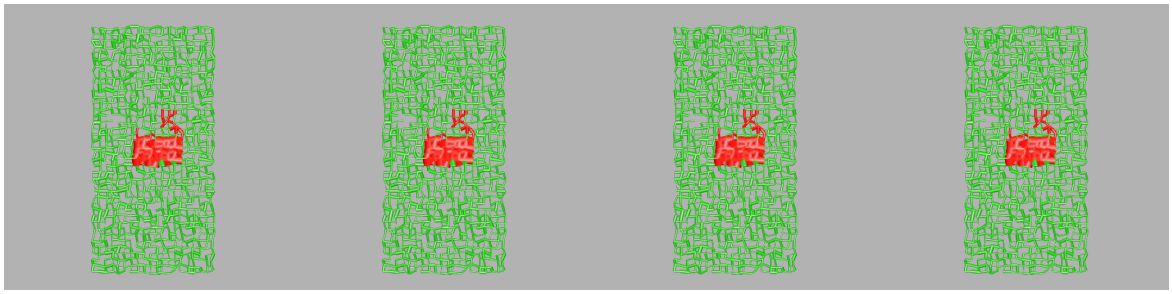

Figure 7.17: Phase distribution at different injection steps for a flow rate equal to 6.10^{-11} ($Ca = 3.10^{-4}$). Pore volumes injected From left to right: 1, 2, 3 and 4. Oil: red; Water: green.

Figure 7.18 shows phase distribution at different states of the injection process as we further increase the water flow rate. A flow rate value of $7.10^{-11} m^3 s^{-1}$ ($Ca = 3.5.10^{-4}$) allows significant mobilisation of the central oil ganglion, which migrates in a capillary dominated fashion through a single finger towards the outlet. The mobilisation is, however, only partial and a significant amount of the oil remains trapped at the end of the simulation.

When oil production stops, the main oil finger has become fragmented into small oil clusters due to counter imbibition flow and the final configuration shows numerous small dispersed oil-filled pores.

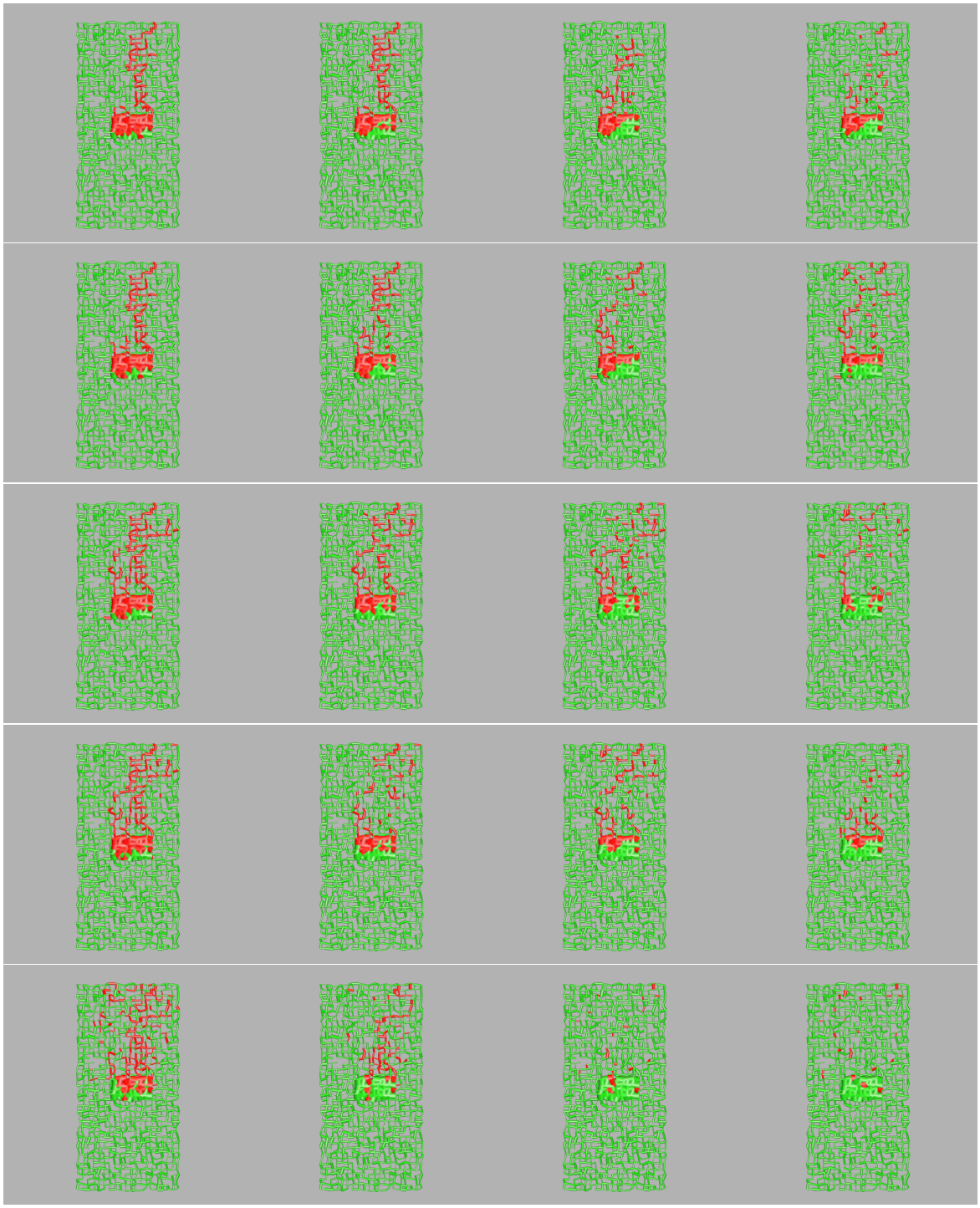

Figure 7.18: Phase distribution at different injection steps for different flow rates; from top to bottom (m^3/s): 7.10^{-11} ($Ca = 3.5.10^{-4}$), 8.10^{-11} ($Ca = 4.10^{-4}$), 9.10^{-11} ($Ca = 4.5.10^{-4}$), 1.10^{-10} ($Ca = 5.10^{-4}$), 5.10^{-10} ($Ca = 2.5.10^{-3}$). Pore volumes injected From left to right: 1, 2, 3 and 4. Water-wet network. Oil: red; Water: green.

As the flow rate increases, two main observations can be seen. First, the oil saturation decreases considerably, and less oil remains trapped at the end of the simulations. This can be confirmed by Figure 7.19 which shows the evolution of water saturation as a function of the flow rate. More than 90% of the network is oc-

cupied by water at the end of simulation for a flow rate equal to $5.10^{-10}m^3s^{-1}$ ($Ca = 2.5.10^{-3}$), compared to only 70% for $8.10^{-11}m^3s^{-1}$ ($Ca = 4.10^{-4}$). Moreover, the manner of upward oil migration is affected by the deployed flow rate. As the latter increases, a noticeable shift can be seen from a biased capillary migration (Figure 7.18, columns 1 and 2) to a dispersed multidirectional mobilisation (Figure 7.18, columns 4 and 5). In fact, as the viscous forces increase, capillarity has less of an effect, and oil has no longer preferential paths to follow; thus it migrates in all directions resulting in the observed dispersion. At these conditions, significant counter imbibition flow is observed which yields the frequent phase fragmentation shown by Figure 7.20.

These observations demonstrate that a critical flow rate threshold needs to be reached before any trapped ganglia mobilisation can occur. Moreover, the flow rates values above this threshold affect both the migration pattern of the trapped ganglia and the fraction of the oil that can be left behind.

We now go on to discuss water injection in an *oil-wet* network.

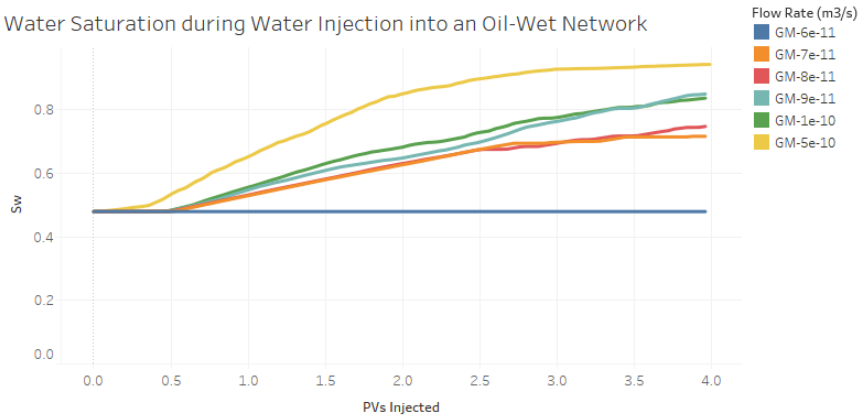

Figure 7.19: Water saturation during water injection for 6 flow rates.

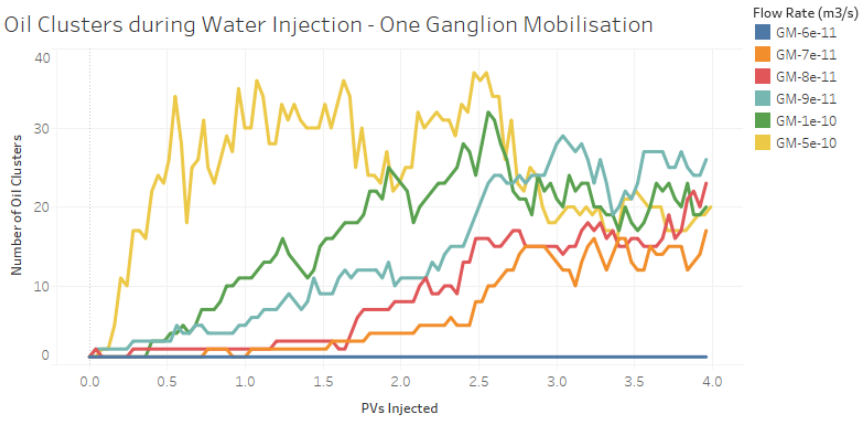

Figure 7.20: Oil clusters number after the injection of 4 pore volumes for 6 flow rates.

7.3.2 Effect of Flow Rate

Although a configuration similar to that described in the previous section may occur in waterflooded reservoirs, it is also possible that trapped oil clusters are surrounded by water fingers rather than a fully interconnected water phase (as usually seen at the end of stable water injection in pore networks). We therefore simulate a drainage process (where water displaces oil in an *oil-wet* network) using both *numSCAL* drainage and *numSCAL* ganglion module and we examine the effect of flow rate on the residual oil and ganglia mobilisation. We use the same 40x20 network described previously without creating the central large area. Oil initially occupies the entire network and oil-wet contact angles (140°) are assigned to the capillary elements.

Figure 7.21 shows the final phase distribution after 4 pore volume injection using both models. For medium flow rates ($1.10^{-12}m^3s^{-1}$ ($Ca = 5.10^{-6}$) and $1.10^{-11}m^3s^{-1}$ ($Ca = 5.10^{-5}$)), similar phase distributions can be seen using the two models. Under such conditions, water keeps flowing through the spanning finger after breakthrough in both cases and no ganglia mobilisation is observed afterwards. For higher flow rates (greater than $1.10^{-10}m^3s^{-1}$ ($Ca = 5.10^{-4}$)), however, the two models yield different results. Whilst additional fingers can be seen in the network using the classical drainage module, a significant amount of oil remains trapped. Conversely, the ganglion model – which is not constrained by trapping rules – allows the water to trigger oil mobilisation once viscous forces become important, yielding further water invasion. Saturation curves (Figure 7.22) show that around 60% of the original oil in place (OIIP) has been displaced for a flow rate value equal to $5.10^{-10}m^3s^{-1}$ ($Ca = 2.5.10^{-3}$) compared to 30% for $1.10^{-11}m^3s^{-1}$ ($Ca = 5.10^{-5}$).

These observations confirm the fact that mobilising trapped ganglia can yield significant additional recovery, although increasing the flow rate does not always guarantee the emergence of this phenomenon. In fact, the flow rates where the upward migration of trapped oil has been observed correspond to high values that may be difficult to achieve in the far-field region without applying means by which the associated capillary number can be increased; for the single ganglion mobilisation case, the onset of mobilisation occurred at a flow rate equal to $7.10^{-11}m^3s^{-1}$ ($Ca = 3.5.10^{-4}$) which corresponds to a frontal velocity of $700m/day$ ($1.10^{-12}m^3s^{-1}$= $10m/day$ in the constructed network). Such a value is unlikely to be reached at any point of the reservoir (except near the wellbore or near a fracture) and thus, increasing the flow rate in this case is not expected to mobilise the trapped ganglia (although additional recovery *can* be achieved through additional invasion of the non trapped oil). It should also be noted that this threshold is related to the rock geometry, as the capillary forces that hold the trapped ganglia are directly linked to the pore size distribution. Hence, for rocks with large capillary elements, increasing the flow rate

might prove to be more efficient at triggering ganglia mobilisation at early stages. Fluid properties – such as water viscosity, contact angles and interfacial tension – are also expected to affect the mobilisation threshold due to their direct impact on the capillary forces. These will be examined in the following sections using the *numSCAL* ganglion module.

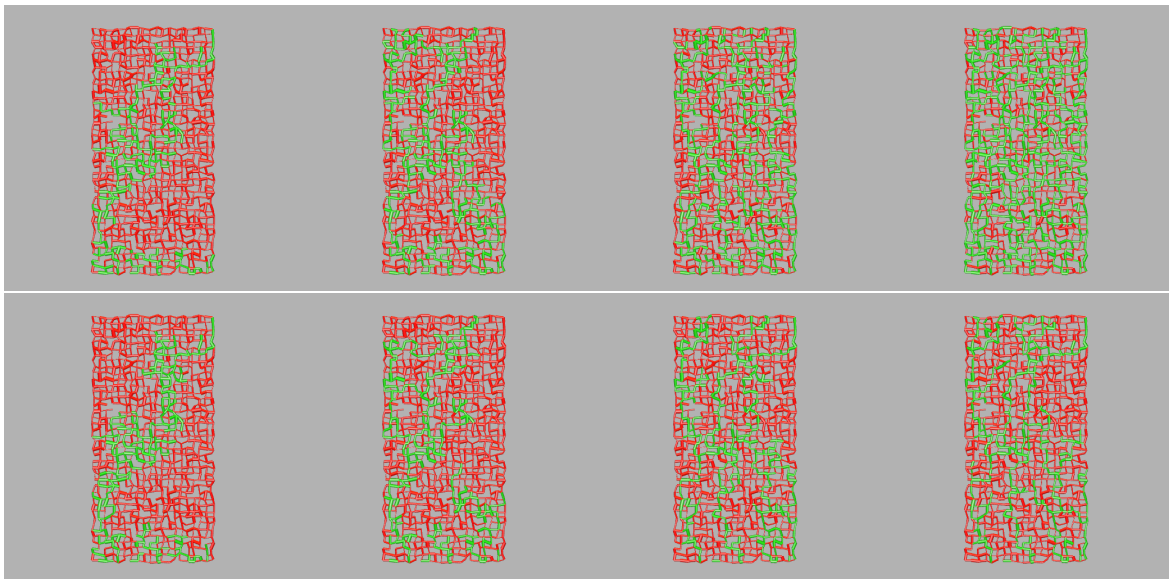

Figure 7.21: Phase distribution after 4 pore volume injection of water into an oil-wet network originally filled with oil for different flow rates; from left to right: $1.10^{-12}m^3s^{-1}$ ($Ca = 5.10^{-6}$), $1.10^{-11}m^3s^{-1}$ ($Ca = 5.10^{-5}$), $1.10^{-10}m^3s^{-1}$ ($Ca = 5.10^{-4}$), $5.10^{-10}m^3s^{-1}$ ($Ca = 2.5.10^{-3}$). The top row shows simulations obtained by the numSCAL ganglion module whilst the bottom one whilst the bottom one shows results generated by the numSCAL drainage module. Oil: red; Water: green.

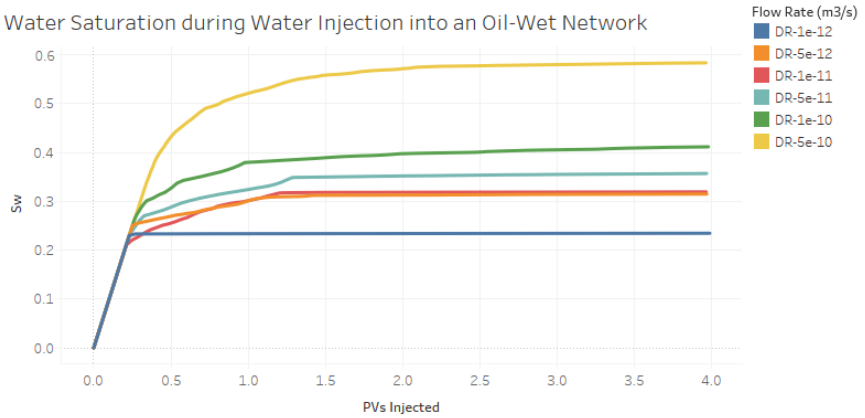

Figure 7.22: Water saturation during water injection for 6 flow rates (numSCAL ganglion module).

7.3.3 Effect of Viscous Ratio

The effect of viscous ratio on ganglia mobilisation is now investigated. We use again the configuration described in the previous section, and we inject water into the oil-wet network for 12 pore volumes using a flow rate equal to $1.10^{-12}m^3s^{-1}$ ($Ca = 5.10^{-6}$). To strengthen viscous forces, water viscosity is doubled after every 2 injected pore volumes according to the profile described by Figure 7.23 (whilst maintaining the injection rate).

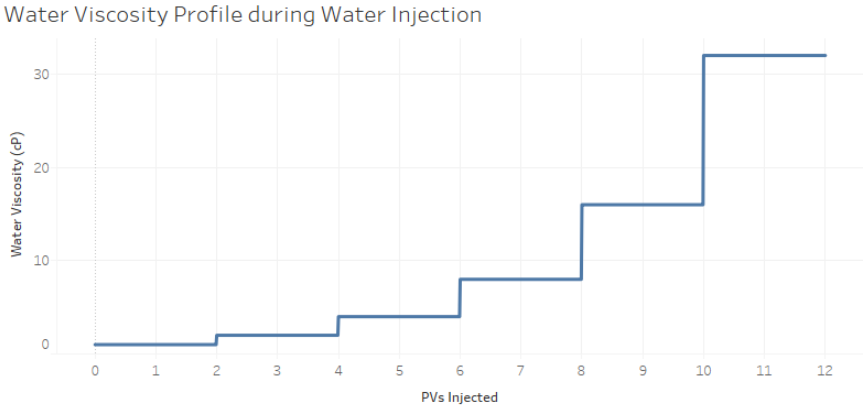

Figure 7.23: Water viscosity profile during 12 pore volume water injection; viscosity is doubled after every 2 pore volume injection.

Figure 7.24 shows the network state after every 2 injected pore volumes. It was found that the increase of water viscosity did not affect water saturation immediately. In fact, only after the injection of 6 pore volumes (and water viscosity increases from $4cP$ to $8cP$) was a noticeable increase in water saturation seen (Figure 7.25). In addition, the fraction of displaced oil is an increasing function of the water viscosity. For instance, only 5% of the OOIP has been displaced when water viscosity shifts from $4cP$ to $8cP$, compared to more than 10% for a water viscosity change from $16cP$ to $32cP$. The increase of water saturation is also accompanied by more oil fragmentation as illustrated by Figure 7.26. Although this can be an effect of the formation of new fingers (which results in more trapped oil clusters), the significant increase over the last two injected pore volumes is visibly due to the breakup of trapped ganglia and their partial mobilisation towards the outlet pores. Such behaviour is mainly explained by the increase of viscous forces in the network due to the change of water viscosity. This can be confirmed by Figure 7.27, where the average pressure gradient across the network increases as the injection proceeds.

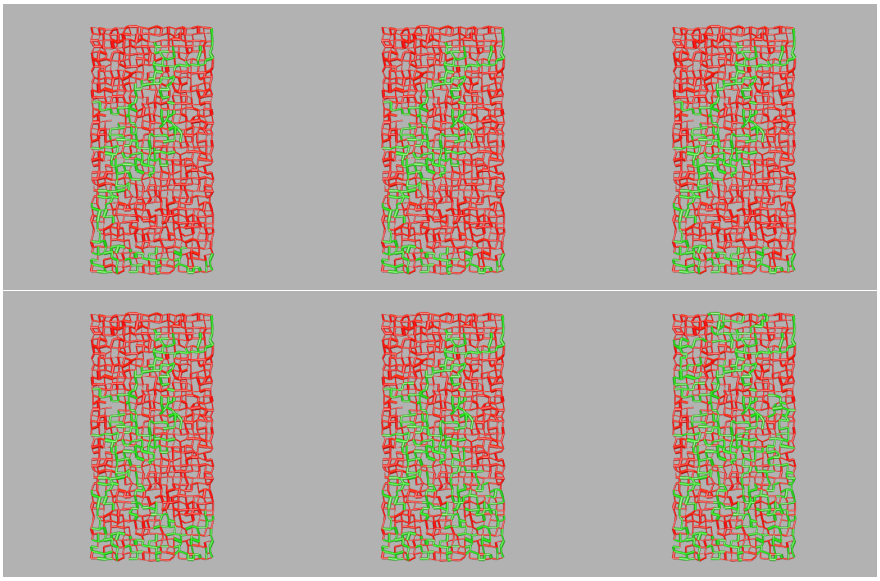

Figure 7.24: Six snapshots of phase distribution during water injection into an oil-wet network originally filled with oil. Water viscosity is doubled every two injected pore volumes. Injected pore volumes from left to right and from top to bottom: 2, 4, 6, 8, 10 and 12. Oil: red; Water: green.

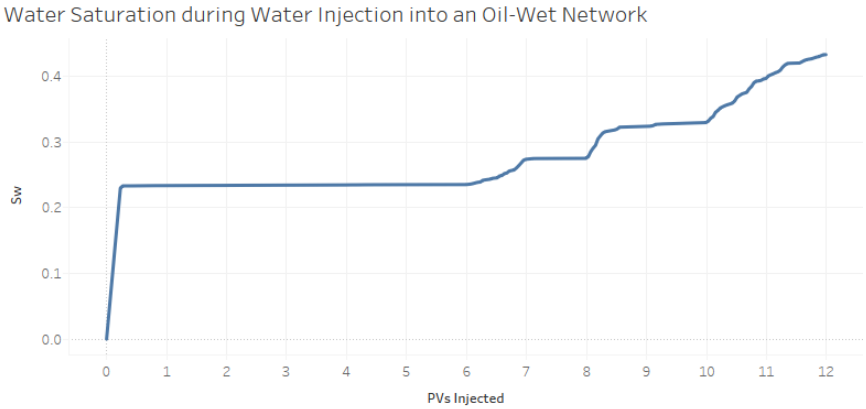

Figure 7.25: Effect of water viscosity change on water saturation during drainage in an oil-wet network.

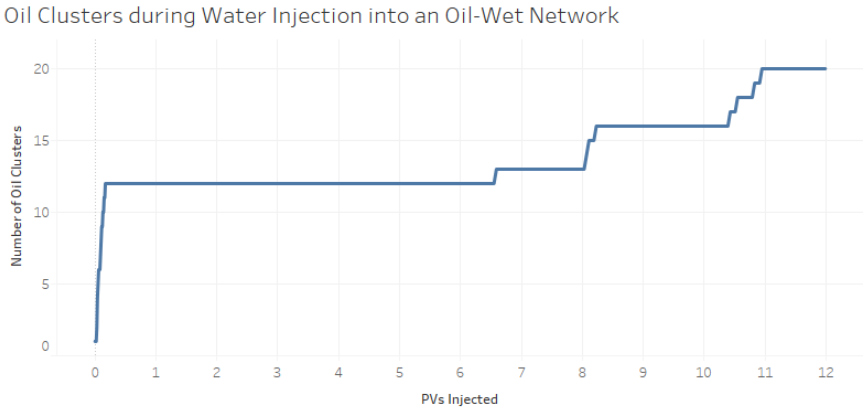

Figure 7.26: Effect of water viscosity change on oil cluster numbers during water injection into an oil-wet network.

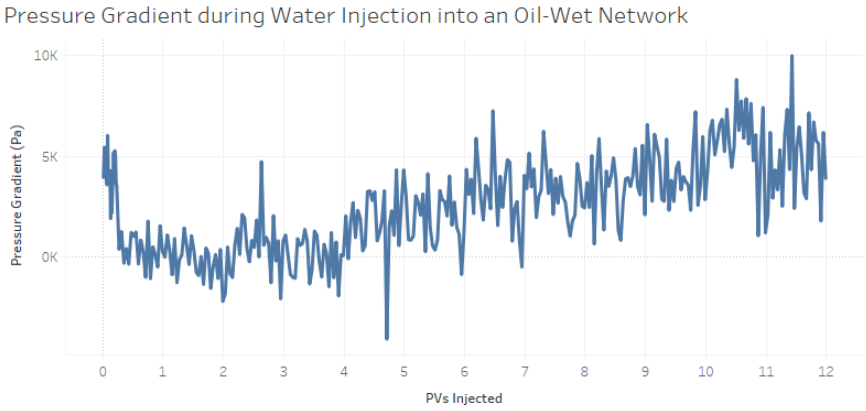

Figure 7.27: Effect of water viscosity change on pressure gradient across the network during water injection into an oil-wet network.

These simulations suggest that affecting the viscous ratio can yield additional recovery due to the fragmentation and displacement of trapped oil clusters. However, the onset of ganglia mobilisation might not occur until a critical viscous ratio change is first achieved. This is an important factor to consider when applying polymer processes to recover trapped oil clusters, as the induced water viscosity change might be insufficient to overcome the constraining capillary forces and trigger the desired mobilisation.

7.3.4 Effect of Contact Angle

We investigate now the effect of contact angle on ganglia mobilisation. We consider a similar process to that described in the previous section, where water is injected for 12 pore volumes using a flow rate equal to $1.10^{-12}m^3s^{-1}$ ($Ca = 5.10^{-6}$). Contact angle values are shifted from 140° towards 91° every 2 injected pore volumes according to the profile described by Figure 7.28.

Figure 7.29 shows the network state after every injection of 2 pore volumes. The decrease of contact angle does not affect the water injection pattern initially. At this rate, and for this PSD, an increase in water saturation can only be seen after the contact angle becomes equal to 95° (after the 6 pore volumes have been injected). This results in the emergence of a new finger in addition to the main spanning water finger. A further reduction of the contact angle to a value equal to 93° leads to the emergence of more fingers which yields additional recovery (more than 10% of the OOIP) as can be shown by Figure 7.30. Note that the new fingers appear to grow into initially-trapped oil clusters which suggests a partial mobilisation of oil ganglia. This can be confirmed by Figure 7.31 where the reduction of contact angle is accompanied by an increase in the number of oil clusters. As the contact angle

reaches 91°, an interesting behaviour is observed. Now, most of the oil is displaced as the last 2 pore volumes are injected and more than 95% of the network volume becomes occupied by water by the end of the simulation. This is explained by the removal of capillary pressures at this stage ($cos\theta \approx 0$) and oil ganglia become easily displaced by the water viscous forces. In fact, the fluctuation of pressure gradient across the network actually *decreases* significantly as the simulation progresses and eventually reaches a steady-state value when the capillary forces become negligible.

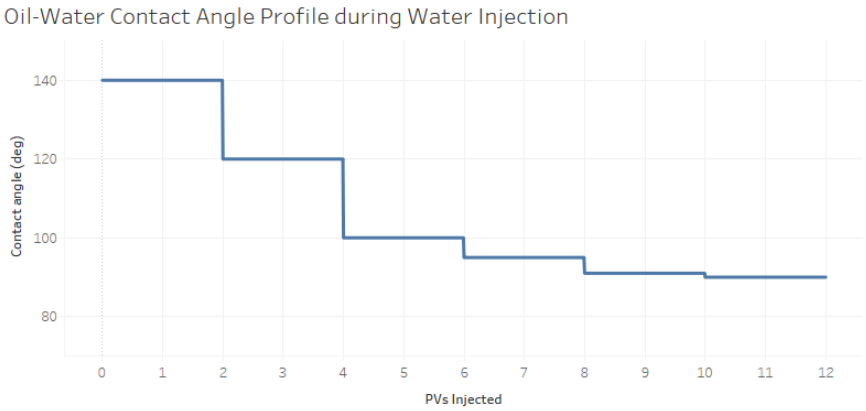

Figure 7.28: Oil-water contact angle profile during 12 pore volume water injection; Oil-water contact angle decreases every 2 pore volume injection: 140 → 120 → 100 → 95 → 93 → 91.

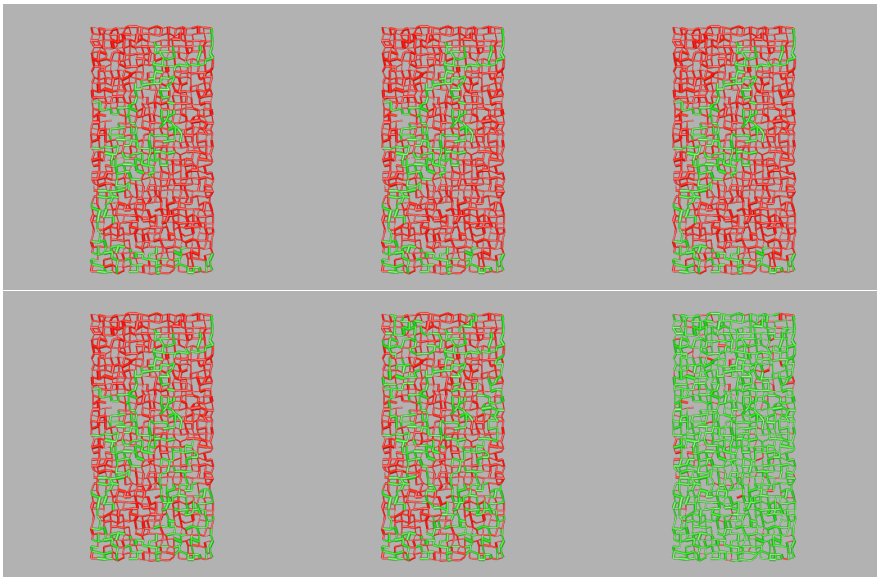

Figure 7.29: Six snapshots of phase distribution during water injection into an oil-wet network originally filled with oil. Oil-water Contact angle decreases every two injected pore volumes. Injected pore volumes from left to right and from top to bottom: 2, 4, 6, 8, 10 and 12. Oil: red; Water: green.

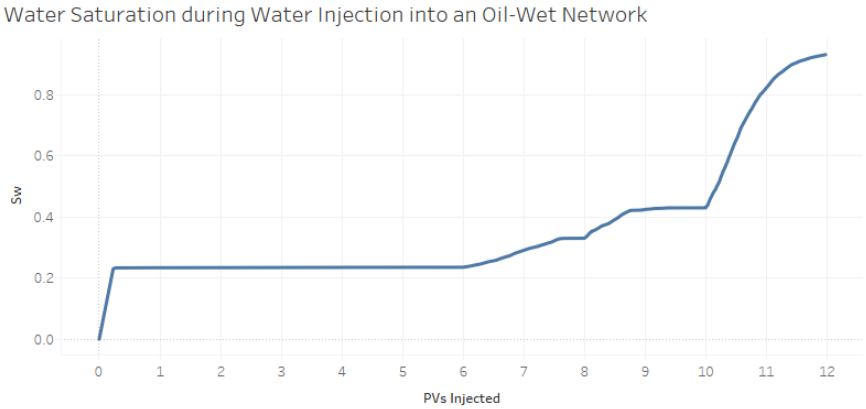

Figure 7.30: Effect of contact angle change on water saturation during drainage in an oil-wet network.

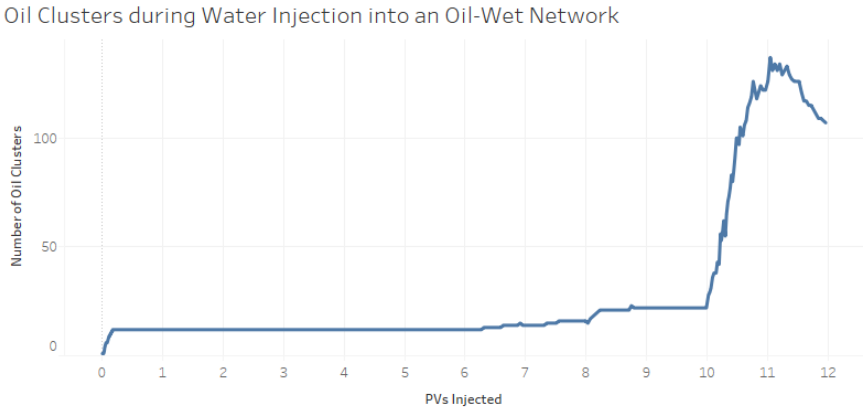

Figure 7.31: Effect of contact angle change on oil cluster numbers during water injection into an oil-wet network.

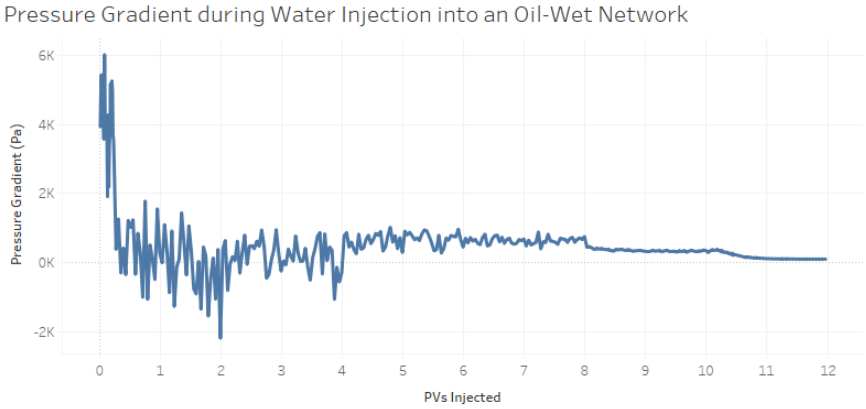

Figure 7.32: Effect of contact angle change on pressure gradient across the network during water injection into an oil-wet network.

These observation suggest again that modification of the contact angle can only be efficient if the wettability configuration is shifted towards a neutral state. This is mainly due to the nature of the cosine function which makes the capillary forces

significantly reduced if the contact angles are close to 90°. Although we have already shown using the *numSCAL* drainage module in the previous section that significant additional oil can be achieved if the contact angle angle reaches a value close to 90° (due to the emergence of new fingers and the swelling of the existing ones), the ganglion model predicts even greater recovery potential due to ganglia mobilisation. Hence, EOR processes such as low salinity water injection could prove useful to displace the trapped oil clusters, although this can be only possible when the induced wettability change is sufficient to bring the network towards a neutral state.

[It is worth noting that similar results were obtained when the same simulation protocol has been applied for the case of a single trapped oil ganglion occupying the centre of a *water-wet* network (Figure 7.15). Contact angles were shifted from 40° towards 89° every 2 injected pore volumes according to the following sequence: 40°, 60°, 80°, 85°, 87° and 89°. Figure 7.33 shows that the oil ganglion began to move upwards - although only slightly - when the contact angle reached 87° ($Ca = 7.4.10^{-5}$) and became fully mobilised as the last 2 pore volumes have been injected (which shifted the contact angle to 89° ($Ca = 2.2.10^{-4}$)).]

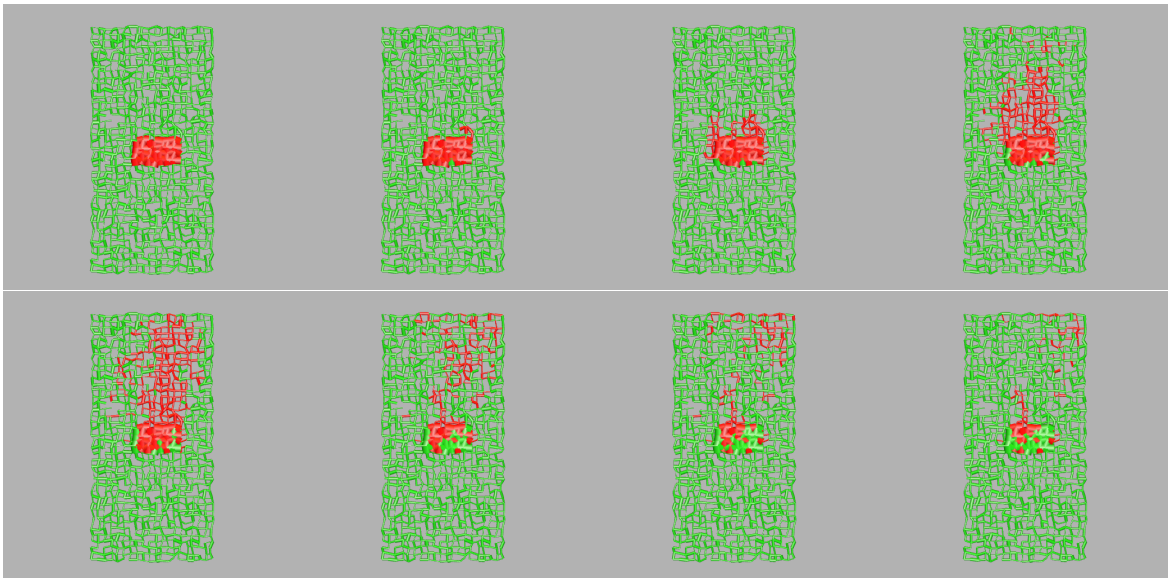

Figure 7.33: The onset of a single ganglion mobilisation in a water-wet network due to the continuous modification of contact angle from 40° to 89° during the injection of 12 pore volumes. Pore volumes injected from left to right and top to bottom: 8, 9, 10, 10.2, 10.6, 11.2, 11.6, 12. Oil: red; Water: green.

7.3.5 Effect of Interfacial Tension

The reduction of interfacial tension is another protocol involved in the application of some EOR processes (e.g. surfactant injection) to reduce the capillary forces and yield additional recovery. Here, we simulate the drainage process using the

same configuration described previously and using a flow rate equal to $1.10^{-12}m^3s^{-1}$ ($Ca = 5.10^{-6}$). The oil-water interfacial tension is halved every injected 2 pore volumes through the entire simulation according to the profile shown in Figure 7.34.

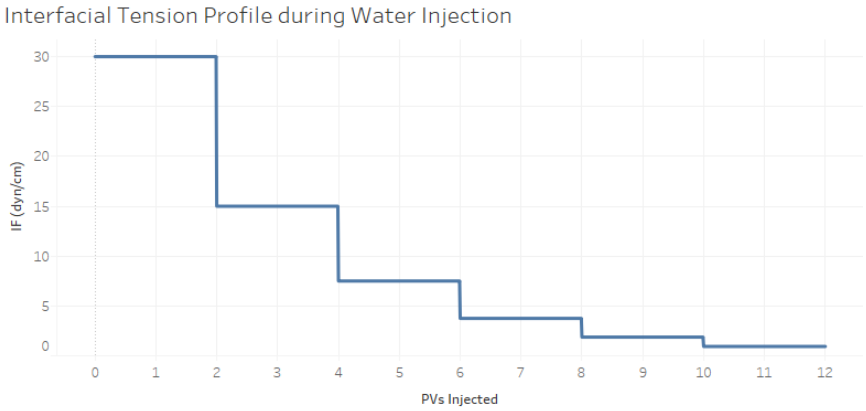

Figure 7.34: Oil-water interfacial tension profile during 12 pore volume water injection; Interfacial tension is halved after every 2 pore volume injection.

Figure 7.35 and 7.36 shows a similar pattern to that observed in the two previous sections. Again, the effect of reducing the interfacial tension does not appear until a critical value is reached. In this case, additional oil recovery is obtained after 6 injected pore volumes when the interfacial tension is around $4dyn/cm$. The water saturation keeps increasing from that point every time the interfacial tension is halved and reaches $\sim 40\%$ (compared to an initial value of $\sim 20\%$ before the interfacial tension is reduced). It can be seen from the last two network states (Figure 7.35) that water breaks into the trapped oil cluster, which confirms the breakup and mobilisation of oil clusters when the interfacial tension is significantly low (this can be also shown in Figure 7.37). This is a direct manifestation of the reduced capillary forces, which become negligible compared to the viscous gradients (Figure 7.38); the fluctuation of the pressure gradient across the network becomes negligible as the simulation progresses and the regime becomes fully viscous dominated by the end of the drainage process.

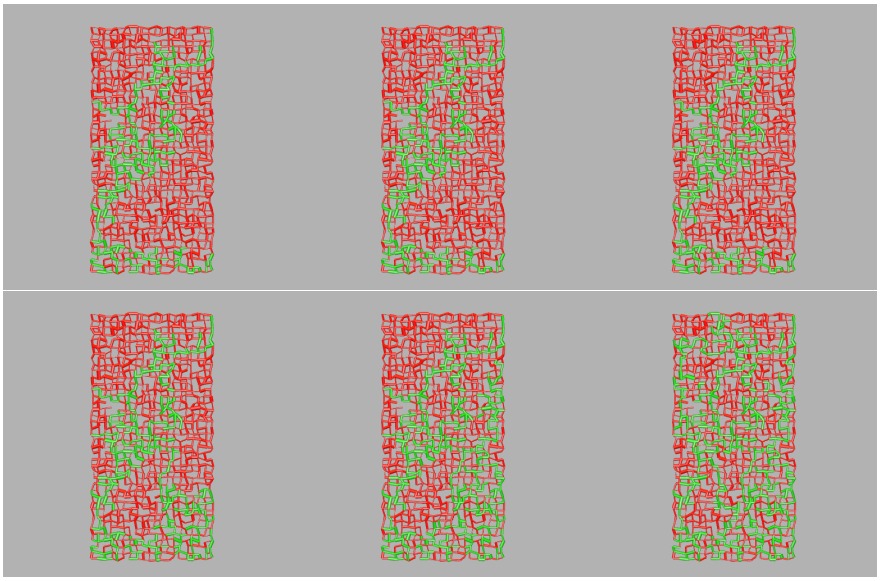

Figure 7.35: Six snapshots of phase distribution during water injection into an oil-wet network originally filled with oil. Oil-water interfacial tension decreases every two injected pore volumes. Injected pore volumes from left to right and from top to bottom: 2, 4, 6, 8, 10 and 12. Oil: red; Water: green.

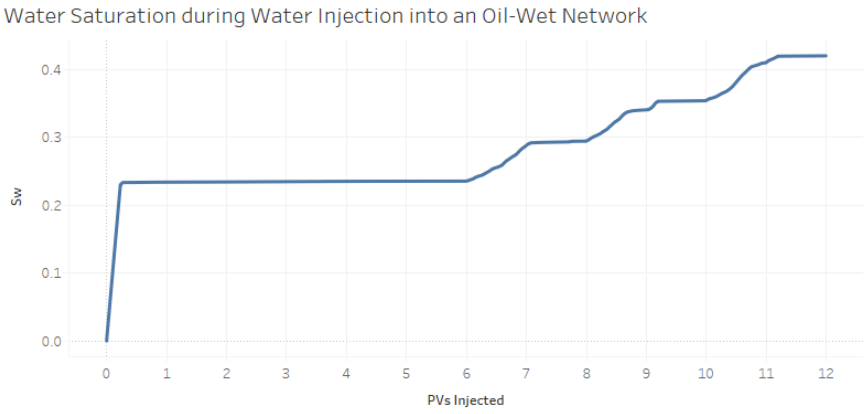

Figure 7.36: Effect of interfacial tension change on water saturation during drainage in an oil-wet network.

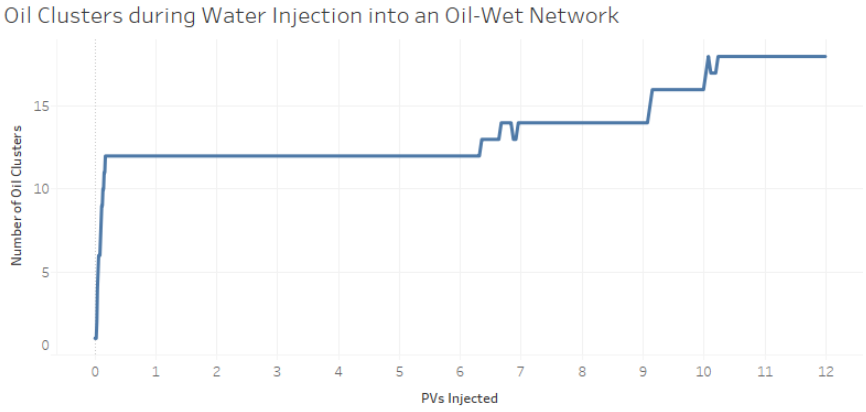

Figure 7.37: Effect of interfacial change on Oil clusters number during water injection into an oil-wet network.

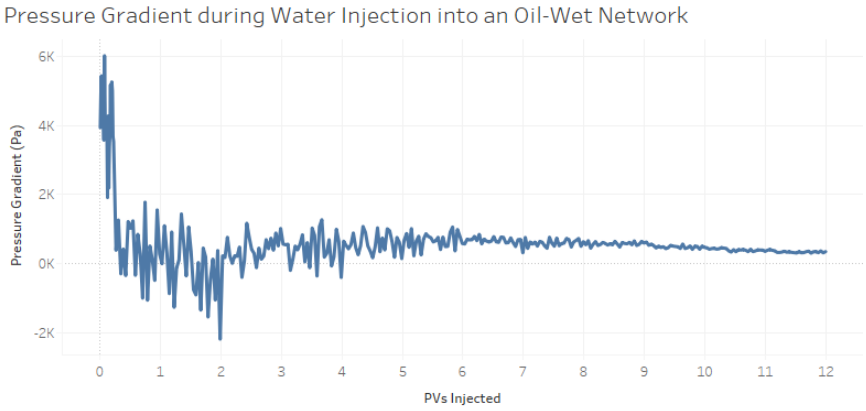

Figure 7.38: Effect of interfacial change on pressure gradient across the network during water injection into an oil-wet network.

These simulations demonstrate that the eventual mobilisation of ganglia is highly linked to the induced reduction of interfacial tension. Thus, such a parameter should be thoroughly investigated experimentally and numerically before the application of surfactant injection processes in order to examine the likelihood of displacing trapped oil clusters at reservoir conditions.

7.4 Conclusions

In this chapter, we introduced a new dynamic model to simulate processes that involve the mobilisation of trapped ganglia. The novelty of the deployed algorithms lies in using the concept of natural trapping that can emerge from the balance between capillary and viscous forces. No rules were implemented to direct the flow towards specific paths or to block counter-imbibition flow. The evolution of phase saturations is solely based on the dynamic pressure field in the underlying network which takes into account the applied flow rate and the capillary forces between the various phases. The model can be applied to simulate processes where no ganglia mobilisation is expected (e.g. simple drainage experiments like those of Lenormand, 1988), as well as scenarios where the viscous forces are sufficiently high to trigger the displacement of the topologically-trapped clusters.

The *numSCAL* ganglion module has been applied to study the effect of various key factors that affect the balance between capillary and viscous forces. We have shown that increasing the flow rate can yield local mobilisation of single ganglia in a 2D network. The flow rate values required for such migration proved to be rather high for the particular case studied and are unlikely to occur in the far-field region (although could be observed near fractures and wellbores). Moreover, we have shown that increasing the water viscosity, and reducing both contact angle and

interfacial tension can yield better recovery if the network state is shifted towards a configuration where capillary forces become significantly weaker compared to viscous forces. It is however important to note that ganglia mobilisation is not always guaranteed when these changes are induced, and we have shown that it is even possible for these parameter combinations to have no effect on oil recovery if the induced variations are below some critical values. In fact, ganglia mobilisation appears to occur only for significantly large perturbations to the initial configuration, which may be difficult to achieve practically. This suggests that ganglia displacement might not be common in reservoirs unless the initial conditions are already close to the required critical values that signal the onset of mobilisation; for instance, mobilisation can be readily triggered in neutral-wet reservoirs compared to strongly-oil wet ones. Figure 7.39 shows a summary of the additional oil recovery obtained for the different protocols we have studied, and shifting the contact angles towards a neutral state appears to be the most efficient scenario.

Currently, one limitation of the model is the high computational time it requires compared to the fast *numSCAL* drainage module. This can be improved in future work by adopting better optimised solvers to compute the pressure field in the network. However, although the model is not currently suitable for large networks, it can be still applied as a testing framework to detect whether ganglia are *likely* to be displaced under a given set flow conditions. In fact, the insights we have gained from this study suggest that ganglia mobilisation is unlikely to occur under normal conditions at flow rates applicable to the far-field region of a reservoir (1 m/day, 10 m/day) – this gives us confidence in using the fast *numSCAL* drainage model to study processes under these conditions, as the absence of ganglia mechanisms is not expected to affect the simulated results.

Although the parameters we examined in the last two chapters are directly linked to EOR processes, we have been comparing separate scenarios corresponding to different values of the associated parameters (i.e. water viscosity, contact angles, interfacial tension). In reality, the propagation of polymer, low salinity water or surfactant occurs gradually in the reservoir and their effect is directly linked to their evolving local concentrations; thus, a dynamic tracking of these quantities is needed to consistently investigate the effect of the corresponding process. This will be considered in the next chapter by implementing a new model extended from the current *numSCAL* drainage module in order to fully simulate various EOR protocols and to capture the possible synergies that can emerge when applied simultaneously.

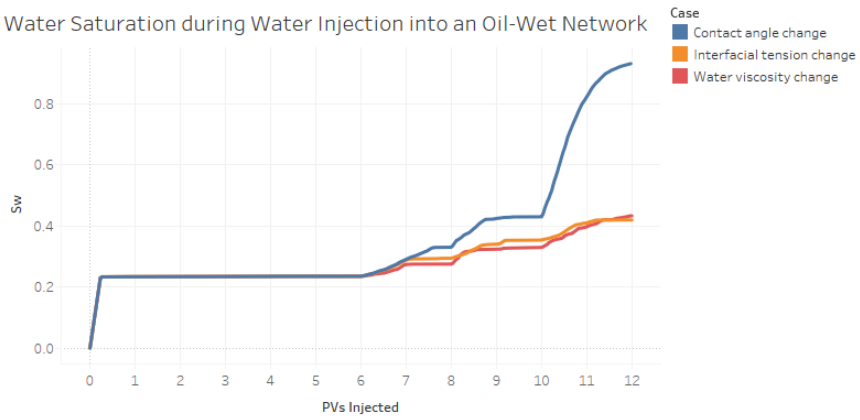

Figure 7.39: Effect of water viscosity, contact angle and interfacial tension on water saturation during drainage in a sample oil-wet network.

Chapter 8

numSCAL EOR Applications

8.1 Introduction

With ever-increasing energy demands across the world, new methods have been developed to maximise recovery from oil reservoirs. Exploiting only natural recovery mechanisms, such as depletion, would leave significant amounts of oil behind, and even secondary recovery processes, such as water injection or gas injection, might not be able to yield the desired recovery profiles (especially for high viscous ratios where viscous fingering would result in poor volumetric sweep).

In order to overcome these limitations, several Enhanced Oil Recovery (EOR) techniques have been developed to maximise the recovered oil quantities. These processes are usually referred to as tertiary recovery mechanisms as they are often deployed after secondary gas or water injection. The basic ideas behind such processes is to alter the interaction between the rock and the reservoirs fluids (by changing the wettability, for instance, and weakening capillary forces), or to alter the interaction between the reservoir fluids (e.g. by increasing the viscous forces acting in the system). As most of these interactions occur at the pore-scale, pore network models can be a useful tool to examine the efficiency of EOR processes and determine the key parameters that affect the additional oil they could eventually yield.

In this chapter, we discuss the mechanisms of two main EOR processes at the pore-scale: Low Salinity (LS) water injection, and polymer Injection. We then describe the implementation of those mechanisms into our unsteady-state drainage model. Simulation results from several scenarios are discussed for various key flow parameters. Finally, possible synergies between LS water and polymer are investigated by considering different flooding protocols where these two EOR methods are applied simultaneously.

8.2 EOR Techniques: Mechanisms on the Pore Scale

Secondary oil recovery processes are usually deployed to maintain high pressure in the reservoir and keep the oil production economically viable. Such approaches often involve the injection of High Salinity (HS) seawater or gas into the reservoir to displace the oil towards the production wells. The efficiency of secondary recovery mechanisms decreases over time however, and the oil pressure can drop significantly. This is also accompanied by higher Water-Oil Ratios (WOR) or Gas-Oil Ratio (GOR), and oil production becomes too costly to maintain, although significant quantities of recoverable hydrocarbon may still be available in the reservoir.

Tertiary recovery methods are often applied at this stage to mobilise some of the oil left behind and to yield additional oil recovery. These techniques are also referred to as Enhanced Oil Recovery processes, as their application is not always restricted to tertiary mode (a secondary recovery approach could sometimes be disregarded when EOR processes are immediately applied after primary recovery).

EOR generally involves the injection of one or multiple fluids to shift the reservoir conditions into a more favourable state that could result in further oil recovery. This could be achieved by decreasing the interfacial tension between oil and water (i.e. surfactant injection), shifting the wettability of the reservoir toward a favourable configuration (i.e. low salinity water injection) or improving the mobility ratio to strengthen the viscous forces of the displacing phase and switch the flow regime from inefficient viscous fingering toward more favourable frontal advance (i.e. polymer injection).

In this work, we investigate two water-based EOR recovery processes – LS water injection and polymer Injection – and develop a new unsteady-state network model capable of investigating their recovery potential.

8.2.1 Low Salinity (LS) Water Injection

LS water injection has been examined in various works in the literature, and several experimental studies have reported additional recovery when fresh or LS water is used to displace oil in both secondary and tertiary modes (Ashraf et al., 2010 [157]; Webb et al,. 2005 [158]; Zhang and Morrow (2006) [159]; Yildiz et al., 1999 [160]; Tang et al. [161]; Tang and Morrow, 1997 [162]; Buckley and Morrow, 1990 [163], Bernard, 1967 [164]). Today, LS water injection is a well-recognised EOR process, and interest in its applications is rapidly increasing (Figure 8.1). In a review

published in 2011, Morrow and Buckley [154] discussed the major advances in LS application and presented the various suggested mechanisms for the so-called Low Salinity Effect (LSE).

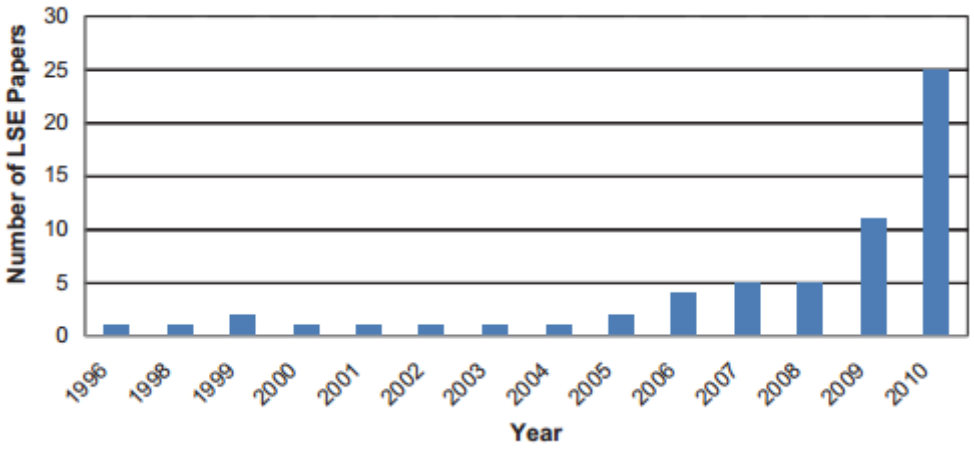

Figure 8.1: The number of publications and presentations focused on LS shows an increasing interest in the last ten years. (Morrow and Buckley, 2011 [154])

Changing the wettability of the rock (by affecting the adhesion of oil molecules to the rock surface and/or changing the brine composition) is believed to be a key consequence of LS injection. This wettability change is associated with a shift in oil-water contact angle that may reduce capillary forces, mobilise trapped oil ganglia, and/or cause water fingers to swell and thicken.

Other suggested LS mechanisms include:

- Fines migration (Tang and Morrow, 1999 [161]): clay components could detach from the rock surface when the water salinity is low. This might trigger partial mobilisation of residual oil attached to clay.
- Microscopic diversion (Spildo et al., 2012 [165]): detached clay components could block small throats resulting in increased pressure gradients in other regions of the network.
- Chemistry-related phenomena, such as pH variation, multi-component ionic exchange, double layer expansion.

It is likely, however, that the LS effect is a manifestation of several mechanisms acting simultaneously (this explains the contradictory results in some cases reported in the literature regarding the additional recovery yielded by LS water injection). The design of experimental protocols becomes therefore difficult to achieve and laboratory results would eventually exhibit large uncertainty. Network modelling can provide an alternative cheap approach to investigate the effect of several key

flow parameters on LS effect. By modelling the effect of wettability alteration on the dynamic pressure field in the host rocks, it is possible to simulate LS water injection processes and to quantify the resulting additional oil recovery. This will be discussed later in Section 8.4.2.

8.2.2 Polymer Injection

Polymer solutions contain large and heavy molecules which make their viscosity higher than that of HS water. This makes polymer injection a useful technique for increasing the viscous forces within the invading phase by reducing viscous instabilities, yielding additional displacement of the remaining oil in the reservoir. Polymer injection can also be used to block fractures or high permeable areas in the reservoir (such a process is usually referred to as gel treatment) to prevent the loss of injected water and to build up the pressure across the reservoir (Willhite et al., 2008 [166], Jenn-Tai et al., 1995 [167]). Sorbie (1991) [168] wrote an exhaustive book about polymer structures, properties and stability, and he examined their transport properties and their potential as an EOR process to displace oil in porous media.

Polymer solutions are believed to increase the oil fractional flow based on Buckley-Leverett fractional flow theory (1942) [169]. According to the Buckley-Leverett formulation, the fractional water flow F_w is given by:

$$F_w = \frac{Q_w}{Q_w + Q_o} \, , \; Q_o = \frac{\kappa_{ro}\mu_w}{\kappa_{rw}\mu_o} \tag{8.1}$$

where Q_w and Q_o are respectively the water and oil flows, κ_{rw} and κ_{ro} are respectively water and oil relative permeabilities, and μ_w and μ_o are respectively water and oil viscosities. Therefore, an increase of water viscosity (usually accompanied by a decrease in water relative permeability as dictated by Darcy's law), would yield a drop in the water fractional flow, and more oil recovery should be expected.

The increase in water viscosity would also decrease the viscous ratio and this could shift the flow regime from a viscous fingering behaviour to a stable or capillary displacement (Figure 8.2), which might result in significant additional oil recovery.

Other mechanisms can play a role in yielding a polymer effect. For instance, microscopic diversion is believed to result in higher pressure gradients when the small pores are blocked (Bolandtaba et al., 2009 [171]).

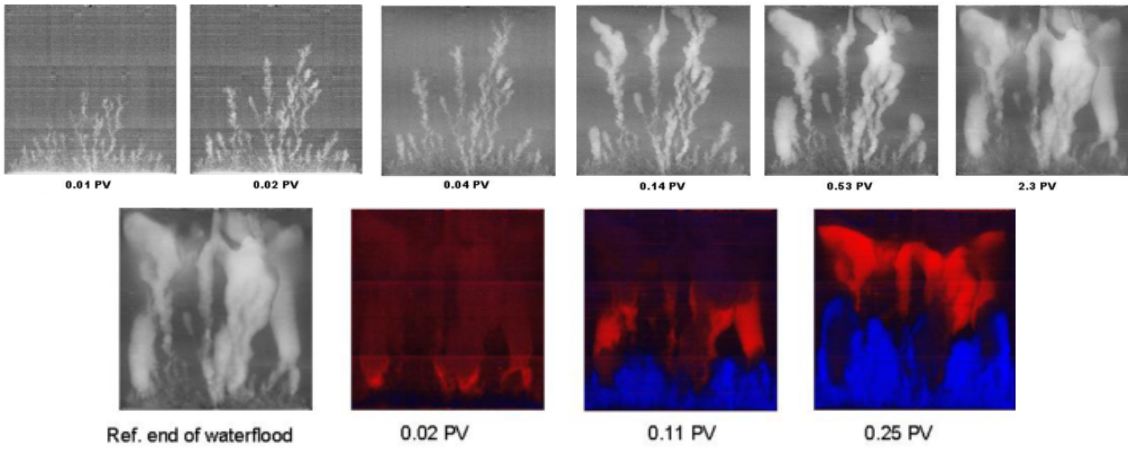

Figure 8.2: (Top) Imaging of water injection into a 2000cP oil-filled Bentheimer slab. Water is coloured in white. (Bottom) Imaging of polymer injection into a 2000cP oil-filled Bentheimer slab. Polymer is coloured in blue. (Skauge et al., 2012 [170])

8.2.3 Synergy between EOR processes

Combining different EOR processes might yield a synergistic behaviour that could result in additional oil recovery over and above that obtained from each EOR process applied separately. This has been investigated in recent experimental work (Shiran and Skauge , 2013 [172]; Mohammadi and Jerauld, 2012[173], Alagic et al., 2010 [174]), and both polymer and surfactant solutions have been reported to be more efficient in a low salinity environment.

8.3 Model Description

The EOR model developed in this work is an extension of the unsteady-state drainage model described in Chapter 6. When modelling the flow of LS water or polymer in the network, the following conditions are considered:

- LS water/polymer are injected in an oil-wet system (imbibition mechanisms are not considered).
- LS water/polymer and HS water are miscible and mix instantly in a capillary element.
- No meniscus is considered between LS water/polymer and HS water.
- LS water and polymer cannot mix with oil or flow through the oleic phase.
- Fines migration during LS injection is not considered.

- Polymer adsorption is not considered.
- Microscopic diversion is not considered.
- When LS water and polymer are flowing together, they are miscible and no chemical interaction is modelled between them.

To capture the effect of LS water and polymer at the pore-scale, we adopt a pragmatic approach where we model the *manifestations* of the EOR mechanism instead of tracking the complex chemistry underlying the interaction between LS water or polymer molecules with the rock surface. We therefore assume that LS water affects essentially the oil/water contact angles, whilst polymer acts primarily by increasing the water viscosity. Mathematical relationships are applied to link both LS water and polymer concentrations to their direct effects.

The workflow of the EOR model is shown in Figure 8.3. The contact angles (affecting directly the capillary pressure in pores) and water viscosity are correlated with LS water and polymer concentrations. The unsteady state drainage model is then called to solve the pressure field in the network and to update the phase saturations in all capillary elements. Finally, the concentrations of LS water and polymer are updated according to mass conservation laws, and the next time step is taken until a user-defined number of pore volumes have been injected.

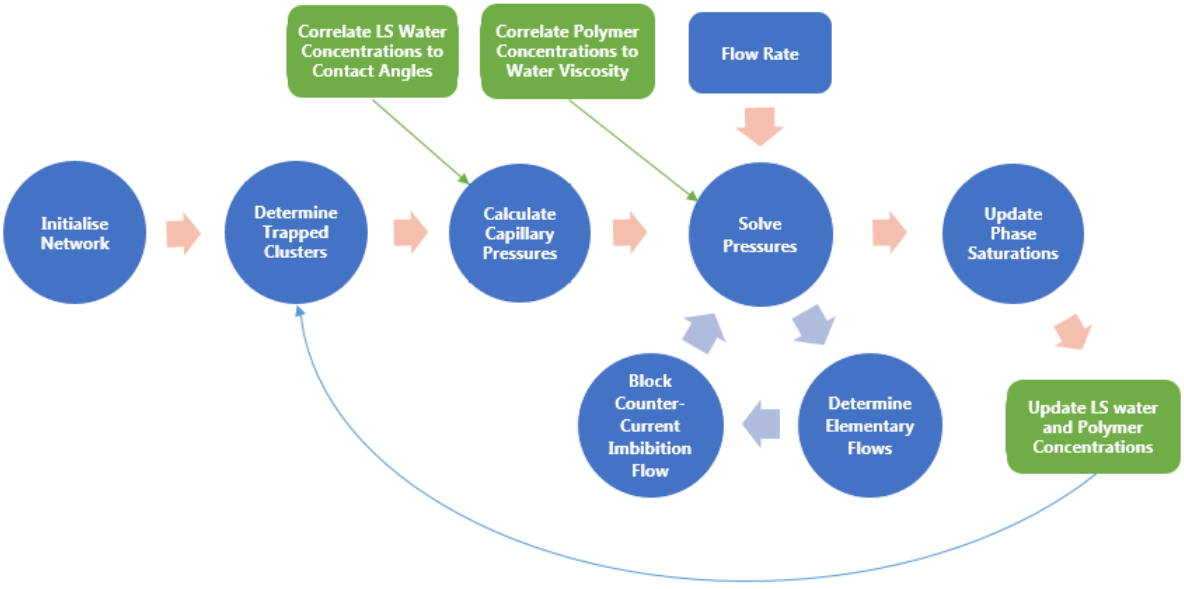

Figure 8.3: EOR model workflow

8.3.1 Tracer Dynamics

LS water and polymer are modelled as two distinct tracers with dimensionless concentrations ranging from zero to one. They can flow from the inlet pores either immediately the simulation starts (secondary mode) or after some period of HS water injection (tertiary mode). In both cases, we use a mass conservation law to update their corresponding tracer concentrations according to the the pressure field in the network. Note that the term "tracer concentration" in the LS study refers to the concentration of LS water and is equivalent to (1-salinity).

A similar approach has been already used in the work of Watson et al. (2017) [175] where the tracer evolution (an unsteady-state process) has been coupled to a steady-state water injection model. In their simulations, the time required to achieve any steady-state volumetric change was estimated in order to update tracer concentrations in the network. Here, however, the tracer dynamics are consistently tied to the unsteady-state drainage model and both tracer concentrations and phase saturations are updated at each iteration using the same time step.

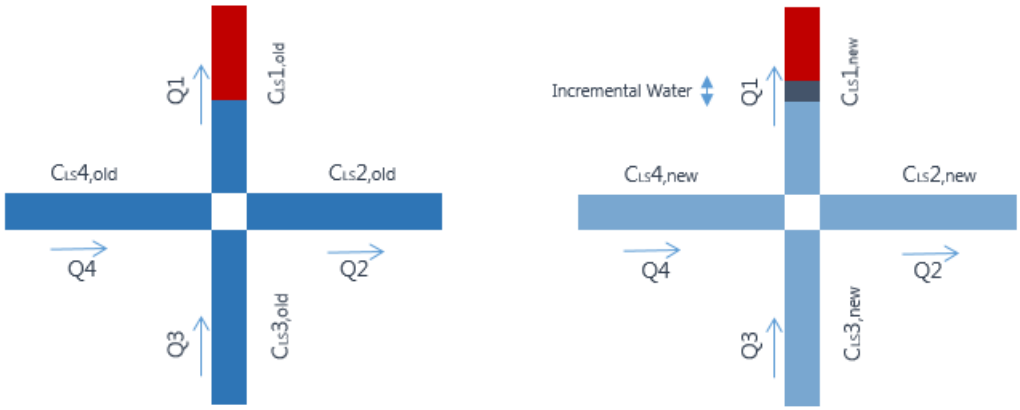

Figure 8.4: Phase configuration for four connected pores in a 2D network (left) at the start of a timestep (right) at the end of the timestep.

Consider the configuration shown by Figure 8.4, and denote the LS water concentration in each pore i by C_i. The flow Q_i in each pore i is determined after solving the flow equations in the network, and the new volumetric water fractions $F_{w,new}$ are updated accordingly in all pores. Next, a new tracer concentration C_{LS_new} in pore 1, after a timestep Δt (calculated using Equation 6.10) is computed after updating elementary water fractions in the network, and is calculated as follows:

$$C_{LS,1_{new}} = \frac{F_{w,1_{old}}}{F_{w,1_{new}}} C_{LS\_1\_old} + \left(\frac{Q_1}{Q_{into,1}} \Phi_{LS,into,node} - \Phi_{LS,outFrom1}\right) \frac{\Delta t}{F_{w,1_{new}} V_1} \quad (8.2)$$

where V_1 is the volume of pore 1 and $Q_{into,1}$ corresponds to the total volumetric flow into node 1. $\Phi_{LS,into,node}$ refers to the mass flux of LS water entering the node and is calculated as:

$$\Phi_{LS,into,node} = Q_3 C_{LS,3_{old}} + Q_4 C_{LS,4_{old}} \tag{8.3}$$

We assume that the LS water is partitioned among the downstream pores in proportion to their individual flows. Thus the mass flux of tracer entering pore 1 is given by $\frac{Q_1}{Q_{into,1}} \Phi_{LS,into,node}$. The mass flux of tracer leaving pore 1 is calculated as:

$$\Phi_{LS,outFrom1} = Q_1 C_{LS,1_{old}} \tag{8.4}$$

When polymer is flowing in the network, the concentration of polymer is computed in a similar fashion. Equation 8.2 remains valid when both LS water and polymer are flowing, as no interaction between the two tracers is considered (although this could be considered in future work).

8.3.2 Coupling the LS Effect and Polymer Effect to Tracer Concentration

LS water

Although the precise cause of any LS effect may be related to a wide variety of pore-scale phenomena, we assume in this work that wettability alteration is the main consequence of the underlying chemistry and hence of any LS effect. This occurs when the initial contact angle attributed to a capillary element changes when it comes into direct contact with LS water. If the contact angle change shifts the network wettability towards a less oil-wet configuration, a reduction of the resisting capillary forces is expected, which could affect recovery.

When an oil-filled pore is being invaded with LS water (or is adjacent to a LS water-filled pores), we assume that its initial oil-water contact angle can change according to its salinity (or the average salinity corresponding to adjacent water-filled pores). The new contact angle is calculated as:

$$\theta_{new,i} = \theta_{initial,i} + \Delta\theta \times \mathcal{H}(C_{LS}) \tag{8.5}$$

where $\Delta\theta$ is a parameter that corresponds to the maximum contact angle change when the concentration of LS water is equal to one and $\mathcal{H}$ refers to a Hill function given by:

$$\mathcal{H}(C_{LS}) = \frac{C_{LS,i}^{n}(1-\Gamma^{n})}{C_{LS,i}^{n}(1-2\Gamma^{n})+\Gamma^{n}} \tag{8.6}$$

Γ refers to the concentration at which half of $\Delta\theta$ is reached, whilst n is the Hill function exponent that determines the rate of change. In this model, we set n equal to 30 and Γ equal to 0.88 (Figure 8.5), meaning that the local *salinity* must be relatively low for a significant contact change to occur.

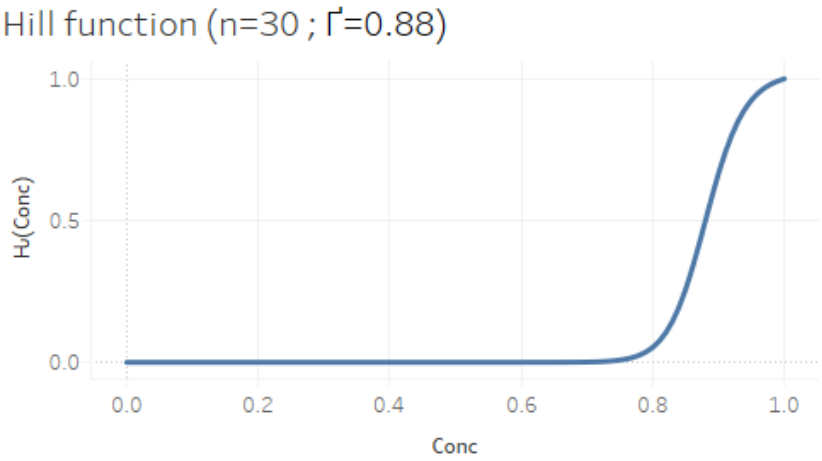

Figure 8.5: Hill Function is used to relate the tracer concentration to LS or Polymer effect.

Polymer

The polymer effect is modelled through a change of water viscosity. We relate the water viscosity in each capillary element to its concentration of polymer and a similar approach to that applied for LS water: thus, the new water viscosity in each pore is given by:

$$\mu_{new,i} = \mu_{HS} + \Delta\mu \times \mathcal{H}(C_{Polymer,i}) \tag{8.7}$$

where μ_{HS} is the high-salinity water viscosity and $\Delta\mu$ is an input parameter that corresponds to the maximum viscosity change when the concentration of polymer is equal to one. A Hill function is again applied to quantify the change using the same parameters described in the previous paragraph.

8.4 Analysis of Oil Recovery during the Application of EOR Protocols

8.4.1 Simulations

In order to study the effect of LS water and polymer on oil recovery, we have run a vast range of simulations covering a wide variation of injection protocols. We start by investigating the effect of LS water and polymer separately, and then go on to investigate their combined effect.

LS water and polymer injection protocols

When simulating the injection of LS water or polymer, two possible scenarios are considered:

- **LS-sec , POL-sec**: This refers to the injection of LS water or polymer in secondary mode – injection of the tracers occurs at the very beginning of the waterflood.
- **LS-ter , POL-ter**: This refers to the injection of LS water or polymer in tertiary mode. Once a spanning HS water cluster forms following a period of HS water injection, a drop in pressure is observed at the system outlet, and no further significant recovery is usually observed. It is at this point that we start the injection of LS and/or polymer tracer.

To simulate the LS effect on contact angle, we consider three scenarios. As described earlier, we correlate the LS concentration to the contact angle change assigned to capillaries in direct contact with the LS brine. Initially, all the capillary elements are considered oil-wet and assigned a contact angle equal to 140°. As the concentration of LS water starts to build up in a capillary element, the associated contact angle starts to decrease until it reaches a minimum value corresponding to a tracer concentration equal to one (i.e. a salinity of zero). The three scenarios studied here are as follows:

- **OWOW**: This corresponds to a change from a strongly oil-wet configuration to a weakly oil-wet configuration. The contact angle change is $\Delta\theta = 30°$ and a shift from 140° to 110° is expected in the contact angles of the capillaries in direct contact with high concentrations of tracer (low salinity brine).

- **OWNW**: This corresponds to a change from a strongly oil-wet configuration to a neutral-wet configuration. The contact angle change is $\Delta\theta = 45°$ and a shift from 140° to 95° is expected in the contact angles of the capillaries in direct contact with high concentrations of tracer (low salinity brine).
- **OWWW**: This corresponds to a change from a strongly oil-wet configuration to a weakly water-wet configuration. The contact angle change is $\Delta\theta = 60°$ and a shift from 140° to 80° is expected in the contact angles of the capillaries in direct contact with high concentrations of tracer (low salinity brine).

The effect of polymer on water viscosity is simulated in a similar fashion. We correlate the polymer tracer concentration to the water viscosity in the corresponding capillary element. Initially, the HS water viscosity is set to $1cP$ and when the polymer starts to invade a pore, the water viscosity inside it is increased (eventually reaching a maximum value when the polymer tracer concentration is equal to one). Two polymer cases are considered in this study.

- **Water viscosity increasing from** $1cP$ **to** $5cP$: This would shift the viscous ratio M from 10 to 2 if we are injecting water into oil with viscosity of $10cP$.
- **Water viscosity increasing from** $1cP$ **to** $10cP$: This would shift the viscous ratio M from 10 to 1 if we are injecting water into oil with viscosity of $10cP$.

The additional recovery yielded by EOR processes can be greatly affected by the flow rate and the initial viscous ratio. We have therefore considered three different values for each, enabling us to investigate a vast range of experimental parameter combinations.

- **M=1 , 10, 100**: the HS water viscosity is fixed at $1cP$ and oil viscosity is adapted according to the value of M of interest (for M=100, oil viscosity is equal to 100cP).
- Frontal advance rates of **V=1m/day , 5m/day, 10m/day**.

Synergy between LS water and Polymer

To study the possible synergistic effects of the combined injection of LS water and polymer, four combinations are examined.

- **(LS+POL)-sec**: LS water and polymer are injected simultaneously at the very start of the simulation.

- **(LS+POL)-ter**: LS water and polymer are injected simultaneously after HS water breakthrough.
- **LS-sec+(LS+POL)-ter**: LS water is injected at the start of the simulation. Once a spanning LS water cluster forms, polymer is injected into the network alongside the LS water.
- **LS-sec+onlyPOL-ter**: LS water is injected at the start of the simulation. Once a spanning LS water cluster forms, LS injection is replaced by HS injection containing polymer.

Base Case

In this study, we use the 2D regular networks described in Chapter 3, Section 3.4.1. As a base case, we consider the networks to be initially oil-wet with contact angles equal to 140°. The initial viscous ratio is equal to 10 ($\mu_{water} = 1cP$, $\mu_{oil} = 10cP$), and water is injected with at average frontal velocity V equal to 5m/day. LS water gradually shifts the contact angles from 140° to 95° (OWNW), whilst polymer modifies water viscosity from 1cP to 5cP.

Table 8.1 summarises the network properties and flow parameters used in the base case study.

Network size	200x100
Coordination number	3.65
Degree of Distortion	0.3
Average Pore Length	100 μm
Maximum Inscribed Radius	30 μm
Minimum Inscribed Radius	1 μm
Pore Size Distribution	Truncated Normal($\mu = 9$,$\sigma = 6$)
3R coefficients ($\bar{C}$,$\bar{A}, \nu, \lambda$)	$(12, 1, 0.5, 4)$
Initial wettability	Oil-Wet ($\theta = 140°$)
(M, $\mu_{HSwater}$, μ_{oil})	(10,1, 10)
Flow Velocity V	5m/day
LS effect	OWNW ($\theta : 140° \Rightarrow 95°$)
Polymer Effect	$\mu_{water} : 1cP \Rightarrow 5cP$

Table 8.1: Networks properties and flow parameters used in the base case of the EOR study

Importance of the Seed

As discussed in Chapter 3, Section 3.4.1, the seed used in the random generator when building a network might affect the simulated results. If we consider two

relatively small networks with similar properties but generated using two different seeds, it is expected that the flow behaviour and the final fluid distributions would be different. This is apparent in Figure 8.6, where HS water injection is simulated on two 2D statistically generated networks with two different seeds. Although both networks share the same properties and the same flow parameters have been used, the final water distributions are rather different.

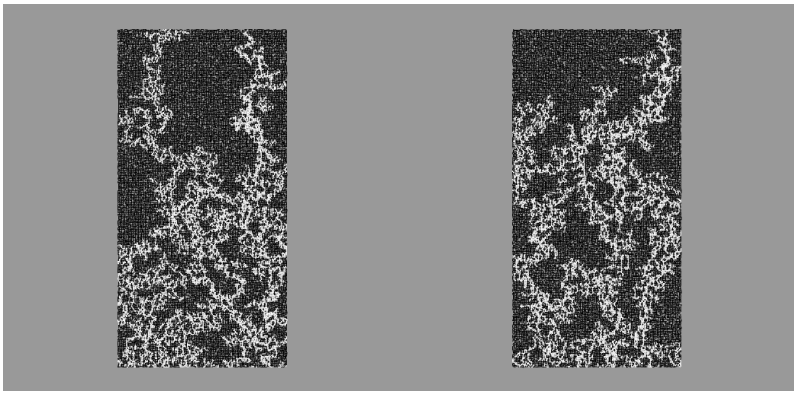

Figure 8.6: HS water distribution in two 2D networks after 4PVs. Base case network properties and flow parameters are used to build and simulate the networks but using two different seeds. Water is coloured in white, oil in black.

The sensitivity to the seed might present some issues when trying to quantify a LS or polymer effect on additional oil recovery. As the regimes can sometimes be affected by the available pathways and the random topology of the underlying networks, it is possible to observe two different EOR outcomes when we simulate the same experiment on two similar networks generated with two different seeds. To illustrate this point, we simulated HS water injection and secondary LS water injection (LS-sec) on two networks with two different seeds. This particular case lies at the crossover between capillary-dominated flow and modest viscous fingering. Figure 8.7 shows a small positive LS effect for the first network whilst a negative effect is observed for the second.

These results highlight the fact that deploying one single simulation using one seed should not be considered as a reliable approach to quantify the effect of the underlying EOR process. To address this, we run multiple simulations for each scenario on several networks generated with multiple different seeds. In this study for instance, every single scenario has been carried out on ten different networks which share the same average properties but which are built with different random structures. The results are presented as statistical distributions rather than single curves. If we consider again the HS water injection versus secondary LS water injection, case shown in Figure 8.7, the range of final recoveries after injecting four pore volumes for different network realisations is illustrated in Figure 8.8.

Using this approach it is apparent that, for this parameter set, secondary LS injection

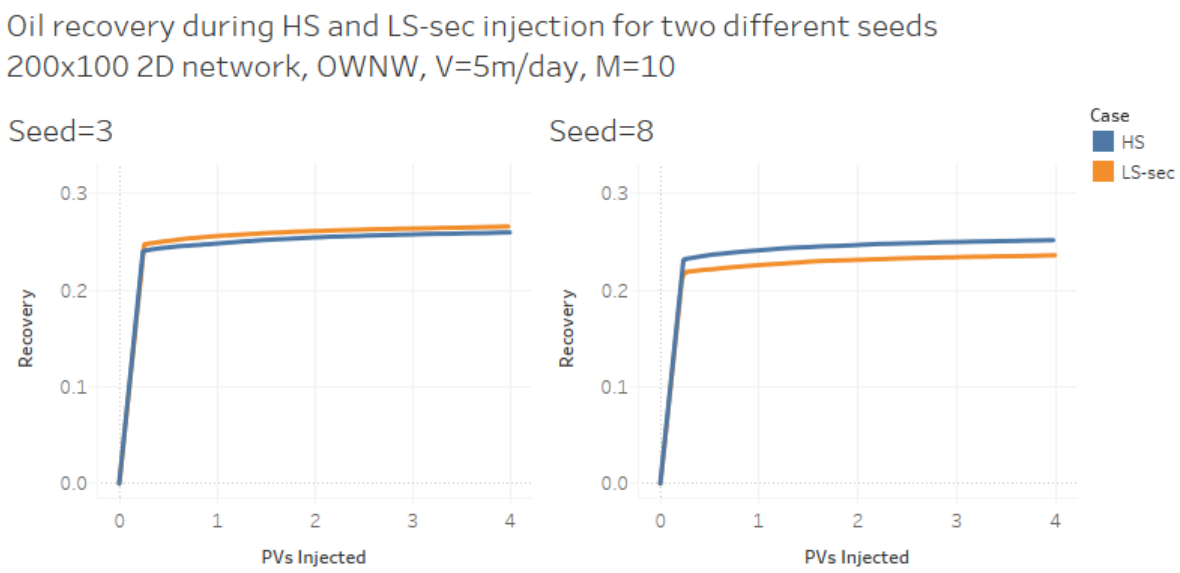

Figure 8.7: Oil recovery during HS and LS-sec injection for two different seeds. Although a positive LS effect was observed for the first seed (left), a negative effect was seen in the second one (right).

yields, *on average*, a negative effect on recovery compared to HS injection. When looking at the simulated results individually, a positive LS effect might be observed for some cases. However, the average shift in recovery can only be seen when looking at the Interquartile Range (IQR) (depicted by the grey area in Figure 8.8), which shows the middle 50% of the simulated final recoveries.

In the following sections, eight LS/polymer synergies are considered, and eight rate/wettability/viscosity ratio combinations are investigated. For each case, ten networks were constructed with different seeds and the final oil recovery after four pore volumes of injected water were measured. This sums to a total of 690 simulations carried out in this study as described in Table 8.2.

Table 8.3 shows the running time of an EOR simulation (four pore volume injection) for different configurations using an i7-3770 processor. The running time proved to be highly affected by key flow parameters (such as the flow rate and initial viscous ratio) as well as the process under investigation (i.e. HS, LS-sec, POL-sec, etc).

8.4.2 Low Salinity Water Effect

Base Case

We will begin by considering the 2D network and flow parameters described in Table 8.1. Both secondary and tertiary LS water injection are simulated, and final oil recovery is compared to the recovery obtained via HS water injection alone (Figure

Table 8.2: Summary table of the 690 simulations carried out in the EOR study. Ten seeds have been considered for every run.

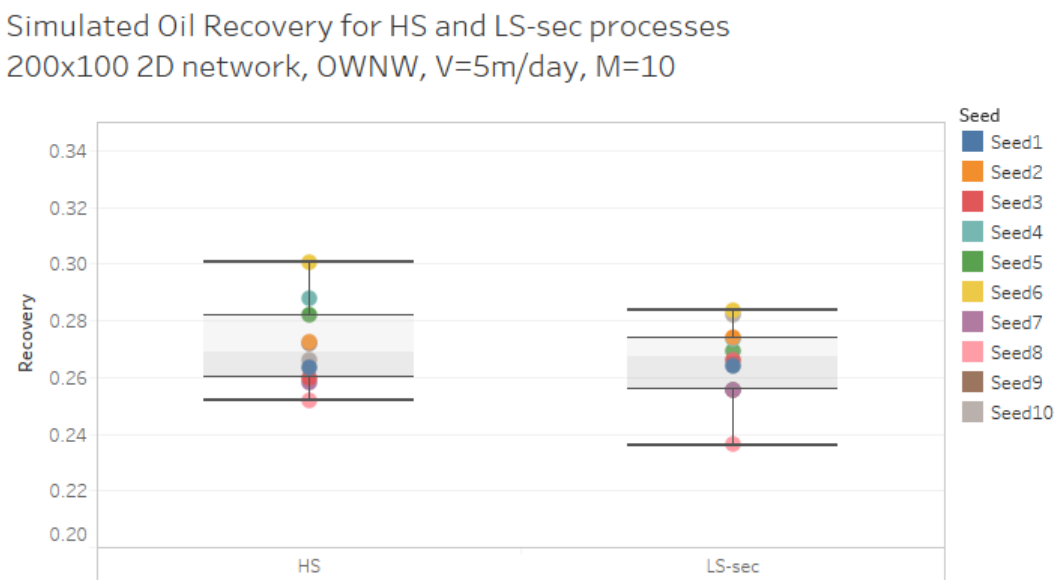

Figure 8.8: Simulated final oil recovery after 4 PVs for HS and LS-sec processes using ten seed values. A statistical dispersion is used to quantify the LS effect instead of referring to a single simulation values.

Network	Num. of capillaries	FR	M	Time (s)		
				HS	LS-sec	POL-sec
200x100	$\backsimeq$ 37000	1m/day	10	150435	168592	215339
200x100	$\backsimeq$ 37000	5m/day	10	147884	125170	203313
200x100	$\backsimeq$ 37000	10m/day	10	130220	85551	160917
200x100	$\backsimeq$ 37000	5m/day	1	171078	207543	192840
200x100	$\backsimeq$ 37000	5m/day	100	139062	87728	98518
75x75	$\backsimeq$ 10000	5m/day	10	18177	17632	28998
50x50	$\backsimeq$ 5000	5m/day	10	2840	3573	5112

Table 8.3: Computational performance of the EOR module. HS: High Salinity water injection, LS-sec: secondary Low Salinity water injection, POL-sec: secondary polymer injection.

8.9). The contact angles of the pores in direct contact with LS water are allowed to change from 140° to 95° (OWNW case).

Results show that LS water injection in secondary mode yields a slightly poorer recovery when compared to recovery due to HS water injection. Whilst this might appear counter-intuitive (the capillary pressures are expected to be reduced at the entry of pores due to the shift of contact angles towards a neutral-wet value and so to the reduction of $cos\theta$), this effect can be explained by examining the final water distribution for each case (Figure 8.10).

Whilst the water invaded the network following a capillary fingering pattern during HS water injection, viscous fingers emerged during LS injection in secondary mode. The contact angle modification has changed the ratio of viscous to capillary forces and shifted the flow regime from capillary displacement to viscous fingering (which

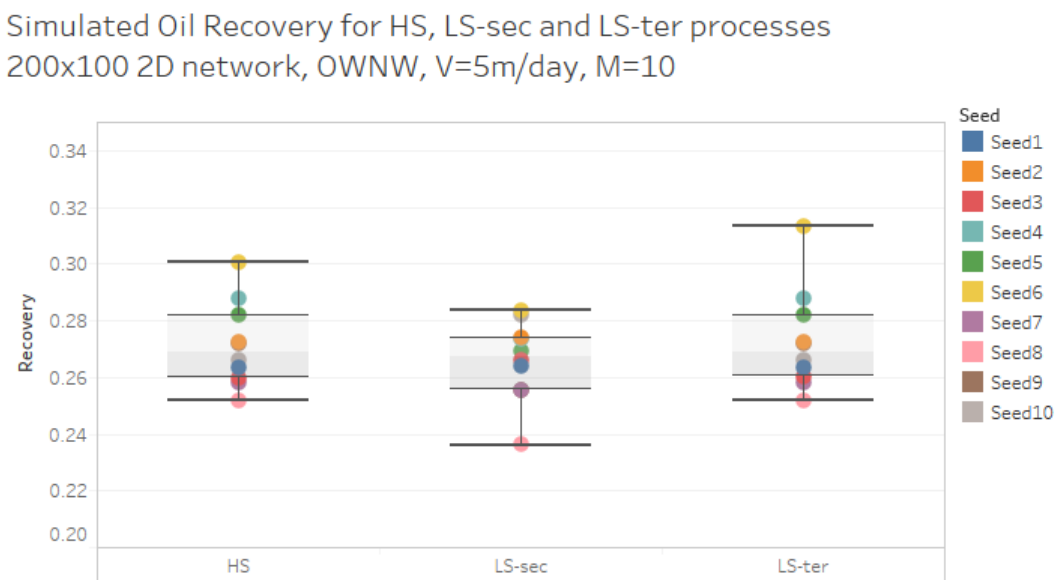

Figure 8.9: Final oil recovery after 4 PVs for: HS, LS-sec and LS-ter processes. Ten seeds are considered for each case.

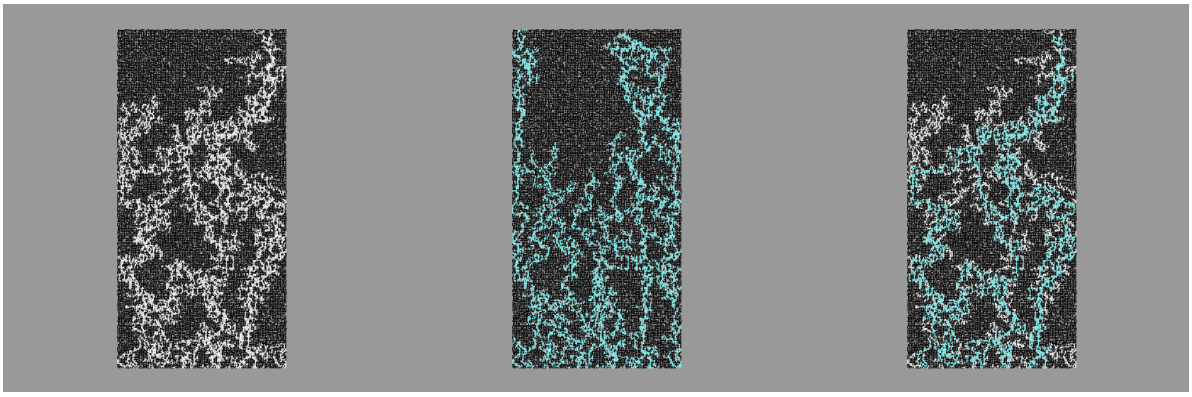

Figure 8.10: Final water distribution after 4PVs of HS water injection (left) LS water injected in secondary mode (middle) and LS water injected in tertiary mode (right). Wettability configuration: OWNW. HS water is coloured in white, LS water in light blue and oil in black.

resulted in thin fingers breaking through the network). Although smaller oil-filled pores might be available at this stage to the invading water, the change of flow regime and thus the elongation of the water clusters has a detrimental effect on the final oil recovery.

Tertiary LS water injection has no positive effect on oil recovery for the base case parameter set. This can be explained by the drop in pressure gradient observed after water breakthrough. Indeed, although the capillary entry pressures have been reduced due to LS-induced contact angle modification, the pressure gradient across the network and at the tips of water clusters are not high enough to displace any additional oil.

Effect of Wettability Modification

The effect of each wettability modification scenario is now studied. We consider both OWOW and OWWW cases, where the contact angles of the capillary elements in direct contact with LS water shift from 140° to 110° and 80° respectively. Final recovery results are presented in Figure 8.11.

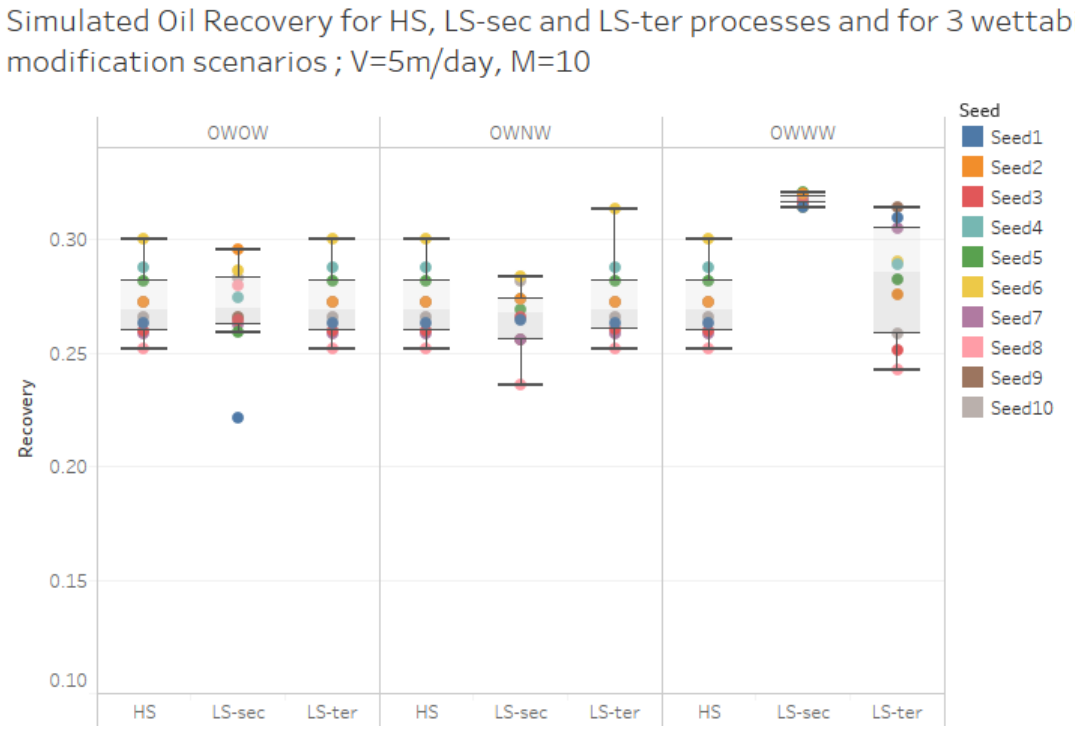

Figure 8.11: Final oil recovery after 4 PVs for: HS, LS-sec and LS-ter processes. Three wettability configurations are considered: OWOW, OWNW and OWWW. Ten seeds are considered for each case.

For the OWOW configuration, the effect of LS water is positive but relatively small for both secondary and tertiary mode. The reduction of contact angle from 140° to 110° corresponds to a drop of the capillary pressures by a factor of 2 ($\frac{cos140}{cos110}$) which is not sufficient to trigger significant additional oil displacements. Conversely, when the wettability of the network is shifted toward a water-wet state (OWWW), a considerable increase in oil recovery is observed for both secondary and tertiary modes. For instance, approximately 33% of the original oil in place (OOIP) is recovered for the LS-sec scenario compared to an average of 27% after HS water injection.

The final water distribution for OWWW case is displayed in Figure 8.12. For the secondary LS water process, the invasion pattern is similar to a stable displacement. Note that this case corresponds to an imbibition process and although the network appears to be fully saturated with water, most of the large pores remain oil-filled and trapped. For the tertiary LS injection case, the wettability switch removes the

capillary pressure barrier at the oil-water interface, which make it possible for fingers to swell transversely to the global pressure gradient.

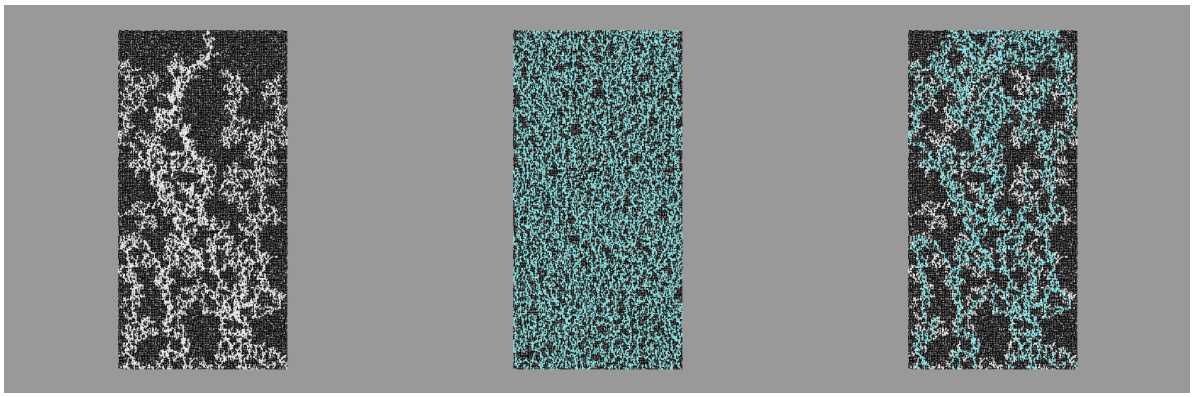

Figure 8.12: Final water distribution after 4PVs of HS water injection (left) LS water injected in secondary mode (middle) and LS water injected in tertiary mode (right). Wettability configuration: OWWW. HS water is coloured in white, LS water in light blue and oil in black.

Effect of Viscous Ratio M

To study the effect of viscous ratio, we consider three oil viscosities: $1cP$, $10cP$, and $100cP$ whilst keeping water viscosity equal to $1cP$. This results in three viscous ratios: 1, 10 and 100. Both secondary and tertiary LS water processes are considered alongside HS water injection, and final oil recovery results are presented in Figure 8.13. This sensitivity was carried out at a frontal advance rate of 5m/day.

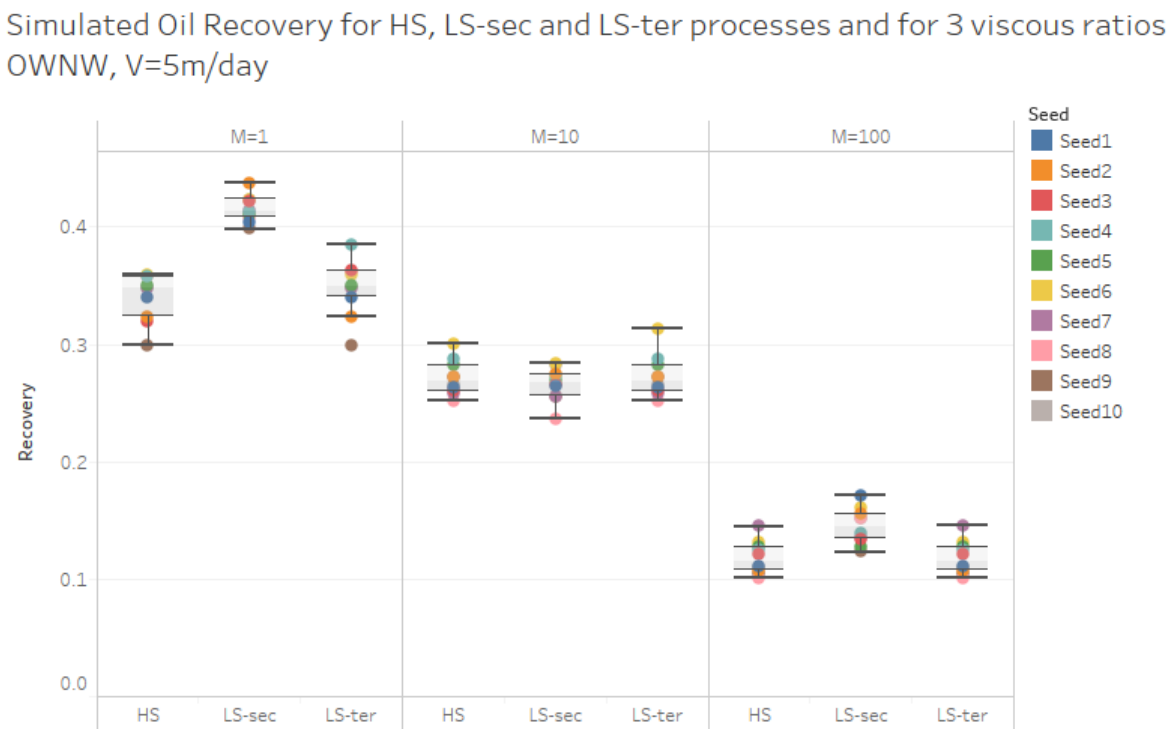

Figure 8.13: Final oil recovery after 4 PVs for: HS, LS-sec and LS-ter processes. Three viscous ratios are considered:1, 10 and 100. Ten seeds are considered for each case.

The viscous ratio is found to have a significant impact on additional oil recovery following LS injection. Whilst a negative secondary LS water effect has been observed for M=10 (base case), both M=1 and M=100 yield a positive LS effect in secondary mode compared to HS injection. This incremental recovery is higher for M=1 (42% total recovery compared to 34% for the HS case), as the viscous forces in the aqueous phase are close to those in the oleic phase. Thus higher pressure values are expected to be maintained in the network and more oil displacements are expected when the capillary pressures are reduced for this viscosity ratio. This also explains the small positive tertiary LS effect, with oil recovery increasing by an average of 2%. Note also that at this viscous ratio, no change of the flow regime is expected (in contrast to the M=10 case), and the growth pattern is expected to remain similar to capillary fingering.

For M=100, the regime is expected to revert to viscous fingering, and secondary LS water injection results in additional recovery (an average of 15% compared to 12% for HS water injection) due to the reduction of capillary entry pressures. No tertiary LS injection effect is observed, however, due to the weak viscous forces in the aqueous phase (which make it difficult to displace more oil after the reduction in contact angles, especially after the decrease in global pressure following breakthrough).

Effect of Flow Rate

We studied the effect of LS water injection in both secondary and tertiary modes for three frontal advance rate values: 1m/day, 5m/day and 10m/day. Simulated final recovery results are presented in Figure 8.14.

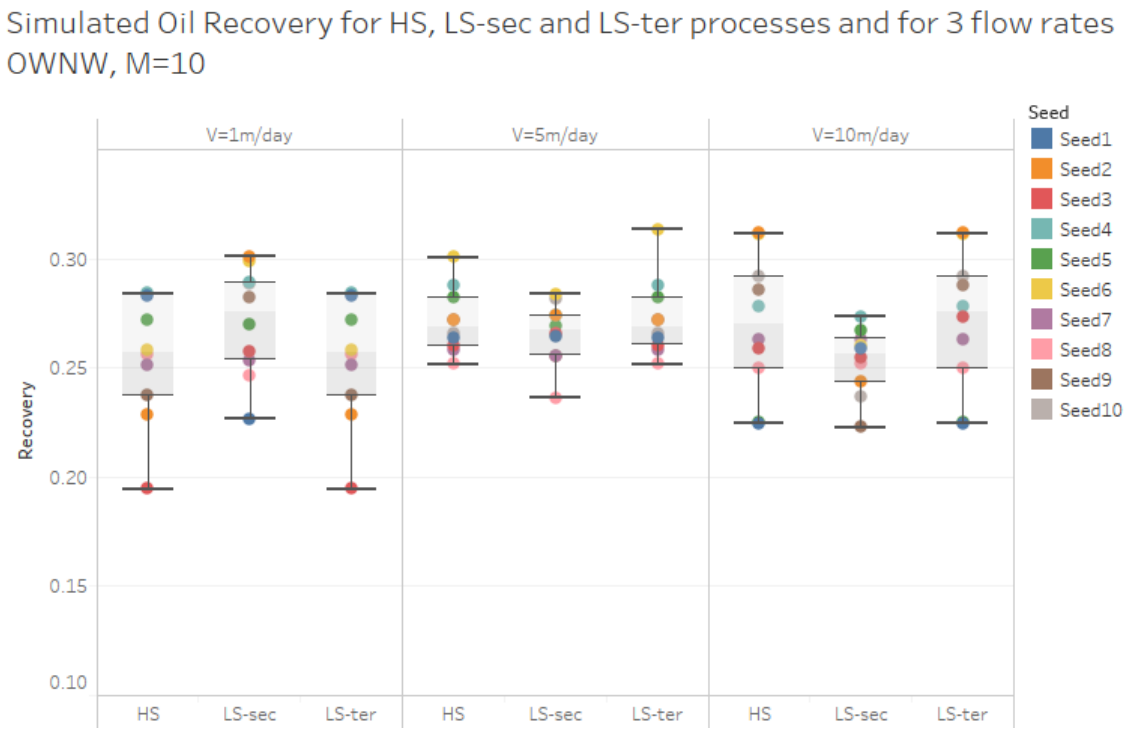

Figure 8.14: Final oil recovery after 4 PVs for: HS, LS-sec and LS-ter processes. Three frontal advance rates are considered: 1m/s, 5m/s and 10m/s. Ten seeds are considered for each case.

These results show that the flow rate also plays a key role in determining the efficacy of LS injection in secondary mode. As discussed earlier, the change of regime from a capillary growth pattern to viscous fingering results in a negative LS effect for V=5m/day (base case). This behaviour is magnified for V=10m/day where the fingers are expected to be thinner, and thus the final recovery is, on averagen 5% less that the final recovery achieved during HS water injection. In contrast, when the flow rate is low enough to prevent any regime change – as is the case for V=1m/day – a positive LS effect is observed (an increase of approximately 4% compared to the HS case). No tertiary LS effect was obtained for the three cases studied .

8.4.3 Polymer Effect

Base Case

We now use the same 2D networks described in the previous section to examine the effect of polymer injection in both secondary and tertiary modes. The polymer applied in the base case scenario changes the water viscosity from $1cP$ to $5cP$ and oil recovery profiles for these two cases are presented in Figure 8.15.

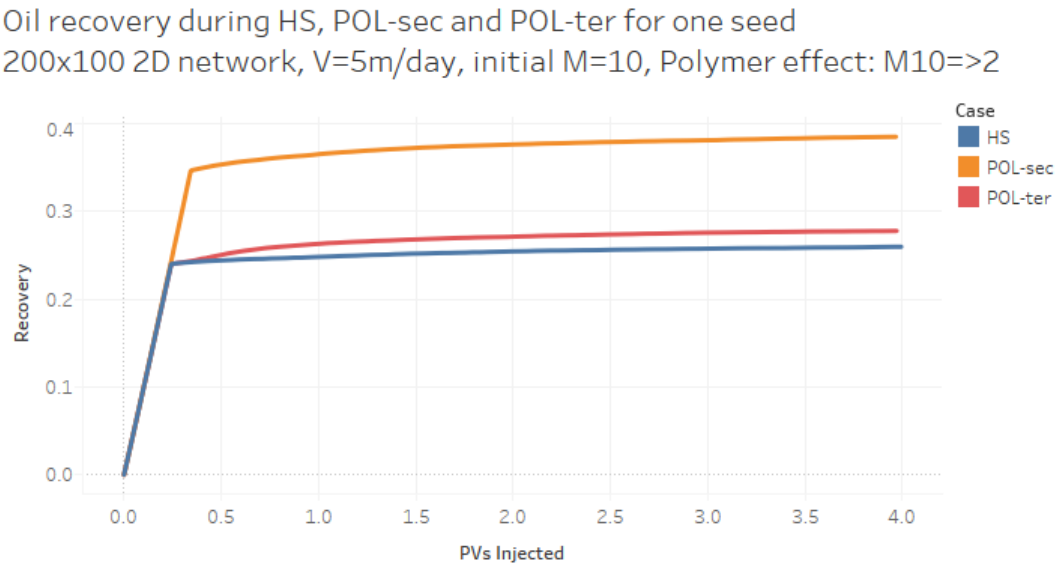

Figure 8.15: Oil recovery profile for HS, POL-sec and POL-ter processes.

Both injection modes yield better recovery compared to HS water injection – polymer injection in secondary mode is particularly efficient as almost 40% of the OOIP is displaced compared to an average of 25% when injecting HS water.

In order to consolidate these findings, ten seeds were used to simulate the same flow configuration on ten statistically-equivalent networks. Final oil recovery results are presented in Figure 8.16.

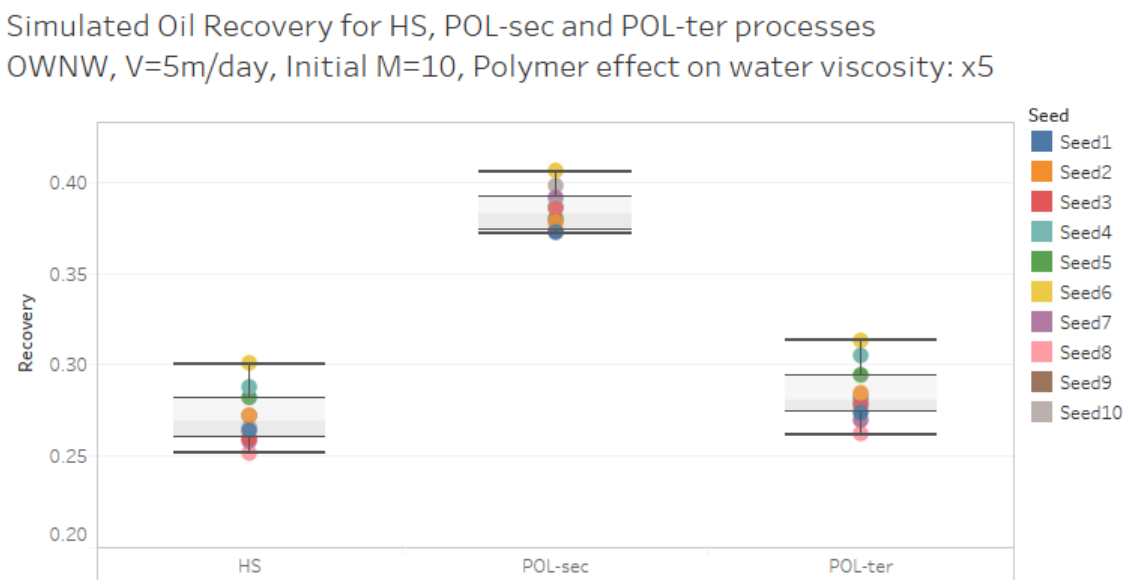

Figure 8.16: Final oil recovery after 4 PVs for: HS, POL-sec and POL-ter processes. Ten seeds are considered for each case.

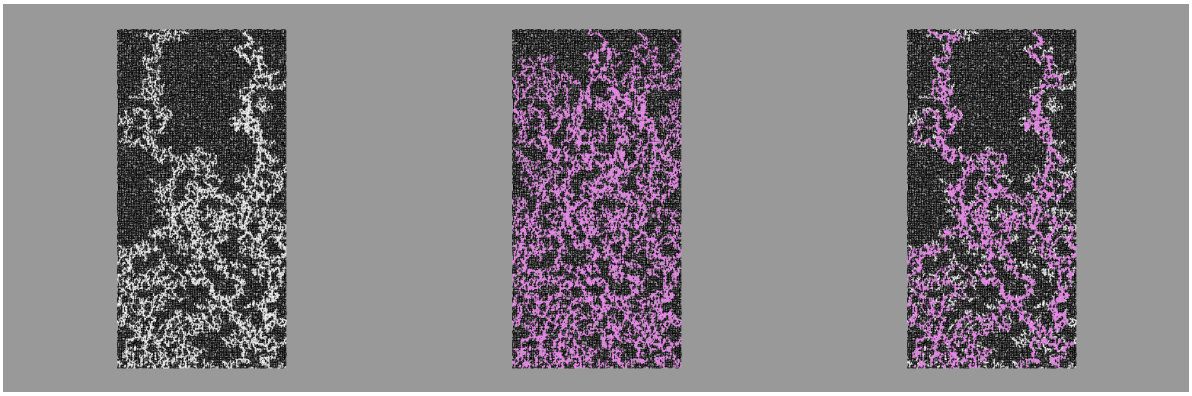

Figure 8.17: Final water distribution after 4PVs of HS water injection (left) Polymer injected in secondary mode (middle) and Polymer injected in tertiary mode (right). Wettability configuration: Oil-Wet. HS water is coloured in white, Polymer in pink and oil in black.

The IQRs corresponding to the ten simulation results for each process clearly confirm a higher recovery when applying polymer in both modes. In secondary mode, the polymer modifies the flow regime from capillary fingering to stable displacement due to the change in capillary number. As for tertiary mode, the polymer causes the water fingers to thicken and swell due to the increased pressure gradients at the tip of the capillary fingers. This is shown in Figure demnstrate8.17 where the water distribution after four pore volumes of injection is displayed.

Degree of Polymer Induced Viscosity Change

We now investigate the impact of the degree of polymer-induced viscosity change on final recovery. We consider two types of polymer – the first changes water viscosity from $1cP$ to $5cP$, whilst the second changes it from $1cP$ to $10cP$. Results of the final oil recoveries are presented in Figure 8.18.

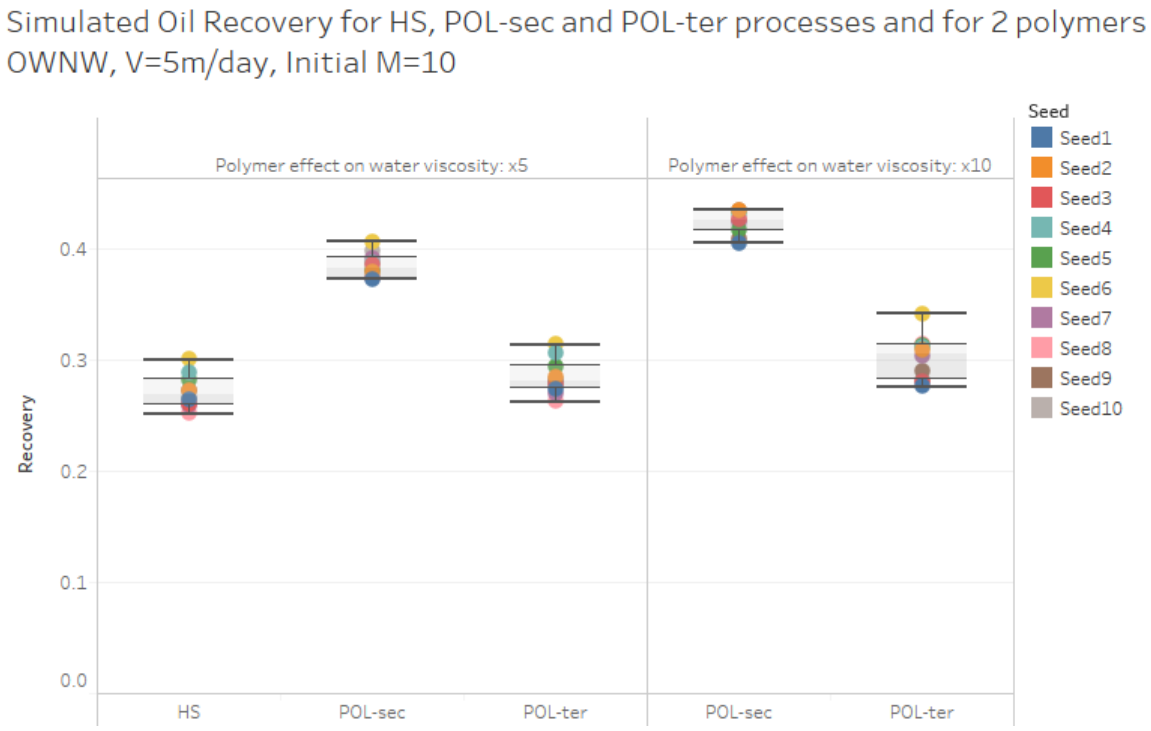

Figure 8.18: Final oil recovery after 4 PVs for: HS, POL-sec and POL-ter processes. Two polymer viscosity changes are considered: $M : 10 \Rightarrow 2$ and $M : 10 \Rightarrow 1$. Ten seeds are considered for each case.

Water viscosity is increased ten times in the second case (compared to five times in the base case) and the oil recovery is slightly higher (for secondary mode, an average of 42% of OOIP is obtained for $\Delta\mu_{water} = 10$ compared to an average of 38% for $\Delta\mu_{water} = 5$). Both secondary and tertiary modes yield a positive effect on recovery. Whilst the injected polymer stabilises the injection front for both $\Delta\mu_{water} = 10$ and $\Delta\mu_{water} = 5$, our results show that the increase in final recovery is not directly proportional to the viscosity change.

Effect of Initial Viscous Ratio M

The effect of initial viscous ratio is examined in this section using the same polymer as was applied in the base case ($\Delta\mu_{water} = 5$). Three oil viscosity values are considered: 1cP (initial M=1), 10cP (initial M=10 – base case), and 100cP (ini-

tial M=100). The final oil recoveries for HS, POL-sec and POL-ter processes are presented in Figure 8.19.

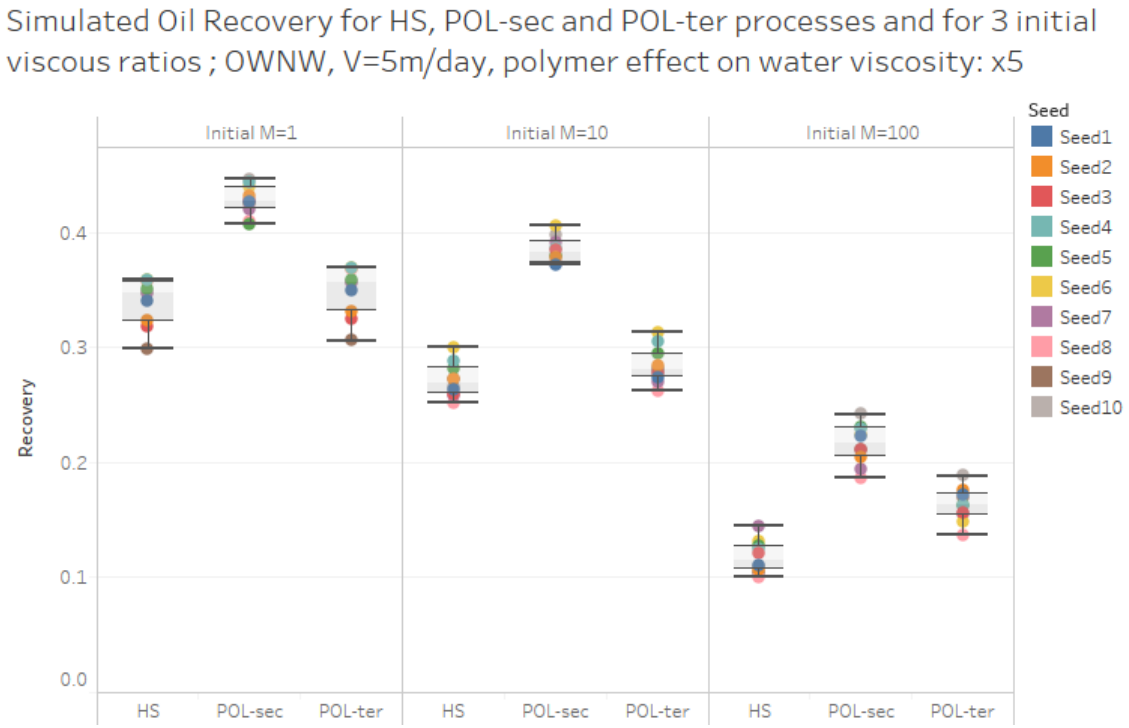

Figure 8.19: Final oil recovery after 4 PVs for: HS, POL-sec and POL-ter processes. Three initial viscous ratios are considered: 1, 10 and 100. Ten seeds are considered for each case.

A positive polymer effect is observed for all cases to a greater or lesser extent. It appears for instance that a greater tertiary effect is observed for $M_{t=0}$=100 (16% oil recovery compared to 12% for HS process), whilst additional oil recovery during tertiary polymer injection is negligible for $M_{t=0}$=1 and $M_{t=0}$=10 cases. This observation is also valid when polymer is injected in secondary mode, with oil recovery for POL-sec almost doubled compared to the HS case for $M_{t=0}$=100. This can be explained once again by a shift of flow regime from viscous fingering to capillary fingering, where polymer injection stabilises the viscous fingers and allows significant additional recovery due to finger swelling and thickening.

Effect of Flow Rate

We end our sensitivity analysis of polymer flooding by examining the effect of flow rate on recovery. Secondary and tertiary polymer injection processes are simulated alongside HS water injection. Three frontal advance rates are used: V=1m/day, V=5m/day and V=10m/day. The final oil recovery results are shown in Figure 8.20.

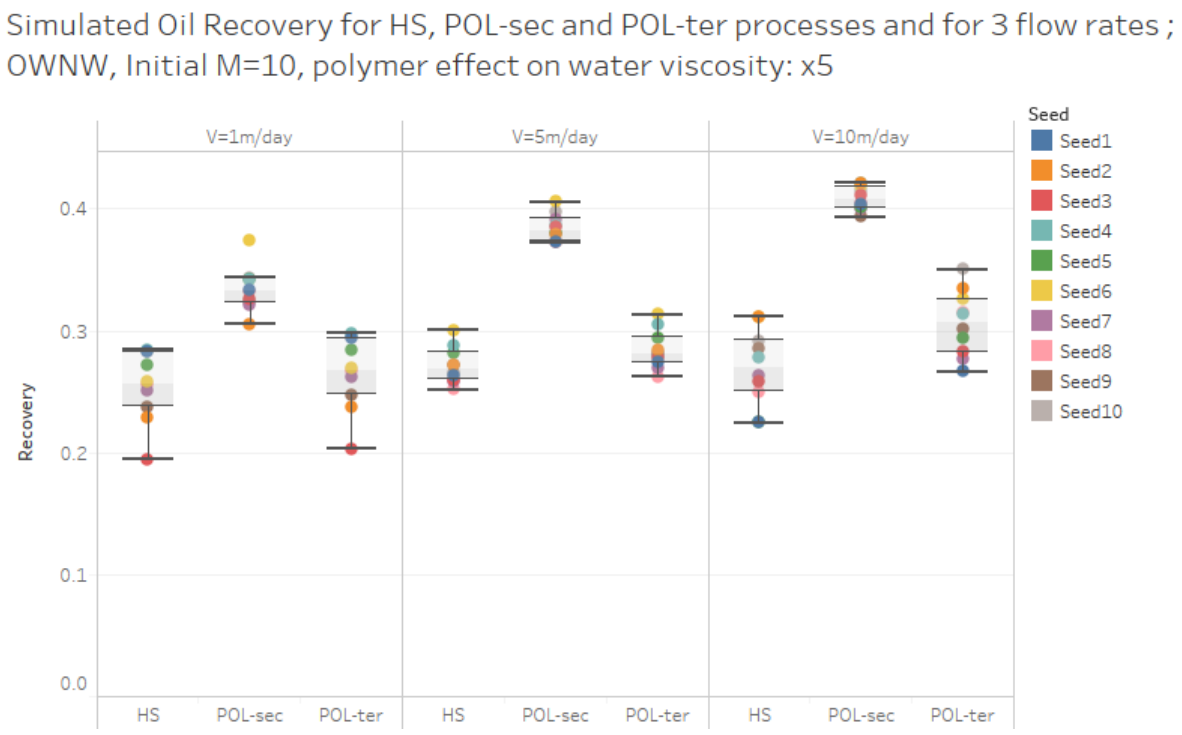

Figure 8.20: Final oil recovery after 4 PVs for: HS, LS-sec and LS-ter processes. Three frontal advance rates are considered: 1m/day, 5m/day and 10m/day. Ten seeds are considered for each case.

Results show that additional oil recovery due to polymer injection increases monotonically with injection rate in both secondary and tertiary mode. For instance, almost 33% of OOIP is recovered for V=1m/day during secondary polymer injection compared to 41% for V=10m/day using the same process. Additional recovery following tertiary polymer injection is also more pronounced for V=10m/day compared to V=1m/day, where additional recovery is relatively small.

The correlation between polymer efficacy and flow rate is due to the fact that an increase in the latter induces steeper pressure gradients across the system, thereby increasing water viscous forces and switching the flood from capillary-dominated to stable frontal advance. This suggests that polymer injection may be more efficient at higher injection rates.

8.4.4 Synergy Between Low Salinity and Polymer

Base Case

We now investigate a number of possible injection synergies by combining both LS water and polymer. As a first set of simulations, we consider the simultaneous injection of polymer and LS water in secondary and tertiary modes, and we maintain

the base case parameters described earlier (LS effect: OWNW, polymer induced viscosity variation: $\Delta\mu_{water}$ = 5, V=5m/day, $M_{t=0}$=10). The oil recovery profiles for these processes simulated using a single random number seed are shown in Figure 8.21.

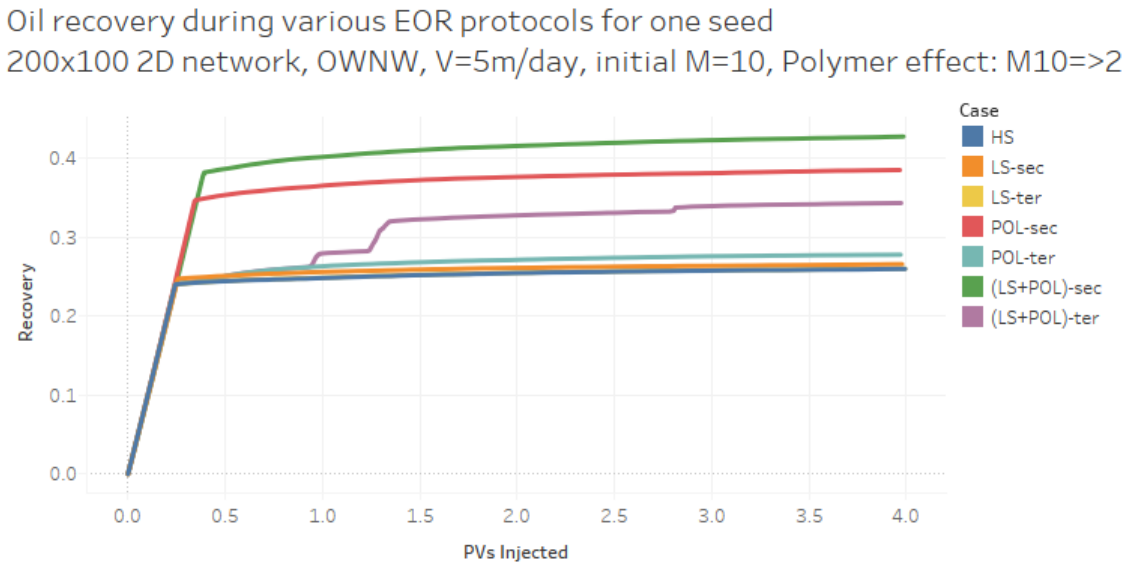

Figure 8.21: Oil recovery profile for HS, POL-sec, POL-ter, (LS+POL)-sec and (LS+POL)-ter processes. [as an aside, the sudden increase in water saturation at PV injected = 0.8, 1.3 and 2.8 for (LS-POL)-ter corresponds to the emergence of new fingers breaking through the network.]

These initial simulations show a clear positive effect when combining both EOR processes. Injecting both LS water and polymer together yields better recovery than those achieved using each one separately – this is valid for both secondary and tertiary modes. To validate these findings, we repeated the simulations for ten seeds for all the injection protocols described in Section 8.4.1. The full range of recovery data are displayed in Figure 8.22.

The statistical dispersion in the final oil recovery results for the base case parameters (over the ten seeds) shows a clear positive synergistic effect when LS water and polymer are combined. Mixing LS water and polymer in secondary mode appears to be more efficient than injecting LS or polymer separately. Similarly, injecting polymer in tertiary mode (i.e. after HS water breakthrough) either prior to or alongside LS water yields better recovery compared to using only polymer or only LS water.

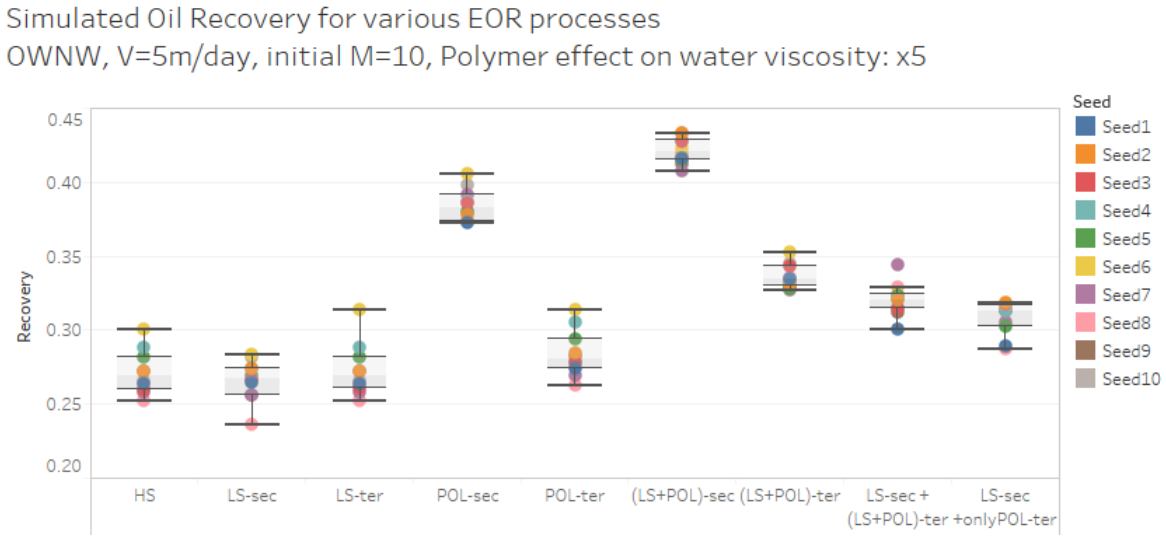

Figure 8.22: Final oil recovery after 4 PVs for various EOR processes. Ten seeds are considered for each case.

Note that despite the negative effect on recovery when LS water is injected alone in secondary mode (due to the regime shift described in the LS section earlier), the combined injection of polymer and LS water gives additional recovery that is greater than that obtained by injecting polymer alone. This can be explained by (i) the stabilisation of the water fingers, and (ii) the fact that LS water is able to access more of the pore network due to the higher viscous forces induced by the polymer. Figure 8.23, which shows the final water distributions after applying all the aforementioned processes in one network, confirms this finding. In secondary mode, the mixture of polymer and LS water stabilises the water profile and shifts the flow regime from viscous/capillary fingering to stable displacement. The mixture of polymer and LS water also causes the capillary fingers to thicken and swell.

Effect of Wettability Change

The way in which LS water modifies the wettability configuration of the pore network and its effect on the synergy between LS water and polymer is now examined. The same wettability modification scenarios discussed in the LS section are considered: OWOW, OWNW and OWWW. Results are displayed in Figure 8.24.

Combining LS water and polymer is found to operate synergetically for most wettability change scenarios (although there are few exceptions). It also appears that the combination works most effectively for OWNW systems compared to OWOW cases. This result can be explained by considering the variation in contact angles, which is larger in the OWNW case ($\Delta\theta = 45°$) compared to the OWOW case ($\Delta\theta = 30°$). This suggests that a positive synergistic effect is expected when LS brine shifts the

wettability of the rock to a more neutral-wet state. The same observation is valid when polymer is injected in tertiary mode with LS water, as greater additional recovery is achieved for the OWNW case compared to the OWOW case.

It appears, however, that combining LS water and polymer in secondary mode is detrimental in the OWWW scenario. Less oil recovery is obtained compared to the case where polymer is injected alone (POL-sec). This apparently contradictory result is related to the trapping of oil clusters. Whilst bypassed oil clusters can be recovered over time due to film flow in the OWNW and OWOW cases, this is not possible for the OWWW case, as the oil-wet pathways initially available to transport oil to the outlet are removed following wettability conversion – oil can no longer escape via films. This effect does not affect the synergy when polymer is injected in tertiary mode, however, and more oil is recovered compared to cases where LS-water and polymer are injected separately for the OWWW scenario.

Effect of the Initial Viscous Ratio M

The impact of the initial viscous ratio is now presented for the various combinations of LS water and polymer injection. The additional oil recovery results are shown in Figure 8.25.

When LS and polymer are injected simultaneously in secondary mode, a significant positive synergetic effect is observed for all viscous ratios. For $M_{t=0}$=1 in particular, the final oil recovery has almost increased by 10% of the OOIP due to the combination of LS water and polymer – the mixture stabilises the frontal advance of water resulting in more stable displacements and only small oil clusters are left behind (yielding better recovery).

When polymer is injected in tertiary mode alongside LS water, the positive synergistic effect is also apparent for the three different viscous ratios. In fact, whilst most of the injected LS brine remains in the main spanning water fingers when LS is injected alone in tertiary mode (which explains the absence of a LS effect for LS-ter case in most cases), the mixture of polymer and LS water allows the latter to reach more network pores yielding more stable frontal advance and greater recovery than that obtained by injecting only polymer or LS water.

Effect of the Flow Rate

We end this section with a discussion of the effect of injection rate on the synergistic effect of combined LS water and polymer flooding. Figure 8.26 shows the extent of

additional oil recovery for the different studied EOR combinations.

When LS water and polymer are injected together in secondary mode, a greater synergy is achieved for lower flow rates (V=1m/day). On average, 42% of oil is recovered compared to 33% when only polymer is injected in secondary mode. As the flow rate increases, the synergistic effect starts to decline and the additional recovery becomes similar to that obtained by injecting only polymer. In fact, as the flow rate increases the viscous forces become predominant whilst the capillary forces become negligible – the effect of LS wettability modification is therefore lost when viscous forces are too high. This highlights the fact that both polymer and LS water affect oil recovery by shifting the balance between viscous and capillary forces and changing the flow regime toward a more favourable configuration. If the effect of one mechanism is negligible compared to another, then no synergy is expected to emerge when these are applied simultaneously.

When polymer is injected in tertiary mode, it is not immediately clear how the synergy between LS water and polymer is affected by the flow rate. It appears that the timing of LS injection plays a key role. For instance, when polymer and LS water are injected simultaneously immediately after HS water breakthrough ((LS+POL)-ter), a greater synergy is observed for high flow rates (V=10m/day, 5m/day). However, when polymer is injected after *LS* water breakthrough (LS-sec+(LS+POL)-ter), greater synergy is achieved for *low* flow rates. These observations show the importance of the order of applied EOR techniques: two scenarios involving the same EOR mechanisms but applied in a different order might yield different oil recovery results. The timing of the application of two or more EOR techniques and the impact on oil recovery provide an interesting area for future study.

8.5 Conclusions

In this chapter, we introduced a new formulation to study the effect of EOR processes using the unsteady-state drainage pore network model. Both LS water and polymer have been considered by adopting a pragmatic approach where the manifestations of the underlying complex chemistry have been implemented. 690 simulations have been carried out (Table 8.4) to study the effect of LS water and polymer injection on oil recovery in 2D oil-wet networks in secondary and tertiary mode. The synergy between the two processes has also been investigated.

A statistical approach has been introduced to quantify the effect of each EOR process. Instead of relying on one single simulation, different seeds have been considered. This has proved to be a crucial aspect when predictions need to be made

at the pore scale, as two similar networks statistically generated with two different seeds might yield contradictory outcomes. We believe this also holds when it comes to the use of microCT digital networks: whilst these networks capture the irregularity of the underlying rocks, one small sample can not be adequate to generate reliable predictions, and large uncertainty is expected when quantitative simulations are made. Hence, it seems that the most appropriate way to use extracted networks from microCT images, is to simulate several samples extracted from various sections of the rock. Results should be then plotted using statistical dispersion graphs or curves representing the average outcome over all the runs.

The EOR study shows that both LS-water and polymer mechanisms can be affected by several key parameters and it is therefore difficult to predict *a priori* any outcome without running the actual simulation. Positive secondary effects have been observed in most cases and a change in the flow regime has been found to be a key mechanism by which an EOR application can affect additional oil recovery. It also appears that possible tertiary effects are more likely to occur for low viscous ratios and for wettability changes that shift the network to a water-wet configuration.

Positive synergy has been captured when both polymer and LS water are injected simultaneously. The combined effect yields a significant increase in oil recovery for several cases, especially when both LS water and polymer are injected in secondary mode. These findings are consistent with experimental observations of Shiran and Skauge (2013) [172]. Polymer injection tends to (i) stabilise the water advance and (ii) help LS-water reach previously unswept areas of the pore space. We also found that the synergistic effect interacts non-linearly with other flow parameters such as the initial viscous ratio and flow rate.

The simulations carried out in this work used mainly 2D networks and, although these networks provide valuable insights into the effect of the EOR processes studied, we note that the third dimension is also an important factor that could affect the results. The trapping mechanisms, for instance, are different between 2D and 3D networks, as water clusters have more space to swell in 3D space. Studying the effect of initial water saturation could also be affected by this aspect and so 3D simulations are needed to consolidate the conclusions reported here. This would require additional computational power, and optimising and speeding up the current code would be an important aspect to consider in the future.

The results presented here correspond to a single pore size distribution, coordination number and other network properties anchored from a Berea sandstone. Changing such parameters could possibly affect the manifestation of EOR mechanisms and yield different results from those shown in this work. This emphasises the complexity of phenomena occurring at the pore-scale and makes the *numSCAL* simulator a

valuable numerical laboratory to investigate a wide variety of experimental data and examine scenarios that can be challenging to realise experimentally.

Additional mechanisms could also be added to improve the modelling of polymer solutions and LS-water. The model currently considers convection as the main mechanism for tracer transport: diffusion could be implemented in future work and this might be relevant at very low flow rates. Polymer adsorption, microscopic diversion and fines migration should also be considered in future models to improve the predictive power of the simulator.

Table 8.4: Summary table of the recovery results in the EOR study. Final oil recovery (top cell) and additional oil recovery compared to HS injection case (bottom cell) are displayed for each EOR process and configuration discussed in this work.

Average Oil Recovery (%OOIP)
0.00% 50.00%

Configuration	Injection Process								
	HS	LS-sec	LS-ter	POL-sec	POL-ter	(LS+POL)-sec	(LS+POL)-ter	LS-sec +(LS+POL)-ter	LS-sec +onlyPOL-ter
Wettability: OW=>NW - V=5m/day - Initial M=10 - Polymer effect on water viscosity: x5	27.13% 0.00%	26.59% -1.90%	27.26% 0.45%	38.44% 41.96%	28.41% 4.73%	42.12% 55.64%	33.60% 24.13%	32.02% 18.36%	30.72% 13.45%
Wettability: OW=>NW - V=5m/day - Initial M=10 - Polymer effect on water viscosity: x10	N/A	N/A	N/A	42.38% 56.59%	30.19% 11.35%	46.71% 72.55%	35.41% 30.97%	33.68% 24.54%	32.28% 19.25%
Wettability: OW=>NW - V=1m/day - Initial M=10 - Polymer effect on water viscosity: x5	25.47% 0.00%	27.12% 7.85%	25.48% 0.00%	33.43% 32.55%	26.57% 4.32%	40.63% 61.46%	28.10% 10.74%	30.76% 21.98%	29.62% 17.73%
Wettability: OW=>NW - V=10m/day - Initial M=10 - Polymer effect on water viscosity: x5	26.98% 0.00%	25.31% -4.75%	27.15% 0.63%	40.89% 53.23%	30.61% 14.09%	42.13% 57.91%	34.14% 27.86%	30.01% 12.58%	29.96% 12.57%
Wettability: OW=>NW - V=5m/day - Initial M=1 - Polymer effect on water viscosity: x5	34.02% 0.00%	41.55% 22.51%	34.77% 2.26%	42.78% 26.16%	34.91% 2.60%	51.61% 52.21%	38.81% 14.17%	43.94% 29.51%	44.10% 30.05%
Wettability: OW=>NW - V=5m/day - Initial M=100 - Polymer effect on water viscosity: x5	11.79% 0.00%	14.49% 24.68%	11.81% 0.09%	21.56% 84.85%	16.26% 39.90%	21.49% 84.57%	19.20% 66.70%	19.40% 66.19%	20.41% 74.98%
Wettability: OW=>OW - V=5m/day - Initial M=10 - Polymer effect on water viscosity: x5	27.13% 0.00%	26.91% -0.63%	27.13% 0.00%	38.44% 41.96%	28.41% 4.73%	41.18% 52.09%	30.28% 11.79%	31.05% 14.65%	31.20% 15.28%
Wettability: OW=>WW - V=5m/day - Initial M=10 - Polymer effect on water viscosity: x5	27.13% 0.00%	31.72% 17.23%	28.18% 4.00%	38.44% 41.96%	28.41% 4.73%	35.87% 32.59%	32.51% 20.07%	31.74% 17.30%	31.74% 17.30%

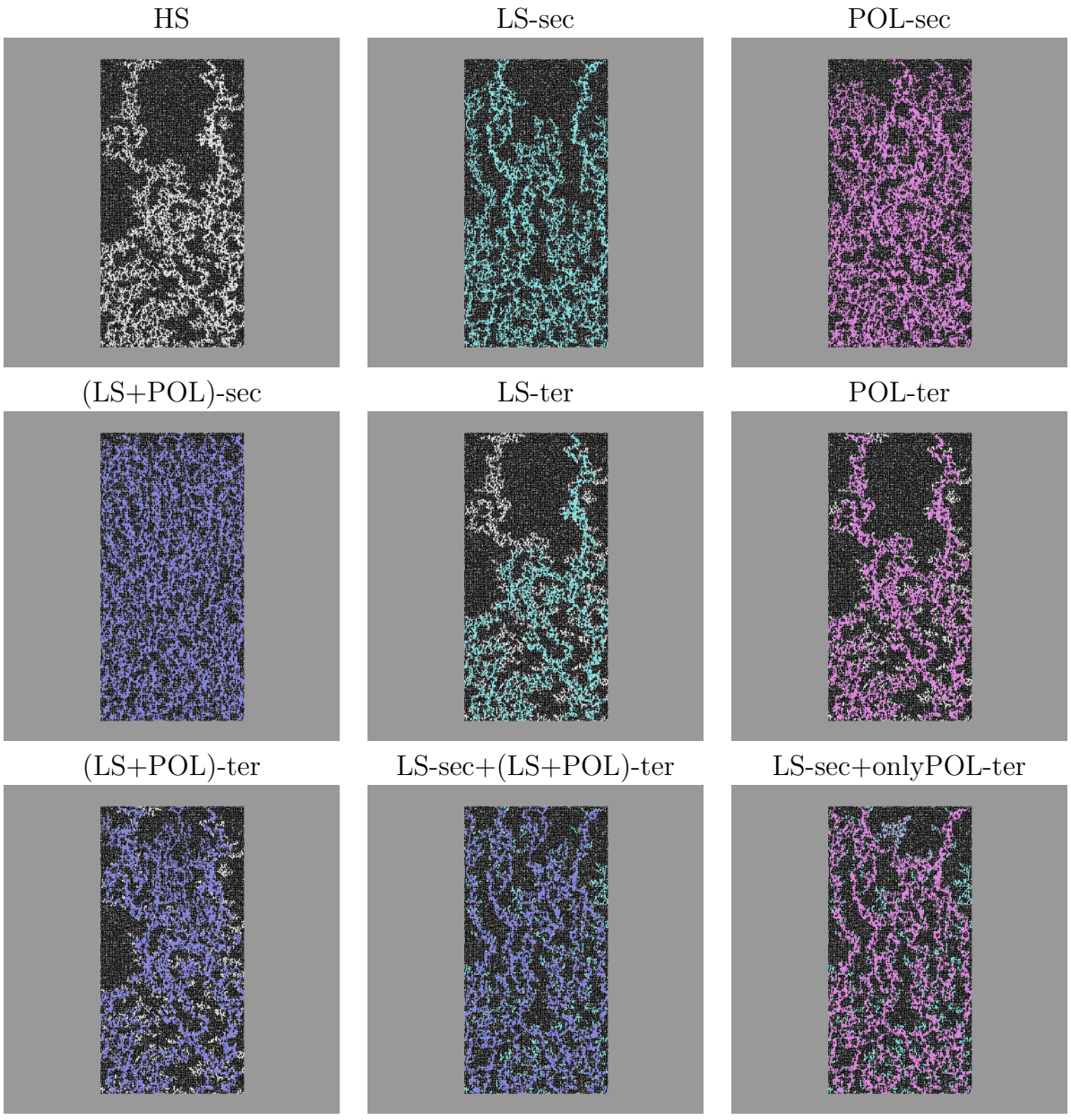

Figure 8.23: Final water distribution after 4PVs of various EOR processes. Wettability configuration: OWNW. HS water is coloured in white, LS water in light blue, Polymer in pink, LS-Polymer mixture in purple and oil in black.

Figure 8.24: Simulated oil recovery after 4 PVs for various EOR processes. Three wettability configurations are considered: OWOW, OWNW and OWWW. Ten seeds are used for each case. V=5m/day; Initial M=10; Effect of polymer on water viscosity: x5.

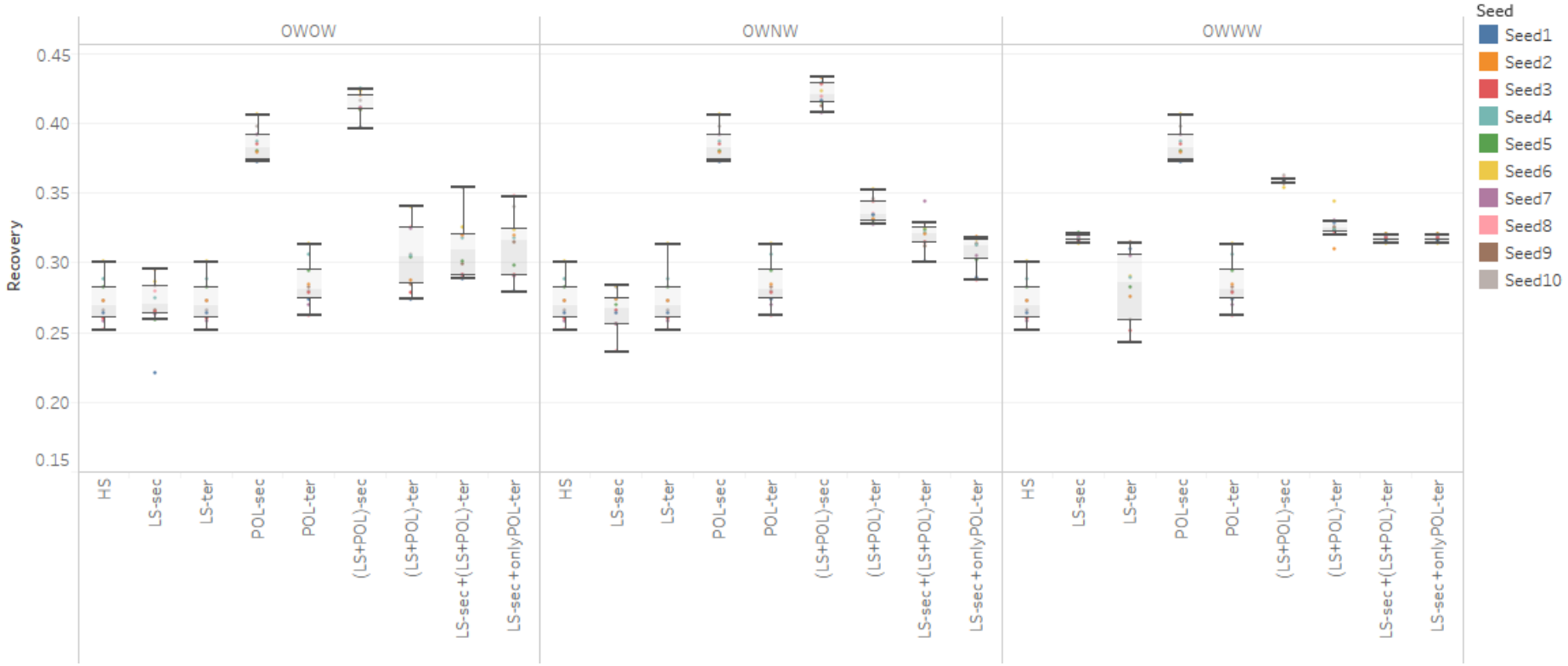

Figure 8.25: Simulated oil recovery after 4 PVs for various EOR processes. Three different initial viscous ratios are considered: 1, 10 and 100. Ten seeds are used for each case. OWNW; V=5m/day; Effect of polymer on water viscosity: x5.

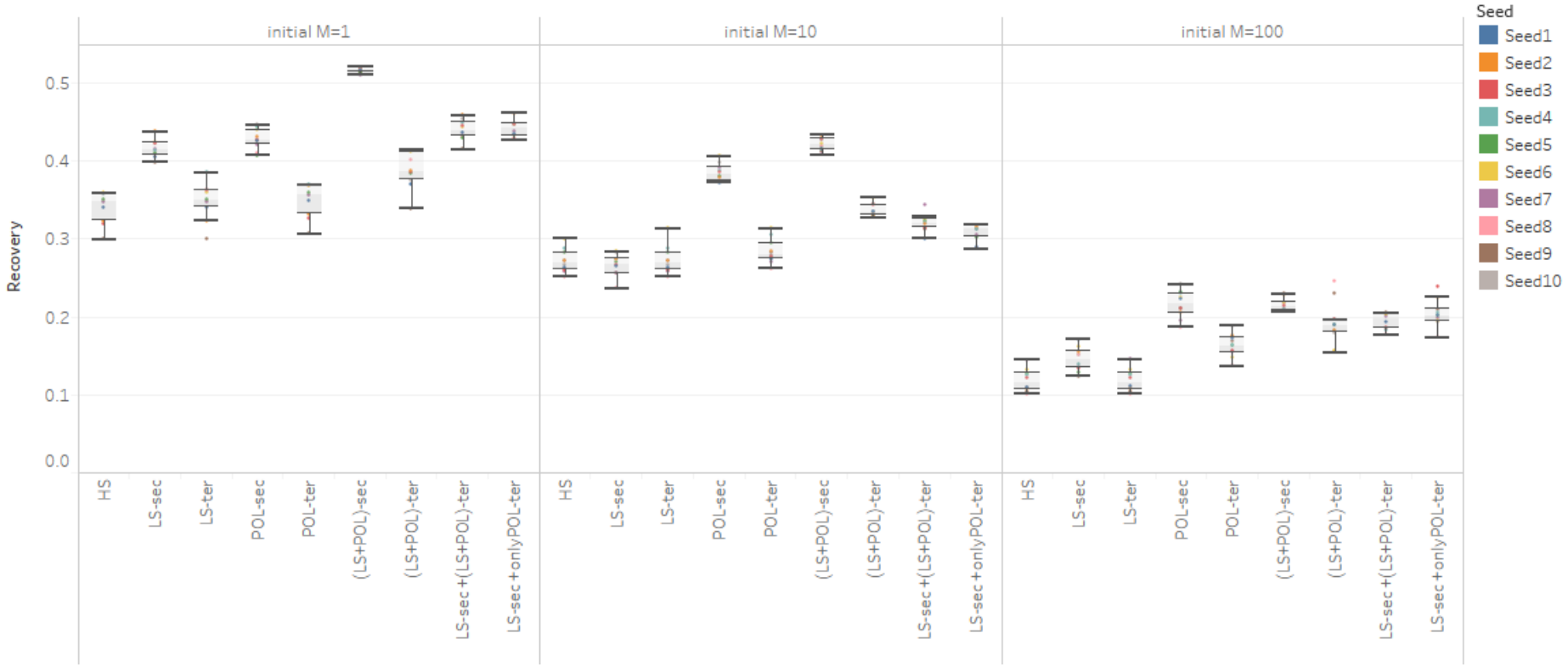

Figure 8.26: Simulated oil recovery after 4 PVs for carious EOR processes. Three different flow rates are considered: 1m/s, 5m/s and 10m/s. Ten seeds are used for each case. OWNW; Initial M=10; Effect of polymer on water viscosity: x5.

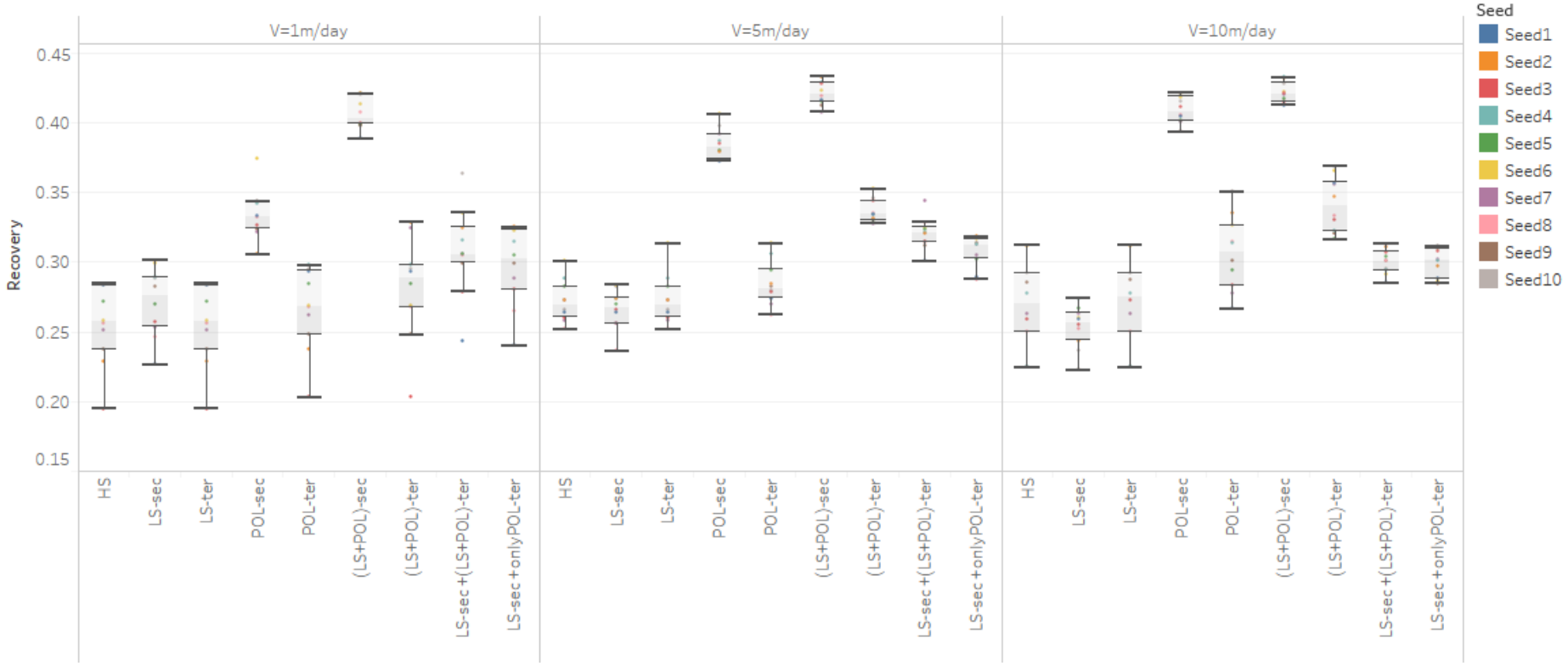

Chapter 9

Beyond the Oil Industry: Pore Network Modelling Applied to Mathematical Biology

9.1 Introduction

The pore network models we have presented so far have been implemented to simulate processes related to oil, gas and water flow in oil reservoirs. The porous structure inside the rock matrix constituted the spatial domain where those fluids were allowed to flow according to various mechanistic approaches. The application of pore network modelling is, however, not unique to petroleum engineering, and similar numerical models can be conceived to simulate many phenomena involving flow in porous media.

Over the last two decades, numerous flow models have been implemented to simulate biological processes involving fluid flow at the micro-scale. The Heriot-Watt pore-network modelling group has been at the forefront of building novel flow models that target phenomena such as tumour growth, angiogenesis, blood flow, wound healing and retina development (McDougall et al., 2012 [176] [177]; Watson et al. 2011[178]; McDougall et al. 2006,2002 [179, 180, 181, 182]). Here, we introduce a new model for simulating drug delivery to a type of brain tumour known as Glioblastoma Multiform (GBM) through an irregular network of blood vessels. The model has been created as part of a new C++ simulator – *bioFLOW* – which has been adapted from the original *numSCAL* package.

We begin this chapter by presenting the *bioFLOW* software and the models it supports, and we go on to discuss the methods implemented to model drug flow in

vascular networks surrounding GBM tumours. We describe the approach adopted to build the network of the vasculature from MRI images, and we discuss both drug perfusion and tissue diffusion algorithms in detail. We finally present the results of simulations carried out to investigate the impact of key parameters – such as membrane permeability and blood flow rate – on the effectiveness of drug therapy.

9.2 *bioFLOW* Features

bioFLOW is a new C++ simulator that has been implemented in this work as a fork of *numSCAL* in order to simulate a wide range of processes related to mathematical biology (Figure 9.1).

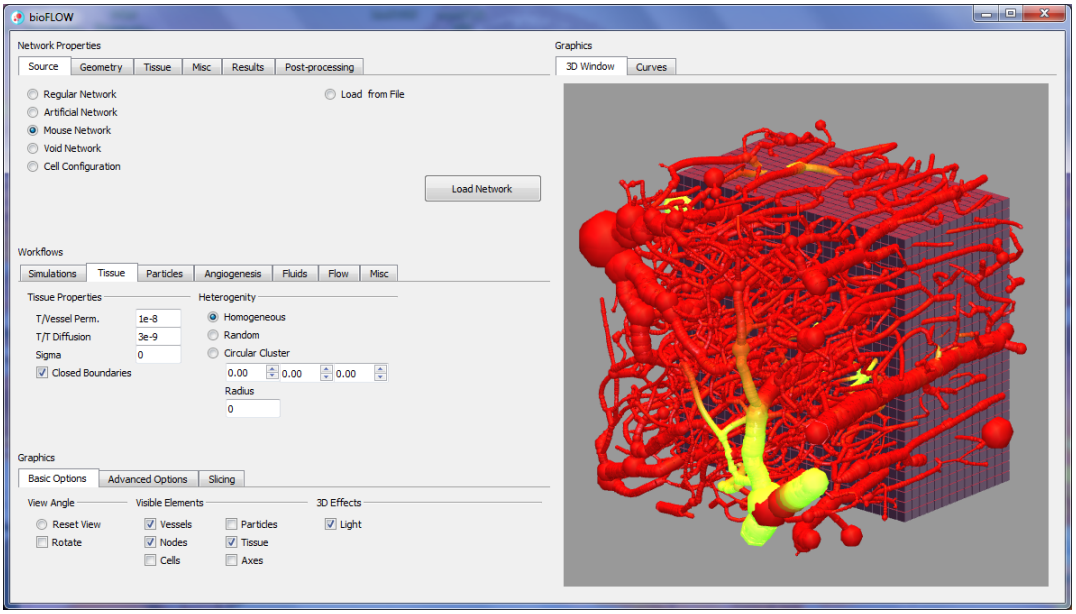

Figure 9.1: A screenshot of *bioFLOW* software.

The capillary bed has a similar structure to rock topology, where interconnected cylindrical elements are used to model a network of blood vessels. Alongside regular networks, realistic networks of vasculature obtained from MRI images are fully supported (Figure 9.2). In addition, when diffusion into the tissue surrounding the vessels is under investigation, we model it using an embedded regular grid consisting of interconnected cubic blocks (Figure 9.2).

At the time of writing, *bioFLOW* is capable of simulating the following phenomena:

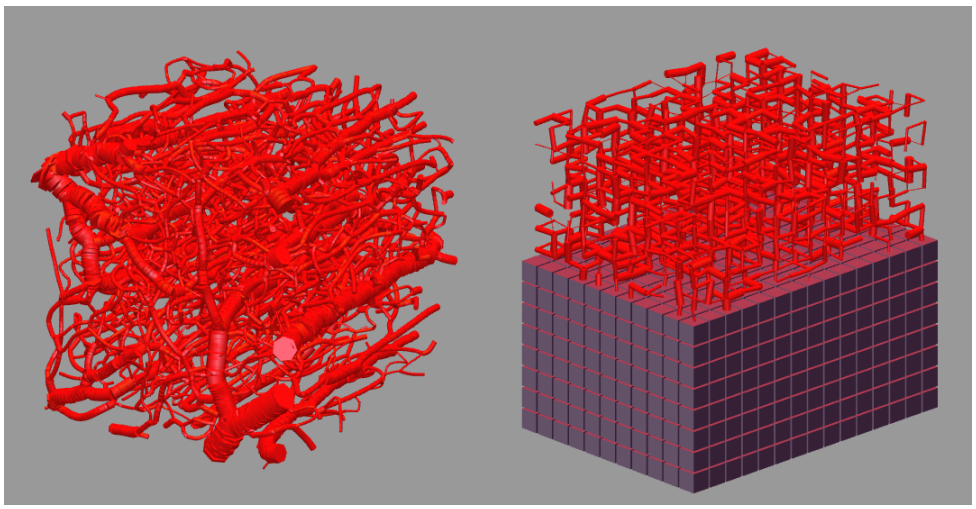

Figure 9.2: A vascular network extracted from MRI images (left) A regular vascular network surrounded by a tissue mesh (right).

Particle Flow

This module simulates the flow of individual particles (e.g. metastatic tumour fragments, or diagnostic microbubbles) through a vascular network (Figure 9.3). The model solves the pressure field in the underlying network and particles are assigned velocities according to the elementary flows in the vessels. When a particle reaches a junction with several downstream vessels, the likelihood for it to enter a particular vessel is directly proportional to its fractional flow. This module has been used in collaboration with a signal processing team at Heriot-Watt University to help build reliable algorithms to track ultrasound particles used to reconstruct vascular maps.

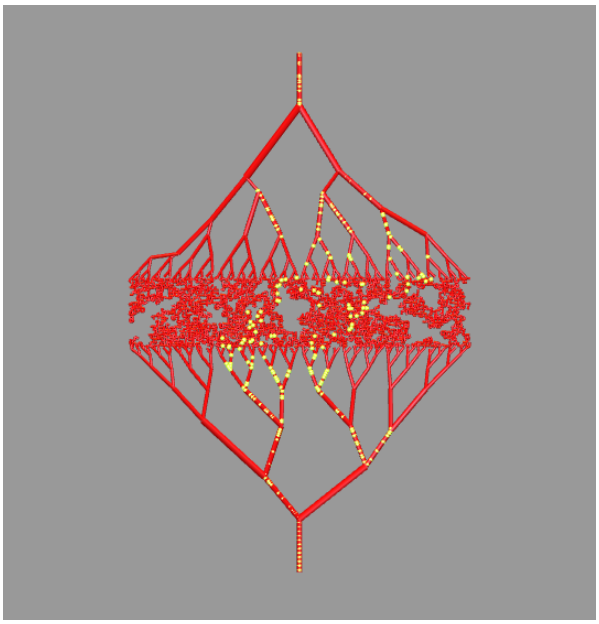

Figure 9.3: Particle flow in an artificial vascular network.

Cell Proliferation

This module simulates the growth and proliferation of individual cancerous cells, and has been implemented in collaboration with a mathematical biology team from St Andrews University (Figure 9.4). The model is currently being adapted to include angiogenesis – the growth of new blood vessels in response to the chemicals sent by cancerous cells.

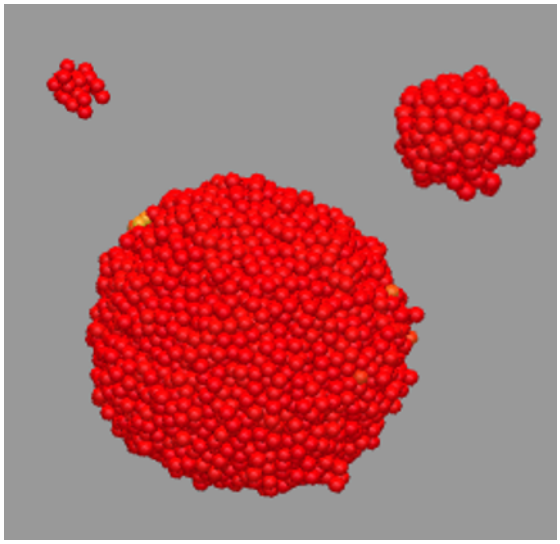

Figure 9.4: Proliferation of cancerous cells at different timesteps.

Drug Delivery

This module simulates drug flow in regular and irregular vasculatures derived from MRI images. The model has been implemented in collaboration with a team from Harvard Medical School and St Andrews University, and will be discussed in detail in the next section (more details can be found in Boujelben et al., 2016 [183]).

9.3 Mathematical Modelling of drug delivery to Glioblastomas

9.3.1 Background

Glioblastoma Multiform (GBM) is a challenging and aggressive tumour with a median overall survival time of less than fifteen months (Stupp et al., 2009 [184]). These tumours are usually perfused by an irregular vasculature characterised by high tortuosity and high membrane permeability. Such abnormal vascular structures are

believed to be the main reason for an impaired blood flow and unsatisfactory response to chemotherapy, as this hinders the delivery of therapeutic agents to the connected tumour (Wen and Kesari, 2008 [185]).

Anti-angiogenic therapy aims to normalise the tumour vasculature and has been hypothesised to improve drug delivery. However, it is of crucial importance to first determine the local drug distribution around the tumour in order to improve our understanding of the main parameters affecting drug effectiveness and design new protocols regarding the timing and dosing of drug injection for individual patients.

In-vivo Magnetic Resonance Imaging (MRI) has proved to be an excellent non-invasive tool to measure drug penetration to brain tumours (Figure 9.5) as well as facilitating the reconstruction of the 3D structure of the complex vascular network surrounding the tumour (Gagnon et al., 2015 [186]). This technique is unable, however, to accurately predict the dynamic evolution of local drug concentrations or to determine the impact of various parameters on drug effectiveness. However, combining the information provided by MRI data with mathematical models could provide such predictive tools to investigate the main mechanisms of drug delivery.

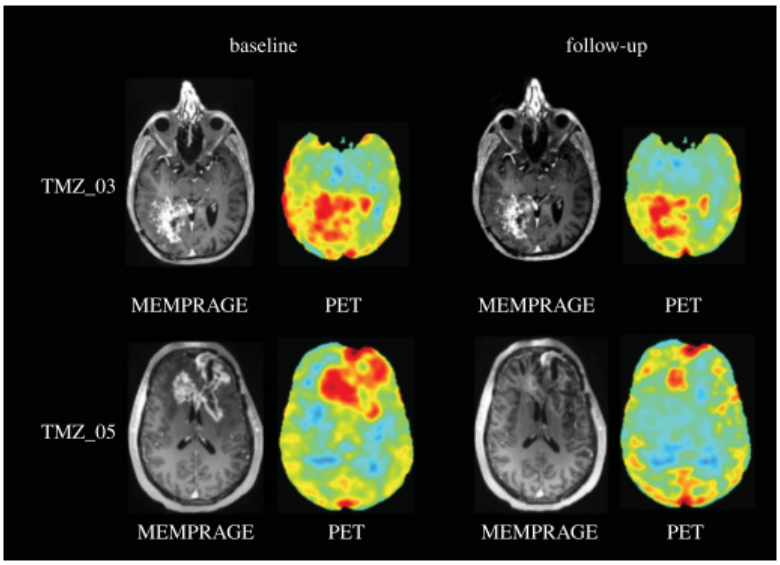

Figure 9.5: Post-contrast magnetic resonance (MR) and positron emission tomography (PET) images showing the distribution of radiolabelled temozolomide for two patients before (baseline, left-hand side) and after (follow-up, right-hand side) anti-angiogenic therapy. (Boujelben et al., 2016 [183])

In this work, we build a novel MRI-based proof-of-concept model to simulate drug flow into the actual structure of blood vessels derived from high resolution 3-D vascular networks surrounding GBM tumours in laboratory mice (Srinivasan et al., 2010 [187]). This allows a realistic investigation of the main features that govern drug delivery, including the membrane permeability of the vessels, the diffusion properties of the interstitial space and the underlying blood perfusion rate.

9.3.2 Model Description

In this work, we model a small block of mouse brain tissue ($0.6mm \times 0.6mm \times 0.6mm$) penetrated by an irregular interconnected network of capillary elements (Figure 9.6). The network is partitioned into nodes and edges and each element is assigned a range of intrinsic attributes (radius, length, vessel type, volume, conductivity). These attributes are extracted directly from MRI images of the mouse brain and incorporated into the structure network.

The network implemented here is completely off-lattice and inlet and outlet pressure boundary conditions are assigned based on the spatial position of venules and arterioles provided by the MRI images. The host tissue surrounding the vascular network is modelled using a regular cubic mesh comprising $30 \times 30 \times 30$ cubes, each of edge length $20\mu m$ (Figure 9.6). Starting initially with a full mesh, we then remove all blocks that lie completely within vessels and identify the capillary surface area between all vessels and their adjacent tissue cubes – this information is used later when computing the diffusive flux from a vessel to an adjacent cube (and vice versa).

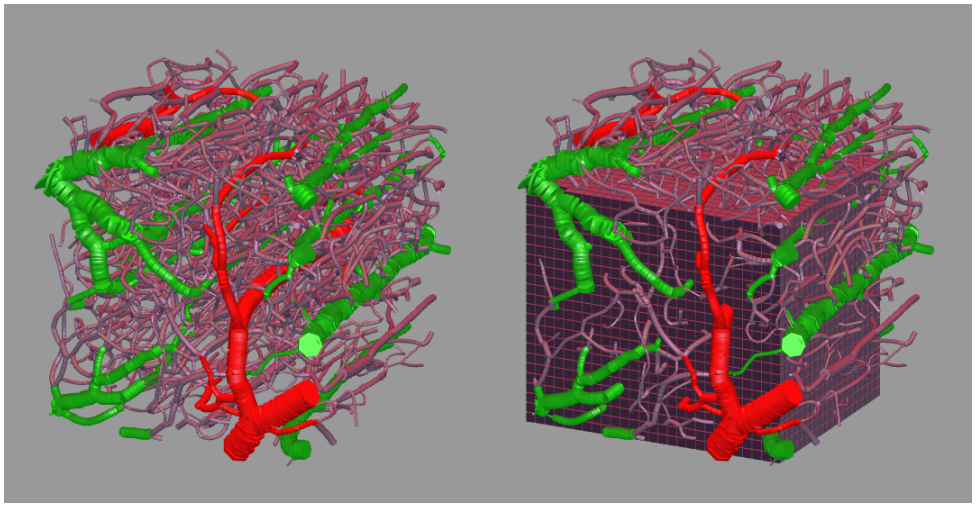

Figure 9.6: (left) Capillary network extracted from optical imaging of vessels surrounding a brain tumour: arterioles are coloured in red, venules in green and capillary elements in purple. (right) The same network surrounded by an 30 x 30 x 30 cubic mesh grid to model the tissue surrounding the vessels – only a slice of the grid is displayed in the figure.

9.3.3 Flow and diffusion

In order to update the tracer concentration within each capillary segment at each time step, we fix an inlet injection rate for the blood flow and compute the nodal pressure field allowing us to calculate the elementary flows within the system. For

each vascular element of shape factor G, length L and radius r, we assume that the flow Q is given by a Poiseuille-type law:

$$Q = \frac{A^2 G}{2\mu L} \Delta P \tag{9.1}$$

where μ is the effective blood viscosity in the element and ΔP the pressure difference acting across the element. By applying the pressure gradient corresponding to the selected blood flow rate, the pressure field inside a network is obtained by applying the mass conservation law at each node i according to:

$$\sum_i Q_{ij} = 0 \tag{9.2}$$

where $Q_{i,j}$ is the flow between node i and node j. We use Cholesky factorization to solve this system of linear equations and determine the pressure value at each node. For this work, we assume the flow of a simple incompressible Newtonian fluid, although complex blood rheology can be incorporated (McDougall et al., 2006 [180]).

When no drug is leaking across the vessel membrane, we can apply mass conservation at nodes to update the contrast agent concentrations within each capillary over time. The initial concentration is set to zero for all elements and we then inject a contrast agent into the inlet arterioles at dimensionless unit concentration.

If we consider the configuration described in Figure 9.7, where $C_{drug,i}$ and Q_i represent, respectively, the contrast agent concentration and the flow in capillary element i; the new tracer concentration after a time step Δt in capillary 1 is given by:

$$C_{drug,1,new} = C_{drug,1,old} + (\frac{Q_1}{Q_1 + Q_2}(C_{drug,3,old}Q_3 + C_{drug,4,old}Q_4) - C_{drug,1,old}Q_1)\frac{\Delta t}{V_1} \tag{9.3}$$

where $C_{drug,i,old}$ is the old tracer concentration in capillary i, and V_1 the volume of capillary 1.

In reality, however, the drug is expected to leak into the surrounding tissue, and thus this approach needs to be adapted to account for the diffusion of contrast agent into the host tissue. To satisfy mass conservation in this scenario, we need to consider:

1. The convective flow of tracer in the vessels (as described above).

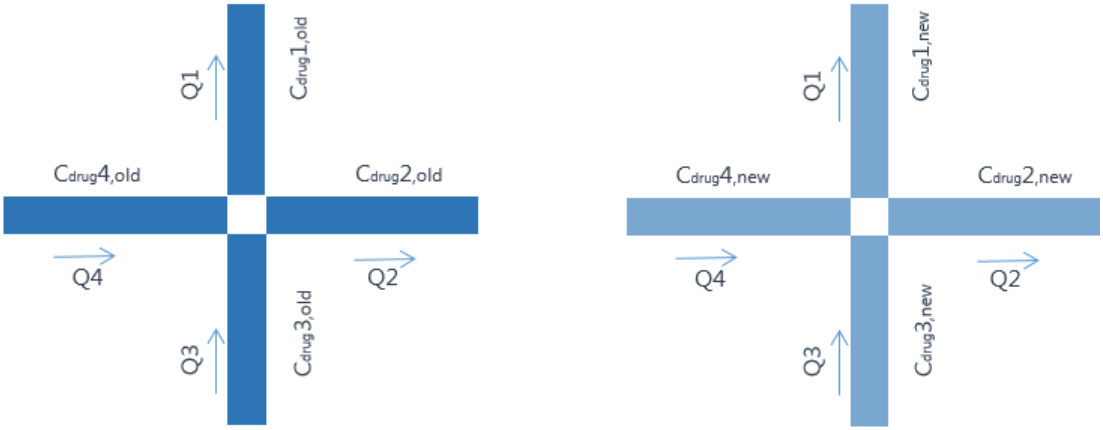

Figure 9.7: A configuration of elementary flows corresponding to four connected vessels meeting at a node j. Mass conservation dictates that $Q_1 + Q_2 = Q_3 + Q_4$.

2. The diffusive flux of agent from the vessels to the tissue (and vice versa).

3. The diffusive transport between tissue blocks.

4. The tracer decay in the tissue.

These four main flow mechanisms are expressed as a coupled system of differential equations as described below:

$$\begin{cases} \frac{dC_V}{dt} = \frac{1}{V_V}\sum_{vessels\,i} Q_{Vi}C_{Vi} - \frac{1}{V_V}Q_V C_V - \frac{1}{V_V}\sum_{blocks\,i} MP_{Vi}(C_V - C_{Ti})A_{Ti} \\ \frac{dC_T}{dt} = D_T \Delta C_T + \frac{1}{V_T}\sum_{vessels\,i} MP_{Vi}(C_{Vi} - C_T)A_{Ti} - \sigma C_T \end{cases} \tag{9.4}$$

where C_V: vessel concentration; V_V: vessel volume; Q_V: flow in vessel V; MP_{Vi}: vessel membrane permeability (MP) between vessel V and tissue block Ti; C_{Ti}: tissue block Ti concentration, A_{Ti}: contact area between vessel V and tissue block i; C_T tissue block T concentration; V_T tissue block T volume; D_T diffusion coefficient in tissue; σ: tissue intake coefficient.

The term $\frac{1}{V_V}\sum_{vessels\,i} Q_{Vi}C_{Vi}$ describes the mass flow of drug carried to vessel V by its neighbouring vessels Vi via convection; $\frac{1}{V_V}Q_V C_V$ refers to the mass flow of drug leaving vessel V via convection; $\frac{1}{V_V}\sum_{blocks\,i} MP_{Vi}(C_V - C_{Ti})A_{Ti}$ refers to the mass flow of drug leaving vessel V via diffusion into the surrounding tissue; $D_T \Delta C_T$ is the expression of diffusive flow between tissue blocks; $\frac{1}{V_T}\sum_{vessels\,i} MP_{Vi}(C_{Vi} - C_T)A_{Ti}$ refers to the mass flow leaving the tissue block to its surrounding vessels via diffusion, and σC_T describes the mass flow of the drug consumed by the tissue.

Solving this coupled system using finite difference methods yields the contrast agent

concentration in each vessel Vi and tissue block $T(i,j,k)$ at every time step Δt as described by the following scheme:

$$\begin{cases} C_V^{t+1} = C_V^t(1 - \frac{\Delta t}{V_V}[Q_V + \sum_{blocks\, i} MP_V A_{Ti}]) \\ \quad + \frac{\Delta t}{V_V}(\sum_{vessels\, i} C_{Vi} Q_{Vi} + \sum_{blocks\, i} C_{Ti} MP_V A_{Ti}) \\ C_{T,i,j,k}^{t+1} = C_{T,i,j,k}^t(1 - \Delta t[2D_T(\frac{1}{hx^2} + \frac{1}{hy^2} + \frac{1}{hz^2}) + \frac{1}{V_V}\sum_{blocks\, i} MP_V A_{Ti} + \sigma]) \\ \quad + \sum_{vessels\, i} C_{Vi} \frac{\Delta t}{V_V} MP_V A_{Ti} \\ \quad + \Delta t D_T(\frac{C_{T,i+1,j,k}^t + C_{T,i-1,j,k}^t}{hx^2} + \frac{C_{T,i,j+1,k}^t + C_{T,i,j-1,k}^t}{hy^2} + \frac{C_{T,i,j,k+1}^t + C_{T,i,j,k-1}^t}{hz^2}) \end{cases} \tag{9.5}$$

The time step has to be chosen to ensure stability (and thus mass conservation). As the dimensionless drug concentration in every vessel and tissue block has to remain within the interval $[0,1]$, we consider the extreme case where every vessel and tissue block receives a drug inflow of concentration 1 from its surrounding vessels and tissue blocks whilst assuming a zero drug outflow. This yields the following expression for the time step:

$$\begin{cases} \Delta t = Min(Min_{vessel\, V} \frac{V_V}{Q_V + \sum_{blocks\, i} MP_V A_{Ti}}, \\ \qquad Min_{blocks\, T} \frac{1}{2D_T(\frac{1}{hx^2} + \frac{1}{hy^2} + \frac{1}{hz^2}) + (\frac{1}{V_T}\sum_{vessels\, i} MP_V A_{Ti}) + \sigma}) \end{cases} \tag{9.6}$$

9.4 Simulated Results

In order to investigate the most relevant parameters affecting tracer distribution within a tissue block or a vessel segment, we simulate a 50-second bolus injection of contrast agent for different values of flow rate (FR), transmural transport coefficient (i.e. membrane permeability MP), and extra-cellular matrix (ECM) diffusion coefficient (DT). Table 9.1 shows a summary of the parameter values used in the simulations.

flow rate ($m^3 s^{-1}$)	$10^{-12}, 5.10^{-12}$
diffusion coefficient ($m^2 s^{-1}$)	$6.10^{-10}, 3.10^{-9}, 10^{-8}$
vessel permeability ($m s^{-1}$)	$10^{-8}, 10^{-7}, 10^{-6}$
tissue intake (s^{-1})	0

Table 9.1: Summary of the parameter values used in the computational simulations carried out in this work.

Images of tracer evolution for some of the explored parameter combinations are shown in Figure 9.8. Each row corresponds to a given set of input parameters.

We first examine the combined effects of vessel membrane permeability (MP) and ECM diffusion (DT) on the average vessel concentration at a fixed flow rate of $5.10^{-12}m^3s^{-1}$ (this average is taken over all vessels in the voxel, and is equal to the experimentally measured flow in the underlying vascular network.). Figure 9.9 shows predictions of the average agent concentration in vessels for two different tissue diffusion coefficients (DT) and various membrane permeabilities (MP). These show that the tracer concentration builds up quickly within the capillary network when the drug injection commences in a non-linear fashion. The build up of agent is faster for less permeable vessels, as expected, and higher vessel concentrations are reached under such conditions (88% for $MP = 10^{-9}$ compared to 62% for $MP = 10^{-6}$). Similarly, at the end of the bolus injection, the clearance of the contrast agent takes longer in the more permeable vasculature. For faster tissue diffusion ($DT = 10^{-8}m^2s^{-1}$), we find that lower vessel concentrations are reached with decreasing vessel permeability (the tissue diffusion change did not affect networks with low permeability), and the tracer is also quickly removed from the network once the injection stops. This is explained by the high rate of the diffusive transport of the contrast agent through the tissue blocks which results into an efficient removal from the vasculature throughout its transit.

The average *tissue* concentrations are shown in Figure 9.10 where the opposite trend to that observed for vessel concentration is shown (i.e. average tissue concentration increases more rapidly as vessel permeability increases). The contrast agent is barely visible for $MP = 10^{-8}$ and $MP = 10^{-9}$. In contrast, it reaches more than 20% when $MP = 10^{-6}$. The increase is again non-linear.

When tissue diffusion is fast, it can be seen that most of the simulations yield tissue concentrations smaller than those seen under slow diffusion conditions. Moreover, it appears from the tracer visualisations (Figure 9.8, last row) that this combination yields a local supply of contrast agent in the area close to the arterioles, where it then diffuses rapidly through the tissue and is quickly re-captured via diffusive transport from tissue into venule segments and then is removed from the network.

The effect of perfusion rate on contrast agent delivery to the tissue is also investigated (Figure 9.11). We observe that both the average tissue and average vessel concentrations reach higher values at higher perfusion rates (around 20% difference for the average vessel concentration at $t = 50s$ between both cases when the perfusion rate is reduced by a factor of 1/5). As the contrast agent perfusion stops, it is removed quicker at higher perfusion rates. This might suggest that, although higher concentrations could be achieved using high perfusion rates, the tumour might stay longer in direct contact with the contrast agent for lower perfusion rates. This is an important factor to consider when deciding whether a higher dosage or a longer

exposure to the drug is best to efficiently affect the tumour.

9.5 Conclusions

Preliminary results from the modelling show that delivery of drug agents to the area surrounding the tumour is highly affected by flow, permeability and diffusion in the interstitial space. The three physiological parameters interact non-linearly to produce the observed average tracer concentration in the vascular network and the surrounding tissue. We find that reductions in the permeability of the vasculature – which is usually targeted using anti-angiogenic therapy – could potentially reduce the delivery of the drug to the tumour, while increased flow is likely to increase drug delivery.

The model can be improved in the future by incorporating permeability heterogeneities within the vascular network (instead of treating membrane permeability as a homogeneous physiological property). Tissue heterogeneities could be also implemented in a similar fashion. Moreover, more protocols of perfusion could be investigated in addition to the constant bolus injection examined in this work. Finally, implementation of blood rheology physics as well as the dynamics of vessel radii adaptation would be an additional milestone towards achieving computationally realistic simulations.

PET/MRI with radiolabelled drugs can be used to non-invasively validate these models. One validation approach would consist of using the model to infer detailed information on vascular perfusion, permeability and interstitial diffusion coefficients, and compare the simulated values to those obtained experimentally by MRI imaging or optical measurements. Once validated, the ultimate goal is to use patient specific MRI parameters as inputs for the model and predict the patient specific response to a therapeutic agent.

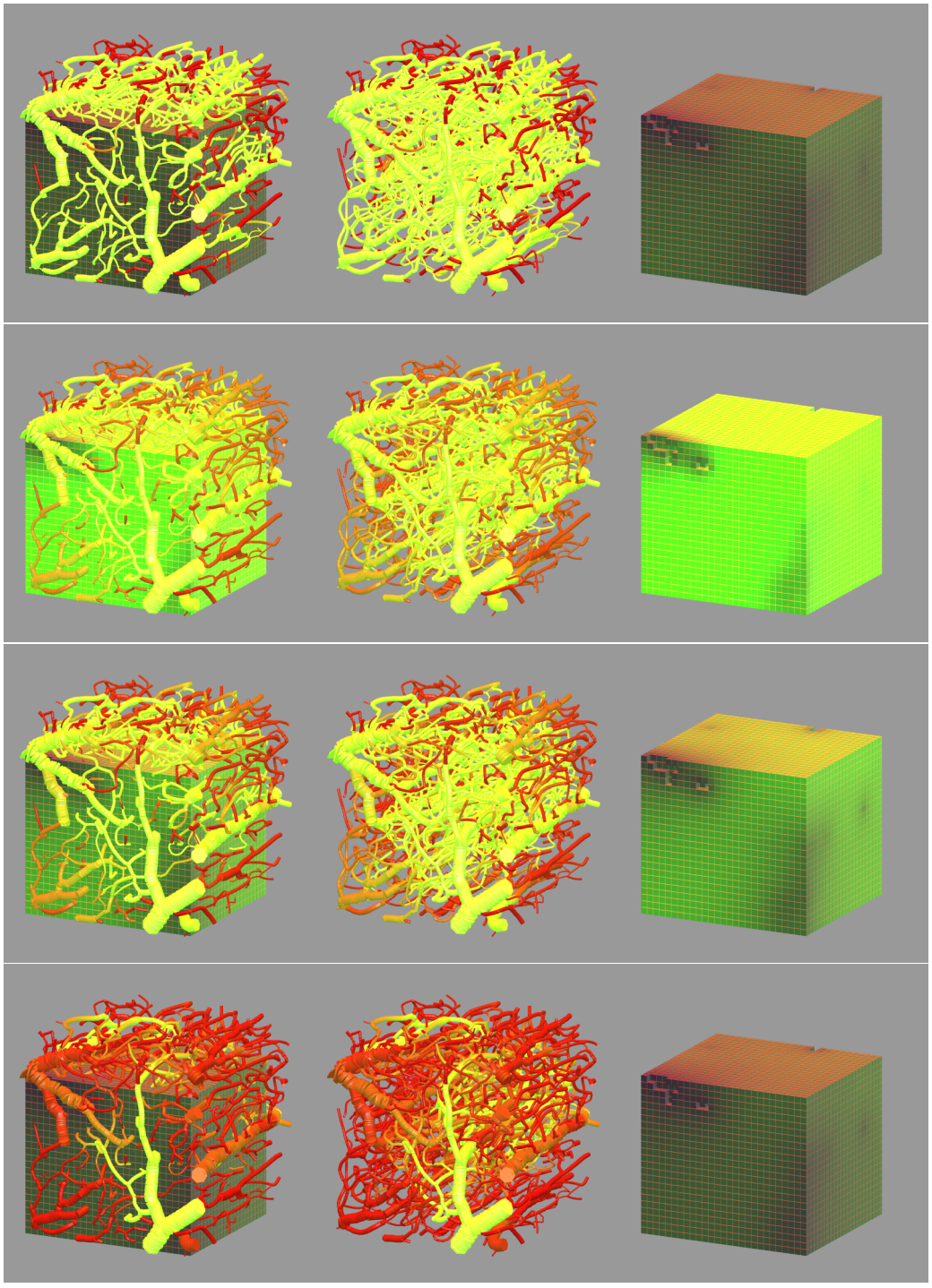

Figure 9.8: 4 simulations displaying tracer concentrations in vessels and tissue after continuous drug injection for 50 s. The left-hand column shows tracer in the entire system block, the middle column shows tracer in vessels only, and the right-hand column shows tracer in tissue only. Row 1 is the baseline simulation case and each other row corresponds to a change of a single parameter (highlighted in brown color).
*Row*1: FR: $5.10^{-12} m^3 s^{-1}$, MP: $1.10^{-7} m s^{-1}$, DT: $3.10^{-9} m^2 s^{-1}$ (baseline);
*Row*2: FR: $5.10^{-12} m^3 s^{-1}$, MP: $1.10^{-6} m s^{-1}$, DT: $3.10^{-9} m^2 s^{-1}$;
*Row*3: FR: $5.10^{-12} m^3 s^{-1}$, MP $1.10^{-6} m s^{-1}$, DT: $10.10^{-9} m^2 s^{-1}$;
*Row*4: FR: $1.10^{-12} m^3 s^{-1}$, MP: $1.10^{-6} m s^{-1}$, DT: $10.10^{-9} m^2 s^{-1}$.

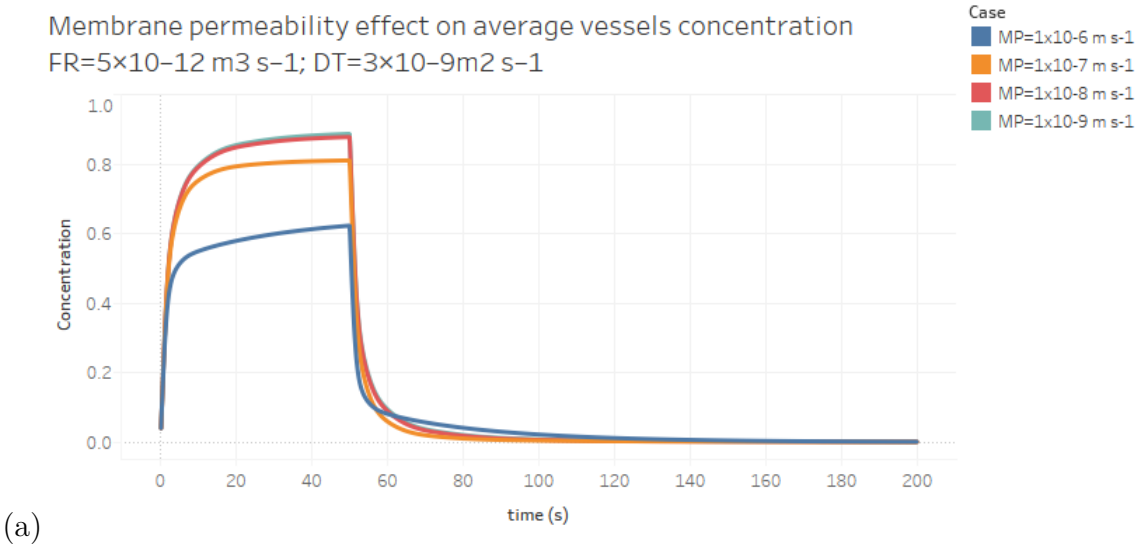

(a)

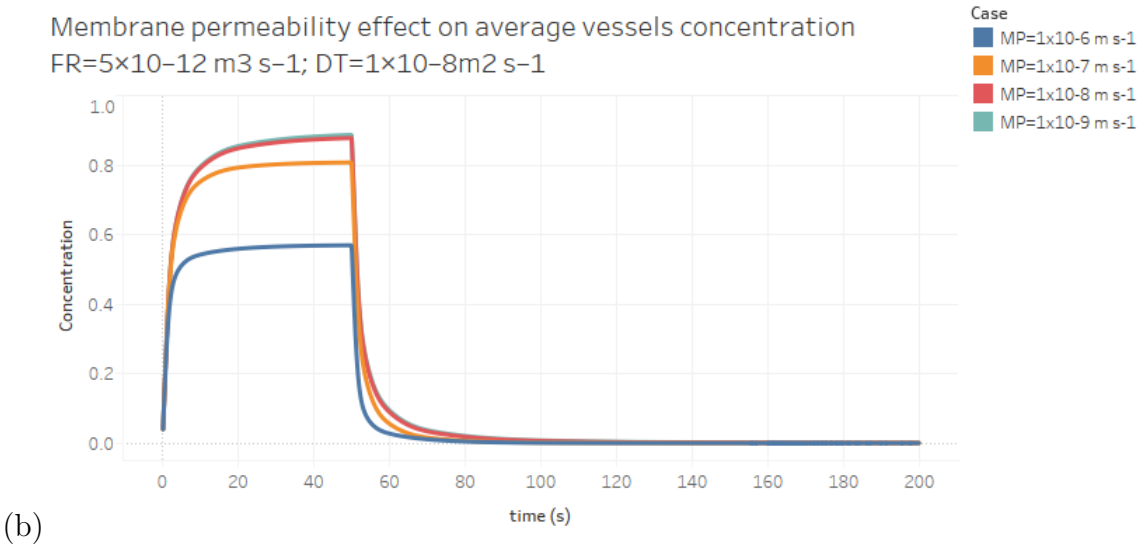

(b)

Figure 9.9: (a) The evolution of average vessel concentration in the voxel during a 50-second bolus drug injection for various vessel membrane permeabilities (normal diffusion coefficient in tissue $DT = 3.10^{-9} m^2 s^{-1}$, and flow rate$FR = 5.10^{-12} m^3 s^{-1}$). (b) The evolution of average vessel concentration in the voxel during a 50-second bolus drug injection for various vessel membrane permeabilities (fast diffusion coefficient in tissue $DT = 1.10^{-8} m^2 s^{-1}$, and flow rate$FR = 5.10^{-12} m^3 s^{-1}$).

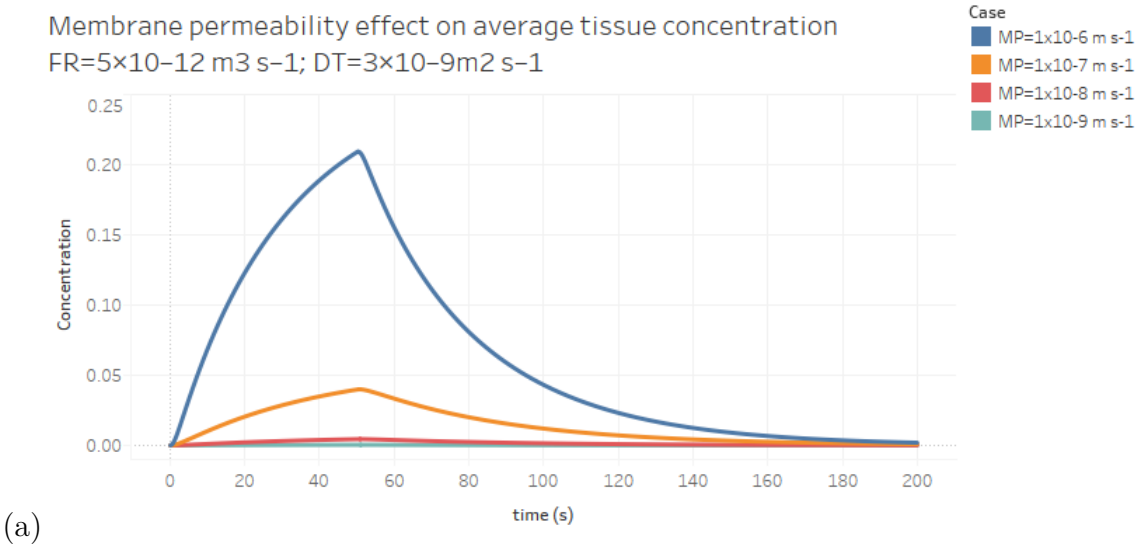

(a)

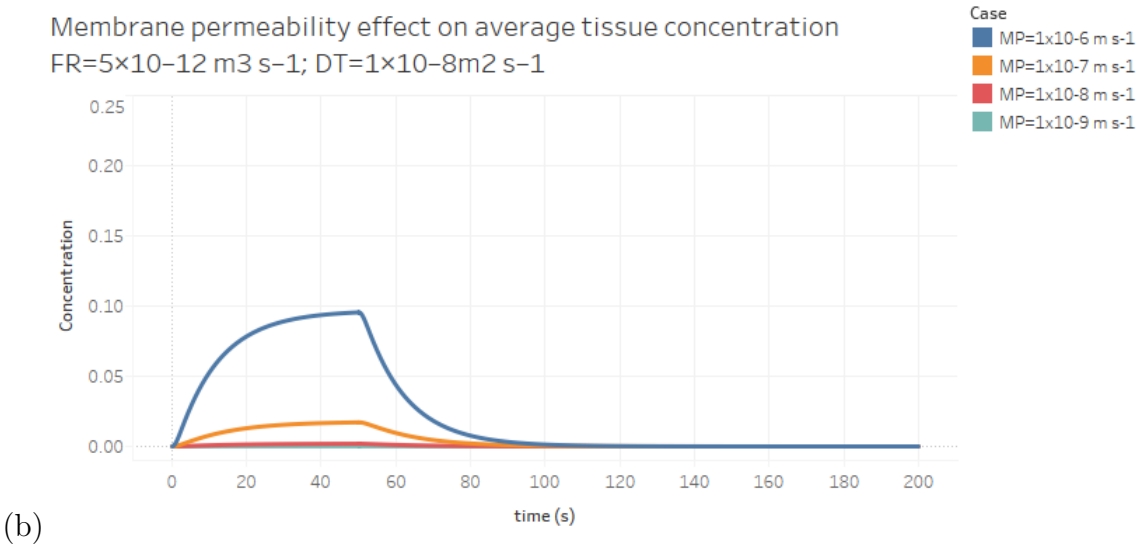

(b)

Figure 9.10: (a) The evolution of average tissue concentration in the voxel during a 50-second bolus drug injection for various vessel membrane permeabilities (slow diffusion coefficient in tissue $DT = 3.10^{-9} m^2 s^{-1}$, and flow rate$FR = 5.10^{-12} m^3 s^{-1}$). (b) The evolution of average tissue concentration in the voxel during a 50-second bolus drug injection for various vessel membrane permeabilities (fast diffusion coefficient in tissue $DT = 1.10^{-8} m^2 s^{-1}$, and flow rate$FR = 5.10^{-12} m^3 s^{-1}$).

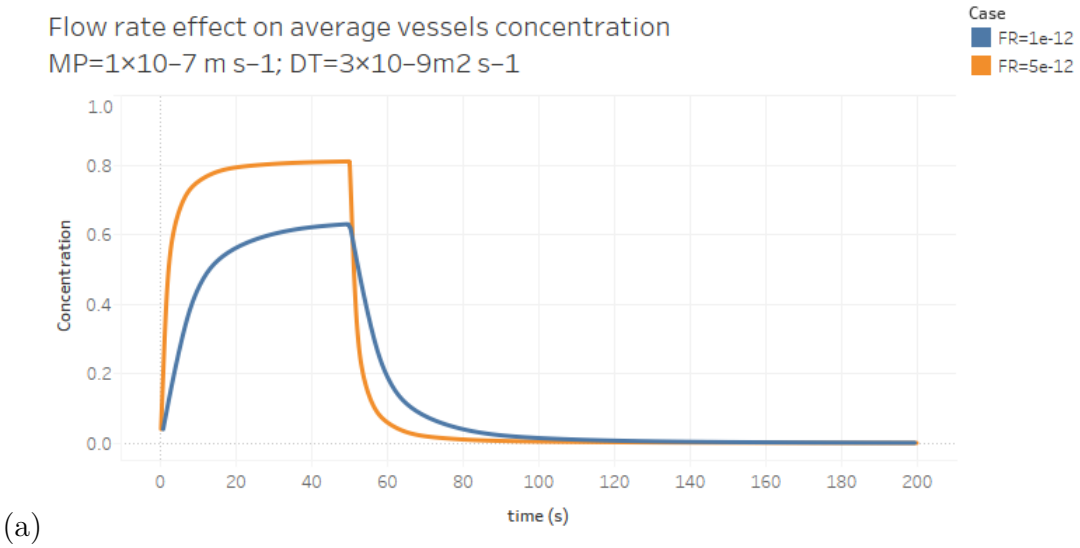

(a)

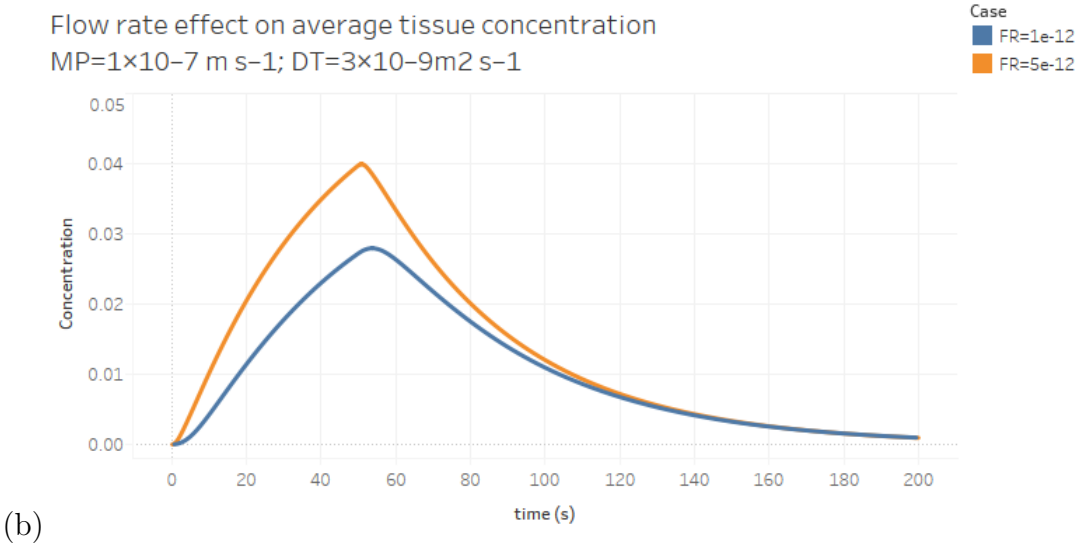

(b)

Figure 9.11: The evolution of (a) average vessel concentration and (b) average tissue concentration in the voxel during a 50-second bolus drug injection for a fixed vessel membrane permeability ($MP = 1.10^{-7} ms^{-1}$) and diffusion coefficient in tissue ($DT = 3.10^{-9} m^2 s^{-1}$) and two flow rates ($FR$): $5.10^{-12} m^3 s^{-1}$, and $1.10^{-12} m^3 s^{-1}$.

Chapter 10

Conclusions and Future Work

10.1 Conclusions

Pore network modelling has proved to be a valuable tool to investigate the effect of key flow parameters on various recovery processes. This numerical technique has often been applied to improve understanding of the underlying mechanisms governing fluid flow at the pore scale and to gain insights into protocols that could yield additional oil recovery. Moreover, pore-scale modelling has exhibited great potential for explaining the different (and sometimes contradictory) results reported in laboratory experiments. This has been illustrated in our literature review in Chapter 2, where the main categories of pore network models have been discussed. Such models have been applied to a wide variety of recovery processes - of particular interest were primary recovery processes (such as depletion) and secondary recovery processes (such as waterflooding).

Several approaches have been proposed in the literature to model fluid flow at this microscopic scale: whilst some researchers have chosen to deploy simplified rule-based algorithms (i.e. steady state models), others have adopted sophisticated dynamic models that track the evolution of phase saturations in time. Flow simulations have been carried out on digital analogues of the rock under investigation and several techniques have been suggested for modelling the physical pore space. These range from building statistically-generated regular networks that are anchored from experimental data, to the reconstruction of realistic networks extracted from microCT images.

Despite the numerous techniques for modelling flow at the pore-scale and the various rock modelling approaches used in the literature, the lack of a generic software package that could be used by SCAL technicians and reservoir engineers to simulate

generic recovery processes has meant that the application of pore network modelling techniques has largely been restricted to research work. In addition, some mechanisms have not yet been modelled extensively at the pore scale, such as depletion in three-phase system and various EOR processes. Within this context, a full pore network simulator - that we call *numSCAL (*numerical Special Core Analysis Laboratory*)* - has been developed in this work and its main features have been discussed in Chapter 3.

numSCAL was implemented to support statistically-generated networks as well as digital analogues extracted from microCT images. Moreover, a new "stitching" approach was implemented to extend the size of the small microCT networks whilst keeping their original petrophysical properties. Several models were implemented into *numSCAL* to simulate various recovery processes, including: two-phase depletion, steady-state three-phase flow, unsteady state drainage, unsteady state ganglion mobilisation and low salinity water/polymer injection. Some of these models reformulated and built upon ideas from earlier implementations (i.e. depletion, unsteady-state drainage) although most required new modelling approaches. The modules subsequently were applied to study the impact of various key parameters relevant to each process.

In Chapter 4, the steady-state depletion module was presented. The full cycle of a typical depletion process was implemented, from the nucleation of the first bubbles to the diffusion of dissolved gas through the gas-liquid interface to the growth of gas clusters and their eventual migration towards the top of the network. The model was applied to 2D networks anchored to a Berea sandstone (as well as digital microCT networks) to study the impact of depletion rate, diffusion coefficient, interfacial tension, network connectivity and pore size distribution on gas growth, bubble density, critical gas saturations and relative permeabilities. We found that most of these parameters have a direct impact on the local supersaturation as well as the competition between nucleated bubbles for dissolved gas, which greatly affected the gas growth and the timing of gas breakthrough. Of particular interest was the fact that protocols increasing bubble density (such as high depletion rates or decreasing the interfacial tensions) appeared to delay gas breakthrough and resulted in high critical gas saturations.

One limitation of the depletion model was the support of only two phases. This was addressed in Chapter 5 through the development of a novel three-phase model that implements concepts from graph theory to model complex multi-displacement chains in oil-water-gas systems. The model used a variant of the Djikstra algorithm to calculate the least energetic paths available to an invading phase and trigger the corresponding displacements at the pore scale. We coupled this approach to both

WAG and depletion processes, and a sensitivity analysis was carried out to investigate some flow parameters during depletion in waterflooded Berea analogues (i.e. initial water saturation, initial wettability and spreading coefficient). The simulations highlighted the interaction between parameters and demonstrated that several competing mechanisms could act simultaneously. Whilst this makes it difficult experimentally to analyse the effect of a single parameter in isolation from the others, the pore network module has proved to be powerful tool for this task.

Two models were also implemented into *numSCAL* to simulate secondary recovery processes. The first model was conceived to model unsteady-state water injection into oil-wet systems and was discussed in Chapter 6. A dynamic approach was adopted, where the pressure field is coupled to a constant flow rate and capillary pressure terms are included in the pressure solution. Some modules inherited concepts from the work of Regaieg et al. (2015) and new features were added, such as the support of microCT analogues. We successfully validated this approach against micromodel experiments from the literature and applied it to simulate various sensitivities on 2D anchored Berea networks. Results showed that both flow velocity and viscous ratio play a crucial role to determine the observed invasion regime and the final oil recovery. Perturbing these parameters by varying the contact angle or interfacial tension appeared to switch the flow regime, with final recovery curves exhibiting non-linear behaviour.

This first unsteady-state model was not designed to model ganglia mobilisation, however (one major assumption in the drainage model was the prevention of counter imbibition flow in capillary elements). This was addressed in Chapter 7 by implementing a novel approach where we introduced the concept of natural trapping emerging from the balance between capillary and viscous forces. Instead of using a rule-based approach to update the meniscii positions, the algorithm was coded in a way that allowed the system to self-equilibrate based on the dynamic pressure field, which took into account the applied flow rate and the evolving capillary forces between the various phases. The model was used to carry out various sensitivities on 2D Berea analogues to examine the onset of ganglia mobilisation for various scenarios. We found that, for the specific rock studied, the flow rate values required for such migration were very high ($Ca \sim 10^{-4} - 10^{-3}$) and unlikely to occur naturally in the far-field region. We also showed that decreasing the interfacial tension or increasing water viscosity in the system did not always allow ganglia mobilisation to occur when the induced variations were below some critical values. Ganglia mobilisation occurred only after significant perturbations had been imposed on the initial configuration - this was particularly the case when the wettability of the network was shifted towards a neutral-wet state.

The unsteady-state drainage model was extended in Chapter 8 to support EOR processes. This was achieved through a dynamic tracking of tracers flowing in the aqueous phase. The tracer concentrations were associated with an induced modification of wettability (LS salinity water processes) and/or water viscosity (polymer processes). The model was used in a large study that investigated the additional recovery yielded by LS water and polymer injection, as well as possible synergetic effects when these were applied simultaneously. A new approach was introduced to take into account the effect of network stochasticity on the final results, and recoveries were presented as statistical averages over ten simulations with different random number generator seeds. Simulations showed that the recovery benefits from both LS-water and polymer mechanisms can be affected by several key parameters such as flow rate, the viscous ratio and the induced alteration yielded by the EOR mechanisms. Positive secondary effects on oil recovery have been observed in most cases, and a change in the flow regime has been found to be a key mechanism by which an EOR application can affect this additional recovery. Tertiary benefits appeared to be more likely for low viscous ratios and for wettability alteration that shifted the network to a water-wet configuration. Results also highlighted the positive synergy that can be obtained when both polymer is injected alongside LS water. The combined effect led to increased recovery in several scenarios, especially when both LS water and polymer are injected in secondary mode, and was also found to interact non-linearly with other flow parameters.

We concluded this study by presenting another research area where pore network modelling could be applied. A new software - *bioFLOW* - was implemented by adopting key features from the *numSCAL* package, and was used to simulate several biological phenomena. We discussed in particular a novel model to simulate drug perfusion in irregular vasculatures surrounding a Glioblastoma Multiform (GBM) tumour. The model took into account the convective flow of a therapeutic drug in the vessels and its subsequent transmural transport and diffusion within the extra-cellular matrix. Several simulations were carried out to investigate the effect of perfusion rate, membrane permeability and tissue diffusion coefficient on drug delivery. We showed that the three physiological parameters interacted in a complex fashion (and often counter-intuitively) in terms of the observed average drug concentration in the vascular network and the surrounding tissue.

Throughout this thesis, the numerical tools we have implemented have proved to be useful for understanding the physical mechanisms governing pore-scale flow in a wide range of contents and for studying the sensitivity of macro-flow properties to various parameters. In addition, we have shown that the software was capable of examining interactions and synergies between these parameters as well as their individual impacts on flow behaviour and oil recovery. Whilst both *numSCAL* and

bioFLOW are already being used by other researchers in their corresponding research areas, their implementations are far from being exhaustive, and numerous areas can be addressed in future work.

10.2 Future Work

One major area for future work is to improve the existing solvers used to calculate the pressure field in the network - this step takes most of the required CPU power, and accelerating the solution process would significantly reduce simulation time. This could be achieved by adopting a hybrid approach such as that proposed by Regaieg and Moncorge (2016) [108], where the pressure field is only solved in the regions where viscous effects are predominant (a fast invasion percolation algorithm is applied elsewhere).

Improving the efficiency of the simulation process will also allow future consideration of larger 3D networks (whose use was rather limited in this study). The stitching approach we proposed Chapter 3 would then be applied to generate large analogues of digital micoCT networks. 3D simulations would not only be used to corroborate the 2D results but also used to study phenomena where the scale and the connectivity of the network are of key importance to the underlying process (i.e. initial water saturation, gravitational effects).

Modelling the dynamic evolution of film swelling is also another milestone to achieve in future implementations. For the steady-state depletion simulations, we have assumed that the invasion of oil-filled capillary elements with oil-wet pathways to the outlet occurs instantaneously - this could be improved by dynamically tracking the film swelling in order to correctly predict the timing of film collapse. For EOR unsteady-state models, the implementation of film flow could be enhanced by allowing the tracer to flow along the walls of capillaries when water-wet pathways are available - this might result in additional exposure of the oil to LS water or polymer and lead to enhanced predictions of the additional recovery yielded by these EOR processes.

Additional EOR dynamics could also be implemented, such as polymer diffusion, fines migration and microscopic diversion. Although these new mechanisms might extend the predictive capabilities of the model, it is important to validate the numerical simulations against experimental data where available. Designing micromodel experiments and collaborating with experimentalists to infer suitable input parameters for the numerical models would be an important area of study.

Ultimately, the model could be used for real case studies by running simulations against anchored models obtained from real reservoir data to predict the impact of particular production strategies on oil or gas recovery. This has been applied in a few cases here and further case scenarios are planned in future work.

Finally, the *bioFLOW* software could be expanded to include additional biological phenomena - this has been already progressed recently and new angiogenesis models are currently being implemented to model the growth of new capillary vessels towards malignant tumours. The model will be coupled to a cell proliferation module, where the vessels can interact with individual cells of the tumour and predict the onset of tumour fragmentation and capillary intravasation (which can cause metastatic tumours to appear). The model parameters would be inferred from experimental data, with the ultimate goal of predicting patient-specific responses to therapeutic agents.

Appendix A

numSCAL: Manual of Use

numSCAL is a pore-scale numerical simulator that has been implemented using C++ and Qt technologies. The software is cross-platform and can be used on Windows, MacOS and Linux machines. Moreover, a Graphical User Interface (GUI) has been coded to allow fast access to the features provided by *numSCAL* (Figure A.1) (although a console version is also available if the simulations are intended to run on a Linux supercomputer).

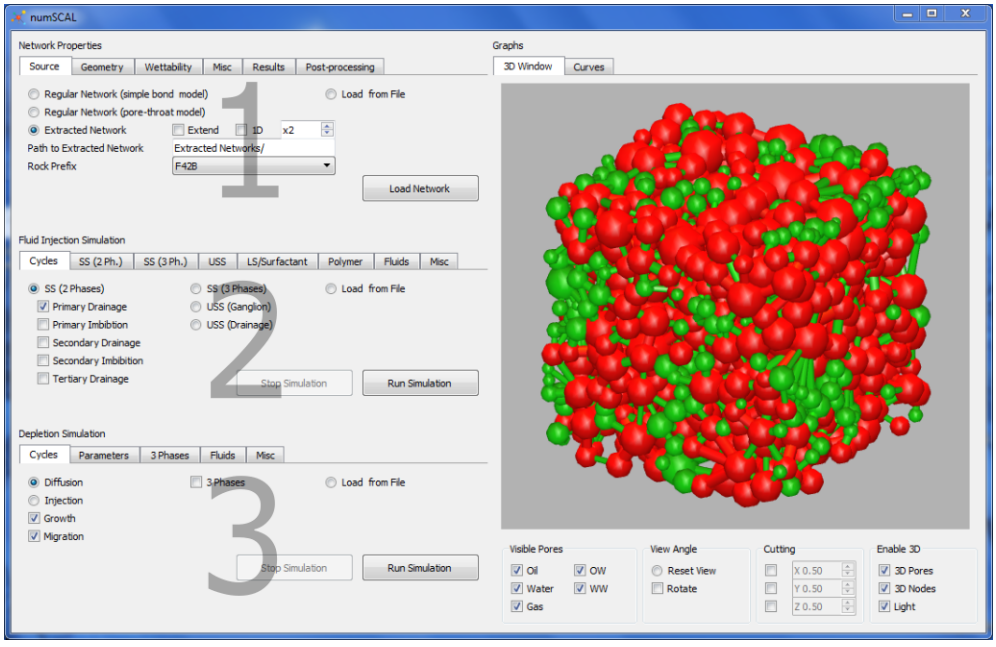

Figure A.1: A screenshot of *numSCAL* software. (1) tabular section for loading the network (2) tabular section for running fluid injection simulations (3) tabular section for running depletion simulations.

A typical simulation workflow consists in two major parts: (1) generating the network (Figure A.1 - 1) and (2) running a flow simulation on the network. The latter involves two subsets of simulations: (i) fluid injection (Figure A.1 - 2) and (ii) depletion (Figure A.1 - 3). We explain the main inputs required for each section in

the following paragraphs.

A.1 Loading the Network

The first tabular section of *numSCAL* simulator is used to set the main inputs required to generate a pore network. We go through each tab separately.

Source (Figure A.2)

This indicates the type of network we want to create.

- Regular Network (simple bond model): a network consisting of interconnected simple bonds elements.
- Regular Network (pore-throat model): a network consisting of nodes connected by throats.
- Extracted network: a network generated using microCT network files. These files need to be located in the "Path to extracted Network" folder. The rock prefix refers to the type of rock represented by the microCT files. By default, the simulator has access to numerous rock analogues downloaded from the Imperial College database
- Load from File: loads the last loaded network.

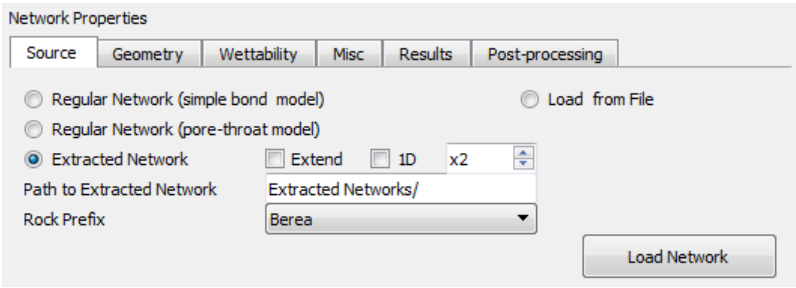

Figure A.2: Network properties - Source.

Geometry (Figure A.3)

- Nx, Ny, Nz: the number of nodes in each direction
- Seed: the seed number used when generating the radii of the capillaries.

- Min Radius, Max Radius (in μm): minimum and maximum values for the radii assigned to bonds (or throats). The assignment is performed according to various possible statistical distributions: Uniform, Rayleigh, Triangular, and Weibull.
- Vol. Cons. Vol. Cons, Cond. Cons. Cond. Exp.: these are the volume and conductivity constants and exponents used in the "3Rs" approach.
- Z: coordination number.
- Distort.: distortion factor.
- A. Ratio.: aspect ratio α. This parameter is used for regular networks with throats and nodes. Each node is assigned a radius r_n based on the following expression:

$$r_n = max(\alpha \frac{\sum_i^{nc} r_i}{n_c}, max(r_i)) \tag{A.1}$$

where i denotes the indices of the n_c neighbouring throats with corresponding radii r_i.

- Length (in μm): the average length of a bond (or throat) - only valid for regular networks.

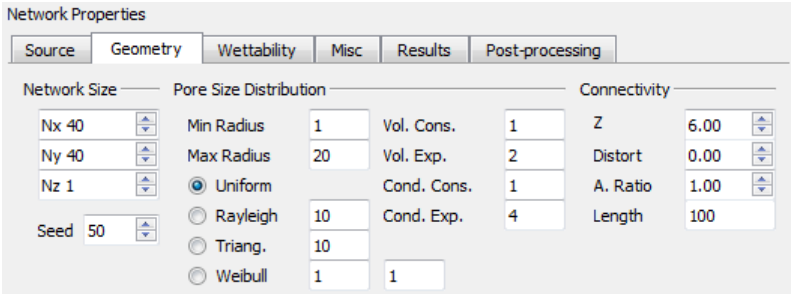

Figure A.3: Network properties - Geometry.

Wettability (Figure A.4)

- Wettability type: the user can select from various wettability configurations: water-wet, oil-wet, fractional-wet, mixed-wet small and mixed-wet large.
- Contact angles (deg): these are assigned by generating a random value between a minimum and a maximum value. For water-wet (oil-wet) elements, the contact angles must be between 0 and 90 (90 and 180).

- OW pores fraction: the fraction of oil-wet pores when a fractional-wet, mixed-wet small or mixed-wet large configuration is selected.
- Shape factor: the shape factor associated to the cross section of capillaries (only for regular networks). The default value corresponds to a circular cross section.

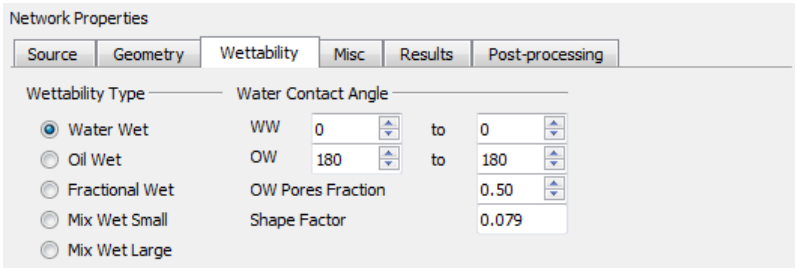

Figure A.4: Network properties - Wettability.

Misc (Figure A.5)

- Solver: the type of solver used for pressure calculation. The user can choose the Cholesky factorisation method (high precision, fast for 2D networks but can be slow for 3D ones) or BICSTAB (bi-conjugate gradient method - lower precision but fast for 3D networks).
- Extract data: when selected, the state of the network (the phase occupying each capillary element + tracer concentrations) is exported into text files in the folder "Results/Network_Status" at each time step.

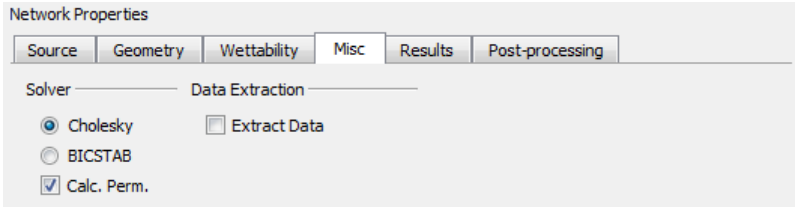

Figure A.5: Network properties - Misc.

Results (Figure A.6)

Once a network is loaded, some of its properties are displayed in this tab: absolute permeability (mDarcy), porosity, total number of pores (throats) and nodes.

- Save network image: this button allows to save a "png" image of the network displayed on the screen.

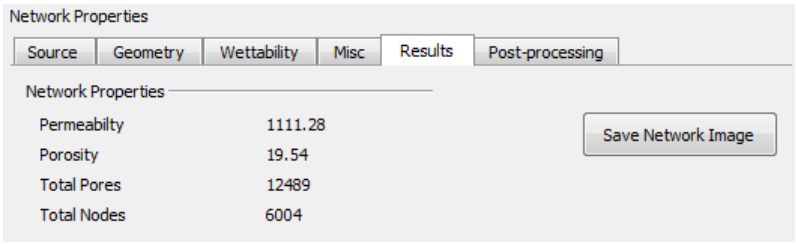

Figure A.6: Network properties - Results.

Post-processing (Figure A.7)

It is possible to recreate the network state after a simulation finishes. This proves to be useful when running the console version of *numSCAL* on Linux supercomputers.

- Render Network Status from Files: the user can recreate a single instant of the simulation by loading the corresponding data files (located in the folder "Results/Network_Status") into the simulator.
- Render a video from Files: the full simulation can be exported as an mp4 video by selecting this option.

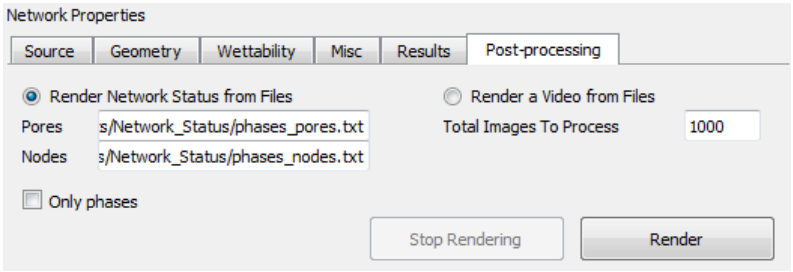

Figure A.7: Network properties - Postprocessing.

A.2 Running a Fluid Injection Simulation

Once the network loaded, the user can run a wide variety of flow simulation.

Cycles (Figure A.8)

This section lists the 4 processes that can be simulated:

- SS (2Phases): a steady-state simulation of alternate oil-water injection, where a full cycle of drainage and imbibition processes can be simulated.

- SS (3Phases): a steady-state simulation of three-phase flow. This includes WAG processes or a custom scenario defined in the "SS (3 Ph.)" tab.
- USS (Ganglion): simulation of unsteady state injection of water using the *numSCAL* ganglion module.
- USS (Fast): simulation of unsteady state injection of water using *the numSCAL* drainage module.
- Load from File: run a simulation with last used settings.

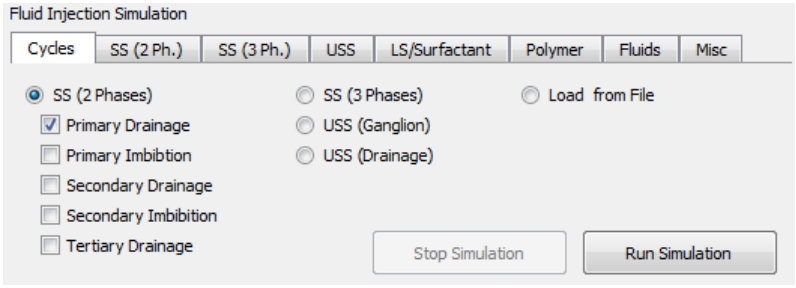

Figure A.8: Injection simulation - Cycles.

Steady-State simulation (2 Phases) (Figure A.9)

- Steps: the number of steps we use to discretise the drop (or increase) of capillary pressure in order to allow oil (or water) to displace all the accessible water (or oil) from the network.
- Ang. Inc. after Aging: the incremental value in contact angles (for Oil-Wet and Water-Wet capillaries) after primary drainage.
- Water/Oil films: a flag that signals whether fluids can escape from capillaries via film flow.

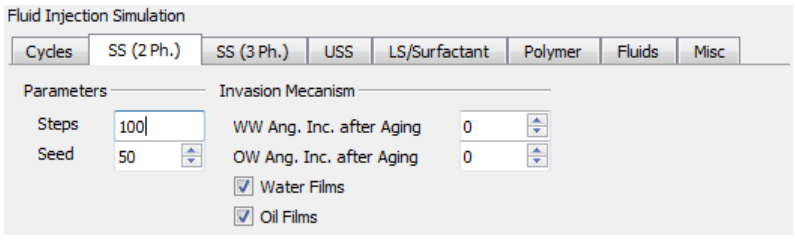

Figure A.9: Injection simulation - Steady-State (2 phases).

Steady-State simulation (3 Phases) (Figure A.10)

- 3 Phase experiments: the user can simulate a full WAG cycle or a custom scenario.
- No snap-off: this flag disables snap-off mechanism during the three-phase simulation.
- Stop at Breakthrough: this flag allows the simulation to stop when the invading phase reaches the outlet pores of the network.
- WAG cycle: each option denotes the process that occurs during the simulation. It is possible to repeat the full cycle for several times if the 'repeat' check box is selected.
- Custom: when a custom scenario is selected, the user can customise the initial defending phases (saturations can be specified in Fluids tab) and the invading phase.

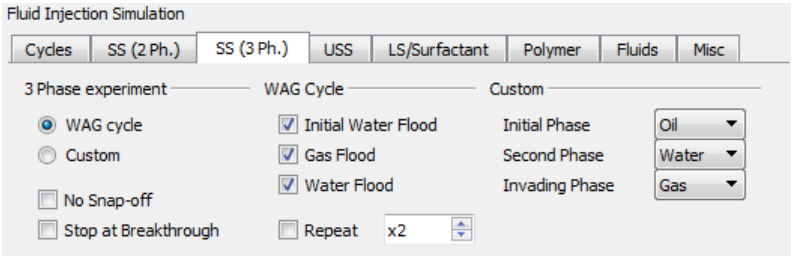

Figure A.10: Injection simulation - Steady-State (3 phases).

Unsteady-state simulation (Figure A.11)

- Flow rate (in $m^3 s^{-1}$): the volumetric rate of fluid flow through the entire network.
- Precision factor (between 0 and 1): the value denotes the critical test fraction used in the ganglion model.
- Simulation time (in s): the duration of the simulation process.
- Injected PVs: this option, when selected, override the simulation time option. The simulation stops when the number of specified pore volumes have been injected.
- Rate bump: when activated, the flow rate is multiplied by a selected factor (4 by default) after a specific duration of the simulation has elapsed (80% by default).

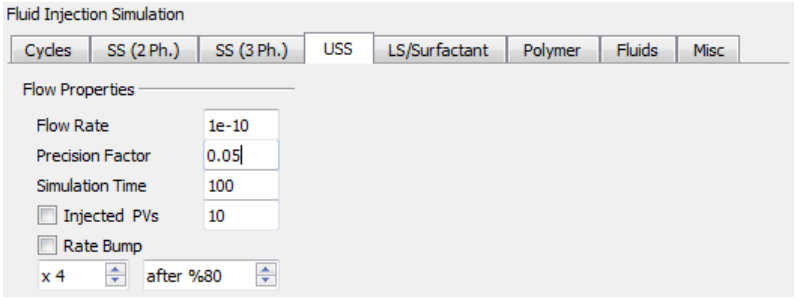

Figure A.11: Injection simulation - Unsteady state.

Low Salinity (Figure A.12)

- Secondary Injection: LS/Surfactant is injected in secondary mode.
- After Breakthrough: LS/Surfactant is injected in tertiary mode.
- After 1/2 Sim. Times. LS/Surfactant is injected after half of the simulation time has elapsed (or half of the chosen pore volumes have been injected).
- Remove after Breakthrough: LS/Surfactant water is replaced by HS water after breakthrough (only valid when LS is injected in secondary mode).
- Remove after 1/2 Sim. Time: LS/Surfactant water is replaced by HS water after half of the simulation time has elapsed.
- Angle change (in deg): the induced contact angle modification for a LS tracer concentration equal to 1 (salinity equal to 0).
- IFT change (in %): the induced IFT modification for a surfactant tracer concentration equal to 1.

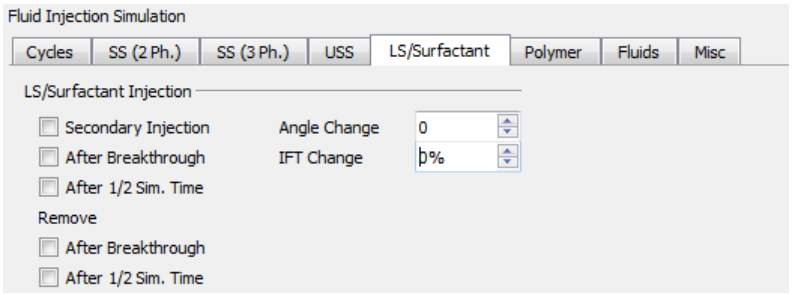

Figure A.12: Injection simulation - Low salinity.

Polymer (Figure A.13)

Most of the parameters here have similar functions to those described in the LS/Surfactant section. The parameters unique to polymer injection simulation are described below.

- Viscosity change (in cP): the induced water viscosity change for a polymer tracer concentration equal to 1.
- Microscopic diversion: capillaries with radii inferior to the value specified by "Crit. Radius" are shut when their polymer concentration reaches 1.

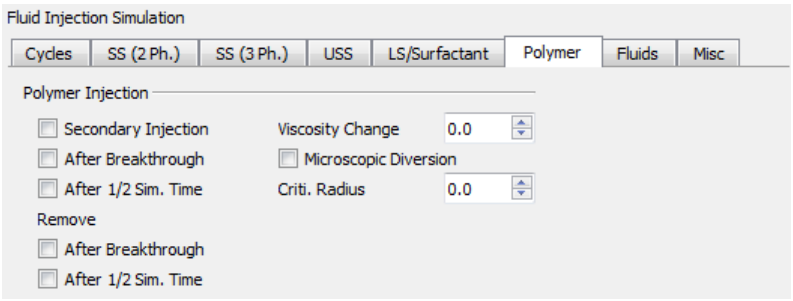

Figure A.13: Injection simulation - Polymer.

Fluids (Figure A.14)

This section includes the fluid properties used for all the simulations.

- Viscosities (in cP): for oil, water and gas.
- IFT (in dyn/cm): for oil-Water (OW), oil-gas (OG) and water-gas (WG).
- Sw: the initial water saturation. (For three-phase simulation - custom scenarios, this is the saturation of the second phase).
- Distribution of the Swi:
  - Random: the water occupies random capillaries.
  - Small: water occupies the smallest capillaries.
  - Large: water occupies the largest capillaries.
  - After PD: a primary drainage (oil invades a water-wet water-filled network) is simulated first until the specified Swi is reached.
- Aging: if this option is selected, capillaries filled with the initial water are assigned a water-wet angle (even when the network is oil-wet).

Misc (Figure A.15)

- Gravity ON: (experimental) a flag that let gravitational forces be included in the capillary entry pressure.

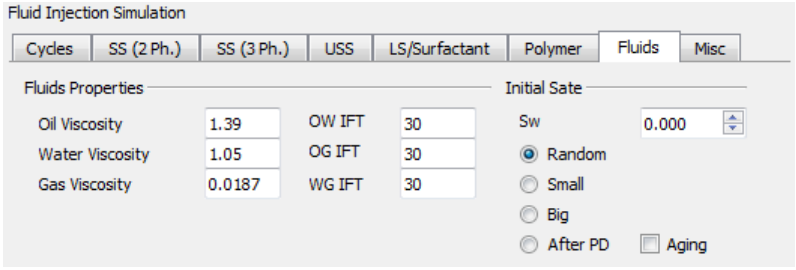

Figure A.14: Injection simulation - Fluids.

- Viscous Forces ON: (experimental) a pressure gradient is applied (P at inlet - P at outlet in Pa) across the network. The viscous drop across each capillary is included a a perturbation to the capillary entry pressure.
- R. Permeabilities: allows the calculation of relative permeabilities (this option is deactivated by default as it can slow down the steady-state simulations).
- Post-processing: the OpenGL screen is recorded in real time and the corresponding video is exported at the end of the simulation (located in Videos folder).

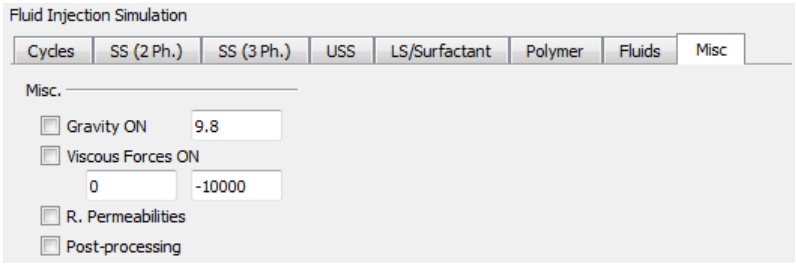

Figure A.15: Injection simulation - Misc.

A.3 Running a Depletion Simulation

After loading the network, the user can also simulate a full depletion process by using the third tabular section of *numSCAL* software.

Cycles (Figure A.16)

- Diffusion/Injection: the gas transfer mode into the nucleated bubbles.
- Growth: simulates bubble growth.
- Migration: simulates bubble migration. Only valid when gravity or viscous forces are activated.

- 3 Phases: needs to be selected for three-phase depletion processes - the three-phase module is called in that case.
- Load from File: run a simulation with last used settings.

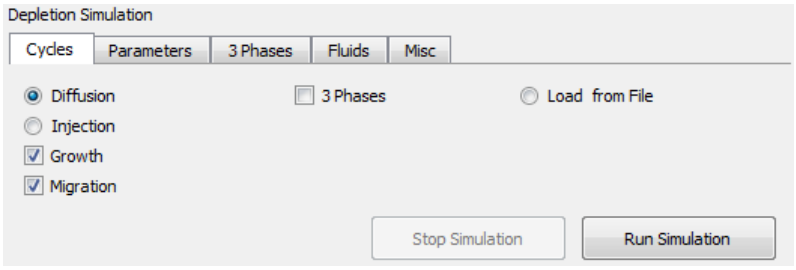

Figure A.16: Depletion simulation - Cycles.

Parameters (Figure A.17)

- BP Pressure (in psi): bubble point pressure.
- Dep. Rate (in psi/day): depletion rate.
- Dep. Time (in days): depletion time.
- Dep. Steps: the number of steps we use to discretise the pressure drop.
- Optimal Step: when selected, the minimum number of steps that ensures mass conservation is applied (might slow down the simulation).
- Injection rate (in $\mu g/day$): the mass of gas injected in the bubbles when injection mode is selected.
- Nucleation parameters: the user can select between instantaneous (IN) or progressive (PN) nucleation.
- Bubble Number: the number of bubbles nucleated using IN module.
- Min/Max Cavity Radius: cavities are assigned radii uniformly sampled between these two values when PN nucleation module is selected.
- Cavity Density: the number of pores per one cavity.
- Growth Parameters: the user can select between the multi-filling module (where gas invades multiple pores simultaneously) or the invasion percolation approach (where the accessible capillaries are sequentially invaded from the largest to the smallest).

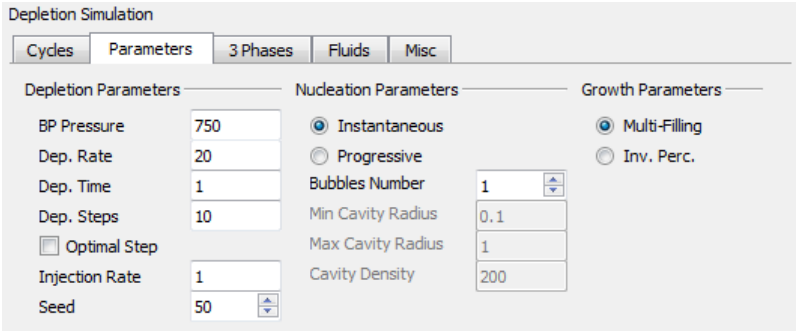

Figure A.17: Depletion simulation - Parameters.

Fluids (Figure A.18)

Most of the fluid options have similar functions to those described in the 'Fluid Injection' section. Those unique to depletion are described below.

- Oil Diff Coeff. (in $10^{-5}cm^2s^{-1}$): oil diffusion coefficient.
- Water Diff Coeff. (in $10^{-5}cm^2s^{-1}$): water diffusion coefficient.
- Data Folder: path to the folder that contains pressure-dependent data (viscosity, IFT, dissolved gas concentration, density, volume factor).
- Override with fixed values: when selected, pressure dependent data are overridden by the fixed values specified in this tab.

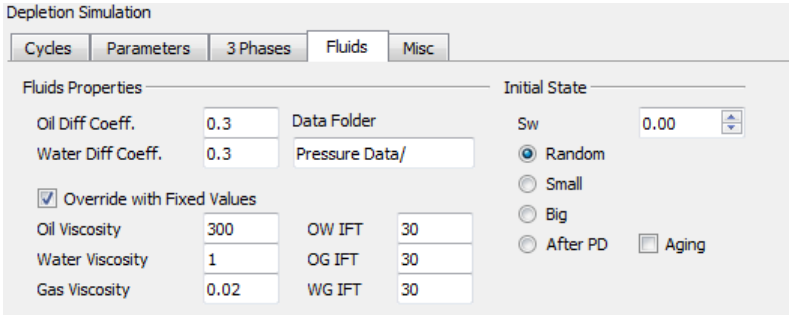

Figure A.18: Depletion simulation - Fluids.

3 Phases (Figure A.19)

These options have similar functions to those described in the 'Fluid Injection' section.

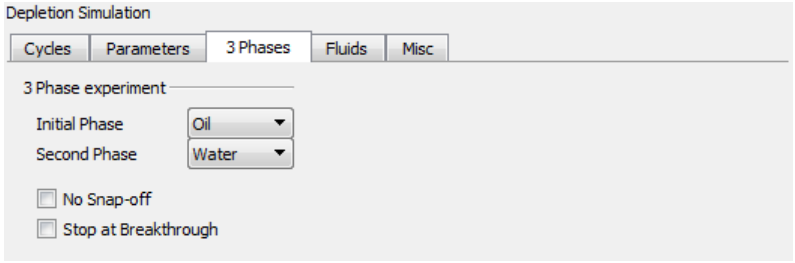

Figure A.19: Depletion simulation - three-Phase.

Misc (Figure A.20)

These options have similar functions to those described in the 'Fluid Injection' section.

Figure A.20: Depletion simulation - miscellaneous.

A.4 Interacting with the Graphical Engine

numSCAL provides an interactive OpenGL screen that enables the user to observe in real time the running simulation on the underlying network. Moreover, more options are provided to allow the visualisation of specific phases or capillaries with specific wettability (Figure A.21 - Visible Pores). It is also possible to display partial slices of the network to observe obstructed elements (Figure A.21 - Cutting). Although the network elements are displayed in 3D by default, these can replaced by simple lines (Figure A.21 - 3D) which can improve performance for very large networks.

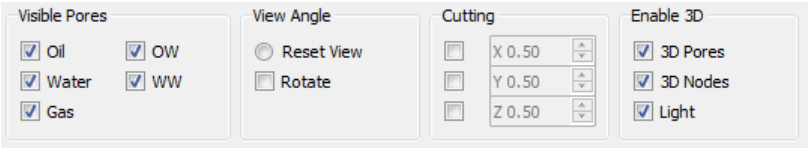

Figure A.21: *numSCAL* Graphics Options.

numSCAL also provides a plotting window in order to minimise the interaction with third-party software. The user can readily display curves of the simulated data by pointing to the corresponding files and several options have been already included to customise the final figure (Figure A.22).

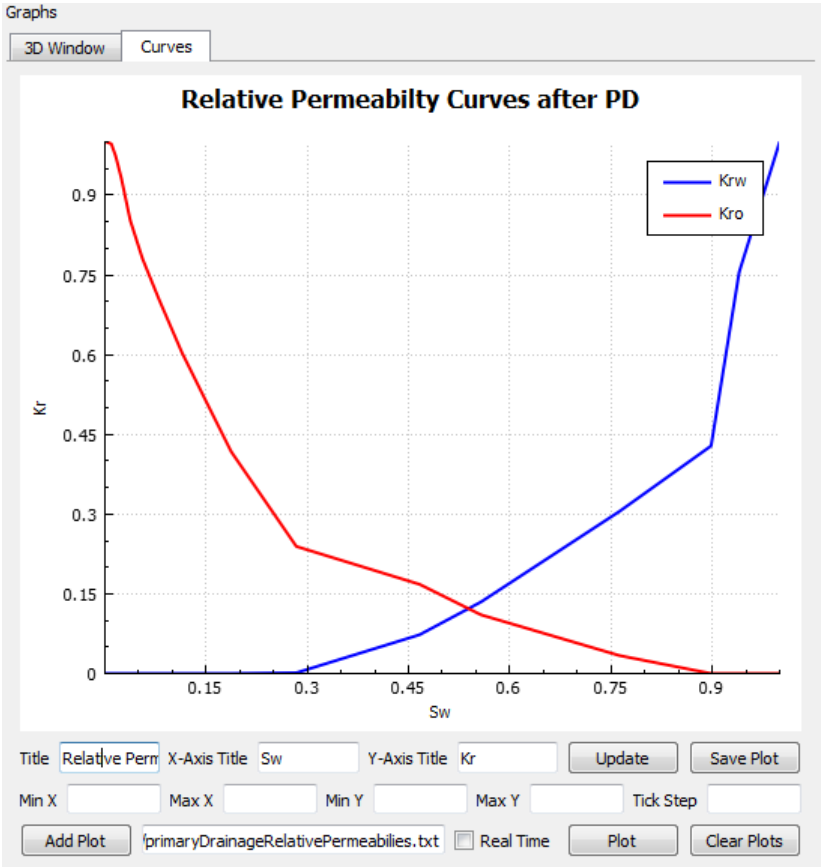

Figure A.22: *numSCAL* Plotting Options.

Appendix B

bioFLOW: Manual of Use

bioFLOW is a pore-scale numerical simulator that has been implemented using C++ and Qt technologies. The software is a fork of the original *numSCAL* package and it is mainly applied to simulate processes related to mathematical biology. *bioFLOW* is cross-platform and can be used on Windows, MacOS and Linux machines. Moreover, a Graphical User Interface (GUI) has been coded to allow fast access to its features (although a console version is also available if the simulations are intended to run on a Linux supercomputer).

A typical simulation workflow consists in two major parts: (1) generating the network (Figure B.1 - 1) and (2) running a flow simulation on the network (Figure B.1 - 2). We explain the main inputs required for each section in the following paragraphs.

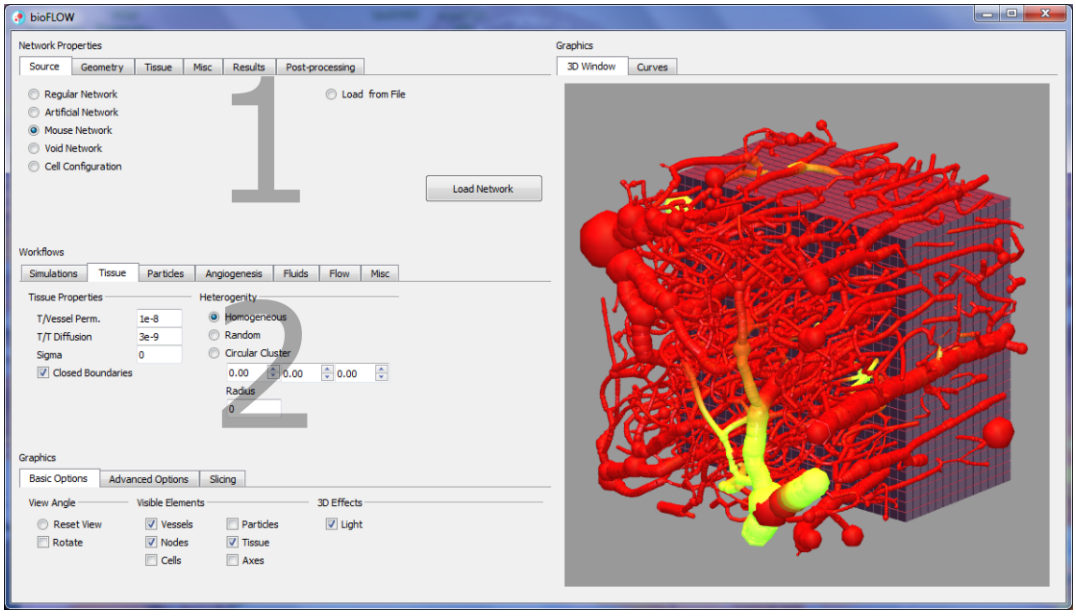

Figure B.1: A screenshot of *bioFLOW* software. (1) tabular section for loading the network (2) tabular section for running simulations.

B.1 Loading the Network

The first tabular section of *bioFLOW* simulator is used to set the main inputs required to generate a vascular network. We go through each tab separately.

Source (Figure B.2)

- Regular Network (simple bond model): a network consisting of interconnected simple bonds elements.
- Artificial network: a network constructed manually to test particle flow module (see Figure 9.3).
- Mouse network: a vascular network generated from MRI images and representing the capillary bed surrounding Gioblastomas Multiform tumour in a mouse brain. The corresponding data has been provide by Harvard Medical School.
- Void Network: this option is selected when the vascular network is progressively constructed during the simulation (i.e. angiogenesis)
- Cell Configuration: loads initial cancerous cells (used for the cell proliferation module).
- Load from File: loads the last loaded network.

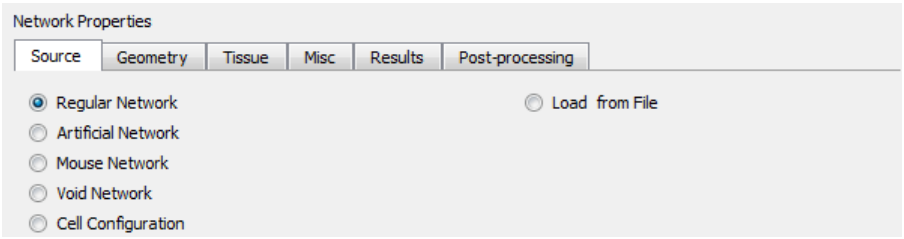

Figure B.2: Network properties - Source.

Geometry (Figure B.3)

- Nx, Ny, Nz: the number of nodes in each direction
- Seed: the seed number used when generating the radii of the capillaries.
- Min Radius, Max Radius (in μm): minimum and maximum values for the radii assigned to vessels. The assignment is performed according to various possible statistical distributions: Uniform, Rayleigh, Triangular, and Weibull.

- Vol. Cons. Vol. Cons, Cond. Cons. Cond. Exp.: these are the volume and conductivity constants and exponents used in the "3Rs" approach.
- Z: coordination number.
- Distort.: distortion factor.

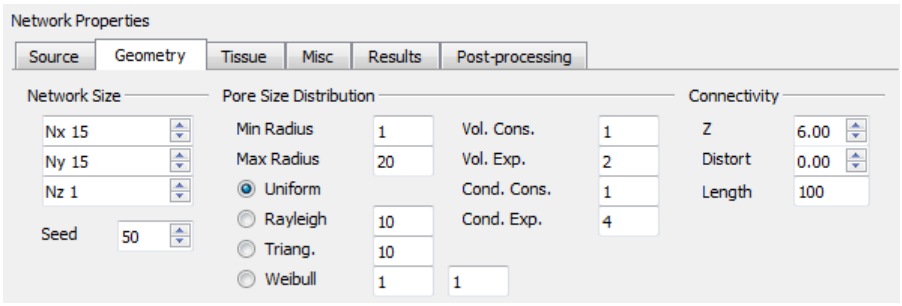

Figure B.3: Network properties - Geometry.

Tissue (Figure B.4)

- Generate tissue: creates a cubic grid of tissue blocks surrounding the vascular network.
- Nx, Ny, Nz: the number of tissue blocks in each direction
- Dx, Dy, Dz: these options are used when only a cubic grid of tissue blocks is simulated (e.g. without a vascular network) and denote the length of the grid in each direction.

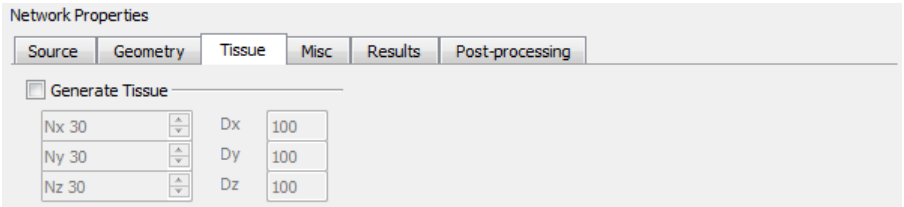

Figure B.4: Network properties - Tissue.

Misc (Figure B.5)

- Solver: the type of solver used for pressure calculation. The user can choose the Cholesky factorisation method (high precision, fast for 2D networks but can be slow for 3D ones) or BICSTAB (bi-conjugate gradient method - lower precision but fast for 3D networks).

- Extract data: when selected, the state of the network (the phase occupying each capillary element + tracer concentrations) is exported into text files in the folder "Results/Network_Status" at each time step.

Figure B.5: Network properties - Misc.

Results (Figure B.6)

Once a network is loaded, some of its properties are displayed in this tab: absolute permeability (mDarcy), porosity, total number of pores (throats) and nodes.

- Save network image: this button allows to save a "png" image of the network displayed on the screen.

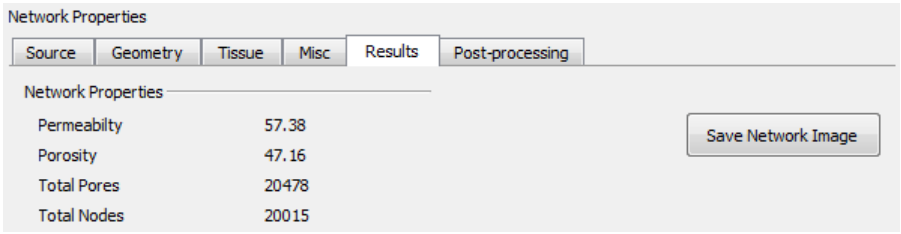

Figure B.6: Network properties - Results.

Post-processing (Figure B.7)

It is possible to recreate the network state after a simulation finishes. This proves to be useful when running the console version of *bioFLOW* on Linux supercomputers.

- Render Network Status from Files: the user can recreate a single instant of the simulation by loading the corresponding data files (located in the folder "Results/Network_Status") into the simulator.
- Render a video from Files: the full simulation can be exported as an mp4 video by selecting this option.

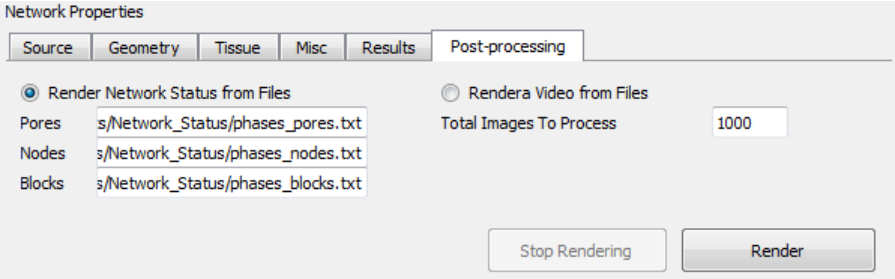

Figure B.7: Network properties - Post-processing.

B.2 Running a Workflow

Once the vascular network loaded, the user can run various simulations.

Simulations (Figure B.8)

- Drug Flow (-Diffusion): simulation of drug perfusion, where only convection is considered.
- Drug Flow (+Diffusion): simulation of drug perfusion, where both convection and diffusion into the surrounding tissue are considered.
- Angiogenesis (experimental feature): simulation of vascular growth towards the tumour (the implementation of this module is in progress).
- Particle Flow: simulation of continuous flow of individual particles in the vascular network.
- Cell Proliferation: Proliferation of individual cancerous cells.
- Load from File: run a simulation with last used settings.

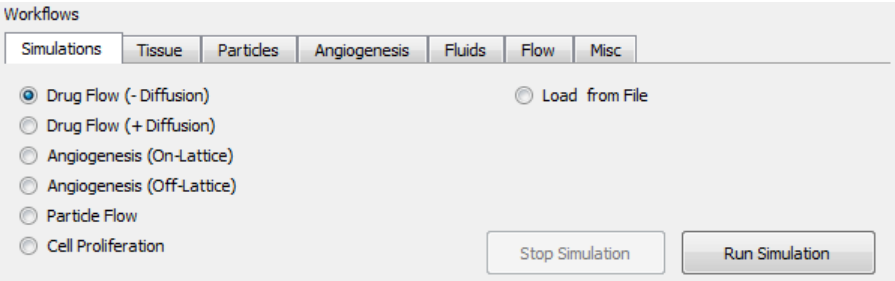

Figure B.8: Workflows - Simulations.

Tissue (Figure B.9)

- T/Vessel Perm. (in $m.s^{-1}$): membrane permeability of the vessels adjacent to tissue blocks.
- T/T Diffusion (in $m^2.s^{-1}$): diffusion coefficient between tissue blocks.
- Sigma (in s^{-1}): tissue intake coefficient.
- Closed Boundaries: a flag that determines whether the drug is allowed to flow through the tissue grid boundaries.
- Heterogeneity: these options allow the user to choose between a homogeneous distribution of vessel permeabilities or a random one. In addition, the user can create a circular region (by specifying the coordinates of its centre and its radius) with increased vessel permeability.

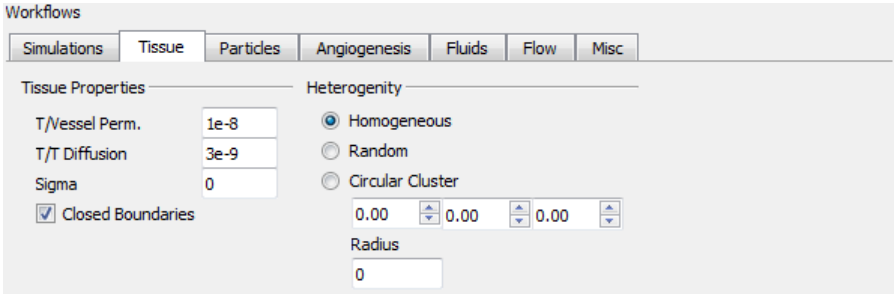

Figure B.9: Workflows - Tissue.

Particles (Figure B.10)

- Injection Interval (in s): the duration between two consecutive injected particles.

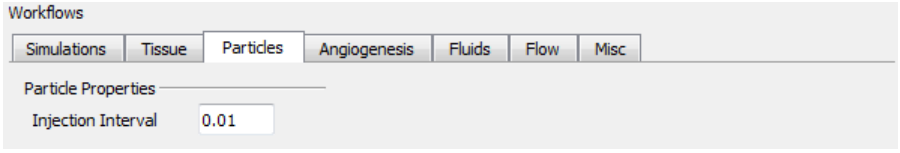

Figure B.10: Workflows - Particles.

Fluids (Figure B.11)

- Fluid viscosities (in cP). More options are being implemented into this section to take blood rheological properties into consideration.

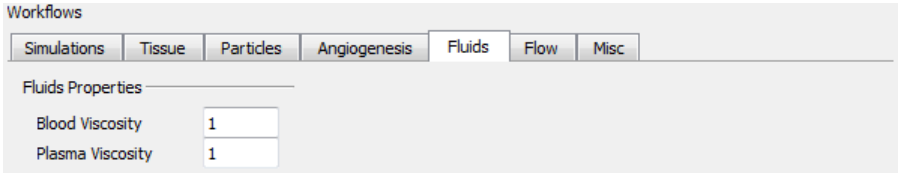

Figure B.11: Workflows - Fluids.

Flow (Figure B.12)

- Flow rate (in $m^3 s^{-1}$): the volumetric rate of fluid flow through the entire network.
- Simulation time (in s): the duration of the simulation process.
- Injection Type - Bolus: the drug is injected for a determined duration
- Injection Type - AIF: the drug concentration profile follows the Arterial Input Function proposed by Parker et al (2006) [188].

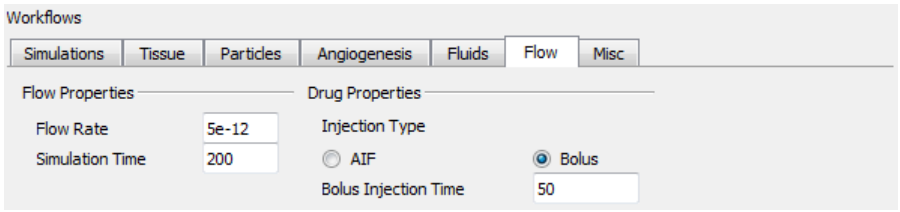

Figure B.12: Workflows - Flow.

Misc (Figure B.13)

- Post-processing: the OpenGL screen is recorded in real time and the corresponding video is exported at the end of the simulation (located in Videos folder).

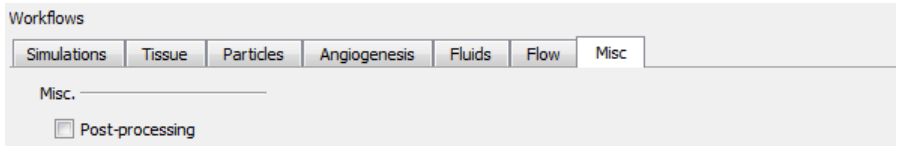

Figure B.13: Workflows - Misc.

B.3 Interacting with the Graphical Engine

bioFLOW provides an interactive OpenGL screen that enables the user to observe in real time the running simulation. Moreover, more options are provided to allow

the visualisation of specific simulation elements such as vessels, tissue blocks, nodes, particles and cells (Figure B.14 - Visible Elements). Although the network elements are displayed in 3D by default, these can replaced by simple lines (Figure B.14 - 3D) which can improve performance for very large networks.

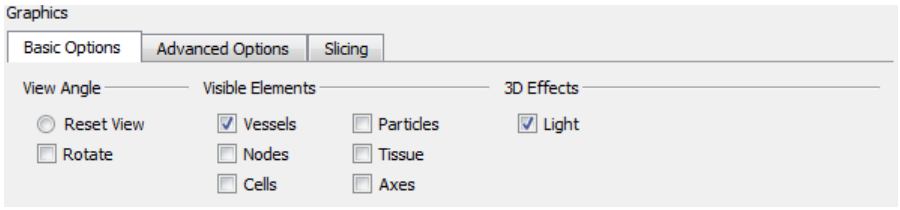

Figure B.14: *bioFLOW* Graphics - Basic options.

The user can display capillaries with specific properties (i.e. arteries, veins) (Figure B.15 - Visible Vessels). In addition, when multiple drugs are injected, the user can display them individually (Figure B.15 - Visible Concentrations).

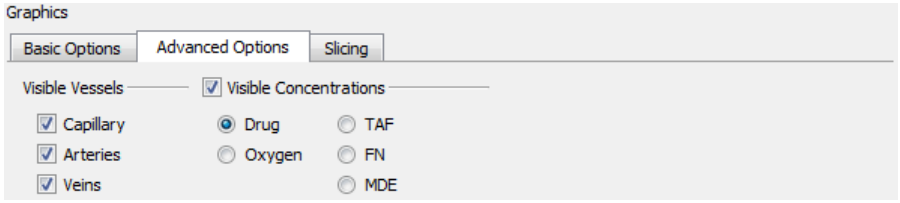

Figure B.15: *bioFLOW* Graphics - Advanced options.

It is also possible to display partial slices of the simulated elements to observe obstructed elements (i.e. vessels, proliferating cells,or tissue blocks) (Figure B.16).

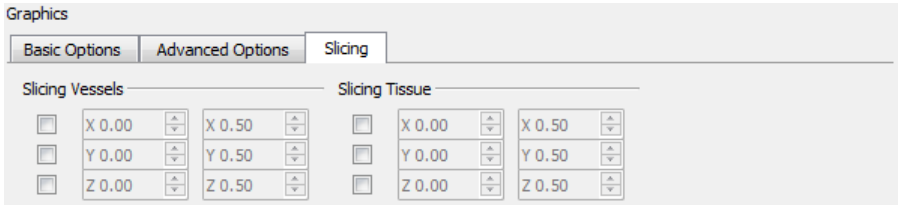

Figure B.16: *bioFLOW* Graphics - Slicing.

Finally, *bioFLOW* provides a plotting window in order to minimise the interaction with third-party software. The user can readily display curves of the simulated data by pointing to the corresponding files and several options have been already included to customise the final figure (Figure B.17).

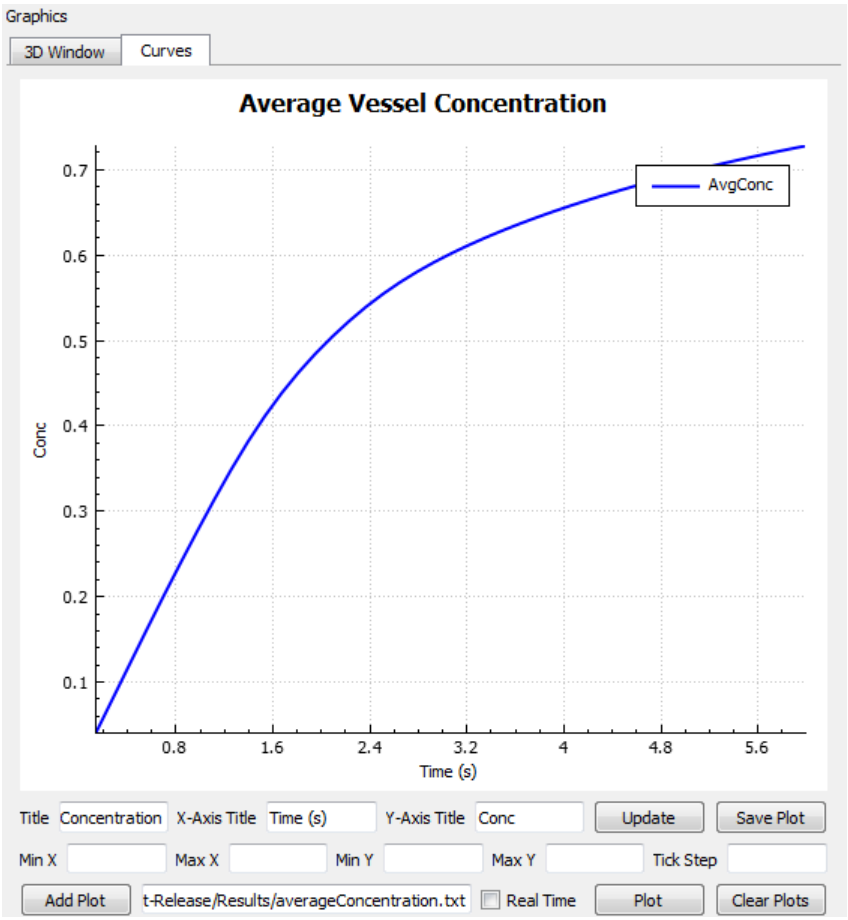

Figure B.17: *bioFLOW* plotting options.

Bibliography

[1] U.S. Energy Information Administration. International Energy Outlook 2016. Technical Report May 2016, 2016.

[2] I. Fatt. The Network Model of Porous Media. *Petroleum Transactions, AIME*, 207:144–181, 1956.

[3] I. Chatzis and F. Dullien. Modelling Pore Structure By 2-D And 3-D Networks With ApplicationTo Sandstones. *Journal of Canadian Petroleum Technology*, 1977.

[4] A.B. Dixit, S R Mcdougall, and K Sorbie. Analysis of Relative Permeability Hysteresis Trends in Mixed-wet Porous Media Using Network Models. *Proceedings of SPE/DOE Improved Oil Recovery Symposium*, 1998.

[5] G. R. Jerauld and S. J. Salter. The effect of pore-structure on hysteresis in relative permeability and capillary pressure: Pore-level modeling. *Transport in Porous Media*, 5(2):103–151, 1990.

[6] G R Jerauld, L E Scriven, and H T Davis. Percolation and conduction on the 3D Voronoi and regular networks: a second case study in topological disorder. *Journal of Physics C: Solid State Physics*, 17(19):3429–3439, 1984.

[7] M. Blunt and P. King. Macroscopic parameters from simulations of pore scale flow. *Physical Review A*, 42(8):4780–4787, 1990.

[8] C. Lin. Three-Dimensional , Randomized , Network Model for Two-Phase Flow through Porous. 28(2):311–324, 1982.

[9] A.A. Heiba, Muhammad Sahimi, L.E. Scriven, and H.T. Davis. Percolation Theory of Two-Phase Relative Permeability. *SPE Reservoir Engineering*, 7(February):123–132, 1992.

[10] W. R. Wise. A new insight on pore structure and permeability. *Water Resources Research*, 28(1):189–198, 1992.

[11] H. Rajaram, L. Ferrand, and M. Celia. Prediction of relative permeabilities for unconsolidated soils using pore-scale network models. *Water Resources Research*, 33(1):43, 1997.

[12] U. Fischer and M. Celia. Prediction of relative and absolute permeabilities for gas and water from soil water retention curves using a pore-scale network model. *Water Resources Research*, 35(4):1089–1100, 1999.

[13] J. Cruichshank, S. Mcdougall, and K. Sorbie. Anchoring methodologies for pore-scale network models: application to relative permeability and capillary pressure prediction. *Petrophysics*, 43(04):365–375, 2002.

[14] I. Bondino, S. R. McDougall, and G. Hamon. A pore-scale modelling approach to the interpretation of heavy oil pressure depletion experiments. *Journal of Petroleum Science and Engineering*, 65(1-2):14–22, 2009.

[15] C.H. Arns, F. Bauget, A. Limaye, A. Sakellariou, T. Senden, A. Sheppard, R. Sok, V. Pinczewski, S. Bakke, L. Berge, P. Oren, and M. Knackstedt. Pore-Scale Characterization of Carbonates Using X-Ray Microtomography. *SPE Journal*, 10(May):26–29, 2005.

[16] C. H. Arns. A comparison of pore size distributions derived by NMR and X-ray-CT techniques. *Physica A: Statistical Mechanics and its Applications*, 339(1-2):159–165, 2004.

[17] D A Coker, S Torquato, and J H Dunsmuir. Morphology and physical properties of Fontainebleu sandstone via a tomographic analysis. *Journal of Geophysical Research*, 101:17497–17506, 1996.

[18] M D Rintoul, S Torquato, C Yeong, D T Keane, S Erramilli, Y N Jun, D M Dabbs, and I A Aksay. Structure and transport properties of a porous magnetic gel via x-ray microtomography. *Physical Review E*, 54(3):2663–2669, 1996.

[19] P. Spanne, J. F. Thovert, C. J. Jacquin, W. B. Lindquist, K. W. Jones, and P. M. Adler. Synchrotron computed microtomography of porous media: Topology and transports. *Physical Review Letters*, 73(14):2001–2004, 1994.

[20] J.H. Dunsmuir, S.R. Ferguson, K.L. D'Amico, and J.P. Stokes. X-Ray Microtomography: A New Tool for the Characterization of Porous Media. *SPE Annual Technical Conference and Exhibition*, 2013.

[21] S. Berg, H. Ott, S. Klapp, A. Schwing, R. Neiteler, N. Brussee, A. Makurat, L. Leu, F. Enzmann, J. Schwarz, M. Kersten, S. Irvine, and M. Stampanoni. Real-time 3D imaging of Haines jumps in porous media flow. *Proceedings of the National Academy of Sciences of the United States of America*, 110(10):3755–9, 2013.

[22] S. Berg, R. T. Armstrong, A. Georgiadis, H. Ott, A. Schwing, R. Neiteler, R. Neiteler, N. Brussee, A. Makurat, M. Rücker, L. Leu, M. Wolf, F. Khan, F. Enzmann, and M. Kersten. Onset of Oil Mobilization and Nonwetting-Phase Cluster-Size Distribution. *Petrophysics*, 56(1):15–22, 2015.

[23] S. Bryant and M. Blunt. Prediction of relative permeability in simple porous media. *Physical Review A*, 46(4):2004–2011, 1992.

[24] S. Bakke. Process Based Reconstruction of Sandstones and Prediction of Transport Properties. *Transport in Porous Media*, 46(2):311–343, 2002.

[25] P. Oren, S. Bakke, and O. Arntzen. Extending Predictive Capabilities to Network Models. *SPE Journal*, 3(December):324–336, 1998.

[26] S. Bakke and P. Ø ren. 3-D Pore-Scale Modelling of Sandstones and Flow Simulations in the Pore Networks. *Society of Petroleum Engineers*, 2(June):136—-149, 1997.

[27] P. Valvatne, M. Piri, X. Lopez, and M. Blunt. Predictive pore-scale modeling of single and multiphase flow. *Upscaling Multiphase Flow in Porous Media: From Pore to Core and Beyond*, 8:23–41, 2005.

[28] M. Piri and M. Blunt. Three-dimensional mixed-wet random pore-scale network modeling of two- And three-phase flow in porous media. I. Model description. *Physical Review E - Statistical, Nonlinear, and Soft Matter Physics*, 71(2):1–30, 2005.

[29] M. Piri and M. Blunt. Three-dimensional mixed-wet random pore-scale network modeling of two- and three-phase flow in porous media. II. Results. *Physical Review E*, 71(2):026302, 2005.

[30] A. Roberts and S. Torquato. Chord-distribution functions of three-dimensional random media: approximate first-passage times of Gaussian processes. *Physical review. E, Statistical physics, plasmas, fluids, and related interdisciplinary topics*, 59(5 Pt A):4953–63, 1999.

[31] P.M. Adler and J-F. Thovert. Real Porous Media: Local Geometry and Macroscopic Properties. *Applied Mechanics Reviews*, 51(9):537, 1998.

[32] C. Yeong and S. Torquato. Reconstructing random media. *Physical Review E*, 57(1):495–506, 1998.

[33] C. Yeong and S. Torquato. Reconstructing random media. II. Three-dimensional media from two-dimensional cuts. *Physical Review E*, 58(1):224–233, 1998.

[34] A. Roberts. Statistical reconstruction of three-dimensional porous media from two-dimensional images. *Physical Review E*, 56(3):11, 1997.

[35] P. M. Adler, C. G. Jacquin, and J. F. Thovert. The formation factor of reconstructed porous media, 1992.

[36] J Quiblier. A new three-dimensional modeling technique for studying porous media. *Journal of Colloid and Interface Science*, 98(1):84–102, 1984.

[37] H. Okabe and M. Blunt. Pore space reconstruction using multiple-point statistics. *Journal of Petroleum Science and Engineering*, 46(1-2):121–137, 2005.

[38] A. Hajizadeh, A. Safekordi, and F. Farhadpour. A multiple-point statistics algorithm for 3D pore space reconstruction from 2D images. *Advances in Water Resources*, 34(10):1256–1267, 2011.

[39] T. Clemens, K. Tsikouris, M. Buchgraber, and L. Castanier. Pore-Scale Evaluation of Polymers Displacing Viscous Oil – Computational Fluid Dynamics Simulation of Micromodel Experiments. *Eighteenth SPE Improved Oil Recovery Symposium*, (May):1–18, 2012.

[40] H. Huang, J. Huang, and X. Lu. Study of immiscible displacements in porous media using a color-gradient-based multiphase lattice Boltzmann method. *Computers and Fluids*, 93:164–172, 2014.

[41] B. Dong, Y. Y. Yan, and W. Z. Li. LBM Simulation of Viscous Fingering Phenomenon in Immiscible Displacement of Two Fluids in Porous Media. *Transport in Porous Media*, 88(2):293–314, 2011.

[42] A. Yiotis, J. Psihogios, M. Kainourgiakis, A. Papaioannou, and A. Stubos. A lattice Boltzmann study of viscous coupling effects in immiscible two-phase flow in porous media. *Colloids and Surfaces A: Physicochemical and Engineering Aspects*, 300(1-2 SPEC. ISS.):35–49, 2007.

[43] K Langaas and Jm Yeomans. Lattice Boltzmann simulation of a binary fluid with different phase viscosities and its application to fingering in two dimensions. *The European Physical Journal B*, 141:133–141, 2000.

[44] S. Chen and G. Doolen. Lattice Boltzmann Method for Fluid Flows. *Annu. Rev. Fluid Mech. 30:329–64*, 30(1):329–64, 1998.

[45] M. Gladkikh and S. Bryant. Prediction of interfacial areas during imbibition in simple porous media. *Advances in Water Resources*, 26(6):609–622, 2003.

[46] G Mason and Dw Mellor. Simulation of drainage and imbibition in a random packing of equal spheres. *Journal of Colloid and Interface Science*, 225:214–225, 1995.

[47] W. Lindquist, S. Lee, D. Coker, K. Jones, and P. Spanne. Medial axis analysis of void structure in three-dimensional tomographic images of porous media. *Journal of Geophysical Research*, 101(B4):8297, 1996.

[48] W. Lindquist and A. Venkatarangan. Investigating 3D geometry of porous media from high resolution images. *Physics and Chemistry of the Earth, Part A: Solid Earth and Geodesy*, 24(7):593–599, 1999.

[49] Z. Jiang. *Quantitative Characterisation of the Geometry and Topology of Pore Space in 3d Rock Images*. PhD thesis, Heriot-Watt University, 2008.

[50] D. Silin, J. Guodong, and T. Patzek. Robust Determination of the Pore Space Morphology in Sedimentary Rocks. *Proceedings of SPE Annual Technical Conference and Exhibition*, (May):69–70, 2003.

[51] D. Silin and T. Patzek. Pore space morphology analysis using maximal inscribed spheres. *Physica A: Statistical Mechanics and its Applications*, 371(2):336–360, 2006.

[52] A. Al-Kharusi and M. Blunt. Network extraction from sandstone and carbonate pore space images. *Journal of Petroleum Science and Engineering*, 56(4):219–231, 2007.

[53] H. Dong and M. Blunt. Micro-CT imaging and pore network extraction. *Earth science and engeneering*, Doctor:217, 2007.

[54] M. Blunt. Flow in porous media - Pore-network models and multiphase flow. *Current Opinion in Colloid and Interface Science*, 6(3):197–207, 2001.

[55] V. Joekar-Niasar and S. M. Hassanizadeh. Analysis of Fundamentals of Two-Phase Flow in Porous Media Using Dynamic Pore-Network Models: A Review. *Critical Reviews in Environmental Science and Technology*, 42(18):1895–1976, 2012.

[56] D. Wilkinson and J. Willemsen. Invasion percolation: a new form of percolation theory. *J. Phys. A: Math. Gen*, 16:3365–3376, 1983.

[57] H. L. Frisch and J. M. Hammersley. Percolation Processes and Related Topics. *Journal of the Society for Industrial & Applied Mathematics*, 11(4):894–918, 1963.

[58] S. R. Broadbent and J. M. Hammersley. Percolation processes. *Mathematical Proceedings of the Cambridge Philosophical Society*, 53(03):642, 1957.

[59] R. Lenormand, C. Zarcone, and A. Sarr. Mechanisms of the displacement of one fluid by another in a network of capillary ducts. *Journal of Fluid Mechanics*, 135:337, 1983.

[60] R. Lenormand and C. Zarcone. Role of Roughness and Edges During Imbibition in Square Capillaries. *Proceedings of SPE Annual Technical Conference and Exhibition*, page 17, 1984.

[61] S.R. McDougall and K.S. Sorbie. The Impact of Wettability on Waterflooding: Pore-Scale Simulation. *SPE Reservoir Engineering*, 10(3):208–213, 1995.

[62] M J Blunt. Pore level modeling of the effects of wettability. *Spe J.*, 2(4):494–510, 1997.

[63] M. Dias and A. Payatakes. Network models for two-phase flow in porous media Part 1. Immiscible microdisplacement of non-wetting fluids. *Journal of Fluid Mechanics*, 164:305–336, 1986.

[64] M. Dias and A. Payatakes. Network models for two-phase flow in porous media Part 2. Motion of oil ganglia. *Journal of Fluid Mechanics*, 164:337–358, 1986.

[65] M. Valavanides, G. Constantinides, and A. Payatakes. Mechanistic Model of Steady-State Two-Phase Flow in Porous Media Based on Ganglion Dynamics. *Transport in Porous Media*, 30(3):267–299, 1998.

[66] M. Valavanides and A. Payatakes. True-to-mechanism model of steady-state two-phase flow in porous media, using decomposition into prototype flows. *Advances in Water Resources*, 24(3-4):385–407, 2001.

[67] H. Princen. Capillary phenomena in assemblies of parallel cylinders: I. Capillary rise between two cylinders. *Journal of Colloid and Interface Science*, 30(3):359–371, 1969.

[68] H. Princen. Capillary phenomena in assemblies of parallel cylinders: II. Capillary rise in Systems with More Than Two Cylinders. *Journal of Colloid and Interface Science*, 30(3), 1969.

[69] H. Princen. Capillary Phenomena in Assemblies of Parallel Cylinders III . Liquid Columns between Horizontal Parallel Cylinders. *Journal of Colloid And Interface Science*, 34(2):171–184, 1970.

[70] T. Patzek. Verification of a Complete Pore Network Simulator of Drainage and Imbibition. *SPE Journal*, 6(02):144–156, 2001.

[71] P. Valvatne and M. Blunt. Predictive pore-scale modeling of two-phase flow in mixed wet media. *Water Resources Research*, 40(7):1–21, 2004.

[72] H. Dong, M. Touati, and M. Blunt. Pore network modeling: analysis of pore size distribution of Arabian core samples. *SPE Middle East Oil & Gas Show and Conference*, 2007.

[73] A. V. Ryazanov, K. S. Sorbie, and M. I J van Dijke. Structure of residual oil as a function of wettability using pore-network modelling. *Advances in Water Resources*, 63:11–21, 2014.

[74] M. I J Van Dijke and K. S. Sorbie. Existence of fluid layers in the corners of a capillary with non-uniform wettability. *Journal of Colloid and Interface Science*, 293(2):455–463, 2006.

[75] M. Sohrabi, D.H. Tehrani, a. Danesh, and G.D. Henderson. Visualization of Oil Recovery by Water-Alternating-Gas Injection Using High-Pressure Micromodels. *SPE Journal*, 9(3):290 – 301, 2004.

[76] D J Element, J H K Masters, N C Sargent, a J Jayasekera, and S G Goodyear. Assessment of Three-Phase Relative Permeability Models Using Laboratory Hysteresis Data. *Proceedings - SPE International Improved Oil Recovery Conference in Asia Pacific*, pages 403–410, 2003.

[77] W. E. Soll, M. A. Celia, and J. L. Wilson. Micromodel studies of three-fluid porous media systems: Pore-scale processes relating to capillary pressure-saturation relationships. *Water Resources Research*, 29(9):2963–2974, 1993.

[78] M J Oak, L E Baker, and D C Thomas. Three-Phase Relative Permeability of Berea Sandstone. *Journal of Petroleum Technology*, 42(8):1054–1061, 1990.

[79] A A Heiba, H T Davis, and L E Scriven. Statistical Network Theory of Three-Phase Relative Permeabilities. *Proceedings of SPE Improved Oil Recovery Symposium, Tulsa, Oklahoma*, 1984.

[80] W V Pinczewski. Pore-Scale Network Modelling of Waterflood by Immiscible Gas Flooding Residual Oil Recovery. *SPE Journal*, 1994.

[81] V. Mani and K. Mohanty. Effect of the Spreading Coefficient on Three-Phase Flow in Porous Media. *Journal of colloid and interface science*, 187(1):45–56, 1997.

[82] G. Pereira. Numerical pore-scale modeling of three-phase fluid flow: Comparison between simulation and experiment. *Physical Review E*, 59(4):4229–4242, 1999.

[83] D. Fenwick and M. Blunt. Three-dimensional modeling of three phase imbibition and drainage. *Advances in Water Resources*, 21(2):121–143, 1998.

[84] C. Laroche, O. Vizika, and F. Kalaydjian. Network modeling as a tool to predict three-phase gas injection in heterogeneous wettability porous media. *Journal of Petroleum Science and Engineering*, 24(2-4):155–168, 1999.

[85] M. I J Van Dijke, K. S. Sorbie, and S. R. McDougall. Saturation-dependencies of three-phase relative permeabilities in mixed-wet and fractionally wet systems. *Advances in Water Resources*, 24(3-4):365–384, 2001.

[86] M. I J Van Dijke, S. R. McDougall, and K. S. Sorbie. Three-phase capillary pressure and relative permeability relationships in mixed-wet systems. *Transport in Porous Media*, 44(1):1–32, 2001.

[87] M. I J Van Dijke and K. S. Sorbie. Pore-scale network model for three-phase flow in mixed-wet porous media. *Physical Review E - Statistical, Nonlinear, and Soft Matter Physics*, 66(4):1–14, 2002.

[88] M. I J Van Dijke and K. S. Sorbie. The relation between interfacial tensions and wettability in three-phase systems: Consequences for pore occupancy and relative permeability. *Journal of Petroleum Science and Engineering*, 33(1-3):39–48, 2002.

[89] M. I J van Dijke and K. S. Sorbie. Pore-scale modelling of three-phase flow in mixed-wet porous media: Multiple displacement chains. *Journal of Petroleum Science and Engineering*, 39(3-4):201–216, 2003.

[90] M. I J van Dijke, K. S. Sorbie, M. Sohrabi, and A. Danesh. Simulation of WAG floods in an oil-wet micromodel using a 2-D pore-scale network model. *Journal of Petroleum Science and Engineering*, 52(1-4):71–86, 2006.

[91] M. I J van Dijke, M. Lorentzen, M. Sohrabi, and K. Sorbie. Pore-Scale Simulation of WAG Floods in Mixed-Wet Micromodels. *SPE Journal*, 15(1):238–247, 2010.

[92] A. Al-Dhahli, S. Geiger, and M. I J Van Dijke. Three-phase pore-network modeling for reservoirs with arbitrary wettability. *SPE Journal*, 18(2):285–295, 2013.

[93] F E Bartell and H J Osterhof. Determination of the Wettability of a Solid by a Liquid. *Industrial & Engineering Chemistry*, 19(11):1277–1280, 1927.

[94] M I J Van Dijke, J E Juri, K S Sorbie, M I J van Dijke, J E Juri, and K S Sorbie. Shortest path algorithm for pore-scale simulation of water-alternating-gas injection. In *ECMOR XI-11th European Conference on the Mathematics of Oil Recovery*, number September 2008, pages 8–11, 2008.

[95] R. G. Larson, L. E. Scriven, and H. T. Davis. Percolation theory of residual phases in porous media. *Nature*, 268(5619):409–413, 1977.

[96] J. Koplik and T.J. Lasseter. Two-Phase Flow in Random Network Models of Porous Media. *Society of Petroleum Engineers Journal*, 25(1):89–100, 1985.

[97] R. Lenormand, E. Touboul, and C. Zarcone. Numerical models and experiments on immiscible displacements in porous media. *Journal of Fluid Mechanics*, 189(-1):165, 1988.

[98] D. A. Kessler, J. Koplik, and H. Levine. *Pattern selection in fingered growth phenomena*, volume 37. 1988.

[99] C. Zhang, M. Oostrom, T. Wietsma, J. Grate, and M. Warner. Influence of viscous and capillary forces on immiscible fluid displacement: Pore-scale experimental study in a water-wet micromodel demonstrating viscous and capillary fingering. *Energy and Fuels*, 25(8):3493–3505, 2011.

[100] S.R. McDougall and K.S. Sorbie. The Combined Effect of Capillary and Viscous Forces on Waterflood Displacement Efficiency in Finely Laminated Porous Media. *SPE Annual Technical Conference and Exhibition*, pages 563–578, 1993.

[101] M. Blunt and H. Scher. Pore-level model of wetting. *Phys. Rev. E*, 52(6):6387–6403, 1995.

[102] E. Aker, K. JØ rgen, A. Hansen, and G. Batrouni. A Two-Dimensional Network Simulator for Two-Phase Flow in Porous Media. *Transport in Porous Media*, 32(2):163–186, 1998.

[103] M. Singh and K. Mohanty. Dynamic modeling of drainage through three-dimensional porous materials. *Chemical Engineering Science*, 58(1):1–18, 2003.

[104] K. Mogensen and E. Stenby. A Dynamic Two-Phase Pore-Scale Model of Imbibition. *Transport in Porous Media*, 32:299–327, 1998.

[105] M. Al-Gharbi and M. Blunt. Dynamic network modeling of two-phase drainage in porous media. *Physical Review E - Statistical, Nonlinear, and Soft Matter Physics*, 71(1):1–16, 2005.

[106] V. Joekar-Niasar and S. Hassanizadeh. Effect of fluids properties on non-equilibrium capillarity effects: Dynamic pore-network modeling. *International Journal of Multiphase Flow*, 37(2):198–214, 2011.

[107] M. Regaieg, S. Mcdougall, I. Bondino, and G. Hamon. Finger thickening during extra-heavy oil waterflooding : simulation and interpretation using pore-scale modelling. (1):1–13, 2013.

[108] M. Regaieg and A. Moncorge. Improving the Computational Efficiency of a Dynamic Pore Network Model - A Hybrid Approach for a Better Performance.

ECMOR XV - 15th European Conference on the Mathematics of Oil Recovery, (September 2016), 2016.

[109] D.J. Ligthelm, G.C.A.M Reijnen, K. Wit, A.J. Weisenborn, and W. Scherpenisse. Critical gas saturation during depressurisation and its importance in the Brent field. *Spe*, (38475):127–134, 1997.

[110] EB Petersen Jr, GS Agaev, and B Palatnik. Determination of critical gas saturation and relative permeabilities relevant to the depressurization of the Statfjord Field. *Symposium of the*, (December):1–15, 2004.

[111] J. J. Sheng, B. B. Maini, R. E. Hayes, and W. S. Tortike. Critical review of foamy oil flow. *Transport in Porous Media*, 35(2):157–187, 1999.

[112] H. Kennedy and C. Olson. Bubble Formation in Supersaturated Hydrocarbon Mixtures. *Journal of Petroleum Technology*, 4(11):271–278, 1952.

[113] D. Wieland and H. Kennedy. Measurements of bubble frequency in cores. *Trans. AIME*, 210:122–125, 1957.

[114] C R Stewart, E B Hunt Jr, F N Schneider, T M Geffen, V J Berry Jr, and Others. The role of bubble formation in oil recovery by solution gas drives in limestones. *Journal of Petroleum Technology*, 5(12):21–28, 1954.

[115] E B Hunt Jr and V J Berry Jr. Evolution of Gas from Liquids Flowing through Porous Media. *AIChE Journal*, 2(4):560–567, 1956.

[116] L L Handy. A Laboratory Study of Oil Recovery by Solution Gas Drive. *Petroleum Transactions, AIME*, 213:310–315, 1958.

[117] A. Chatenever, M. Indra, and J. Kyte. Microscopic Observations of Solution Gas-Drive Behavior. 1959.

[118] J. M. Dumore. Development of Gas-Saturation During Solution-Gas Drive in an Oil Layer Below a Gas Cap. *Society of Petroleum Engineers*, 1970.

[119] A. Danesh, J.M. Peden, D. Krinis, and G.D. Henderson. Pore Level Visual Investigation of Oil Recovery by Solution Gas Drive and Gas Injection. *Proceedings of SPE Annual Technical Conference and Exhibition*, pages 233–241, 1987.

[120] X. Li and Y.C. Yortsos. Visualization and Numerical Studies of Bubble Growth during Pressure Depletion. *SPE Annual Technical Conference and Exhibition*, 1991.

[121] A. Dominguez, S. Bories, and M. Prat. Gas cluster growth by solute diffusion in porous media. Experiments and automaton simulation on pore network. *International Journal of Multiphase Flow*, 26(12):1951–1979, 2000.

[122] X. Li and Y. Yortsos. Critical Gas Saturation: Modeling and Sensitivity Studies. *Society of Petroleum Engineers*, 1993.

[123] J. C. Moulu. Solution-gas drive: experiments and simulation. *Journal of Petroleum Science and Engineering*, 2(4):379–386, 1989.

[124] A. Firoozabadl, B. Ottesen, and M. Mikkelsen. Measurements of supersaturation and critical gas saturation. *SPE Formation Evaluation*, 7(4):337–344, 1992.

[125] I. Tsimpanogiannis and Y. Yortsos. The critical gas saturation in a porous medium in the presence of gravity. *Journal of Colloid and Interface Science*, 270(2):388–395, 2004.

[126] T. Kortekaas and F. van Poelgeest. Liberation of solution gas during pressure depletion of virgin and watered-out oil reservoirs. *SPE Reservoir Engineering*, 6(03):329–335, 1991.

[127] R. Kumar, M. Pooladi-darvish, and T. Okazawa. An Investigation into Enhanced Recovery under Solution Gas Drive in Heavy Oil Reservoirs. *Spe*, 2000.

[128] J. Kamath and R. Boyer. Critical Gas Saturation and Supersaturation in Low-Permeability Rocks. *Society of Petroleum Engineers*, (December):247–253, 1995.

[129] E J Mackay, G D Henderson, D H Tehrani, and a Danesh. The Importance of Interfacial Tension on Fluid Distribution During Depressurization. *SPE Reservoir Evaluation & Engineering*, 1(5):408–415, 1998.

[130] A. Firoozabadi and D. Kashchiev. Pressure and Volume Evolution During Gas Phase Formation in Solution Gas Drive Process (includes associated papers 38340 and 38565). *SPE Journal*, 1(3):219–228, 1996.

[131] H. Sheikha and M. Pooladi-Darvish. Micro Bubbles in Solution-Gas Drive in Heavy Oil: Their Existence and Importance. *Transport in Porous Media*, 93(3):495–516, 2012.

[132] M. Lago, M. Huerta, and R. Gomes. Visualization study during depletion experiments of Venezuelan heavy oils using glass micromodels. *Journal of Canadian Petroleum Technology*, 41(1):41–47, 2002.

[133] B. Maini, B. Busahmin, and K. Vafai. Foamy Oil Flow and its Role in Heavy Oil Production. 103:103–108, 2010.

[134] S.F Jones, G.M Evans, and K.P Galvin. Bubble nucleation from gas cavities - a review. *Advances in Colloid and Interface Science*, 80(1):27–50, 1999.

[135] M. Blander. Bubble Nucleation in Liquids. *Advances in Colloid and Interface Science*, 10:1–32, 1979.

[136] L.E. Scriven. On the dynamics of phase growth. *Chemical Engineering Science*, 10(1-2):1–13, 1959.

[137] M. Blander and J. Katz. Bubble nucleation in liquids. *AIChE Journal*, 21(5):833–848, 1975.

[138] Y.C. Yortsos and M. Parlar. Phase Change in Binary Systems in Porous Media: Application To Solution Gas Drive. *SPE Annual Technical Conference and Exhibition*, 1989.

[139] A. El Yousfi, C. Zarcone, S. Bories, and R. Lenormand. Physical Mechanisms for Bubble Growth during Solution Gas Drive, 1997.

[140] I. Tsimpanogiannis and Y. Yortsos. Model for the gas evolution in a porous medium driven by solute diffusion. *AIChE Journal*, 48(11):2690–2710, 2002.

[141] S R McDougall and E J Mackay. The impact of pressure-dependent interfacial tension and buoyancy forces upon pressure depletion in virgin hydrocarbon reservoirs. *Chemical Engineering Research & Design*, 76(A5):553–561, 1998.

[142] S. R. McDougall and Ken S. Sorbie. Estimation of critical gas saturation during pressure depletion in virgin and waterflooded reservoirs. *Petroleum Geoscience*, 5(3):229–223, 1999.

[143] I. Bondino, S. R. McDougall, and G. Hamon. Pore Network Modeling of Heavy Oil Depressurization: A Parametric Study of Factors Affecting Critical Gas Saturation and Three-Phase Relative Permeabilities. *SPE Journal*, 10(2):196–205, 2005.

[144] C. Ezeuko, S. McDougall, I. Bondino, and G. Hamon. Dynamic Pore-Network Simulator for Modeling Buoyancy-Driven Migration During Depressurization of Oil-Saturated Systems. *SPE Journal*, 15(4):906–916, 2010.

[145] I. Bondino, S. R. McDougall, and G. Hamon. Pore-scale modelling of the effect of viscous pressure gradients during heavy oil depletion experiments. *Journal of Canadian Petroleum Technology*, 50(2):45–55, 2011.

[146] I Bondino, W Kallel, and D Kachuma. Relative permeabilities from simulation in 3D rock models and equivalent pore networks: critical review and way forward. *TOTAL E&P École Polytechnique de Tunisie*, 54(1123123):1–12, 2012.

[147] N. Idowu. *Pore-Scale Modeling: Stochastic Network Generation and Modeling of Rate Effects in Waterflooding*. PhD thesis, University of London, 2009.

[148] J. Hoshen and R. Kopelman. Percolation and cluster distribution. I. Cluster multiple labeling technique and critical concentration algorithm. *Physical Review B*, 14(8):3438–3445, 1976.

[149] X. Li and Y.C. Yortsos. Theory of multiple bubble growth in porous media by solute diffusion. *Chemical Engineering Science*, 50(8):1247–1271, 1995.

[150] E W Dijkstra. A Note on Two Probles in Connexion with Graphs. *Numerische Mathematik*, 1(1):269–271, 1959.

[151] R E Bellman. On a Routing Problem. *Quarterly of Applied Mathematics*, 16(1):87–90, 1958.

[152] M. L. Fredman, R. Sedgewick, D. D. Sleator, and R. E. Tarjan. The Pairing Heap: A New Form of Self Adjusting Heap. *Algorithmica*, 1(1):111–129, 1986.

[153] D. Fenwick and M. Blunt. Network Modeling of Three-Phase Flow in Porous Media. *SPE Journal*, 3(1):5–8, 1998.

[154] N.R. Morrow and J. Buckley. Improved Oil Recovery by Low-Salinity Waterflooding. *Journal of Petroleum Technology*, 63(5):106–112, 2011.

[155] M. Rücker, S. Berg, R. T. Armstrong, a. Georgiadis, H. Ott, a. Schwing, R. Neiteler, N. Brussee, a. Makurat, L. Leu, M. Wolf, F. Khan, F. Enzmann, and M. Kersten. From connected pathway flow to ganglion dynamics. *Geophysical Research Letters*, 42(10):3888–3894, 2015.

[156] S. Youssef, E. Rosenberg, H. Deschamps, R. Oughanem, E. Maire, and R. Mokso. Oil ganglia dynamics in natural porous media during surfactant flooding captured by ultra-fast x-ray microtomography. *International Symposium of the Society of Core Analysts*, (SCA2014-023):1–12, 2014.

[157] A. Ashraf, N. Hadia, O. Torsaeter, and M. Tweheyo. Laboratory Investigation of Low Salinity Waterflooding as Secondary Recovery Process: Effect of Wettability. *SPE Oil and Gas India Conference and Exhibition*, (1998), 2010.

[158] K.J. Webb, C.J.J. Black, and I.J. Edmonds. Low Salinity Oil Recovery - The Role of Reservoir Condition Corefloods. In *13th European Symposium on Improved Oil Recovery - Budapest, Hungary, 25 - 27 April 2005*, 2005.

[159] Y Zhang and N R Morrow. Comparison of Secondary and Tertiary Recovery with Change in Injection Brine Composition for Crude Oil/ Sandstone Combinations. *SPE/DOE Symposium on Improved Oil Recovery*, 2006.

[160] H. O. Yildiz, M. Valat, and N. R. Morrow. Effect of brine composition on wettability and oil recovery of a prudhoe bay crude oil. *Journal of Canadian Petroleum Technology*, 38(1):26–31, 1999.

[161] G.Q. Tang and N. R. Morrow. Influence of brine composition and fines migration on crude oil/brine/rock interactions and oil recovery. *Journal of Petroleum Science and Engineering*, 24(2-4):99–111, 1999.

[162] G.Q. Tang and N.R. Morrow. Salinity, Temperature, Oil Composition, and Oil Recovery by Waterflooding. *SPE Reservoir Engineering*, 12(November):269–276, 1997.

[163] J.S. Buckley and N.R. Morrow. Characterization of Crude Oil Wetting Behavior by Adhesion Tests. In *SPE/DOE Enhanced Oil Recovery Symposium*, pages 871–877, 1990.

[164] G. Bernard. Effect of Floodwater Salinity on Recovery of Oil from Cores Containing Clays. *Spe 1725*, 1967.

[165] K. Spildo, A. Johannessen, and A. Skauge. Low Salinity Waterflood at Reduced Capillarity. *Eighteenth SPE Improved Oil Recovery Symposium*, pages 1–13, 2012.

[166] G P Willhite, R E Pancake, and Murfin Drilling Co. Controlling Water Production Using Gelled Polymer Systems. *Water*, (January 2004):17–21, 2008.

[167] L. Jenn-Tai and R.S. Seright. Further Investigations of Why Gels Reduce Water Permeability More Than Oil Permeability. *SPE Production & Facilities*, 12(November):282–286, 1997.

[168] K.S. Sorbie. *Polymer-Improved Oil Recovery*, volume 28. 1991.

[169] S Buckley and M Leverett. Mechanism of fluid displacement in sands. *Trans. AIME*, 146(1337):107–116, 1942.

[170] A. Skauge, P. Ormehaug, T. Gurholt, B. Vik, I. Bondino, and G. Hamon. 2-D Visualisation of Unstable Waterflood and Polymer Flood for Displacement of Heavy Oil. *Proceedings of SPE Improved Oil Recovery Symposium*, pages 154292–MS, 2012.

[171] S Bolandtaba, A Skauge, and E Watt. Pore Scale Modelling of Linked Polymer Solution (LPS) - A New EOR Process. *15th European Symposium on Improved Oil Recovery*, (April 2009), 2009.

[172] B. Shiran and A. Skauge. Enhanced Oil Recovery (EOR) by Combined Low Salinity Water/Polymer Flooding. *Energy and Fuels*, 27(3):1223–1235, 2013.

[173] H. Mohammadi and G. Jerauld. Mechanistic Modeling of the Benefit of Combining Polymer with Low Salinity Water for Enhanced Oil Recovery. *The SPE Imroved Oil Recovery Symposium-USA*, (2012):1–11, 2012.

[174] E. Alagic and A. Skauge. Combined low salinity brine injection and surfactant flooding in mixed-wet sandstone cores. *Energy and Fuels*, 24(6):3551–3559, 2010.

[175] M. G. Watson, I. Bondino, G. Hamon, and S. McDougall. A Pore-Scale Investigation of Low-Salinity Waterflooding in Porous Media: Uniformly Wetted Systems. *Transport in Porous Media*, 118(2):1–23, 2017.

[176] M. G. Watson, S. R. Mcdougall, M.A. J. Chaplain, A. H. Devlin, and C. A. Mitchell. Dynamics of angiogenesis during murine retinal development : a coupled in vivo and in silico study Dynamics of angiogenesis during murine retinal development : a coupled in vivo and in silico study. *Journal of the Royal Society Interface*, 9(March):2351–2364, 2012.

[177] S. R. McDougall, M. G. Watson, A. H. Devlin, C. A. Mitchell, and M. A J Chaplain. A Hybrid Discrete-Continuum Mathematical Model of Pattern Prediction in the Developing Retinal Vasculature. *Bulletin of Mathematical Biology*, 74(10):2272–2314, 2012.

[178] M. Machado, M. G. Watson, A. H. Devlin, M. A. J. Chaplain, S. R. Mcdougall, and C. A. Mitchell. Dynamics of Angiogenesis During Wound Healing: A Coupled In Vivo and In Silico Study. *Microcirculation*, 18(3):183–197, 2011.

[179] S. R. McDougall, A. R. A. Anderson, and M. A. J. Chaplain. Mathematical modelling of dynamic adaptive tumour-induced angiogenesis: Clinical implications and therapeutic targeting strategies. *Journal of Theoretical Biology*, 241(3):564–589, 2006.

[180] A. Stéphanou, S. R. McDougall, A. R. A. Anderson, and M. A. J. Chaplain. Mathematical modelling of the influence of blood rheological properties upon adaptative tumour-induced angiogenesis. *Mathematical and Computer Modelling*, 44(1-2):96–123, 2006.

[181] S. R. McDougall, A. R. A. Anderson, M. A. J. Chaplain, and J. A. Sherratt. Mathematical Modelling of Flow Through Vascular Networks: Implications for Tumour-induced Angiogenesis and Chemotherapy Strategies. *Bulletin of Mathematical Biology*, 64(4):673–702, 2002.

[182] A. Stéphanou, S. R. McDougall, A. R. A. Anderson, and M. A. J. Chaplain. Mathematical modelling of flow in 2D and 3D vascular networks: Applications to anti-angiogenic and chemotherapeutic drug strategies. *Mathematical and Computer Modelling*, 41(10):1137–1156, 2005.

[183] A. Boujelben, M. G. Watson, S. R. Mcdougall, Y. Yen, E. R. Gerstner, C. Catana, T. Deisboeck, T. Batchelor, D. Boas, B. Rosen, J. Kalpathy-cramer, and M. A. J. Chaplain. Multimodality imaging and mathematical modelling of drug delivery to glioblastomas. *Interface focus*, 6(20160039), 2016.

[184] R. Stupp, M. Hegi, W. Mason, M. van den Bent, M. Taphoorn, R. C. Janzer, S. K. Ludwin, A. Allgeier, B. Fisher, K. Belanger, P. Hau, A. A. Brandes, J. Gijtenbeek, C. Marosi, C. Vecht, K. Mokhtari, P. Wesseling, S. Villa, E. Eisenhauer, T. Gorlia, M. Weller, D. Lacombe, J. G. Cairncross, and R. Mirimanoff. Effects of radiotherapy with concomitant and adjuvant temozolomide versus radiotherapy alone on survival in glioblastoma in a randomised phase III study: 5-year analysis of the EORTC-NCIC trial. *The Lancet Oncology*, 10(5):459–466, 2009.

[185] P. Wen and S. Kesari. Malignant Gliomas in Adults — NEJM. *Malignant gliomas in adults*, pages 492–507, 2008.

[186] L. Gagnon, S. Sakad i, F. Lesage, J. J. Musacchia, J. Lefebvre, Q. Fang, M. a. Yucel, K. C. Evans, E. T. Mandeville, J. Cohen-Adad, J. R. Polimeni, M. a. Yaseen, E. H. Lo, D. N. Greve, R. B. Buxton, a. M. Dale, a. Devor, and D. a. Boas. Quantifying the Microvascular Origin of BOLD-fMRI from First Principles with Two-Photon Microscopy and an Oxygen-Sensitive Nanoprobe. *Journal of Neuroscience*, 35(8):3663–3675, 2015.

[187] V. Srinivasan, S. Sakadžić, I. Gorczynska, S. Ruvinskaya, W. Wu, J. Fujimoto, and D. Boas. Quantitative cerebral blood flow with Optical Coherence Tomography. *Optics Express*, 18(3):2477, 2010.

[188] G. Parker, C. Roberts, A. Macdonald, G. Buonaccorsi, S. Cheung, D. Buckley, A. Jackson, Y. Watson, K. Davies, and G. Jayson. Experimentally-derived functional form for a population-averaged high-temporal-resolution arterial input function for dynamic contrast-enhanced MRI. *Magnetic Resonance in Medicine*, 56(5):993–1000, 2006.